

# The last stages of star formation in the dwarf spheroidal galaxy Sextans

THÈSE N° 6643 (2015)

PRÉSENTÉE LE 3 JUILLET 2015  
À LA FACULTÉ DES SCIENCES DE BASE  
LABORATOIRE D'ASTROPHYSIQUE  
PROGRAMME DOCTORAL EN PHYSIQUE

ÉCOLE POLYTECHNIQUE FÉDÉRALE DE LAUSANNE

POUR L'OBTENTION DU GRADE DE DOCTEUR ÈS SCIENCES

PAR

Romaine THELER

acceptée sur proposition du jury:

Prof. V. Savona, président du jury  
Prof. G. Meylan, Dr P. Jablonka, directeurs de thèse  
Prof. G. Meynet, rapporteur  
Dr L. Mashonkina, rapporteur  
Prof. A. Bay, rapporteur



ÉCOLE POLYTECHNIQUE  
FÉDÉRALE DE LAUSANNE

Suisse  
2015



Marcher en nous-même  
à la recherche d'une étoile.  
— Antoine de Saint-Exupéry





# Acknowledgements

I would like to thank first my co-director Dr. Pascale Jablonka for her support, motivation, patience, and enthusiasm. My thanks also go to Dr. Pierre North who also followed my research and transmitted his knowledge.

Besides, I am grateful to International Space Science Institute (ISSI) in Bern for supporting and funding the international team *First stars in dwarf galaxies* and to all the people I have met during these workshops.

Finalemnt je tiens à adresser un grand merci à mes parents qui m'ont soutenue durant ces 4 longues années.



# Preface

Auguste Comte affirmait en 1829, dans la dix-neuvième leçon de son cours de philosophie positive : *"Les astres sont ainsi, de tous les êtres naturels, ceux que nous pouvons connaître sous les rapports les moins variés. Nous concevons la possibilité de déterminer leurs formes, leur distance et leurs mouvements tandis que nous ne saurions jamais étudier par aucun moyen leur composition chimique ou leur structure minéralogique, et à plus forte raison la nature des corps organisés qui vivent à leur surface... Nos connaissances positives par rapport aux astres sont nécessairement limitées à leurs seuls phénomènes géométriques et mécaniques, sans pouvoir nullement embrasser les autres recherches physiques, chimiques, physiologiques et même sociales que comportent les êtres accessibles à tous nos divers moyens d'observation. "*

N'oublions donc pas que ... Toute *vérité* scientifique n'est vraie que jusqu'à preuve de son contraire.



# Abstract

This thesis is anchored in the research of better understanding of the chemical evolution of galaxies. Many dwarf spheroidal galaxies are orbiting the Milky Way displaying various star formation histories. The formation of these dwarf galaxies and the drivers of their evolution are still not well understood.

We studied in detail one of them, Sextans, a low mass dwarf spheroidal galaxy composed of an old population. 90% of Sextans stars were formed 11-14  $10^9$  years (Gyr) ago (Lee et al. 2009). Battaglia et al. (2011) show the presence of a radial metallicity gradient in Sextans considering observation based on intermediate resolution spectroscopy until the tidal radius. For a projected radius  $R < 0.8$  deg stars cover the whole range of  $[\text{Fe}/\text{H}]$ , while for  $R > 0.8$  deg all stars are metal-poor  $[\text{Fe}/\text{H}] < -2.2$  dex. Due to its distance and its low surface brightness high resolution spectra are required to obtain accurate abundances.

Up to recently only 14 Sextans stars have been observed in high resolution spectroscopy (Shetrone et al. 2001; Aoki et al. 2009; Tafelmeyer et al. 2010; Honda et al. 2011) but in majority they were focused only on extremely metal-poor stars. In order to understand the chemical evolution of Sextans we needed to study a statistically significant sample of stars covering a larger metallicity range. This has been done in this work based on the largest high resolution spectroscopic sample of 87 red giant branch stars ever obtained in such low mass dwarf spheroidal galaxies. Our sample of stars located in the center of Sextans displays a large metallicity distribution ranging from -1.0 dex to -3.5 dex. We derived abundances of 10 elements : 3  $\alpha$ -elements (Mg, Ca and Ti), 5 iron-peak elements (Sc, Cr, Mn, Co and Ni) and 2 neutron-capture elements (Ba and Eu).

Combining the results we had the first picture of the chemical evolution of Sextans. From  $[\alpha/\text{Fe}]$  distribution reflecting the ratio between supernovae  $[\text{SNeII}/\text{SNeIa}]$ , we found that the domination of SNeIa in chemical evolution occurred around  $[\text{Fe}/\text{H}] = -2.0$  dex. A lower knee than for Fornax and Sculptor suggests that star formation was less efficient in Sextans in agreement with their respective estimated mass. The absence of intrinsic scatter in  $[\alpha/\text{Fe}]$  showed that in the center of Sextans the interstellar medium has been homogeneously enriched through star formation. Some hypothesis like tidal interactions with the Milky Way could explain this homogeneous enrichment in the center of the galaxy and the metallicity gradient toward the outskirts. Abundances in iron-peak elements and neutron-capture ele-

## **Preface**

---

ments give new observational constraints for a better understanding of the various elements nucleosynthesis sources.

Key words: galaxy evolution, dwarf galaxies, Local Group, Sextans, chemical abundances, stellar evolution

# Résumé

Cette thèse s'inscrit dans la recherche d'une meilleure compréhension de l'évolution chimique des galaxies. De nombreuses galaxies naines sphéroïdales orbitant autour de la Voie Lactée présentent des histoires de formation stellaires différentes. La formation de ces galaxies naines et les mécanismes régissant leur évolution ne sont pas encore bien compris.

Nous avons étudié en détails l'une d'entre elles, Sextans, une galaxie naine sphéroïdale de relativement faible masse composée d'une population stellaire âgée. En effet 90% des étoiles de Sextans ont été formées il y a 11 à 14 milliards d'années (Lee et al. 2009). Battaglia et al. (2011) montre la présence d'un gradient radial de métallicité dans Sextans en considérant des observations jusqu'à la limite de Roche basées sur de la spectroscopie à moyenne résolution. Pour un rayon projeté de  $R < 0.8$  deg, les étoiles couvrent toute la palette de métallicité tandis que pour  $R > 0.8$  deg toutes les étoiles ont une métallicité plus basse que  $[Fe/H] = -2.2$  dex. A cause de sa distance et de sa faible brillance de surface, des spectres à haute résolution sont nécessaire à l'obtention d'abondances correctes.

Jusqu'à récemment, seulement 14 étoiles avaient été observées à haute résolution dans Sextans (Shetrone et al. 2001; Aoki et al. 2009; Tafelmeyer et al. 2010; Honda et al. 2011). Cependant ce sont en majorité des étoiles de très faible métallicité. Pour pouvoir comprendre l'évolution chimique de Sextans nous avons besoin d'étudier un échantillon statistiquement grand couvrant une grande gamme de métallicité. C'est ce qui a été réalisé dans ce travail qui se base sur le plus grand échantillon à haute résolution jamais observé dans une galaxie naine de faible masse et composé de 87 géantes rouges. Les étoiles de notre échantillon se trouvent dans la partie centrale de Sextans et montrent une distribution en métallicité allant de -1.0 dex à -3.5 dex. Nous avons dérivé les abondances de 10 éléments : 3 éléments  $\alpha$  (Mg, Ca and Ti), 5 éléments du pic du fer (Sc, Cr, Mn, Co and Ni) et 2 éléments de capture par neutrons (Ba and Eu).

En combinant les résultats nous avons obtenu une première compréhension de l'évolution chimique de Sextans. De la distribution des éléments  $\alpha$ , reflétant le rapport entre les supernovae [SNeII/SNeIa], nous avons observé que la domination des SNeIa sur les SNeII dans l'évolution chimique a eu lieu à une métallicité de  $[Fe/H] = -2.0$  dex. Un coude placé à plus basse métallicité que pour Fornax et Sculptor suggère une formation stellaire moins efficace pour Sextans en accord avec l'estimation de leur masse respective. L'absence de dispersion

## Preface

---

intrinsèque en  $[\alpha/\text{Fe}]$  montre qu'au centre de Sextans le milieu interstellaire a été enrichi de manière homogène par formation stellaire. L'hypothèse d'interactions de marée avec la Voie Lactée pourrait expliquer l'homogénéité des abondances au centre de la galaxie et le gradient de métallicité. Les abondances obtenues pour les éléments du pic du fer et des éléments de captures de neutrons sont de nouvelles contraintes pour une meilleure compréhension des différents canaux de nucléosynthèse stellaire de ces éléments qui pour l'instant ne sont pas tous compris.

Mots clefs : évolution des galaxies, galaxies naines, Groupe Local, Sextans, abondances chimiques, évolution stellaire



# Contents

<b>Acknowledgements</b>	<b>i</b>
<b>Preface</b>	<b>iii</b>
<b>Abstract (English/Français)</b>	<b>v</b>
<b>List of figures</b>	<b>xiii</b>
<b>List of tables</b>	<b>xvii</b>
<b>1 Introduction: Dwarf galaxies</b>	<b>1</b>
1.1 Galaxy formation theory . . . . .	1
1.1.1 Lambda cold dark matter . . . . .	1
1.1.2 Successes in large scale structures but failures at small scale . . . . .	1
1.2 Inventory of dwarf galaxies in the Local Group . . . . .	3
1.2.1 First observations . . . . .	3
1.2.2 Location of dwarf galaxies in the Local Group . . . . .	3
1.2.3 Definition and morphological description of dwarf galaxies . . . . .	4
1.2.4 Stellar Mass-metallicity relation . . . . .	8
1.2.5 Role of the total initial mass and central density . . . . .	11
1.3 Understanding star formation histories and chemical evolutions . . . . .	12
1.3.1 Color magnitude diagram and age-metallicity degeneracy . . . . .	12
1.3.2 Probe the interstellar medium using red giant branch stars (RGBs) over galaxy history . . . . .	13
1.3.3 Stellar evolution and chemical enrichment . . . . .	13
1.4 Spectroscopy on resolved stellar populations . . . . .	17
1.4.1 First important results . . . . .	17
1.4.2 Four classical dSphs : Fornax, Sculptor, Carina, Sextans . . . . .	17
1.4.3 Other classical dwarfs around the Milky Way . . . . .	22
1.4.4 Ultra faint dwarfs . . . . .	22
1.5 Simulations of chemical evolution . . . . .	23
1.6 Aim of the thesis . . . . .	24
	ix

<b>2</b>	<b>Stellar photospheres</b>	<b>25</b>
2.1	Stellar nucleosynthesis . . . . .	25
2.1.1	Origin of elements . . . . .	25
2.1.2	Elements lighter than iron . . . . .	25
2.1.3	$\alpha$ -elements . . . . .	28
2.1.4	Iron-peak elements . . . . .	29
2.1.5	Neutron-capture elements . . . . .	31
2.2	Lines formation . . . . .	35
2.2.1	Context . . . . .	35
2.2.2	Radiative transfer : equation and solution . . . . .	35
2.2.3	Form of source function . . . . .	37
2.2.4	Shape of spectra line / Line profile . . . . .	38
2.2.5	Absorption coefficients . . . . .	39
2.3	Model atmosphere . . . . .	47
2.3.1	Definition . . . . .	47
2.3.2	Assumption and computation . . . . .	47
2.3.3	Spectroscopic or photometric derivation of $T_{\text{eff}}$ , $\log g$ and $v_{\text{turb}}$ . . . . .	48
<b>3</b>	<b>The dwarf spheroidal galaxy Sextans</b>	<b>51</b>
3.1	Observations with FLAMES/GIRAFFE . . . . .	51
3.1.1	Description of the Fibre Large Array Multi Elements Spectrograph (FLAMES) . . . . .	51
3.1.2	Data sample . . . . .	56
3.2	Data reduction process . . . . .	60
3.3	Selection of stars : our sample . . . . .	77
3.4	Determination of radial velocities . . . . .	77
3.4.1	Doppler-Fizeau effect . . . . .	77
3.4.2	DAOSPEC : a tool to derive radial velocities . . . . .	78
3.4.3	Distribution of the radial velocities . . . . .	81
3.4.4	Binaries . . . . .	81
3.5	Carbon stars . . . . .	83
3.6	Normalization of spectra . . . . .	86
3.7	Estimation of the signal-to-noise ratios . . . . .	89
3.8	Determination of stellar parameters . . . . .	91
3.8.1	Effective temperature . . . . .	91
3.8.2	Surface gravity . . . . .	91
3.8.3	Microturbulence velocity . . . . .	92
3.8.4	Final stellar parameters . . . . .	92
3.9	Metallicity determination method . . . . .	94
3.9.1	Notation . . . . .	94
3.9.2	Two methods of deriving abundances . . . . .	94

3.9.3 Description of the synthesis method . . . . .	95
3.10 Error budget on [Fe/H] . . . . .	103
3.10.1 Systematic errors . . . . .	103
3.10.2 Random errors . . . . .	105
3.11 Remarks on [Fe/H] determination . . . . .	109
3.12 Abundances determination method . . . . .	111
3.13 Error budget on [X/H] . . . . .	114
3.13.1 Systematic errors . . . . .	114
3.13.2 Random errors . . . . .	116
3.14 Analysis of the results . . . . .	119
3.14.1 S08-3 as a benchmark star . . . . .	119
3.14.2 Sub-sample of brightest stars: comparison with results from classical method . . . . .	122
3.14.3 Metallicity distribution function and comparison with Ca II Triplet survey	130
3.14.4 Alpha-elements . . . . .	132
3.14.5 Iron-peak elements . . . . .	142
3.14.6 Neutron-capture elements . . . . .	148
 <b>4 Conclusion</b>	 <b>153</b>
 <b>A An appendix</b>	 <b>155</b>
 <b>Bibliography</b>	 <b>207</b>
 <b>Acronyms</b>	 <b>209</b>
 <b>Curriculum Vitae</b>	 <b>213</b>



# List of Figures

1.1	Location of dwarf galaxies associated with the Milky Way (McConnachie 2012)	5
1.2	Location of dwarf galaxies associated with M31 and isolated dwarf galaxies of the Local Group (McConnachie 2012)	5
1.3	HI fraction in dwarf galaxies as a function of proximity to their giant galaxy (McConnachie 2012)	7
1.4	Structural properties for different types of galaxies : absolute magnitude $M_V$ , central surface brightness $\mu_V$ and half light radius $r_{1/2}$ (Tolstoy et al. 2009)	9
1.5	The stellar mass–metallicity relation for Local Group dwarf galaxies and more massive SDSS galaxies (Kirby et al. 2013)	10
1.6	Properties of the four selected simulated models representing Fornax, Sculptor, Sextans and Carina (Revaz & Jablonka 2012).	15
1.7	Schematic enrichment of $\alpha$ elements in function of metallicity for the MW and several dSphs (de Boer et al. 2014a)	16
2.1	Schematic view of the different nuclear burning phases and the fate of stars in function of the stellar initial mass (Karakas & Lattanzio 2014)	29
2.2	Average binding energy per nucleon in MeV in function of number of nucleons	30
2.3	Solar abundance distribution from Karakas & Lattanzio (2014) using data from Asplund et al. (2009).	33
2.4	Definition of the equivalent width	46
2.5	Observed curve of growth for Fe I line (Lemasle et al. 2007)	46
3.1	Panorama of the ESO VLT observation site.	51
3.2	The map of the current instruments distribution among the four VLT Unit Telescopes.	52
3.3	Picture of the OzPoz fiber positioner	54
3.4	GIRAFFE spectrograph layout	55
3.5	Picture of the GIRAFFE spectrograph	55
3.6	Schematic layout of the MEDUSA spectral format	58
3.7	Example of a raw science exposure frame in setup HR10	59
3.8	Example of a master bias frame in setup HR10.	63

## List of Figures

---

3.9	Example of a master dark frame in setup HR10. . . . .	64
3.10	Example of a master flat frame in setup HR10. . . . .	65
3.11	Example of a extracted de-biased dark-subtracted science frame in setup HR10. . . . .	66
3.12	Example of a extracted de-biased dark-subtracted flat-field frame in setup HR10. . . . .	67
3.13	Example of an arc lamp frame in setup HR10. . . . .	68
3.14	Example of an extracted arc lamp frame in setup HR10. . . . .	69
3.15	Example of an extracted arc lamp frame in setup HR10 after wavelength calibration. . . . .	70
3.16	Example of a de-biased dark-subtracted flat-fielded wavelength calibrated science frame in setup HR10. . . . .	71
3.17	Example of polluted spectrum in setup HR13 with emission lines due to proximity to simultaneous calibration fibers. . . . .	73
3.18	Example of telluric absorption lines in HR10 spectrum of star S08-3 and in HR13 spectrum of star S05-60 . . . . .	75
3.19	Reduced spectra for star S05-10 in the three setups after the old reduction and after the new ESO reduction process . . . . .	76
3.20	Spatial distribution of Sextans targets . . . . .	78
3.21	Color Magnitude Diagram of the Sextans stars . . . . .	79
3.22	Radial velocity distribution of our sample . . . . .	81
3.23	Radial velocity intervals for the 13 probable binaries . . . . .	82
3.24	Spectra in setup HR10 of star S08-111 and of the carbon-star S08-306 . . . . .	84
3.25	Parts of spectrum of S08-3 and the carbon-star S08-306 around carbon molecular lines (CN and C <sub>2</sub> ) . . . . .	85
3.26	Spectra of S08-242 and corresponding continua derived from 2 different techniques . . . . .	87
3.27	HR10 spectrum of S05-10 before and after the normalization and the radial velocity shift. . . . .	88
3.28	Location of the three continuum zones used to define the signal-to-noise ratios in each setup . . . . .	89
3.29	Histogram of the signal-to-noise ratios per setup and in average. . . . .	90
3.30	Relations between the effective temperatures and the surface gravities for our members . . . . .	93
3.31	Relations between the surface gravities and the micro-turbulence velocities for our members . . . . .	93
3.32	Example of convolutions of a synthetic spectrum with gaussian functions . . . . .	97
3.33	Location of selected intervals around Fe I lines in setup HR10 . . . . .	99
3.34	Location of selected intervals around Fe I lines in setup HR13 . . . . .	100
3.35	Location of selected intervals around Fe I lines in setup HR14 . . . . .	101
3.36	Curve of $\chi^2$ for [Fe/H] determination for stars S05-47, S08-250 and S08-292 . . . . .	102
3.37	Systematic errors on surface gravities, micro-turbulence velocities and metallicities due to a variation of $\pm 100$ K of the effective temperatures . . . . .	104

3.38 Distribution of 1000 couples of ( $\chi_{min}^2$ , [Fe/H]) obtained by Monte Carlo simulated spectra for star S08-38. . . . .	106
3.39 Distribution of 1000 couples of ( $\chi_{min}^2$ , [Fe/H]) obtained on Monte Carlo simulated spectra for star S08-292. . . . .	107
3.40 Random errors of [Fe/H] in function of average signal-to-noise ratios . . . . .	108
3.41 Deviation between $T_{eff}$ and $\log g$ and the closest values adopted in the synthetic spectra library. . . . .	109
3.42 Impact of redetermining the stellar parameters using the final [Fe/H] . . . . .	110
3.43 Curve of $\chi^2$ for [Mg/H] determination for star S05-47 . . . . .	112
3.44 Curve of $\chi^2$ for [Ba/H] determination for star S08-250 . . . . .	112
3.45 Parts of observed spectrum in setup HR10 of three stars S08-6, S08-242 and S05-67 with their best fitted synthetic spectrum. . . . .	113
3.46 Systematic errors of [X/H] . . . . .	115
3.47 Distribution of 1000 couples of ( $\chi_{min}^2$ , [Ca/H]) obtained by Monte Carlo simulated spectra for star S08-38. . . . .	116
3.48 Distribution of 1000 couples of ( $\chi_{min}^2$ , [Ti2/H]) obtained by Monte Carlo simulated spectra for star S08-38. . . . .	117
3.49 Random errors for [X/H] in function of signal-to-noise ratios . . . . .	118
3.50 Abundance distribution of star S08-3 over three studies. . . . .	120
3.51 Complete spectra of star S08-3 with its best fitted synthetic spectra. . . . .	121
3.52 Comparison with [Fe/H] obtained from classical method for a sub-sample of 11 brightest stars . . . . .	123
3.53 Comparison of iron equivalent widths for stars S08-3 and S08-6 derived from classical and synthesis methods . . . . .	124
3.54 Relations linked with the variation of micro-turbulence velocities for the sub-sample of 11 brightest stars. . . . .	126
3.55 Dependence between variations of [Fe/H] with differences of $T_{eff}$ and $\log g$ for stars presenting a $\Delta v_{turb} < 0.1$ among the sub-sample of 11 brightest stars . . .	127
3.56 Comparison between abundances [X/H] derived by EQW and synthesis method for a sample of highest S/N stars. . . . .	128
3.57 Histogram of differences between abundances [X/H] derived by EQW and synthesis method for a sample of highest S/N stars. . . . .	129
3.58 Metallicity Distribution Function of the Sextans stars . . . . .	131
3.59 Comparison of [Fe/H] between our values and values derived from CaT survey. . . . .	131
3.60 The distribution of $[\alpha/Fe]$ for Sextans and Milky Way stars. . . . .	133
3.61 Comparison of Mg line for the three outliers in [Mg/Fe] . . . . .	135
3.62 The distribution of $[\alpha/Fe]$ for Sextans, the Milky Way and other dwarf galaxies stars. . . . .	137

## List of Figures

---

3.63	Position of the knee in the [Mg/Fe] distribution of several dwarf galaxies as a function of absolute magnitude. . . . .	140
3.64	The distribution of [Sc/Fe] and [Ni/Fe] for Sextans and Milky Way stars. . . . .	145
3.65	The distribution of [Sc/Fe] and [Ni/Fe] for Sextans, the Milky Way and other dwarf galaxies stars. . . . .	145
3.66	The distribution of [Cr/Fe] and [Mn/Fe] for Sextans and Milky Way stars. . . . .	146
3.67	The distribution of [Cr/Fe] and [Mn/Fe] for Sextans, the Milky Way and other dwarf galaxies stars. . . . .	146
3.68	The distribution of [Co/Fe] for Sextans and Milky Way stars. . . . .	147
3.69	The distribution of [Co/Fe] for Sextans, the Milky Way and other dwarf galaxies stars. . . . .	147
3.70	The distribution of [Ba/Fe], [Eu/Fe], and [Ba/Eu] for Sextans and Milky Way stars.	150
3.71	The distribution of [Ba/Fe], [Eu/Fe], and [Ba/Eu] for Sextans, the Milky Way and other dwarf galaxies stars. . . . .	151



# List of Tables

1.1	Properties of four classical dSphs : Fornax, Sculptor, Sextans, Carina . . . . .	18
3.1	Characteristics of the three FLAMES/GIRAFFE gratings. . . . .	56
3.2	Observations log . . . . .	57
3.3	Distribution of the fibers for the three setups and the two Medusa plates. . . . .	58
3.4	Scatter and mean of errors on $[\alpha/\text{Fe}]$ for Mg, Ca and Ti for Sextans stars with $[\text{Fe}/\text{H}] > -2.0$ dex. . . . .	142
3.5	Scatter and mean of errors on $[\alpha/\text{Fe}]$ for Mg, Ca and Ti for Sculptor stars with $[\text{Fe}/\text{H}] > -1.8$ dex. . . . .	142
A.1	Position, photometry and radial velocities of our targets. . . . .	156
A.2	Color temperatures, bolometric corrections, bolometric magnitudes, Ca II triplet $[\text{Fe}/\text{H}]$ of our targets. . . . .	161
A.3	Signal-to-noise ratios of our targets. . . . .	164
A.4	List of stars polluted by simultaneous calibration fibres. . . . .	167
A.5	Radial velocities measured by DAOSPEC in each setup and in average. . . . .	168
A.6	Line list of the studied elements. . . . .	172
A.7	Stellar parameters of our members : effective temperatures, surface gravities, micro-turbulence velocities and metallicities. . . . .	180
A.8	Atomic abundances for Fe, Mg, and Ca. . . . .	183
A.9	Atomic abundances for Sc, Ti1 and Ti2. . . . .	186
A.10	Atomic abundances for Cr, Mn and Co. . . . .	189
A.11	Atomic abundances for Ni, Ba and Eu. . . . .	192
A.12	Results of the classical analysis for the sub-sample of high signal-to-noise stars: stellar parameters and abundances for Mg, Ca, Sc, Ti. . . . .	195
A.13	Results of the classical analysis for the sub-sample of high signal-to-noise stars: abundances for Cr, Mn, Co, Ni, Ba and Eu. . . . .	196



# 1 Introduction: Dwarf galaxies

## 1.1 Galaxy formation theory

### 1.1.1 Lambda cold dark matter

Emerging in early 1980s the cold dark matter (CDM) hypothesis has become a key aspect of the cosmic structure formation theory proposing growth of structures by hierarchical clustering. Cold dark matter is composed of weakly interacting particles which preserved primordial fluctuations down to very small scales due to their small velocity dispersion in the early universe.

Born from the combination of hierarchical structure formation theory with important results as the proof of cosmic acceleration with supernovae of type Ia (SNeIa) observations (Perlmutter et al. 1998; Riess et al. 1998; Schmidt et al. 1998) and the cosmic microwave background (CMB) evidence for a flat universe, the  $\Lambda$  cold dark matter ( $\Lambda$ CDM) is considered today as the standard model of cosmology. This model is characterized by cold dark matter, inflationary initial conditions and a cosmological constant  $\Lambda$ .

### 1.1.2 Successes in large scale structures but failures at small scale

Predictions of the  $\Lambda$ CDM model of hierarchical galaxy formation are tested comparing numerical simulations with observations. Large scale properties of our Universe are successfully reproduced by predictions of the  $\Lambda$ CDM scenario like the presence of anisotropies in the CMB or the distribution of the large-scale structures but some controversies emerged on small scales. Two major problems occurred : the *cuspy-core problem*, and the *missing satellite problem* also referred as the *too big to fail problem*.

The former indicates that the theory over-predicts the quantity of dark matter (DM) in the central few kilo parsec (kpc) of galaxies. Indeed  $\Lambda$ CDM simulations lead to cuspy DM halo

profiles, in contradiction with observed galaxy rotation curves showing a relatively constant core density distribution (Flores & Primack 1994; Moore 1994; Navarro et al. 1997; Moore et al. 1999b). One solution may come from baryonic physics according to Navarro et al. (1996) : episodic gas outflows due to supernovae (SNe) feedback lead to rapid fluctuations of the gravitational potential, energy is then injected in DM particles and less particles cross the center of the halo decreasing its density. Simulations using different code approaches find that episodic SNe feedback could imply a flattening of DM cusp profile (Governato et al. 2012; Pontzen & Governato 2012; Teyssier et al. 2013).

The second tension between observation and simulations concerns the number of substructures : simulated (DM-only) halos retain a large amount of substructures formed by earlier collapse on smaller scales predicting hundreds or thousands of sub-halos. This is inconsistent with the number of observed classical dwarf galaxies (Klypin et al. 1999; Moore et al. 1999a) and more recently discovered ultra faint dwarf galaxies (Willman et al. 2005; Belokurov et al. 2007) forming only a few tens. One possible answer assumes that the majority of sub-halos remain dark invoking two processes related with baryonic physics : a) reionization - the intergalactic gas is heated by the ultraviolet photo-ionizing background suppressing the gas accretion and avoiding formation of luminous matter b) the gas of the low mass halos could be driven out by SNe feedback from the first generation of stars. Boylan-Kolchin et al. (2011) show that the majority of the most massive sub-halos in simulations are too dense to host any of the bright Milky Way (MW) satellites. Numerical simulations of  $\Lambda$ CDM structure formation predict too much mass in the central regions of halos and sub-halos. The DM dominated Milky Way satellites seem to have a lot less dark matter than the simulations would predict.

Instead of baryonic physics two variants of DM physics are also proposed to solve these small scale controversies: warm dark matter (WDM) or self-interacting dark matter (SIDM). In the case of WDM, the DM particles would have in the early universe high enough velocities to erase primordial fluctuations on sub-galactic scales. Despite a better fit to observed galactic rotation curves (but not across the full range of mass, Avila-Reese et al. (2001)) and a better agreement with the number of dwarf satellites, this model is not well favored because in conflicts with Lyman alpha forest and substructures observations (Kuzio de Naray et al. 2010). A more hopeful model could be the SIDM in which frequent elastic scattering in the dense central regions of the halos would redistribute energy and angular momentum leading to an isothermal core of approximatively constant density (Berkert 2000). Numerical simulations of SIDM (Rocha et al. 2013; Peter et al. 2013) show that the cusp-core problem can be solved leaving enough sub-halos.

As no indirect detection of DM via  $\gamma$  ray emission (expected products of DM particles annihilation) observed yet, only upper limits can be derived. During four years The Fermi-LAT Collaboration et al. (2013) looked unsuccessfully for significant  $\gamma$ -rays in 25 Milky Way dwarf satellite galaxies thanks to the Fermi Large Area Telescope, and five of them were imaged without results by the atmospheric Cherenkov telescopes of the High Energy Stereoscopic

---

## 1.2. Inventory of dwarf galaxies in the Local Group

System (H.E.S.S.) collaboration (Abramowski et al. 2014).

As no definitive conclusion can be given today, more observations and progress in simulations are needed to constrain theories. In particular, understanding the evolution and star formation history (SFH) of dwarf galaxies is essential to improve our knowledge about the structure formation mechanisms.

## 1.2 Inventory of dwarf galaxies in the Local Group

### 1.2.1 First observations

Historically, the first observations of dwarf galaxies date from the 18th century. C. Messier first then W. Herschel, J. Herschel, E.E. Barnard, and M. Wolf discovered early-type dwarf galaxies around Andromeda galaxy (M31) (M3, NGC 205, NGC 185, etc.) . All were simply cataloged at that time as *faint nebulae* without any notion of distance. The extra-galactic origin of these objects was only understood in the end of the 1920s after the application of the Cepheid distance scale to the galaxy NGC 6822 by E. Hubble in 1926. It was not until the 1938 that H. Shapley discovered the first dwarf galaxies around the MW, Fornax and Sculptor. This was the beginning of large campaigns of observation aimed to extend catalogs of observation of dwarf galaxies until beyond the Local Group (LG).

### 1.2.2 Location of dwarf galaxies in the Local Group

The Local Group (physical radius of  $\sim 1.2$  mega parsec (Mpc)) is composed of three massive spiral galaxies : M31 (the Andromeda galaxy), the Milky Way and M33 and about 70 dwarf galaxies grouping preferentially around M31 and the MW according to McConnachie (2012) and references therein. Only two dwarfs (the Pisces and Andromeda XXII) might be companions of the smallest spiral M33. There is apparently an association of marginal dwarf galaxies which seems not to be bound to any spiral galaxy standing far away : NGC 3109, Antila, Sextans A and B, and Leo P (McConnachie 2012; Bernstein-Cooper et al. 2014). Figure 1.1 and 1.2 show the distribution of the MW dwarf galaxies (red circles), M31 dwarfs (blue circles) and remaining isolated dwarf galaxies (green circles) on Aitoff projections from McConnachie (2012). The total number of dwarf galaxies is today unknown but has continuously increased during the last years thanks to deep and wide area sky surveys like the Sloan Digital Sky Survey (SDSS) sensitive to fainter galaxies.

Recently Pawlowski et al. (2012) and Ibata et al. (2013) show that the MW and M31 are surrounded by thin planes of mostly co-orbiting satellite galaxies called respectively the vast polar structure (VPOS) and the Great Plane of Andromeda (GPoA). The VPOS spreads out to 250 kpc and is oriented perpendicular to the Galactic disk. Most of the MW satellites are co-orbiting in the VPOS and also the young halo globular clusters and streams are aligned with it. This

correlated distribution is inconsistent with the  $\Lambda$ CDM galaxy formation theory which expects a near-isotropic distribution. One possible hypothesis explaining this particular structure could be : a major galaxy interaction implying formation of tidal dwarfs from tidal debris. This leads to a fundamental and unanswered key question : are the progenitors of dwarf galaxies different from progenitors of MW halo and globular clusters (GCs) ?

### 1.2.3 Definition and morphological description of dwarf galaxies

How to define a dwarf galaxy ? The answer to this question is not simple. Several first definitions used the size and the presence of DM to characterize dwarf galaxies (Mateo 1998). Tammann (1994) give a working definition : all galaxies spatially more extended than GCs and fainter than  $M_B \leq -16$  ( $M_V \leq -17$ ) are dwarf galaxies. Variety of dwarf galaxies are then defined according to their morphology and content :

- dwarf spheroidal galaxies (dSphs) : They are devoid of gas and present no sign of on-going star formation (SF). They are composed of intermediate and old stellar populations and are located close to M31 and the MW.
- dwarf elliptical galaxies (dEs) : Gas has been detected in them and they are located close the M31. It seems that they are not present around the MW. They present complex star formation history and exhibit young, intermediate and old stellar populations.
- dwarf irregular galaxies (dIs) : With irregular shapes they are atomic-gas (HI) dominated systems with on-going star formation but old stellar populations have also been detected in them (e.g. in Leo I by Held et al. (2001)). They are preferentially distant from their spiral companion or isolated systems.
- ultra faint dwarf galaxies (UFDs) : They are extremely faint systems presenting low surface brightness.
- ultra cold dwarf galaxies (UCDs) : They have similar compactness to globular clusters, and mainly found in Fornax and Virgo clusters.
- blue compact dwarf galaxies (BCDs) : They are centrally concentrated actively star forming galaxies located beyond the Local Group.

Dwarf galaxies are not randomly distributed in the Local Group. Gas-poor early-type dwarf galaxies (dSphs, dEs) are located close to their giant galaxy (the MW or M31) and on the contrary gas-rich late-type dwarf galaxies (dIs) are located far away. This observation leads to the first indication of a possible morphological evolution. Figure 1.3 presents the HI fraction, expressed as  $M_{HI}/L_V$  in solar units, as a function of proximity to a giant galaxy from

## 1.2. Inventory of dwarf galaxies in the Local Group

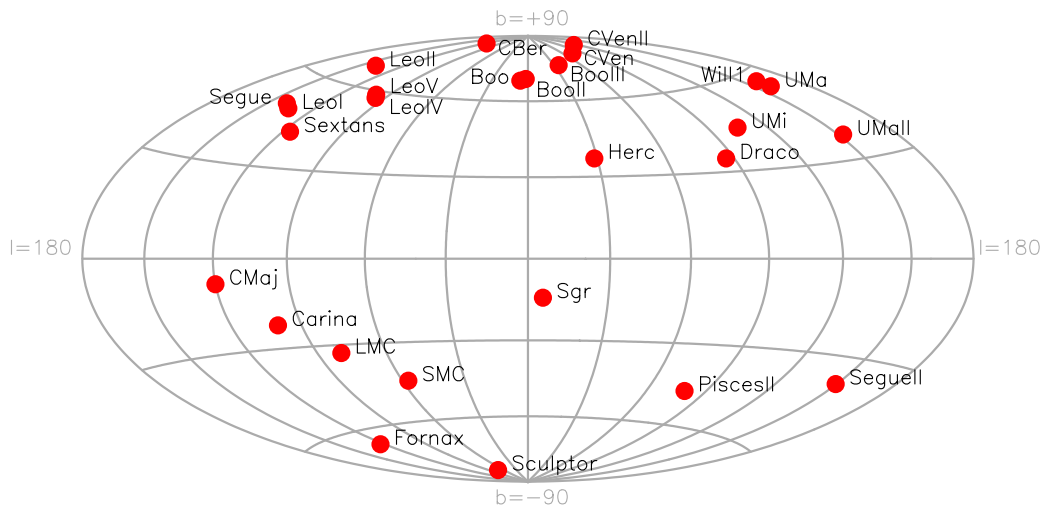


Figure 1.1: Location of dwarf galaxies associated with the MW (red circles) from McConnachie (2012).

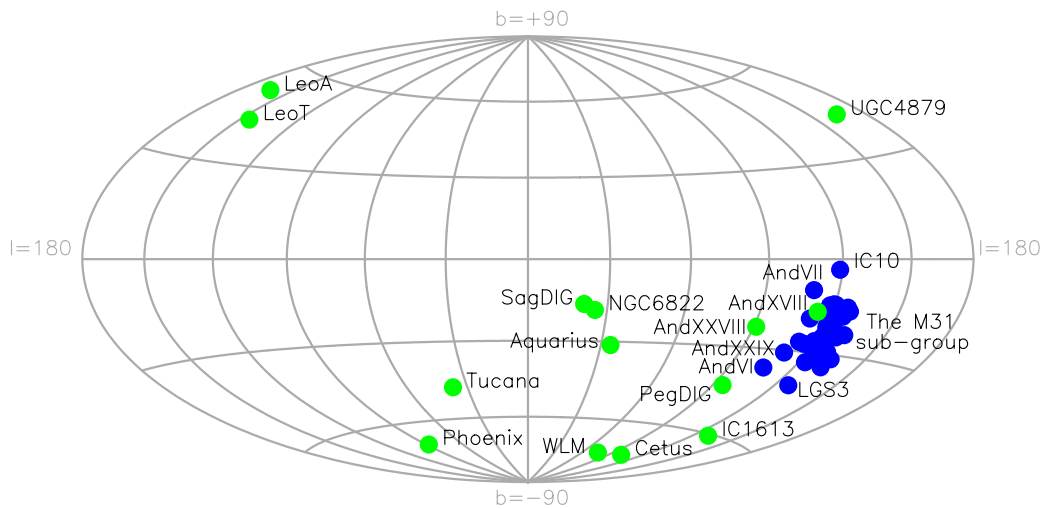


Figure 1.2: Location of dwarf galaxies associated with M31 (blue circles) and isolated dwarf galaxies of the LG (green symbols) from McConnachie (2012).

## Chapter 1. Introduction: Dwarf galaxies

---

McConnachie (2012). The orange arrows represent the gas-deficient galaxies almost all located within the virial radius of MW/M31 indicated by the dashed line. Only two distant dSphs, Cetus and Tucana, are exceptions to this trend. Gas-rich galaxies indicated by blue diamonds are located at larger distances to their giant galaxy. Already Kormendy (1985) proposed that early-type dwarfs are the same as late-type dwarfs but stripped of gas, as they share similar properties.

The major process that sculpts galaxies is gas removal which can be induced by different internal or environmental processes :

- Tidal interactions : between the giant galaxy and its satellites, the best known cases are the Magellanic Clouds and the dSph Sagittarius, the closest dwarfs orbiting the MW.
- SNe feedback : kinetic energy is transferred from SNe to surrounding gas. If the gas velocity is sufficient to over-pass the galaxy potential well the gas can escape.
- Ram pressure stripping : if the intra-cluster medium is dense enough that its ram pressure exceeds its gravitational force then the dwarf moving in this medium could partially or totally lose its gas content.

We know from observations that cold gas ( $T \leq 10^4$  Kelvins (K)) seems to be concentrated within 50 kpc from the MW and M31 (Richter 2012), and hot gas ( $T \geq 10^4$  K) in the outer areas of the LG (Sembach et al. 2003; Gupta et al. 2012). However the densities of these two components are not yet measurable.

Gas removal is the trigger of any transformation and is applied differently depending on the mass, the orbit of the considered dwarf and the medium it is traveling in (Carraro 2014).

Morphological classification of dwarfs is only useful if it is sustained by a physical understanding. From the properties presented in Figure 1.4 taken from Tolstoy et al. (2009) there is no clear distinction between dwarf types and with larger galaxies. In the upper plot they show the absolute magnitude,  $M_V$ , versus central surface brightness,  $\mu_V$ , plane, and in the lower plot the  $M_V$  versus half light radius,  $r_{1/2}$ , plane. The first observation is that dwarf galaxies cover a large range of distances, sizes and surface brightnesses. For the top plot, there are similarities between the early and late-type dwarfs overlapping with BCDs and other larger late-type systems as well as faint spiral galaxy disks. The UFDs are separated but follow the same trend. However there is a distinction for GCs and elliptical galaxies. As they are interacting together and with the MW, the Magellanic Clouds are particular cases : the Large Magellanic Cloud (LMC) is close to low luminous spiral galaxy and the Small Magellanic Cloud (SMC) is rather a larger dI. For the lower plot, there is a clear and expected trend of size increasing with luminosity. There is an overlap between dSphs, dIs and BCDs. UFDs are a bit shifted but this shift could be attributed to difficulties in accurately measuring their size.



## 1.2. Inventory of dwarf galaxies in the Local Group

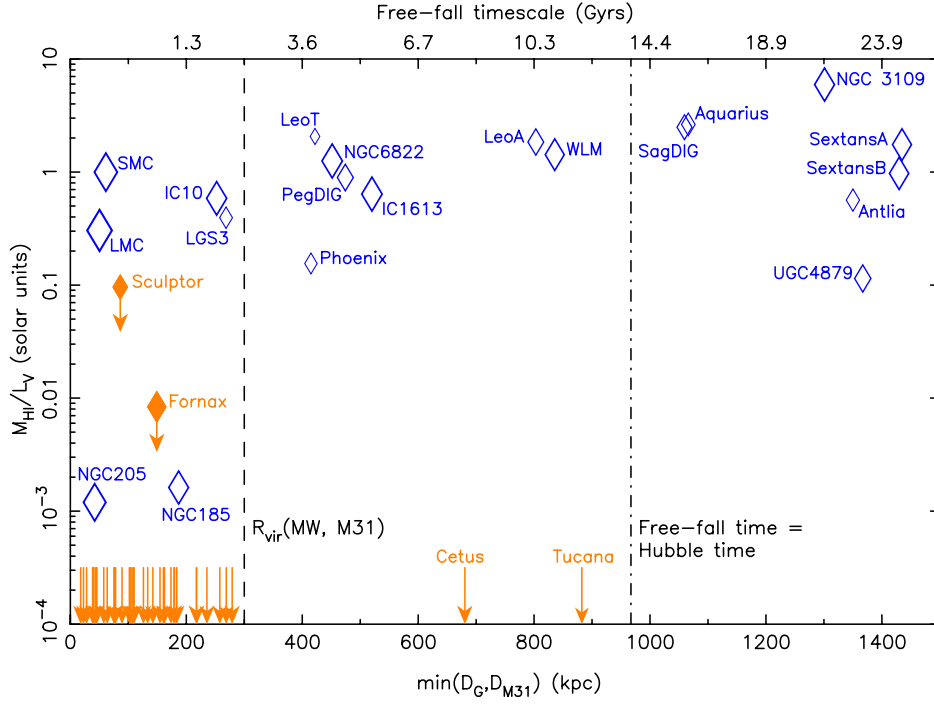


Figure 1.3: HI fraction, expressed as  $M_{HI}/L_V$  in solar units, as a function of proximity to their giant galaxy from McConnachie (2012). Blue diamonds present galaxies with confirmed HI content while orange arrows indicate the separation of gas-deficient galaxies from either the MW or M31. Sculptor and Fornax are indicated by orange diamond and arrows due to ambiguous presence of HI in them. The symbols are size-coded in function of absolute visual magnitudes. The vertical dashed line corresponds to the approximate virial radius of the MW/M31. The top x-axis gives the time required for a galaxy to accelerate and reach the MW/M31 from rest. The dot-dashed line represents the separation at which this time equals a Hubble time.

Dwarf galaxies are no different from bigger galaxies as far as galactic properties are concerned. The only reason to classify them as dwarf galaxies is to specifically study these simpler systems at small scale. For example gas-poor dwarf kinematics can be only inferred from stellar velocity dispersion. For gas-rich dwarfs, kinematics can be estimated easily from the gas but not from red giant branch stars velocities due to larger distances.

### 1.2.4 Stellar Mass-metallicity relation

In comparison with our Galaxy, dwarf galaxies present metal-poor content. Kirby et al. (2013) show the impressive uniformity of the mass-metallicity relation (MZR) measured for 15 MW dSphs, 7 LG dIs and 13 M31s dSphs :  $Z_* \propto M_*^{0.30 \pm 0.02}$ . The MZR originates from two relations : luminosity-mass and luminosity-metallicity. Figure 1.5 presents the relation between the average metallicity and the mass of the studied dwarfs in Kirby et al. (2013) and adding data from massive galaxies of the SDSS from Gallazzi et al. (2005). Although the techniques for determining both mass and metallicity differ between the two studies, the MZR is roughly continuous over nine orders of magnitude in stellar mass. This relation can be explained in different ways : i) retention of metals in the galaxies gravitational potential wells (Dekel & Silk 1986) : low mass galaxies have shallow potential wells that can not resist expulsion of gas by feedback mechanisms. Larger fraction of gas is expelled for low mass halo due to SNe feedback and subsequent population of stars are born from metal-poor gas than in case of more massive halo. ii) correlation between star formation efficiency and stellar mass (Matteucci 1994; Calura et al. 2009; Magrini et al. 2012; Pipino et al. 2013) : rapidly evolving massive galaxies can reach high metallicity through high stellar mass and low gas fraction. Low mass galaxies slowly evolving can have high gas reservoir diluting metals created by stellar population leading to a metal-poor medium. However this second interpretation is less favored because it is not quite coherent with the gas fraction of all galaxies.

The average metallicity of a dwarf galaxy depends on its stellar mass, but the galaxy type is linked to the metallicity distribution. They show after comparing metallicity distribution functions with simplistic chemical evolution models that dIs resemble simple leaky box chemical evolution models whereas dSphs require an additional parameter, such as gas accretion to be better fitted.

Kirby et al. (2013) proposed that luminous dSphs were forming stars when they entered the potential well of the MW. Then due to tidal or ram pressure stripping their SF would be stopped rapidly. The stop of chemical evolution of low luminous dSphs could be due to either reionization or internal mechanisms before they fell into the MW potential well.

This universal relation shows an inextricable link between the retention of metals and acquisition of stellar mass. Despite various signatures of SFH due to metal and gas loss the MZR is preserved over a large range of stellar masses.

## 1.2. Inventory of dwarf galaxies in the Local Group

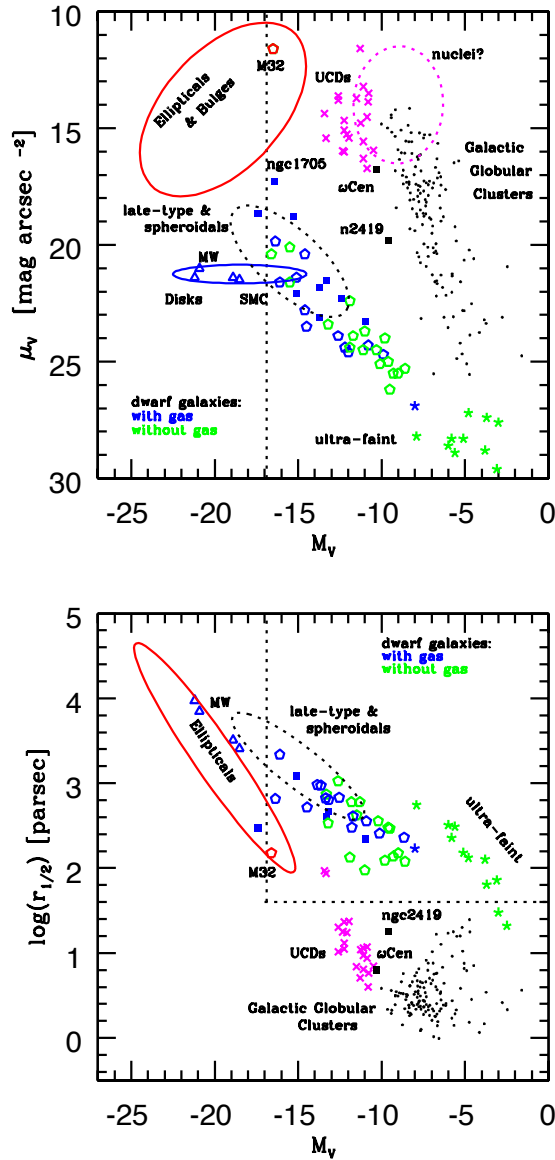


Figure 1.4: Tolstoy et al. (2009) plotted the relationships between structural properties for different types of galaxies (after Kormendy (1985); Binggeli (1994); Kormendy & Fisher (2008)). The dotted lines represent the classical limits of the dwarf galaxy class as defined by Tammann (1994). Upper plot : absolute magnitude  $M_V$  versus central surface brightness  $\mu_V$ . Lower plot : absolute magnitudes  $M_V$  versus half light radius  $r_{1/2}$ . The colored ellipses indicates the typical locations of Elliptical galaxies & bulges (red), spiral galaxy disks (blue), galactic nuclei (dashed magenta) and large early (spheroidal) and late-type systems (dashed black). Small black points correspond to individual Galactic globular clusters. Blue open triangles represent M31, the MW, M 33 and LMC while blue solid squares mark some BCDs having well studied color magnitude diagrams. Magenta crosses show UCDs observed in the Virgo and Fornax clusters. Open pentagons are used to plot dwarf galaxies : gas-rich in blue and gas-poor in green. The recently discovered UFDs follow the same color code with stars symbols.

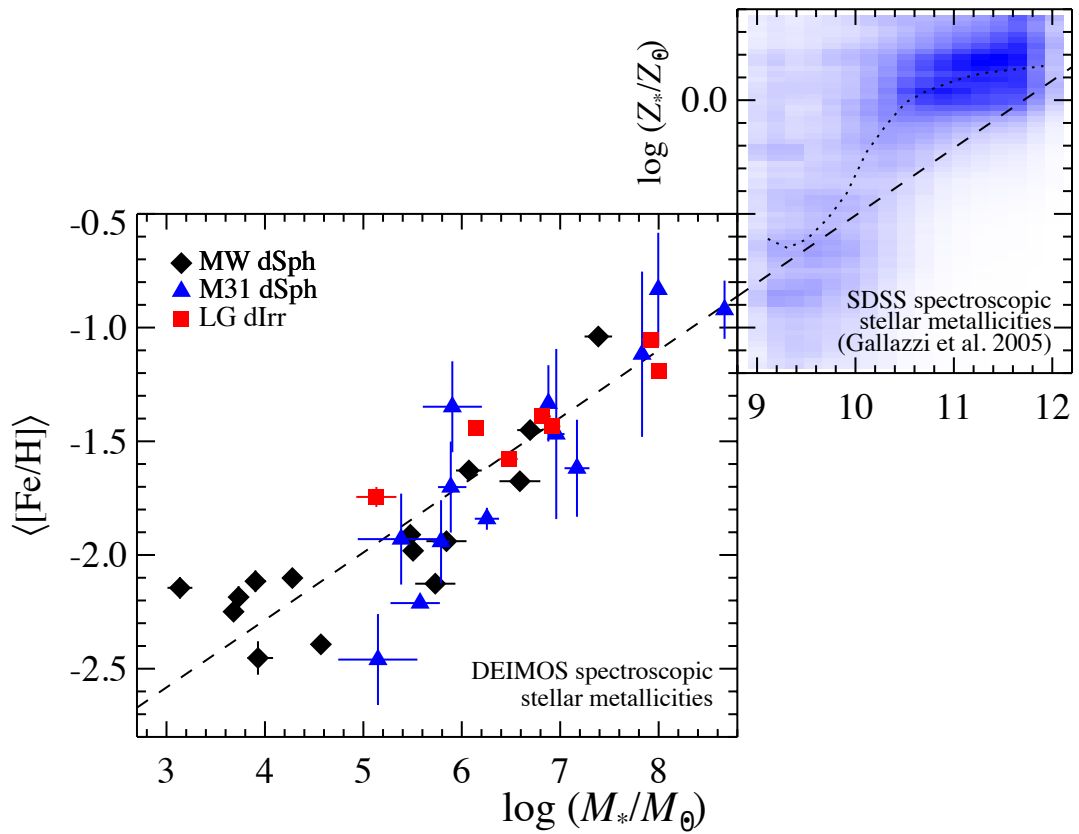


Figure 1.5: The stellar mass–metallicity relation for LG dwarf galaxies and more massive SDSS galaxies from Kirby et al. (2013). The black diamonds (MW dSphs) and red squares (dIs) are the average spectroscopic  $[Fe/H]$  from individual stars. The blue triangles (M31 dSphs) are the average spectroscopic  $[Fe/H]$  from co-added groups of similar stars within each M31 dwarf galaxy. The SDSS metallicities ( $\log(Z_*)$ ) come from a combination of absorption lines (mostly Mg and Fe). The dashed line corresponds to the least-squares fit to the LG galaxies, and the dotted line shows the moving median for the SDSS galaxies.

### 1.2.5 Role of the total initial mass and central density

Thanks to self-consistent hydrodynamical Nbody/Tree-SPH simulations of isolated dSphs Revaz et al. (2009) show that the main driver of the evolution of these systems is their total initial mass composed of gas and dark matter. The initial mass means the halo mass reached along the hierarchical clustering before the first star formation. Dwarf galaxies evolve in self-regulation regimes by successive periods of star formation and quiescence. The delay between star formation episodes depends on the cooling time which depends itself on the mass of the system. When a supernova explosion occurs a huge amount of energy is transferred into the gas which is heated and ejected as outflows from the central region (SNe feedback). As long as the gas is heated by supernovae star formation is quenched. Indeed stars are formed through collapse of gas clouds which need very low temperatures (around 10-100 K) in order for gravity to overcome internal pressure. The gas is cooled by radiative cooling through re-combination of H which is efficient only for temperature higher than  $10^4$  K. During cooling regime, the gas loses a huge amount of energy and sinks in central regions.

We can separate systems in two regimes :

- massive systems with initial mass  $> 4 \cdot 10^8 M_{\odot}$  : They have temperatures above  $10^4$  K allowing an effective radiative cooling. The cooling time is then short of the order of  $100 \cdot 10^6$  years (Myr). The intervals between star formation are so brief they resemble continuous star formation. The evolution is uniform creating homogeneous metal-rich systems where the cooling always dominates the SNe feedback.
- systems less massive than  $3 \cdot 10^8 M_{\odot}$  : Displaying temperatures below  $10^4$  K, the cooling time is longer of the order of several Gyr because low efficient radiative cooling. Only episodic periods of star formation separated by long periods of quiescence are expected as observed in Carina. This evolution leads to an inhomogeneous ISM depicted by a large scatter in abundances. The episodic star formation does not allow an homogeneous enrichment of the system.

For an extreme case of a very low mass system of initial mass lower than  $10^8 M_{\odot}$  no stars are expected due to a cooling time longer than 10 Gyr.

Adapting a complex treatment of the baryon physics of their simulations Revaz & Jablonka (2012) show that initial gas central density is the second important driver of the evolution. They make distinctions between feedback from SNeIa and supernovae of type II (SNeII). Between the two types of supernovae, the gas heating is different because they have different spatial distribution. They have relative different numbers and display a factor of 10 of variation in energy feedback. After the star formation is ignited in the central part of the galaxy, massive stars explode rapidly as SNeII. The increase of central density is counterbalanced by the injection of

energy. The strong and quick energy injected by SNeII (that quenched star formation) explains the sharp decrease of the star formation rate (SFR) just after the rapid initial rise of intensity. The galaxy contracts in its center being decoupled from gas. With time longer lived lower mass stars explode in SNeIa. In the central part (of the order of 0.2 parsec (pc)), they become the dominant source of heating preventing the gas to cool. SNeIa dominate the heating over SNeII because they are more concentrated. Then the long period of low star formation or quiescence (of the order of a few Gyr) is due to the explosion of centrally concentrated SNeIa.

Figure 1.6 shows the SFR obtained for simulated models of Fornax, Sculptor, Sextans and Carina (Revaz & Jablonka 2012) in the first panel of each figure. Fornax and Sculptor more massive galaxies display continuous star formation after two first peaks while Sextans and Carina less massive galaxies show successive episodic bursts of star formation.

At the end of the simulations in isolation the dSphs always present similar quantities of gas as observed in dIs ( $10^6 - 10^7 M_{\odot}$ ). Such amount of gas are not observed in dSphs. This is an other hint that gas could have been removed by external processes.

### 1.3 Understanding star formation histories and chemical evolutions

#### 1.3.1 Color magnitude diagram and age-metallicity degeneracy

The first resolved stellar population (colors of individual stars) were obtained in 1940s by W. Baade for the M31 dwarf galaxies. Baade (1944a,b) noticed that MW stars displayed various colors and that stars grouped together when represented in Hertzsprung-Russell Diagram. Later Searle et al. (1973) showed the importance of determining precisely the colors in individual stars understanding that their position on color magnitude diagram (CMD) give information about their evolutionary sequence in stellar evolution. Star formation histories can be inferred from CMD because they preserve imprints of fundamental parameters like age, initial mass function (IMF) according to stellar evolution models. An important unknown deriving SFH from CMD is the variation of metallicity of the stellar population. Without spectroscopic measurements the metallicity is assumed to be the value of the stellar evolution model in best agreement (colors and morphology) with the observed CMD. However an age-metallicity degeneracy exists : for example metal-poor RGBs from an old population can be located in the same area of the CMD as the metal-rich RGBs of a younger population. To infer a correct and complete SFH we need to know magnitude, color and metallicities of stars to break this degeneracy and determine ages of stars thanks to isochrone fitting. This is why more than an accurate photometry of resolved stellar population we need spectroscopic observations of individual stars giving metallicity determination. Of course age uncertainties rise with decreasing metallicity, and in some cases taking into account the photometric and color errors the uncertainties on age may unfortunately correspond to the entire age range (2-12 Gyr).

### 1.3. Understanding star formation histories and chemical evolutions

---

The age-metallicity breaks for main sequence turnoff star but they are often not observable because too faint to be resolved. Since 1980s developments of techniques and instruments allowed improvements in accurate photometry. Especially thanks to the power and resolution of the Hubble Space Telescope (HST) and coupled-charged device (CCD), we were able to observed distant systems in crowded areas.

#### 1.3.2 Probe the interstellar medium using RGBs over galaxy history

The idea is to obtain accurate abundances of stars covering different ages of the history of the considered dwarf galaxy. A large range in age means also large range in colors and magnitudes. The choice was then to study low mass stars which have long lifetimes (considering stars with mass  $\leq 0.8M_{\odot}$  their lifetime could be as long as the age of the Universe). The photosphere of low mass stars of different ages are used to probe the ISM from which they are formed, measuring the chemical enrichment of the gas, giving information about the products of SNe, and influences of the environment. The abundances are representative of the gas out of which the stars were born. Given the distance to dwarf galaxies and abilities of our instruments, the only choice is to look at the brightest stars, the RGBs formed during 1-15 Gyr. The assumption used here is that RGBs have retained much of their original gas in their external atmosphere. Using high resolution (HR) spectroscopy of RGBs, it is possible to probe stars until 1.5 Mpc. In order to observe in the boundaries of the LG and beyond more luminous stars can be used as the blue super-giant stars (BSGs) but being much younger they give information about only the present day metallicities (Venn et al. 2003; Kaufer et al. 2004). The term *Chemical Tagging* born from Freeman & Bland-Hawthorn (2002) is the method using the stellar abundances and kinematics to disentangle different stellar populations and study their properties in order to understand the chemical evolution of the galaxy. This method as been used for example on the MW to separate the disk and halos stars.

#### 1.3.3 Stellar evolution and chemical enrichment

Galaxies are end products of stellar evolution and our aim is to understand their evolution. From stellar evolution models, we know that during successive generations of stars in galaxy evolution, stars of various masses enrich the galaxy with different elements on time-scales related to the stellar masses.

For example death of a massive stars occurs through a rapid core-collapse and a violent explosion called SNeII. The elements synthesized by these events are the  $\alpha$ -elements : C, N, O, Ne, Mg, Si, S, Ar, Ca, Ti. Mainly iron but also iron-peak elements (from Sc to Ge) are produced by SNeIa (low mass stars). This event occurs when a white dwarf, accreting matter from its companion in a binary system, reaches its mass limit. All heavier elements than iron are created by neutron-capture nucleosynthesis defined in two processes : the rapid neutron capture

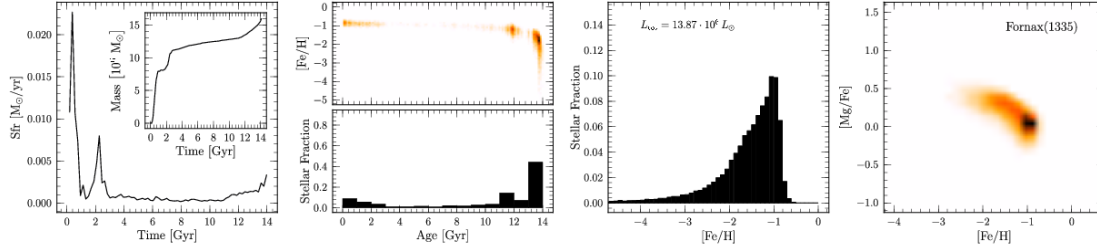
process (r-process) during SNeII and the slow neutron capture process (s-process) mostly in asymptotic giant branch stars (AGBs). Actually the sources of neutron-capture elements are still under debate. Other models have been recently proposed as an alternative or a complementary part to the production of r-process elements : neutrino-driven proto-neutron star proto-neutron stars (PNSs) wind of core-collapse supernovae (Wanajo 2013), binary neutron star (neutron star (NS)-NS) mergers (Wanajo et al. 2014; Just et al. 2014).

More details about the different nucleosynthesis processes are given in the next chapter.

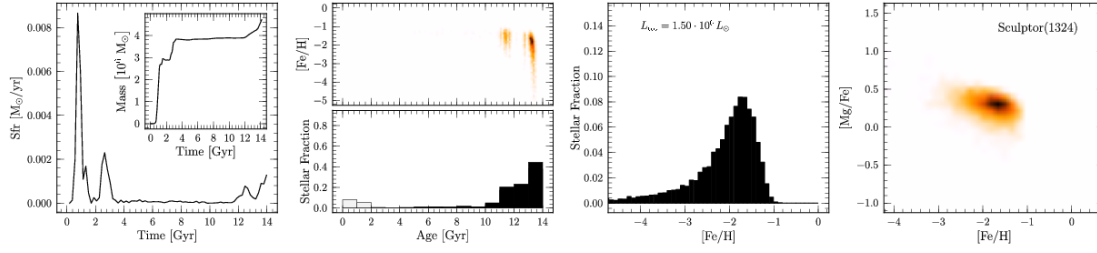
Then studying ratios between specific elemental abundances gives information about the distribution of initial masses for stellar populations and star formation time-scale. The best common example, the  $[\alpha/\text{Fe}]$ , is used to trace the star formation time-scale because it reflects the [SNeII/SNeIa]. The idea come from Tinsley (1979) who suggested that enhanced  $[\alpha/\text{Fe}]$  in MW halo stars could be explained by the time delay between Type II and Type Ia SNe. As SNeII have shorter time scale than SNeIa, the first stars born in an  $\alpha$  enriched interstellar medium (ISM) would present high  $[\alpha/\text{Fe}]$ , and stars formed ( $\sim 1$  Gyr) later, when SNeIa contribute to iron enrichment, would present decreasing  $[\alpha/\text{Fe}]$ . The knee corresponds to the metallicity at which the  $[\alpha/\text{Fe}]$  starts to decrease. The position of the knee informs about the state of the metal-enrichment of a system when SNeIa start to dominate the chemical evolution (Matteucci & Brocato 1990; Matteucci 2003). The common considered delay between SNeII and SNeIa is between  $10^8$  years and 1 Gyr. The more a system is efficiently forming stars and retaining metals, the more the knee is located at a higher metallicity. A knee at low  $[\text{Fe}/\text{H}]$  could be caused by either loss of metals through SNe outflows or a faint low SFR or both. Moreover the values of  $[\alpha/\text{Fe}]$  reached by metal-poor stars give information about the IMF and also galactic winds. Concerning the Milky Way, the metal-poor stars of the Galactic halo present  $[\alpha/\text{Fe}] \sim +0.4$  decimal exponent (dex), the knee is defined around -1.0 dex and the stars of the thick and thin disk show a decrease in  $[\alpha/\text{Fe}]$  until reaching solar value for the highest metallicities (McWilliam 1997; Venn et al. 2004). Figure 1.7 from de Boer et al. (2014a) presents schematic evolution of  $[\alpha/\text{Fe}]$  versus  $[\text{Fe}/\text{H}]$  for the MW (small grey points) and five dwarfs : Sagittarius, Sculptor, Carina, Fornax and LMC. For the two latter they choose to trace the outer envelopes of abundance distribution due to uncertainties about the exact location of the knee. Each galaxy displays a different location of the knee but a similar evolution trend : a plateau with constant values of  $[\alpha/\text{Fe}]$  for low metallicities (lower than the respective knee) and a decrease in  $[\alpha/\text{Fe}]$  from the knee.



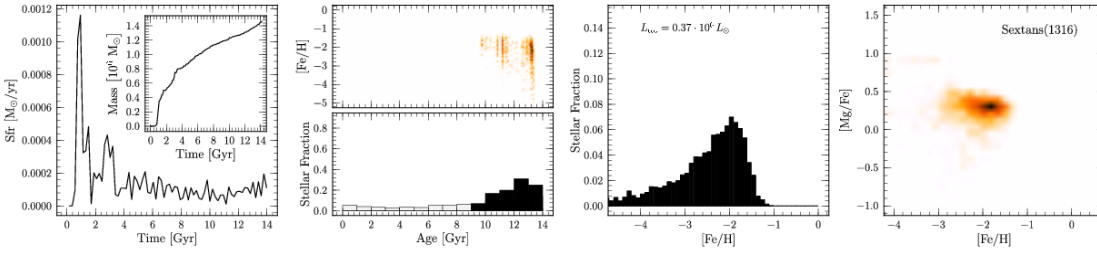
### 1.3. Understanding star formation histories and chemical evolutions



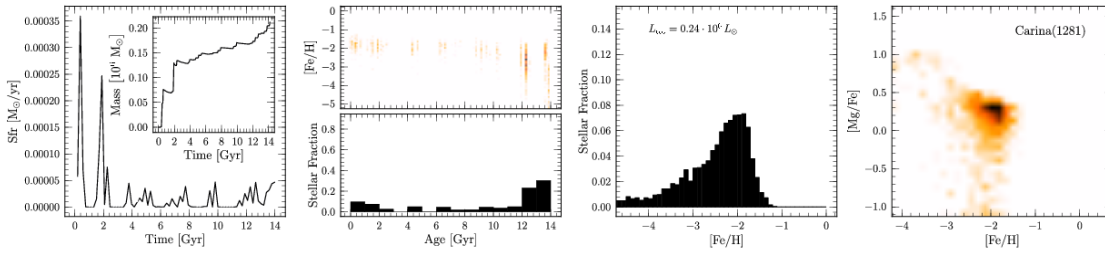
(a) Properties of selected model representing Fornax.



(b) Properties of selected model representing Sculptor.



(c) Properties of selected model representing Sextans.



(d) Properties of selected model representing Carina.

Figure 1.6: From Revaz & Jablonka (2012) : Properties of the four selected models representing Fornax, Sculptor, Sextans and Carina. In each line the plots display, the star formation rate and the evolution of the stellar mass, the normalized stellar age distribution, together with the evolution of  $[Fe/H]$ , and the final  $[Fe/H]$  distribution and ratio  $[Mg/Fe]$  as a function of  $[Fe/H]$ . For Fornax and Sextans they need to stop artificially their star formation. The grey regions in the stellar age distribution of these two dSphs correspond to stellar population without truncation. These populations are not represented in  $[Fe/H]$  distribution and in abundance ratios. The age of the calculated the V-band luminosities corresponds to 14 Gyr.

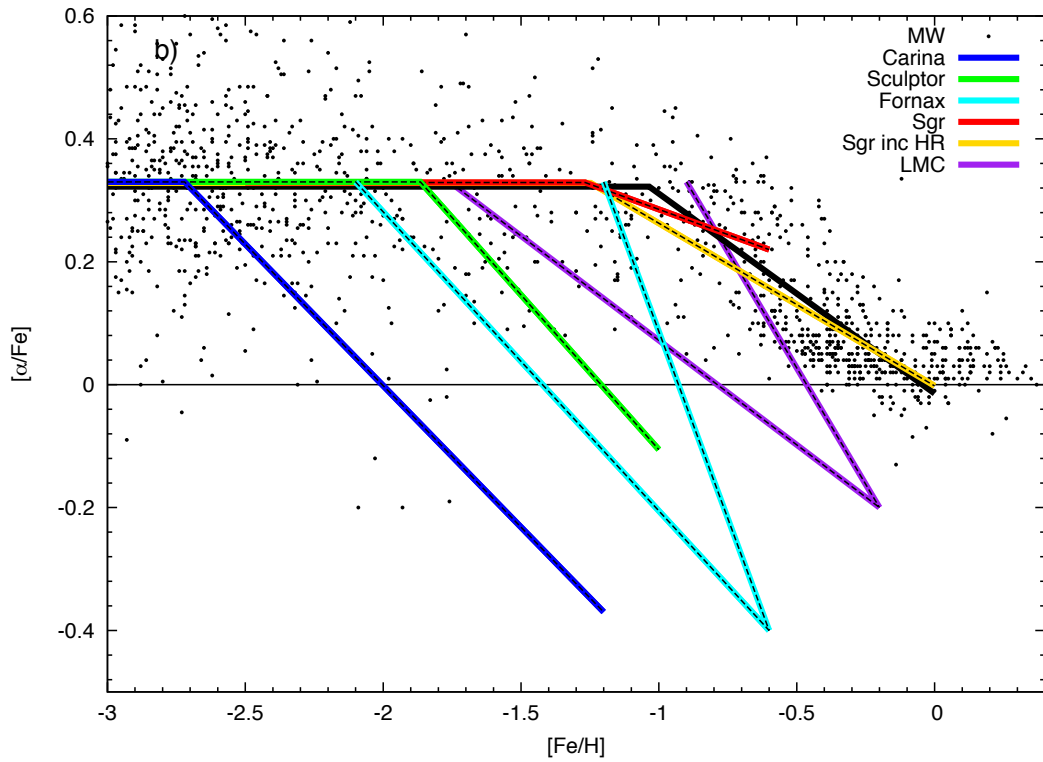


Figure 1.7: For systems with robust knee determinations in LG (Sagittarius, MW, Sculptor and Carina) de Boer et al. (2014a) show the best-fit models (single colored lines), while for other systems (Fornax and LMC) they show lines tracing the outer envelopes of the abundance distribution (two colored lines) (Venn et al. 2004; Letarte et al. 2010; Lemasle et al. 2012). The MW stars are represented by small gray points and the MW schematic enrichment by a black line.

### 1.4 Spectroscopy on resolved stellar populations

#### 1.4.1 First important results

Among the first important spectroscopic results obtained about the dwarf galaxies to quote are Shetrone et al. (2003) and Tolstoy et al. (2003) presenting the first measurements of  $[\alpha/\text{Fe}]$  evolution in function of  $[\text{Fe}/\text{H}]$  of three dSphs over Gyr time scales (15 stars in Sculptor, Fornax, Carina and Leo I). The main important conclusion they obtained is that dSphs could not be building blocks of similar MW galaxies because there is no compatible nucleosynthesis signature between the dSphs stars and the MW stars. This result has been then confirmed many times through observations as presented in Tolstoy et al. (2009) : metal-poor stars in dSphs show similar chemical abundance patterns to equivalent stars of the Galactic halo. However stars at higher metallicities show different abundance ratios from the MW and dSphs exhibit complex star formation histories.

Therefore, the admitted general idea is that observed dSphs are thought to be the descendants of the small initial systems or at least gathering similar characteristics. These observations suggests a different evolution between large and small systems after this early merging period. During their life, dwarf galaxies experienced transformations due to gas removal through several processes (ram pressure stripping, internal stellar evolution, tidal interactions) but they are affected differently depending on their mass, orbit and the medium they are moving in Carraro (2014).

In order to have a statistical appreciation of the chemical evolution the need is to increase the number of studied stars at high resolution. A great break through occurred thanks to the new generation of multi-spectrographs like the Fibre Large Array Multi Element Spectrograph (FLAMES) at the Very Large Telescope (VLT) or the Magellan Inamori Kyocera Echelle spectrograph (MIKE) at the Magellan telescope. In one observation a sample of 100 stars could be observed simultaneously in a field of view of 25 arcminutes (arcmin). Several large surveys were dedicated to studying individual stars in nearby dSphs, determining their kinematics and abundances using the largest telescopes (VLT, Magellan telescopes). For the following lines we mainly focus on the results obtained by the Dwarf Abundances Radial velocity Team (DART) directly linked with the data we worked on.

#### 1.4.2 Four classical dSphs : Fornax, Sculptor, Carina, Sextans

The goal of DART was at first to study a large sample of stars through photometry and spectroscopy, in Sculptor, Fornax, Sextans and Carina through several fields of observations covering space out to their tidal radius. From the low resolution ( $R \sim 6500$ ) mode in VLT/FLAMES using near infra-red spectra, metallicities and radial velocities are derived. The former are estimated using the calcium II triplet (CaT) and the latter are generally used as membership

Table 1.1: Properties of four classical dSphs : Fornax, Sculptor, Sextans, Carina. The  $V$ -band luminosity, the surface brightness, the distance, the tidal radius, the average metallicity, the mean heliocentric radial velocity, the velocity dispersion, the estimated position of the  $\alpha$ -knee.

dSph	$L_V$ $10^6 L_\odot$	$\Sigma_0$ mag/arcmin <sup>2</sup>	$d$ kpc	$r_{\text{tidal}}$ arcmin	[Fe/H] dex	$\langle v_{\text{rad}} \rangle$ km/s	$\sigma$ km/s	knee dex
Fnx	14	$14.4 \pm 0.3$	$138 \pm 8$	$71.1 \pm 4$	-1.15	$54.1 \pm 0.5$	$11.4 \pm 0.4$	-1.9
Scl	1.4	$14.6 \pm 0.5$	$86 \pm 5$	$76.5 \pm 5$	-1.96	$110.6 \pm 0.5$	$10.1 \pm 0.3$	-1.8
Sex	0.41	$18.2 \pm 0.5$	$95.5 \pm 2.5$	$160 \pm 50$	-1.9	$226.0 \pm 0.6$	$8.4 \pm 0.4$	...
Car	0.24	$16.6 \pm 0.5$	$106 \pm 2$	$28.8 \pm 3.6$	-1.7	223.9	7.5	-2.5 and ?

criterion. The empirical relation between the equivalent widths of the Ca II lines and the estimated metallicity was first calibrated on globular clusters. Using this relation leads to an apparent and unexpected lack of extremely metal-poor stars in dSphs. Starkenburg et al. (2010) showed that this empirical method was biased to low metallicity regime and provide a new calibration valid down to -4.0 dex. Therefore extremely metal-poor star were observed and confirmed in dSphs (Tafelmeyer et al. 2010).

As a second step, each central field is also studied with FLAMES in HR spectroscopy giving the opportunities to derive several abundances (light elements, alpha-elements, iron-peak elements and neutron capture elements). For some dSphs, offset fields have also been studied in HR modes.

The main properties of these four classical dSphs are summed up in Table 1.1. References are given in the following order Fornax (Fnx), Sculptor (Scl), Sextans (Sex), Carina (Car) : the  $V$ -band luminosity  $L_V$  : Walker et al. (2009); the surface brightness  $\Sigma_0$  : Irwin & Hatzidimitriou (1995); the distance  $d$  : Mateo (1998); Pietrzyński et al. (2008); Lee et al. (2003); Pietrzyński et al. (2009); the tidal radius  $r_{\text{tidal}}$  : Irwin & Hatzidimitriou (1995); the average metallicity [Fe/H] : Battaglia et al. (2006); Tolstoy et al. (2004); Battaglia et al. (2011); Koch et al. (2006); the mean heliocentric radial velocity  $\langle v_{\text{rad}} \rangle$  : Battaglia et al. (2006, 2008, 2011); Koch et al. (2006); the velocity dispersion  $\sigma$  : Battaglia et al. (2006, 2008, 2011); Koch et al. (2006); the estimated position of the  $\alpha$ -knee : Lemasle et al. (2014); Tolstoy et al. (2004); de Boer et al. (2014b).

The following paragraphs develop the knowledge acquired about the SFH and chemical evolution of these four dSphs.

## Fornax

Fornax is the second most luminous and metal-rich dSph after Sagittarius. Rarely observed in dSphs Fornax present 5 GCs. At least three over-densities have been observed at its proximity and Fornax stars are well separated three distinct stellar components. The two first over-densities were discovered by Coleman et al. (2004, 2005) presenting shell-like structures and dominated by relatively young stellar populations (age  $\approx$  2 Gyr). They proposed a scenario of

## 1.4. Spectroscopy on resolved stellar populations

---

recent merger to explain the presence and properties of these over-densities. Later de Boer et al. (2013) re-analyzing the two known over-densities and discovering a new one with stars at solar metallicity, proposed the hypothesis that over-densities were formed by re-accretion of previously expelled gas after finding a age-metallicity relation consistent with the young field stars. This scenario was previously proposed by Olszewski et al. (2006). 9 RGBs were studied in 3 of the 5 GCs showing similar abundances to MW GCs, Letarte et al. (2006) conclude that at epoch of their formation, MW and Fnx GCs should share the same initial conditions. Battaglia et al. (2006) present the 3 distinct stellar populations : young pop (few 100 Myr old) in the center (main sequence stars in the CMD), intermediate pop (2-8 Gyr old) and old pop (> 10 Gyr). Metal-rich stars ( $[\text{Fe}/\text{H}] \geq -1.3$ ) are more concentrated spatial distribution and colder kinematics. Coleman & de Jong (2008) proposed the following SFH for Fornax from CMD based on HST data : an early phase of rapid enrichment, then SF gradually decreased, and  $\sim 4$  Gyr ago a sudden burst of strong SF with substantial chemical enrichment, followed by weak SF episodes (tentative of very young stars  $\leq 100$  Myr). The most recent SF burst produced stars with metallicity close to solar. From their age-metallicity relation de Boer et al. (2012) deduce : rapid increase of average  $[\text{Fe}/\text{H}]$  from  $\leq -2.5$  to  $-1.5$  dex between 8-12 Gyr ago, then more gradual enrichment to reach  $-0.3 \approx 3$  Gyr ago and rapid decrease of  $[\text{Mg}/\text{Fe}]$  from  $[\text{Fe}/\text{H}] \geq -1.5$  dex : definition of the  $\alpha$  knee correspond to 7-10 Gyr ago. Two HR spectroscopic studies were conducted one in the center (Letarte et al. 2010) and one in an offset field (Lemasle et al. 2014). The 81 stars in the center are dominated by young and metal-rich stars (1-4 Gyr old). Unusually low  $[\alpha/\text{Fe}]$ ,  $[\text{Ni}/\text{Fe}]$  and  $[\text{Na}/\text{Fe}]$  compared to the Milky Way stars at same  $[\text{Fe}/\text{H}]$  are seen and hints of creation of s-process elements through stellar winds from low metallicity AGBs. In general small dispersion of abundance ratios are observed, leaving Fornax similar to Sculptor, Sagittarius and MW halo. The 47 stars of the outskirts show that the onset of supernova of type Ia (SNIa) (knee) occurred between a metallicity of  $-2.0$  and  $-1.8$  dex, between 12-10 Gyr ago. They also show from abundances influences of SNIa and AGB on the younger stellar populations. The position of the knee is confirmed in Hendricks et al. (2014) given a value of  $-1.9$  (based on two offset field of total 58 stars in HR spectroscopy). Several studies and comparisons with chemical models (e.g. Orban et al. (2008)) show that the recent SF event needs gas accretion but without confirming either a fall-back of previously expelled gas or a merger event.

### Sculptor

At a distance of 86 kpc (Irwin & Hatzidimitriou 1995) Sculptor seems to be a good example of isolated system evolution. It harbors two distinct ancient stellar components (both 10 Gyr old) : one metal-rich,  $-0.9 \geq [\text{Fe}/\text{H}] \geq -1.7$ , and one metal-poor,  $-1.7 \geq [\text{Fe}/\text{H}] \geq -2.8$  (Tolstoy et al. 2004). The metal-rich population is more centrally concentrated than the metal poor, and on average appears to have a lower velocity dispersion,  $\sigma_{\text{metal-rich}} = 7 \pm 1$  km/s, whereas

$\sigma_{\text{metal-poor}} = 11 \pm 1$  km/s. The sculptor dynamical mass is estimated by Battaglia et al. (2008) on 470 members to  $M_{\text{dyn}} = 3 \cdot 10^8 M_{\odot}$ , within 1.8 kpc, which results in an  $M/L \sim 160$ . A sign of intrinsic rotation is revealed by the evidence of a velocity gradient. Sculptor is the first dSph in which the age-metallicity relation was quantified thanks to deep wide-field photometry going down to the oldest Main Sequence Turn-Off stars : an extended metal-poor population was formed at the oldest times, and subsequent more metal-rich, younger stars were formed more towards the center until the gas was depleted or lost roughly 7 Gyr ago (de Boer et al. 2011). The SFH at different radii and detailed time-scales for evolution of individual chemical elements were estimated by de Boer et al. (2012). Within 1.5 kpc from the center, a total mass in stars of  $7.8 \cdot 10^6 M_{\odot}$  was formed, between 14 and 7 Gyr ago, with a peak at 13-14 Gyr ago. For alpha-elements the knee at -1.8 dex corresponds to an age of  $10.9 \pm 1$  Gyr, suggesting that SNIa enrichment began  $\sim 2 \pm 1$  Gyr after the start of star formation. The chemical evolution of Sculptor seems to be simple with an early burst of SF (13-14 Gyr ago) and slowly continuing until 6-7 Gyr ago and presenting no signs of recent tidal interactions.

### Sextans

As Carina, Sextans is at the low mass end of classical dSph and shows old and intermediate age populations. Thanks to medium resolution spectroscopy on 173 members Battaglia et al. (2011) confirmed the presence of a metallicity gradient in Sextans : stars located in the center are more metal-rich than stars from the outer parts. From kinematics they observed that metal-rich stars displayed colder kinematics than stars from the outskirts. They found that the shape of the metallicity distribution function (MDF) changes with the radius and that Sextans seems to have two populations: a metal-rich population within 0.8 deg and a metal-poor population beyond 0.8 deg. From Jeans modeling of the observed line-of-sight velocity dispersion profile (out to a projected radius of 1.6 deg) Battaglia et al. (2011) derive a mass of  $2 - 4 \cdot 10^8 M_{\odot}$  and a estimated  $(M/L)_{V, \odot} = 460 - 920$ . Kirby et al. (2010) determine metallicities and abundances of  $\alpha$ -elements (Mg, Si, Ca, Ti) up to 109 stars but due to their small extent on the Sextans field Kirby et al. (2010) were not able to detect a metallicity gradient (Battaglia et al. (2011) fields extended to 1.8 deg and Kirby et al. (2010) only to 21.4 arcmin). SFH of Sextans was derived by Lee et al. (2009) from Canada-France-Hawaii Telescope (CFHT) photometry adopting a closed box model for chemical evolution. They find that for the adopted age of Sextans 15 Gyr, the majority of stars were formed in the first 4 Gyr ( $\sim 65\%$  of the stars formed 13 to 15 Gyr ago while  $\sim 25\%$  formed 11 to 13 Gyr ago). They detect star formation continued to at least 8 Gyr ago. As expected the star formation history is more extended in the central regions than the outskirts, and the difference in SFR between the central and outer regions is most marked 11 to 13 Gyr ago. During the first Gyr the metallicity in the central region increased rapidly up to  $[\text{Fe}/\text{H}] = -1.6$  while only to  $[\text{Fe}/\text{H}] = -1.8$  in the outer areas and varied slowly since then. The first HR spectroscopic study performed in Sextans date from Shetrone et al. (2001) using

## 1.4. Spectroscopy on resolved stellar populations

---

Keck/HIRES spectra with 5 stars covering a metallicity of  $-2.85 \leq [\text{Fe}/\text{H}] \leq -1.45$ . The other high resolution spectroscopic studies about Sextans stars were dedicated to the research of extremely metal poor stars (EMPs) (9 stars having  $[\text{Fe}/\text{H}] \leq -2.7$  Aoki et al. (2009), Tafelmeyer et al. (2010), Honda et al. (2011)).

Sextans is the less studied among these four classical dwarfs firstly because lately discovered by Irwin et al. (1990) and having a large extent on the sky located in crowded fields (contaminated by a lot of MW interlopers).

### Carina

Carina corresponds to the low mass end of the classical dSphs and presents a very complex SFH with unusual episodic SF. Lemasle et al. (2012) derive the enrichment history for each SF episode : a short (2-3 Gyr) rapid enrichment of the whole galaxy to a metallicity of -1.5 dex with both SNeII and SNeIa, after a gap of 3-4 Gyr forming 70% stars but with little evolution in either  $[\text{Fe}/\text{H}]$  or  $[\alpha/\text{Fe}]$ . Venn et al. (2012) suggests that Carina may be at the critical mass where some chemical enrichments are lost through SNeII driven winds. This argument is based on HR spectroscopy of 9 RGBs showing evidence of inhomogeneous mixing (large scatter in  $[\text{Mg}/\text{Fe}]$ , offset in  $[\alpha/\text{Fe}]$  between old and intermediate age populations), and a potential evidence of SNeII driven winds because one star seems to be born in a pocket enhanced SNeIa/SNeII products. Presence of extended structures has been confirmed by Battaglia et al. (2012) being unambiguous signs of tidal disruption first time observed in an other dwarf than Sagittarius or LMC/SMC. They find a negative age gradient in Carina directly from its main sequence turnoffs stars, which trace out to very large distances from the galaxy center. The signs of interaction with the Milky Way make it unclear whether the age gradient was already in place before Carina underwent tidal disruption. Recently de Boer et al. (2014b) reveal some details about the episodic SF of Carina. Two main episodes of star formation occurred at old ( $\geq 8$  Gyr) and intermediate (2-8 Gyr) ages (which represent  $60 \pm 9$  percent of the total number of stars), both enriching stars starting from low metallicities ( $[\text{Fe}/\text{H}] \leq -2$  dex). Furthermore, within the tidal radius of 888 pc a total mass in stars of  $1.07 \pm 0.08 10^6 M_{\odot}$  was formed, giving a stellar mass-to-light ratio of  $1.8 \pm 0.8$ . The oldest episode displays a tight age-metallicity relation during  $\approx 6$  Gyr with steadily declining  $\alpha$ -element abundances and a possible  $\alpha$ -element knee visible at  $[\text{Fe}/\text{H}] \approx -2.5$  dex. The intermediate age sequence displays a more complex age-metallicity relation starting from low metallicity and a sequence in  $\alpha$ -element abundances with a slope much steeper than observed in the old episode, starting from  $[\text{Fe}/\text{H}] = -1.8$  dex and  $[\text{Mg}/\text{Fe}] \approx 0.4$  dex and declining to Mg-poor values ( $[\text{Mg}/\text{Fe}] \leq -0.5$  dex). This indicates clearly that both episodes of star formation formed from gas with different abundance patterns, inconsistent with simple evolution in an isolated system. A first knee could be estimated around -2.5 and at least a second one could be too but its location is for the moment not well defined.

### 1.4.3 Other classical dwarfs around the Milky Way

**Sagittarius** Sagittarius is the most luminous and closest dSph around the MW (distance of 25 kpc). It was discovered relatively late, as it is located behind the MW bulge (Ibata et al. 1995). Several studies show that Sagittarius suffers from Galactic tides and forming stellar streams wrapping around the MW (e.g., Johnston et al. (1995); Lynden-Bell & Lynden-Bell (1995); Ibata et al. (2001); Majewski et al. (2003); Belokurov et al. (2006a). Dolphin (2002) derive a SFH of stars forming over a period of 8-10 Gyr which stopped forming stars 2-3 Gyr ago. Despite difficulties linked to very crowded areas spectroscopic studies present results for the main body of the dwarf which is dominated by metal-rich stars ( $[\text{Fe}/\text{H}] \geq -1.5$ ) (e.g., Monaco et al. (2005); Sbordone et al. (2007); Carretta et al. (2010); McWilliam et al. (2013)). de Boer et al. (2014a) determine for the first time a knee at  $-1.27 \pm 0.05$  dex. A top-light IMF is invoked to explain the observed abundances. This means an initial mass function lacking the most massive SNeII.

**Leo II** Distant of  $207 \pm 10$  kpc Leo II presents indications of a slow enrichment. Shetrone et al. (2009) show that stellar metal-poor abundances are similar to the MW halo and that metal-rich stars present a decline of  $[\alpha/\text{Fe}]$  with increasing  $[\text{Fe}/\text{H}]$ . This confirms the fact that the slow chemical enrichment histories of the dSphs is universal, independent of any interaction with the Milky Way.

**Ursa Minor** The observation of 16 stars in Ursa Minor ( $64 \pm 5$  kpc) lead to similar SFH as Leo II. Cohen & Huang (2010a) show that the stellar population is dominated by uniformly old stars (13 Gyr). The abundances are similar to outer halo stars and the duration of SF is smaller than in other dSph.

**Draco** Draco located at  $72 \pm 3$  kpc seems to be chemically inhomogeneous : a spread in (heavy) elements is revealed (Kinman & Kraft 1980; Stetson 1984; Smith 1984). This difference with other dSph has been explained by internal chemical evolution. This is a good example where the presence of a dark matter halo would help such low mass dwarf sustain SF with a low SFR.

### 1.4.4 Ultra faint dwarfs

During the last decade, many UFDs ( $L \leq 10^5 L_{\odot}$ ) have been discovered in the LG (Willman et al. 2006; Zucker et al. 2006; Belokurov et al. 2006b) pointing out the question about the formation mechanisms of the smallest galaxies. Are they formed from a low mass system or are they stripped remnants of much larger systems (disrupted system)? Due to the faint



brightness of most of them only a few number of stars have been studied (difficulties to confirm membership) but showing that UFDs contain only old metal-poor stars and could retain the signatures of the first generation of stars. They are numerous and very old ( $\sim \geq 10$  Gyr), and they contain extremely metal-poor stars at lower metallicities than observed in other dSphs (Kirby et al. 2008; Norris et al. 2008; Frebel et al. 2010). It seems that UFDs extend the metallicity-luminosity relation down to the lower luminosities (Simon & Geha 2007). They have similar luminosities than GCs but internal velocity dispersions confirm that they are largely DM dominated. Brown et al. (2012) show from HST photometry that UFDs are at least as old as the oldest known GC. No evidence of intermediate population has been observed in them (Bellazzini et al. 2006). As an example, Ursa Major II and Segue I do not show any enrichment of SNeIa leading to a very short and early period of SF (Frebel & Bromm 2012; Vargas et al. 2013). Globally UFDs are the least luminous, most dark-matter dominated, and least chemically-evolved galaxies known. Processes that could be responsible for their early termination of SF are : reionization affecting low galactic mass, gas depletion, and supernova feedback. If the apparent synchronicity of their SF termination is confirmed this could be an argument in favor to the reionization scenario (Jarosik et al. 2011).

## 1.5 Simulations of chemical evolution

Two kinds of modeling individual galaxies have been developed : standard chemical evolution models and chemo-dynamical systems. The former is based on very simplistic assumptions on stellar and gas dynamics and take into account the general properties of the system as mass, IMF, gas flows, chemical yields. The latter are based on dynamical processes expressed in great details more designed to follow small-scale, short-term phenomena leaving them less successful to follow galactic scale evolution over more than a Gyr. Then large-scale, long-term phenomena are better reproduced by standard models but with the disadvantage of simplistic treatment of dynamics. Using SFHs of Carina, Draco, Sagittarius, Sextans, Sculptor and Ursa Minor derived from HST deep photometry, Lanfranchi et al. (2008) show with their standard models that low SF and high winds are needed to reproduce the observed abundances. The chemo-dynamical codes are rather used to study in details the effects of feedback from SNe, tidal interactions and ram pressure. As SNe contribute significantly to driving interstellar turbulence and accelerating gas, if strong feedback is not taken into account in galaxy formation models, they end up with galaxies converting their gas into stars 100 times too rapidly (Hopkins et al. 2011; Agertz et al. 2013) and too many stars (e.g., White & Frenk (1991); Kereš et al. (2009); Moster et al. (2010); Behroozi et al. (2010); Faucher-Giguère et al. (2011)). Stellar feedback is an essential ingredient in galaxy formation but implementations are based on ad hoc approximations and often have tunable parameters.

Many efforts have been done recently to reconstruct orbits of dSphs. Studies provided accurate proper motions of SMC/LMC and orbits have been calculated in order to better understand

this three body problem. The orbit of Sagittarius is better constrained as its tidal arm can be traced (Majewski et al. 2004). For the other MW dwarfs only six have proper motion estimations but measurement uncertainties are still too large to derive solid orbits (Pasetto et al. 2003; Pasetto & Chiosi 2009; Pawlowski & Kroupa 2013). Nichols et al. (2014) show through chemodynamical simulations the impact of gravitational tides on dwarf galaxies. Tidal forces are sufficient (after one perigalacticon passage) to quench SF. The more the tidal interactions are important the more the metallicity gradient is lowered. It seems that dwarfs are inefficient to recycle the metals from SNe and loose the majority of their metals.

Mayer et al. (2006) confirm using Nbody/gas-dynamical simulations that ram-pressure can be the most efficient process to remove gas from a dwarf galaxy in a cluster of galaxies, but depending a lot on the evolutionary status of the dwarf and on properties of the interstellar cluster medium. For the moment the density of the two gaseous component of the LG are not well understood leaving large uncertainties in the exact role of the ram pressure stripping on dwarfs.

### 1.6 Aim of the thesis

Despite the continuous discoveries of dwarf systems until today the true nature of these objects is still not well understood. How are they formed ? Which evolution do they follow ? How their faith is linked with the neighbor spiral galaxies ? Why are they so diverse ? Is there a link between the different types of dwarf galaxies ? What are the parameters that drive their evolution ?

Studying the LG dwarf galaxies is very interesting and relevant because understanding their evolution is a key step in the understanding of the evolution and formation of all galaxies. Following the principle that we are not at a peculiar place in the Universe, the Local Group is the closest small scale laboratory from which we can deduce hints about the rest of our Universe.

Anchored in this context, this thesis is dedicated to the study of the largest sample of stars ever observed in HR spectroscopy in Sextans : 87 members in the central field of the dwarf galaxy. Reduction of the data, membership determination, stellar parameters, abundance calculations and analysis of the results are the key steps presented in the next chapters.

Sextans is an interesting dSph because its range of mass places it at the turning point between a homogeneous and inhomogeneous ISM. The aim is to obtain a good picture of the chemical evolution of Sextans. The large number of stars of the sample allow to test the homogeneity of the ISM, and a first estimation of the location of the knee. Other hints about the chemical evolution of Sextans and the nucleosynthesis sites are derived studying iron-peak elements and neutron-capture process elements.

## 2 Stellar photospheres

### 2.1 Stellar nucleosynthesis

#### 2.1.1 Origin of elements

A great step in understanding the origin of the elements was reached when the energy production in stars was explained by nuclear fusion reactions (Gamov 1928 with the tunnel effect, Bethe and Critchfield 1930 for pp-chain reactions and von Weizsacher 1938 and Bethe (1939) for the CNO cycle). An experimental confirmation of the stellar origin of elements was given by Merrill (1952) through the discovery of technetium (Tc) lines in AGBs. As Tc isotopes are short lived in comparison to the age of AGBs (low mass long lived stars) the only possible conclusion was that nuclear reactions within the star had synthesized this element.

According to Burbidge et al. (1957) and Wallerstein et al. (1997), the common admitted origin of elements is composed of three sources : i) Big Bang Nucleosynthesis : A few minutes after the Big Bang occurred, the temperature and density conditions were so extreme that light elements could be formed through nuclear fusion reactions (interaction of elemental particles). H, D, He and traces of  ${}^7\text{Li}$  were created in the early days of the Universe. ii) cosmic ray spallation :  ${}^7\text{Li}$ , Be and B were formed by nuclear fission through collisions between cosmic rays and interstellar matter. iii) Stellar nucleosynthesis : Li and all other elements heavier than B are produced in stars through diverse nuclear processes described in the next sections.

#### 2.1.2 Elements lighter than iron

The life of a star is a perpetual balance between gravitational forces in competition with transfer of energy looking for hydrostatic equilibrium. The key parameter in stellar evolution which determines the fate of a star and its lifetime is its initial mass. The energy produced in the center of the star through nuclear reaction is transported by two processes : convection

and radiation depending on the temperature gradient and opacity of the star layers. Radiative transfer is dominant in layers with low opacity and low temperature gradient. On the contrary when the temperature is sufficient, energy is transported via convective processes. In low mass stars  $M_{*ini} \lesssim 2M_{\odot}$  the H burning occurs through pp-chain conducting no temperature gradient. Radiative transfer dominates the central portion of low mass stars. The outer layers are cool enough that H is neutral then opaque to photons. The energy transport is convective in the external layers of the star. For more massive stars the energy transfer are inverted : a convective core and radiative envelope. This due to the fact that H burning is dominated by CNO chains which are very sensitive to temperature. In the core, the temperature gradient is steep enough to allow convective transfer while in the outer layers the temperature is high enough that H is nearly fully ionized and transparent to radiation.

A star is born through the collapse of a molecular cloud in the interstellar medium. During the collapse, the temperature is increased due to contraction and when reaching a few million of Kelvin the fusion of hydrogen is initiated in the core. The threshold initial mass that allows the ignition of H fusion is around  $M_{ini} \geq 0.08M_{\odot}$ . When the contraction stops, this leads to an hydrostatic equilibrium, a new state called the main sequence during which all hydrogen of the core is converted into helium through nuclear reactions. Depending on the initial mass of the stars and their central temperature, two different channels of H burning into He take place : pp-chains for low initial mass stars ( $T_C \geq 10^6$  K,  $M_{ini} \leq 2M_{\odot}$ ) and CNO cycles for more massive stars ( $T_C \sim 10^7$  K,  $M_{ini} \geq 2M_{\odot}$ ).

For the next step of stellar evolution we consider different ranges of initial masses.

Figure 2.1 taken from Karakas & Lattanzio (2014) presents a schematic view of the different nuclear burning phases and the fate of stars in function of the stellar initial mass. The mass boundaries are not exactly the same developed in the text because some variations exist between studies. We do not discuss in details all the proposed cases in this figure.

$0.5 < M_{ini} < 2 M_{\odot}$  The main sequence ends when the hydrogen fuel is exhausted thus stopping the nuclear reactions. Without nuclear reactions the hydrostatic equilibrium is lost and the star starts again to collapse under the gravity force. The consequence is the heating of the first shell just outside the core allowing the fusion of hydrogen into helium in this region. While H is burning in the shell, the mass of the He core increases until it became degenerate. Due to addition of mass from H burning shell, the degenerate core contracts, central temperature and nuclear reactions rate increase and the envelope expands. During this phase the luminosity is also increased and the star become a red giant branch star. The first dredge-up occurs when the convective envelope goes deeper and some element are dredged up toward the stellar atmosphere. As the H burning shell propagates outside it will reach the layer mixed with the convective envelope. The modification of the chemical environment decrease the nuclear reaction rate and the luminosity. A new mixing of CNO cycles products occurred. In the core He burning take place when the temperature reaches  $10^8$ K producing

C via triple  $\alpha$ -reactions. This new source of energy increase the central temperature but as the core is degenerate it is not possible to cool it by extension. This situation leads to an helium flash during which a huge amount of energy is released removing the degeneracy of the core and increasing the luminosity. A new equilibrium is then reached, called the horizontal branch. Energy is produced by a stable core He burning and shell H burning during which the envelope contracts, the core expands and the luminosity decreases again. When He lacks in the core, the star contracts again and ends its life forming a planetary nebulae with a CO white dwarf (WD) in its center.

$2 < M_{\text{ini}} < 8 M_{\odot}$  In this case stars follow a different evolution because their He core is not degenerate. Come back to the first burning H phase in the stellar core. As the core is convective due to high temperature gradients (CNO cycles), mixing is present and H from the border is driven to the center to be burned. When H is exhausted the temperature decreases then the core contracts provoking an increase of the temperature and ignition of H burning in a thin shell surrounding the core. During the He production the core contracts, and the envelope expands. The star reaches the red giant branch phase and the first dredge-up occurred. As the He core is non-degenerate the increase of temperature implies a pressure increase and when the temperature reaches  $10^8$  K He burning is ignited in the core. Due to this new source of energy the central temperature increases, the core expands and the envelope contracts. The star is considered as a Blue Loop star. The amount of C increases in the core and new nuclear reactions start to create O. The CO core become degenerate. During the asymptotic giant branch phase a second dredge-up occurred and processed material are driven to the atmosphere. As the He burning shell is moving towards it meets the H burning shell and re-ignite it. However, the He burning shell is unstable leading to thermal pulses linked with mass losses. Between pulses, mixing occurs and s-process elements are created. During the third dredge-up the s-process elements reach the stellar atmosphere. The star life end with a expulsion of the outer layers forming a planetary nebulae and leaving a WD in the center. The material expelled is composed of C, O and heavier element produced via s-process.

$8 < M_{\text{ini}} < 12 M_{\odot}$  For that complex range of masses three scenarii are possible : i) After the formation of a CO core, the fusion of C takes place in the degenerate center probably leading to a carbon deflagration ii) After the fusion of carbon, the star is composed of a very degenerate ONeMg core. As the central temperature is smaller than the photo-desintegration temperature of Ne, He burns in shells. It increases the core mass reaching the Chandrasekhar limit of  $1.4 M_{\odot}$ . It follows an electron capture core-collapse and the formation of a neutron star through supernova explosion (supernova of type II (SNII)). iii) After the fusion of carbon, the star is composed of a ONeMg core very degenerate. Non destructive flashes of Ne, O and Mg occurred. An iron core is formed similarly as in more massive stars. Finally the star explode in

a SNI leaving a neutron star.

$12 < M_{\text{ini}} < 120 M_{\odot}$  When the central temperature reaches  $10^9$  K Ne burning takes place in the core producing O and Mg, followed by O burning creating Si and S and finally Si burning forming Ca, Ti and iron-peak elements. At the end of these successive burning phases the star is composed of a iron rich core surrounded by shells of Si, O, Ne, C and He. As no more energy is given by nuclear reactions, the core contracts increasing temperature until reaching the photo-desintegration of the Fe and He nuclei. The core is then composed of protons, neutrons and free electrons. During the collapse, neutrons and neutrinos are produced through fusion of protons and electrons. As the density increases, the neutron core becomes degenerate stopping the gravitational collapse. The infalling material rebounds and meet the other infalling layers. The shock wave and neutrinos winds provoke the expulsion of the envelope leading a core-collapse supernovae (SNeII). The stellar remnant can be either a neutron star or a black hole depending on the density reached. The material expelled from this explosion is composed of elements from C to iron-peak elements.

### 2.1.3 $\alpha$ -elements

C, N, O, Ne, Mg, Si, Ca, and Ti are called  $\alpha$ -elements since their are obtained by successive  $\alpha$ -captures (they are multiples of  $\alpha$ -particles).  $\alpha$ -elements are produced in various burning stages of massive stars by  $\alpha$ -capture and are dispersed mainly by SNeII in the ISM. According to Woosley et al. (2002), Mg is produced in hydrostatic C and Ne burning phases. Ca is mainly produced in hydrostatic and explosive O burning phases in massive stars. Small fraction of Ca is also produced in hydrostatic C and Ne burning phases. Some isotopes of Ca can be produced in the  $\alpha$ -rich freeze out (Woosley et al. 1973). This occurred in explosive Si burning phase when the density is low and the expanding time is fast leading a lot of free  $\alpha$  particles. Ti is mainly produced in explosive O and Si burning phases.

Kobayashi et al. (2006) show that the SNeII yields of  $\alpha$ -elements are mass dependent : more  $\alpha$ -elements are produced in most massive stars due to their larger mantle mass. However in smaller fractions than in SNeII, Ca, Ti and Mg (in tiny minority) can also be produced in SNeIa. Thielemann et al. (2004) show that the general nucleosynthesis outcome of SNeIa is dominated by iron-peak elements products but involves also sizable fractions of Si to Ca and minor amounts of unburned or pure C burning products as C, O, Ne, Mg, etc. Besides, some isotopes of Ca and Ti can be produced in two rare varieties of SNeIa : carbon deflagration in WD very near to Chandrasekhar mass (Woosley 1997; Iwamoto et al. 1999), and helium detonation SNeIa (Woosley & Weaver 1995).

## 2.1. Stellar nucleosynthesis

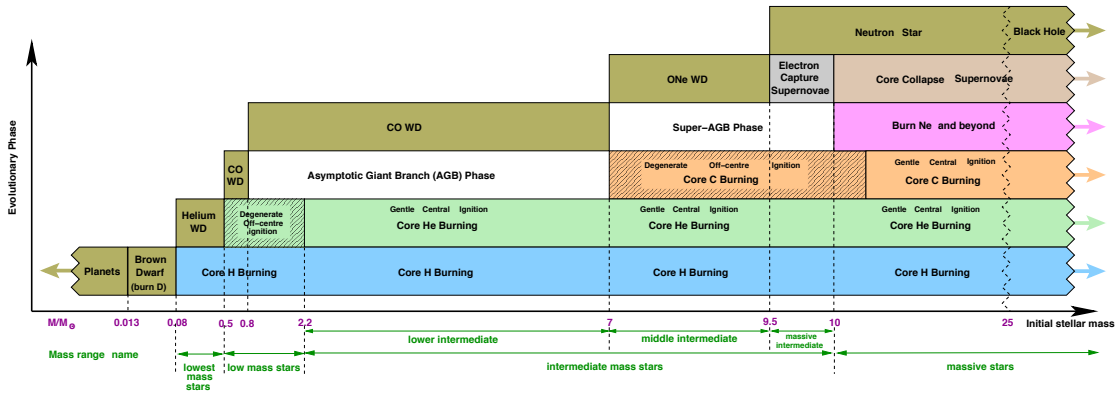


Figure 2.1: From Karakas & Lattanzio (2014) : schematic view of the different nuclear burning phases and the fate of stars in function of the stellar initial mass.

### 2.1.4 Iron-peak elements

Elements from Sc to Ge are defined as iron-peak elements because elements having an atomic number close to iron. They form a specific positive peak when representing the relative abundances of elements of the Solar System in function of the atomic numbers. This peak is a direct consequence of the nuclear binding energy of nuclei represented in figure 2.2 : until Fe nuclear fusion (forming heavier elements) releases energy, conversely for element heavier than Fe, the energy is released when nuclear fission occurs (converting in lighter elements). Nuclear fusion of elements heavier than iron is then endothermic.

Oddo-Harkins rule shows that elements with even atomic number present always a slightly higher abundance than odd elements (rule valid for elements with atomic number  $\geq 5$ ). The argument resides in ability to capture protons : odd atomic number elements having one unpaired proton are more likely to capture protons whereas even atomic number elements are more stable having paired protons. Moreover Coulomb barriers for charged-particle reactions increase with heavy proton number.

Although produced in SNeII of massive stars, iron and iron-peak elements are efficiently formed through SNeIa. The SNeIa yields for iron-peak elements are still weakly constrained and strongly dependent on the adopted model for the SNeIa. It is not clear which type of binary evolution leads to the SNeIa explosion (single or double degenerate scenario) and how the explosion occurred (fast detonation mechanism or delayed detonation Iwamoto et al. (1999)).

SNeIa occurred through thermonuclear explosion of a CO white dwarf in close binary system when its mass reaches the Chandrasekhar limit accreting mass from a companion (Hoyle & Fowler 1960; Nomoto et al. 1997). A more detailed description of the physics of the SNeIa can be found in Thielemann et al. (2004). The nature of the mass donor in the binary system is not well defined for the moment. The classical case called the single degenerate scenario is

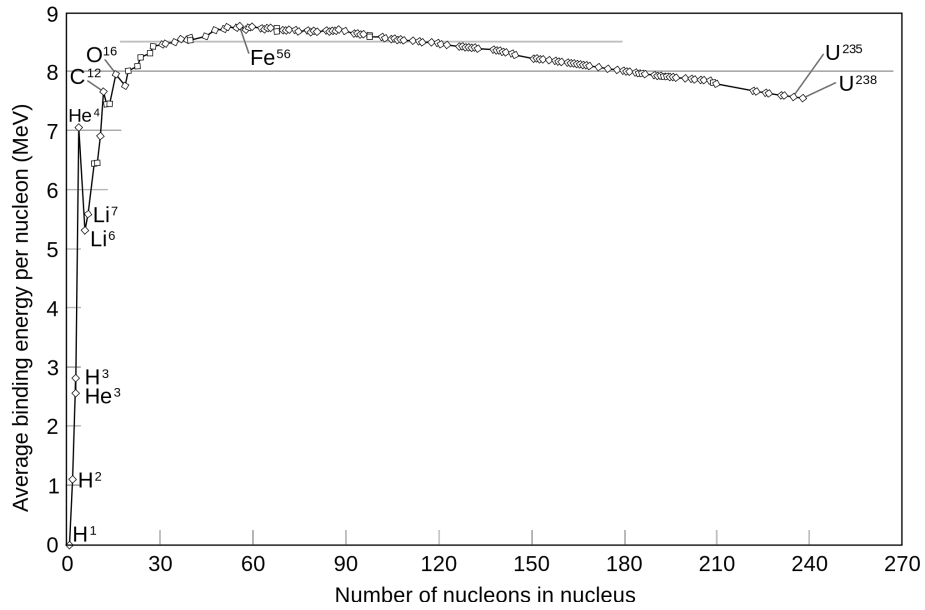


Figure 2.2: Average binding energy per nucleon in MeV in function of number of nucleons. Source : [http://commons.wikimedia.org/wiki/File:Binding\\_energy\\_curve\\_-\\_common\\_isotopes.svg](http://commons.wikimedia.org/wiki/File:Binding_energy_curve_-_common_isotopes.svg)

when the companion is a normal star (Whelan & Iben 1973; Iben & Tutukov 1984b). But an other scenario is proposed, the double degenerate one, where the explosion results from the merger of two WDs (Webbink 1984; Iben & Tutukov 1984a). This latter scenario could explain the diversity observed in SNeIa varying the masses of the two WDs (Pakmor et al. 2011).

Kobayashi et al. (2006) present a discussion about the lifetime of the SNeIa. In order to explain for example the decrease in  $[\alpha/\text{Fe}]$  and the formation time-scale we often use the SNeIa lifetime of approx 1.5 Gyr. However several effects need to be taken into account to estimate the lifetime of a SNeIa : the lifetime distribution, the metallicity effect of SNeIa, the mass and energy dependencies of the nucleosynthesis yields of SNeIa and an uncertainty of the IMF. The shortest lifetime of SNeIa depends on the SNeIa model : e.g., 0.1 Gyr for the double-degenerate model (Tutukov & Yungelson 1994), 0.3 Gyr for the Matteucci & Recchi (2001) model and 0.5 Gyr for the single-degenerate model Kobayashi et al. (1998).

Following Thielemann et al. (2004), as the CO white dwarf is almost fully burned, the SNeIa yields are predominantly composed of iron-peak elements (on average 0.6-0.8  $M_{\odot}$ ), small amount of Si to Ca and minor quantities of unburned or pure C burning products as for example C, O, Ne, Mg.

According to Woosley et al. (2002), scandium is produced only by SNeII through different channels (C and Ne hydrostatic burning phases,  $\alpha$  freeze out and neutrino-powered wind) and not by SNeIa. Scandium is located between calcium and titanium in the periodic table then in between  $\alpha$ -elements.



Isotopes of chromium are produced in the two varieties of rare SNeIa : carbon deflagration in WD very near to Chandrasekhar mass (Woosley 1997; Iwamoto et al. 1999), and helium detonation SNeIa Woosley & Weaver (1995). However chromium isotopes are also produced in massive stars during explosive O and Si burning phases (and during  $\alpha$  rich freeze out).

Mn is produced both in SNeIa and in explosive Si burning of massive stars. Some Mn can be also produced neutrino-powered winds.

Co is produced in SNeIa and through different channels by SNeII (helium burning s-process,  $\alpha$  rich freeze out and neutrino-powered winds).

Ni is produced by rare helium detonation SNeIa (Woosley & Weaver 1995) and by SNeII through two channels (helium burning s-process,  $\alpha$  rich freeze out).

Concerning SNeII yields of iron-peak element, Umeda & Nomoto (2002) show that K, Co, Zn and V are produced in complete Si-burning in deep layers ( $T_{peak} > 5 \cdot 10^9$ ), while Cr and Mn are produced in incomplete Si-burning regions ( $4 \cdot 10^9 < T_{peak} < 5 \cdot 10^9$ ). They try to explain the rise trend for [Cr/Fe] and [Mn/Fe] and the decreasing trend of [Co/Fe] with [Fe/H] observed for MW stars ([Fe/H] < -2.5 dex) arguing that the mass cut that divides the ejecta and the compact remnant tends to be deeper for more massive SNeII. Umeda & Nomoto (2005) propose that less massive SNeII may have higher mass cut or less energetic explosion even the physics is for the moment not well understood. If the mass cut is deeper in the most massive SNeII, more Co and Zn will be produced than in less massive SNeII. The trend is inverted for Mn and Cr following the same arguments. Nickel is supposed to be created in both complete and incomplete Si-burning which seems to be confirmed by observations with constant behavior for MW halo stars.

### 2.1.5 Neutron-capture elements

Elements up to iron-peak are produced by stellar nucleosynthesis and heavier elements are formed by SNe nucleosynthesis. Nuclei beyond zinc are formed through neutron capture process free from any Coulomb barrier. The mechanisms is the following : nuclei capture neutrons and if the resulting nuclei are unstable they can transform neutrons into protons via  $\beta$  decay (emitting an electron and an electron antineutrino), producing progressively all heavier elements. Two types of neutron-captures processes can be defined depending on the competition between neutron-capture and  $\beta$  decay time scales.

- rapid (r)-process : when the time scale for neutron capture is faster than radioactive  $\beta$  decay time scale. It occurs in high neutron density regions where the nuclei have no time to decay between two neutron captures. A large number of neutron are captured per second and the typical neutron density is of  $10^{24} - 10^{28} \text{ cm}^{-3}$  (Kratz et al. 2007). Following successive neutron captures the atomic number remain unchanged but the nuclei mass increase creating radioactive and neutron-rich elements far from the Valley

of stability. The highly unstable nuclei obtained decay afterwards through  $\beta$  decay increasing their atomic number.

- slow (s)-process : when the time scale for neutron captures is slower than radioactive  $\beta$  decay time scale. It occurs in small neutron densities ( $\leq 10^8 \text{ cm}^{-3}$ ) where a single neutron is captured by a nucleus. The time between two neutron captures is of the order of hundreds to thousands of years. If the nuclei just obtained is unstable it will decay instead of capturing an other neutron. The nuclei created by s-process are close to the Valley of stability.

As the nuclei involved in the s-process are relatively long-lived their properties (mass, half-live) can be obtained experimentally. On the contrary we are lacking experimental properties of nuclei involved in r-process because their typical radioactive half-lives are of the order of 0.01-0.1 seconds. This is why most of r-process nuclei data rely only on theoretical developments (e.g., Lunney et al. (2003)). Some elements are called pure r- or s- process because they can be formed by only one channel. For example, some stable isotopes are pure r-process because they are preceded by an unstable isotope of short half-life. In between stable isotopes could be produced by both s- and r-processes through different paths .

The observed peaks (after iron) in Solar System abundance distribution presented in figure 2.3 can be explained by the s-and r-processes. Particular nuclei presenting magic number of nucleons are known to be extremely stable. For magic nucleon number, the neutron capture cross-section decreases a lot, stopping the s-process and leading to an accumulation of magic isotopes. Sr, Y and Zr form the first s-process peak (light-s element), Ba, La, Ce, Pr and Nd the second peak (heavy-s elements). A third peak is located at the end of the s-process at Pb and Bi. The heavier element produced by s-process is Bi. The r-process also induced peaks that are horizontally shifted (lower Z than in s-process). An enhancement of neutron-rich unstable elements with magic neutron number is produced by r-process, leading after  $\beta$  decays to an enhancements of elements at lower Z.

Sources of r- and s-process need very different astrophysical environments depending on the contrast in neutron densities. Thanks to theoretical studies and observations, sources of s-process elements are identified as : i) low and intermediate mass thermally pulsating AGBs (Snedden et al. 2008) and ii) massive stars during He and C burning phases. In the case of AGBs as sources of s-process, the contribution to chemical enrichment is delayed by 100-300 Myr allowing to probe the star formation in similar time-scale to alpha-elements. According to Burbidge et al. (1957) and Cameron (1957a,b) the sources of r-process required an explosive environment, like during SNe events. The nature of the r-process elements is still a puzzling question. The first and usual considered channel production is the core-collapse supernovae (Woosley et al. 1994; Qian & Wasserburg 2007). If production of r-process elements are associated with massive stars nucleosynthesis their contribution to enrichment should not suffer from time delay. However Wanajo (2013) show that SNeII seem to fail to synthesize

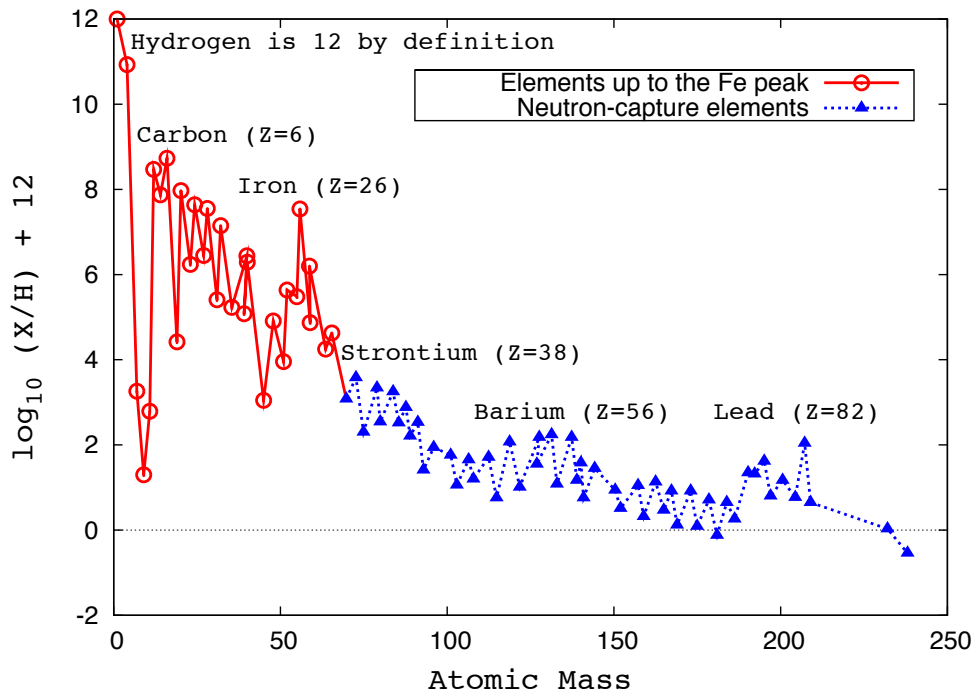


Figure 2.3: From Karakas & Lattanzio (2014) : Solar abundance distribution using data from Asplund et al. (2009).

the heavy r-process elements. Alternatively other models have been recently proposed for the production of r-process elements : neutrino-driven proto-neutron-star PNS wind of core-collapse supernovae (Wanajo 2013), and binary neutron star (NS-NS) mergers (Wanajo et al. 2014; Just et al. 2014). Rare events but able to reproduce light and heavy elements r-process elements according to their models.

The two r- and s-process can be separated into weak and main contributions.

The weak s-process occurred in massive stars at the end of the He and C burning phase and create light neutron capture elements ( $A \leq 90$ , up to first peak elements). The main s-process occurred in AGBs as explained above and form the heavy neutron capture elements ( $A \geq 90$ , beyond the first peak and up to Pb). However Travaglio et al. (2005) show that the s-process production in AGBs is strongly dependent on the metallicity (the AGB yields are metallicity-dependent). At solar metallicity large amount of the first s-process peak elements are produced (Sr, Y and Zr) because more nuclei capture neutrons. At lower metallicity more second s-process peak elements (Ba, La, Ce, Nd) are preferentially created because more

neutron per nuclei are available.

The main r-process dominates the production of heavy neutron capture elements for relatively metal-rich stars ( $[\text{Ba}/\text{H}] \geq -2.5$ , this corresponds more or less to  $[\text{Fe}/\text{H}] \geq -2.3$  dex in the Galaxy). François et al. (2007) show that a weak r-process is required to explain the synthesis of light (first peak) neutron capture elements in metal-poor stars. From observations comparing abundances [light/heavy] elements versus [heavy/H] they suggest 3 different regimes : solar ratio for  $[\text{Ba}/\text{H}] \geq -2.5$  (corresponding to the main process), increasing over-abundance for decreasing  $[\text{Ba}/\text{H}]$  for  $-4.5 \leq [\text{Ba}/\text{H}] \leq -2.5$  (weak process), and again solar values for  $[\text{Ba}/\text{H}] \leq -4.5$  corresponding to  $[\text{Fe}/\text{H}] \simeq -3$ . The heavy neutron-capture elements (like Ba or Eu) are produced by the main r- and s-processes. The origin of the light neutron-capture elements (as Sr, Y, Zr) is more complex : at solar  $[\text{Fe}/\text{H}]$  they are formed through main s-process (Travaglio et al. 2004; Bisterzo et al. 2014) but at low  $[\text{Fe}/\text{H}]$  they are formed dominantly by weak r-process (François et al. 2007).

Some exceptions exist like Eu which is almost exclusively produced by r-process. Europium in the Sun is almost entirely produced via the r-process (Snedden et al. (2008) quote the value of 97%).

## **2.2 Lines formation**

### **2.2.1 Context**

Stellar spectra are considered as a precious sources of information about stars. We can derive radial velocities and chemical composition of the outer layers of their atmospheres. Lines formation is the result of the interaction between the electromagnetic radiations (photons coming from the center of the star) and the matter composing the stellar atmosphere (atoms and molecules). Through interactions, energy is absorbed by the matter leading to formation of absorption lines. Determining the wavelength of the absorption lines, we are able to deduce the corresponding elements thanks to the quantum physics and accurate laboratory measurements. In this way studying carefully absorption lines tell us which elements are present in the atmosphere of the star and in which relative proportions. The more the atoms are numerous, the more the lines are stronger. The characteristics of the lines depend on many physical parameters as radiative transfer, parameters of the stellar photosphere and the quantity of absorption element. Between the production of the radiation in the stellar core and its liberation out of the stellar surface, a huge number of absorptions and re-emissions take place in the photosphere.

The next developments follow the formalism of Gray (2008).

### **2.2.2 Radiative transfer : equation and solution**

A stellar atmosphere is composed of a plasma of particles (atoms, ions, electrons, molecules, dust grains, photons) with number densities varying between  $10^6 - 10^{16} \text{ cm}^{-3}$  and temperatures around  $10^3 - 10^6 \text{ K}$ . The physical description of a stellar atmosphere is supported by a kinetic theory with the Boltzmann equation and hydrodynamic equations describing the continuity, impulsion equations and conservation of energy and particles number. If we consider a local thermodynamical equilibrium (LTE), it means that radiation and matter are locally at thermodynamical equilibrium. At a microscopic scale it means that all of the emitted photons are re-absorbed producing a black body spectrum (the source function can be considered as the Planck function under LTE condition). The medium can be then simply characterized by its temperature and density of particles. At a macroscopic scale an LTE assumption is described by 3 uni-vocal distribution functions : the Maxwell speed distribution function for particles, the Boltzmann excitation equation, and the Saha ionization equation. In reality, the LTE assumption is not applicable for the outer layers from where are coming the photons because energy is lost by radiation and a temperature gradient is present. In the outer layers the opacity is small and a large number of photons can escape the surface. The more we go deep in the star the more we go close to the LTE approximation (increasing opacity). Many physical conditions favor deviations from LTE (non local thermodynamical

## Chapter 2. Stellar photospheres

---

equilibrium (NLTE)) : low density (giant and super giant stars), intensive radiation fields (hot stars).

The radiative transfer is the dominant transport of energy in the outer layers of the star and it determines how much light can escape the star. The equation of radiative transfer shows the variation of intensity produced by a radiation field traveling a medium of density  $\rho$ . During this event, many interactions between the radiation field and the medium occur implying emissions and absorptions of energy. The general equation of transfer is the following :

$$\left( \frac{1}{c} \frac{\partial}{\partial t} + \vec{n} \cdot \vec{\nabla} \right) I(\vec{r}, \vec{n}, \nu, t) = j(\vec{r}, \vec{n}, \nu, t) - \kappa(\vec{r}, \vec{n}, \nu, t) I(\vec{r}, \vec{n}, \nu, t) \quad (2.1)$$

where  $I$  is the specific intensity,  $j$  the emission coefficient,  $\kappa$  the absorption coefficient,  $\vec{r}$  the position vector,  $\vec{n}$  is normal to the direction to the observer,  $\nu$  is the frequency of the radiation and  $t$  the temporal parameter. Here the intensity change is expressed per unit length.

Considering a situation independent on the time and in a 1D case, the radiative transfer equation simplifies as follows :

$$dI_\nu = -\kappa_\nu \rho I_\nu ds + j_\nu \rho ds \quad (2.2)$$

it represents the variation in specific intensity  $I_\nu$  passing through a volume of length  $ds$  and density  $\rho$  summing energy gains  $j$  and losses  $\kappa I_\nu$ . The absorption and emission coefficient are defined per unit mass.

Introducing two new important physical variables : the optical depth  $d\tau_\nu = \kappa_\nu \rho ds$ , and the source function  $S_\nu = \frac{j_\nu}{\kappa_\nu}$ , the equation can be rewritten as a differential :

$$\frac{dI_\nu}{d\tau_\nu} = S_\nu - I_\nu \quad (2.3)$$

As a physical meaning, the optical depth is a measurement of the radiation attenuation. The optical depth is zero at the surface of the star (all the radiation can escape), and the more we enter the star the more the radiation is absorbed. Considering the case without emission ( $j = 0$ ), the radiation will be absorbed exponentially in function of the optical depth. In other words the optical depth is a measurement of the quantity of matter between the observer and the origin of the photons.

The source function is proportional to the number of emitted photons in all directions divided by the optical depth.

After integration the formal solution is :

$$I_\nu(\tau_\nu) = \int_0^{\tau_\nu} S_\nu(t_\nu) e^{-(\tau_\nu - t_\nu)} dt_\nu + I_\nu(0) e^{-\tau_\nu} \quad (2.4)$$

The radiation at the point  $\tau_v$  is composed of the sum of intensities  $S_v$  originating at point  $t_v$  but suffering attenuation according to optical depth separation  $(\tau_v - t_v)$  and any incident radiation at  $\tau_v = 0$  called  $I_v(0)$  suffering extinction of factor  $e^{-\tau_v}$ .

The key resides in solving this equation, therefore the function  $S_v(t_v)$  is required to be known. Considering the specific geometry of a plane-parallel atmosphere, we define the optical depth not along the line of sight but along a vertical axis  $dx$  separated by an angle  $\theta$ . Adopting this convention we obtain  $dx = -dr$  along the stellar radius (polar coordinates) and  $d\tau_v = \kappa_v \rho dx$ . The solution is given by :

$$I_v(\tau_v) = - \int_c^{\tau_v} S_v(t_v) e^{-(\tau_v - t_v) \sec \theta} \sec \theta dt_v \quad (2.5)$$

where the previous term  $I_v(0)e^{-\tau_v}$  is replaced by the integration constant  $c$  in the integration limit.

### 2.2.3 Form of source function

For the moment the unknown in the solution is the expression of the source function. The source function has two origins : emission and absorption linked respectively to the continuum  $j_v^c, \kappa_v$  and to the line  $j_v^l, l_v$ . Therefore the source function can be expressed as :

$$S_v = \frac{j_v^l + j_v^c}{l_v + \kappa_v} = \frac{S_l + (\kappa_v / l_v) S_c}{1 + \kappa_v / l_v} \quad (2.6)$$

where  $S_l = \frac{j_v^l}{l_v}$  is the line source function and  $S_c = \frac{j_v^c}{\kappa_v}$  the continuum source function.

In order to express the line coefficients we consider transitions between an upper level  $u$  and a lower level  $l$  separated by an energy  $h\nu$ . Then  $N_u$  and  $N_l$  are the number of excited atoms per unit volume in level  $u$  and  $l$ ,  $A_{ul}$  is the Einstein probability coefficient for spontaneous emission. Similarly  $B_{ul}$  and  $B_{lu}$  are Einstein probability coefficient for stimulated emission and true absorption. The frequency dependence of the spontaneously emitted radiation is defined by  $\psi(\nu)$  and  $\phi(\nu)$  for absorption and stimulated emission. We have to put in perspective the spontaneous emitted radiation with the absorption and stimulated emission : the emission coefficient is  $j_{nu}^l \rho = N_u A_{ul} \psi(\nu) h\nu$  and the absorption coefficient is  $l_v \rho = N_l B_{lu} \phi(\nu) h\nu - N_u B_{ul} \phi(\nu) h\nu$ . Putting together the line source function becomes :

$$S_v = \frac{j_v^l}{l_v} = \frac{N_u A_{ul} \psi(\nu)}{N_l B_{lu} \phi(\nu) - N_u B_{ul} \phi(\nu)} \quad (2.7)$$

Thanks to general relations deriving from the Planck's radiation law,  $B_{ul} = B_{lu} \frac{g_l}{g_u}$  and  $A_{ul} = \frac{2h\nu^3}{c^2} B_{ul}$ , where  $g_u$  and  $g_l$  are the statistical weights of the upper and lower levels, the source

function is transformed :

$$S_\nu = \frac{2h\nu^3}{c^2} \frac{1}{(N_l/N_u)(g_u/g_l) - 1} \frac{\psi(\nu)}{\phi(\nu)} \quad (2.8)$$

In order to solve the radiative equation (2.5) we need to know  $S_\nu$  but  $S_\nu$  is expressed in function of  $N_l/N_u$  dependent on  $I_\nu$ . One solution is considering a LTE because under this assumption the fraction  $N_l/N_u$  can be given by the Boltzmann excitation equation 2.9 and Saha ionization equation 2.10 gives the ratio between populations of two ionization states.

$$\frac{N_u}{N_l} = \frac{g_u}{g_l} e^{\frac{-h\nu}{kT}} \quad (2.9)$$

$$\frac{N_{i+1}}{N_i} P_e = \frac{(2\pi m_e)^{3/2} (kT)^{5/2}}{h^3} \frac{2u_{i+1}}{u_i} e^{\frac{-I}{kT}} \quad (2.10)$$

where  $u_{i+1}$  and  $u_i$  are the partition functions of ions and neutral atoms,  $P_e$  the electronic pressure,  $m_e$  the mass of the electron,  $h$  the Planck constant,  $k$  the Boltzmann constant, and  $I$  the ionization potential. In LTE, we assume that at each emission must correspond one absorption, this means that  $\psi(\nu) = \phi(\nu)$ . Finally and under LTE assumption the line source function takes the form of the Planck function :

$$S_l = B_\nu(T) = \frac{2h\nu^2}{c^2} \frac{1}{e^{\frac{h\nu}{kT}} - 1} \quad (2.11)$$

### 2.2.4 Shape of spectra line / Line profile

The shape of the spectral line is given by the flux at the stellar surface following the general definition of the flux :

$$\mathcal{F}_\nu = 2\pi \int_0^\pi I_\nu \cos\theta \sin\theta d\theta \quad (2.12)$$

If we use the 2.5 in this equation 2.12 and deriving the flux at the stellar surface we end with this expression :

$$\mathcal{F}_\nu(\tau_\nu = 0) = 2\pi \int_0^\infty S_\nu(\tau_\nu) E_2(\tau_\nu) \tau_\nu d\tau_\nu \quad (2.13)$$

where the  $E_2$  function is an exponential integral decreasing with  $x$  :  $E_n(x) = \int_1^\infty \frac{e^{-xw}}{w^n} dw$ .

The interpretation of the flux per unit area at the surface is given by : the sum of the source functions from the surface to the interior of the star while the layer is not opaque. The source



function is weighted by the extinction factor decreasing towards the center of the star. For the next developments, we keep only the line source function in consideration  $S_\nu = S_l$  and define a new variable, the reference optical depth  $\tau_0$ , corresponding to a precise wavelength (here 5000 Å) at which the temperature is known.

$$\tau_n u(\tau_0) = \int_{-\infty}^{\log \tau_0} \frac{l_\nu + \kappa_\nu}{\kappa_0} t_0 \frac{d \log t_0}{\log e} \quad (2.14)$$

The flux can be rewritten :

$$\mathcal{F}_\nu(\tau_\nu = 0) = 2\pi \int_0^\infty B_\nu(T) E_2(\tau_\nu) \frac{d\tau_\nu}{d\tau_0} d\tau_0 = 2\pi \int_{-\infty}^\infty B_\nu(T) E_2(\tau_\nu) \frac{l_\nu + \kappa_\nu}{\kappa_0} \tau_0 \frac{d \log \tau_0}{\log e} \quad (2.15)$$

If  $\mathcal{F}_\nu$  corresponds to the shape of the spectral line, the spectrum can be expressed as :  $\frac{\mathcal{F}_c - \mathcal{F}_\nu}{\mathcal{F}_c}$  where  $\mathcal{F}_c$  is the continuous flux. Taking the case of a weak line, an analytical approximation using 2.14 shows that the weak line strength is proportional to the ratio  $\frac{l_\nu}{\kappa_\nu}$ .

$$\frac{\mathcal{F}_c - \mathcal{F}_\nu}{\mathcal{F}_c} = \text{cst} \frac{l_\nu}{\kappa_\nu} \quad (2.16)$$

According to equation 2.16, the strength of a spectral line can be increased by increasing line absorption or by decreasing continuous absorption.

### 2.2.5 Absorption coefficients

In order to obtain a correct expression of the equation 2.15, we need to know in more details the continuous absorption coefficient  $\kappa_\nu$  and the line absorption coefficient  $l_\nu$ . Absorptions could be linked to three transition types : i) bound-free transitions : photo-ionization when an atom absorbs a incident photo and eject an electron, ii) free-free transitions : an electron moving in an electromagnetic field of a ion absorbs a photon (modifying the kinetic energy of the electron), iii) bound-bound transitions : transition of atom (or a ion) from one bound state to another bound state after absorbing a photon. The shape of the continuum is due to bound-free and free-free transitions while the shape of the line is due to bound-bound transitions.

In theory the absorption lines should be  $\delta$ -peaks occurring at the wavelengths corresponding to the energy differences of transition levels. However several processes taking place in the photosphere are responsible of the broadening of the lines. A list of each of these phenomena is given below. Each of this broadening mechanism gives its respective absorption coefficient (dependent on the wavelength) and the width of the each profile is determined by a damping constant. These constants can be determined either by theory or by experiments. Finally the realistic line profile is obtained by a convolution of the diverse individual absorption

coefficients.

### Microscopic effect

**Natural broadening** The classical model for a photon interacting with matter is given by a plane of electromagnetic wave interacting with dipoles. Following this formalism the basic form of the absorption coefficient is given by :

$$l_\nu \rho = N\alpha = N \frac{\pi e^2}{mc} \frac{\gamma}{\Delta\omega^2 + (\gamma/2)^2} \quad (2.17)$$

where  $l_\nu$  is the mass absorption coefficient,  $\alpha$  the absorption coefficient per atom,  $\Delta\omega$  the distance from the center of the line,  $\rho$  the density of the medium,  $N$  is the number of dipoles,  $e$  is the electric charge of the electron,  $m$  is its mass.

The expression of  $\alpha$  corresponds to a damping profile, also called Lorentzian profile with a width determined by the *normal* damping constant  $\gamma$ . The natural broadening can be understood as consequence of the Heisenberg uncertainty principle : the energy level of an excited state of an atom can never be determined precisely because its life time is finite.

**Pressure (collision) broadening** Pressure broadening is due to collisional interactions between the absorbing atoms and other particles (ions, electrons, atoms, molecules). The collisions alter the energy of the atomic levels of the absorbers. This frequency variation depends on the separation  $R$  between the two particles in interaction and a constant  $C$  varying in function of the type of the transitions.

$$\Delta\nu = \frac{C_n}{R^n} \quad (2.18)$$

The integer  $n$  varies in function of the nature of the perturbers. The most important effect acting in cool stars come from collisions with neutral hydrogen atoms called van der Waals broadening and corresponding to  $n = 6$ . Secondary effect are due to linear Stark broadening  $n = 2$  where the perturbers are the protons and electrons but effects are focused on hydrogen lines. Quadratic Stark broadening effects  $n = 4$  are dominant in hot stars and correspond to cases where the perturbers are ions and electrons. In the case of pressure broadening the absorption coefficient per atom is defined as :

$$\alpha = \text{cst} \frac{\gamma_n/4\pi}{(\nu - \nu_0)^2 + (\gamma_n/4\pi)^2} \quad (2.19)$$

where the damping constant is  $\gamma_n = 2/\Delta t_0$  and  $\Delta t_0$  is the average collision time which depends on the pressure and temperature parameters. The interaction constants  $C_n$  are either mea-

sured in laboratory or calculated for each transition and each interaction.

The dominant pressure broadening for stars cooler than 10000 K (which is the case of our studied stars) is the van der Waals broadening.

**Thermal Doppler broadening** Due to its thermal motion each absorber particle has a random velocity. The radial component (along our line of sight) of this thermal velocity induce a Doppler shift leading to a broadening of the line. The wavelength shift caused by the radial velocity  $v_r$  can be expressed :

$$\frac{\Delta\lambda}{\lambda} = \frac{v_r}{c} \quad (2.20)$$

Applying a Maxwellian distribution of the velocities, the distribution of  $\Delta\lambda$  gives :

$$\frac{dN}{N} = \frac{1}{\pi^{1/2}\Delta\lambda_D} e^{-(\Delta\lambda/\Delta\lambda_D)^2} d\Delta\lambda \quad (2.21)$$

where the Doppler wavelength shift is defined as :

$$\Delta\lambda_D = \frac{v_0}{c} \lambda_0 = \frac{\lambda_0}{c} \sqrt{\frac{2kT}{m}} \quad (2.22)$$

where  $v_0$  is the variance related to the temperature by  $v_0^2 = 2kT/m$ .  $m$  is the mass of the atom,  $k$  is the Boltzmann constant and  $\lambda_0$  is the central wavelength of the line. Finally the absorption coefficient per atom is :

$$\alpha = \frac{\pi^{1/2} e^2}{mc} f \frac{\lambda_0^2}{c} \frac{1}{\Delta\lambda_D} e^{-(\Delta\lambda/\Delta\lambda_D)^2} \quad (2.23)$$

where  $f$  is the oscillator strength. The broadening of the line is given by the Doppler wavelength shift.

**Micro-turbulence velocity** Except the random thermal velocity the particles are subject to small scale velocities in stellar atmosphere. If the dimensions of the particles are small in comparison to the optical depth they are called micro-turbulence velocities. They infer also Doppler shifts similarly to the thermal case and produce a gaussian line broadening with a broadening constant  $v_{turb}$ . Combining the thermal Doppler broadening and the effect of micro-turbulence velocity, the Doppler shift can be re-written :

$$\Delta\lambda_D = \frac{\lambda_0}{c} \sqrt{\frac{2kT}{m} + v_{turb}^2} \quad (2.24)$$

The typical values of micro-turbulence vary from 0 for dwarfs up to 5 km/s for super giants (increasing with luminosities). In the case of our RGBs the values range from 1.4 to 2.5 km/s.

**The line profile combining the microscopic effects** Dealing with cool stars (effective temperature  $\leq 10000$ ), which is the case in this study, we can neglect the (quadratic) Stark broadening and as we are interested in metal lines we also neglect the linear Stark broadening. Taking into account the other four broadening mechanisms developed above, the final line profile is obtained by convolving their respective absorption coefficient :

$$\alpha_{\text{tot}} = \alpha_{\text{natural}} * \alpha_{\text{Waals}} * \alpha_{\text{thermal}} * \alpha_{\text{microturbulence}} \quad (2.25)$$

The first convolution leads to a new dispersion profile with damping constant of  $\gamma_{\text{natural}} + \gamma_6$  and the last convolution gives a gaussian broadening function with a dispersion expressed as 2.24. The final convolution is then between a dispersion profile and a gaussian function. After calculations the total absorption coefficient takes the following form:

$$\alpha_{\text{tot}} = \frac{\pi^{1/2} e^2}{mc} \frac{f}{\Delta v_D} H(u, a) \quad (2.26)$$

where  $H$  is the Hjerting function :

$$H(u, a) = \frac{a}{\pi} \int_{-\infty}^{\infty} \frac{e^{-u_1^2}}{(u - u_1)^2 + a^2} du_1 \quad (2.27)$$

with  $a = \frac{\gamma}{4\pi} \frac{1}{\Delta v_D}$  and  $u = \frac{\Delta v}{\Delta v_D}$ . An other function called the Voigt function  $V$  is often used to describe the line profile instead of the Hjerting function :

$$V(u, a) = \frac{H(u, a)}{\pi^{1/2} \Delta v_D} \quad (2.28)$$

The Hjerting function can be expanded in simple series as :

$$H(a, u) = H_0(u) + aH_1(u) + a^2H_2(u) + a^3H_3(u) + a^4H_4(u) \quad (2.29)$$

The first term of the expansion is a gaussian function showing that the center of the line is dominated by a gaussian core while the wings of dispersion component grow with the increase of variable  $a$ . If the line is weak enough to be dominated by only a gaussian core the abundances can be determined by measurement of equivalent width through gaussian fits. Otherwise considering lines with prominent wings the abundances will be better determined using the synthesis method comparing the observed line with a synthetic line computed taking into account all the broadening mechanisms.

The final line absorption coefficient is found thanks to the relation  $l_\nu = \frac{\alpha N}{\rho}$ .

**Other effects : splitting the energy levels giving new possible transitions** Three types of splitting can occur implying a broadening of the lines : i) the hyperfine structure splitting only for an odd atomic number isotope due to interaction of the nuclear spin with the angular momentum of the rest of the atom ii) isotopic splitting due to slightly different mass between isotopes iii) Zeeman splitting when absorbers are in a magnetic field.

### Macroscopic effect

Other physical effects on macroscopic scale induce broadening of lines. Two among the three listed below are linked to characteristics of the star and the third one is linked with the instrument of observation.

**Rotation** The rotation of a star originates from the conservation of angular momentum during its formation. Due to rotation the lines are affected by the Doppler shift of the photons coming from different parts of the stellar disk. Photons are redshifted if emitted from the side spinning away from us and blueshifted if they are emitted from the side spinning towards us. If the star is close and big enough that we can resolve its disk, the line profile can be used as 1D map of the stellar disk linking position on the stellar disk and Doppler shift within the profile. Moreover the broadening induced by rotation depends on the orientation of the rotation axis in function of the line of sight. A bigger effect is expected for equator-on objects. The stellar rotation are given in function of their projected equatorial velocity  $v \sin i$  where  $i$  is the angle between the rotation axis and the line of sight direction. For giants stars, the rotation is expected to be slow with typical values of  $\leq 5$  km/s. Gray (1989) present a empirical relation for the stellar rotation for giants in function of their spectral type :

$$v = \frac{4}{\pi} \langle v \sin i \rangle = 15.6 - 4.2 Sp \quad (2.30)$$

where  $Sp$  corresponds to a different constant for each spectral type (G2, G3, ...). In our study the rotation velocities are neglected because dealing with giants stars (RGBs).

**Macro-turbulence velocity** Other Doppler shifts are induced by a velocity field acting on macroscopic scale (the size of the turbulent elements is on the order of the optical depth). All lines are broaden by a photospheric velocity field. The characteristic shape of lines broaden by macro-turbulence velocity fields is a triangular shape for weak lines and asymmetries are often a typical signature due to granulation.

**Instrumental broadening** Although telescopes are wonderful instruments, they are not ideal and due to their finite resolution  $R$  they imply a line broadening linked to their point spread function (instrumental response). Then the instrumental line profile results in the convolution of the line profile coming from the stars with the telescope point spread function which is often approximated by a gaussian function following :

$$R = \frac{\lambda_0}{\Delta\lambda} \quad (2.31)$$

where  $R$  is the resolution of the spectrum,  $\Delta\lambda$  corresponds to the full width at half maximum (FWHM) of the gaussian function linked with the instrumental broadening.

### Continuous absorption coefficient

The continuous absorption is the sum of absorptions resulting from many physical processes : bound-free transitions through ionizations and free-free transitions through acceleration of a charge passing close to an other one.

The importance of contributors (atoms, ions, metal, molecules) depends greatly on the stellar characteristics (temperature, metal content) and the considered wavelengths.

H, the neutral hydrogen, is the main contributor to continuous absorption for hot stars ( $T_{\text{eff}} \geq 8000$  K).  $\text{H}^-$ , the negative hydrogen ion formed of an hydrogen atom bound with an extra electron, is one of the main continuous absorber for  $\lambda \leq 16421 \text{ \AA}$ . Ions  $\text{H}_2^+$  are preferentially absorbers in very cool stars ( $T_{\text{eff}} \leq 3000$  K) where molecular hydrogen  $\text{H}_2$  is more numerous than atomic hydrogen. He is a significant absorber for  $T_{\text{eff}} \geq 10000$  K hence typically for hot O and B stars. Other sources of continuous absorption could come from metals like C, Si, Al, Mg, Fe producing bound-free transitions dominant in UV ( $\lambda \leq 2500 \text{ \AA}$ ), molecular ions as  $\text{CN}^-$ ,  $\text{C}_2^-$ ,  $\text{H}_2\text{O}^-$  dominant in late-type stars, molecules as TiO,  $\text{TiO}_2$ , CrH, FeH, VO, MgH dominant in cool stars ( $T_{\text{eff}} \leq 3700$ ).

Finally the continuous opacity could be also due to lines (bound-bound transitions) when they are many and overlapping them creating a crowded area. This effect is almost observed for very cool stars where molecules create a large number of spectra lines.

### Equivalent width and curve of growth

The measurement of the strength of a line called the equivalent width (EW) is given by the following relation :

$$W = \int_0^\infty \frac{\mathcal{F}_c - \mathcal{F}_v}{\mathcal{F}_c} dv = \frac{\text{cst}}{\kappa_v} \int_0^\infty l_v dv \quad (2.32)$$

The equivalent width corresponds to the width of a rectangle with a length of 1 and presenting the same surface as the normalized spectral line as presented in figure 2.4. The integral can be calculated using the relation  $l_\nu \rho = N\alpha$  where  $\rho$  is the mass density,  $N$  the number of line absorbers per unit volume and  $\alpha$  the atomic absorption coefficient.

$$W = \text{cst} \frac{\pi e^2}{mc} \frac{\lambda^2}{c} f \frac{N}{\kappa_\nu} \quad (2.33)$$

where  $e$  and  $m$  are respectively the charge and the mass of the electron and  $f$  is the oscillator strength related to the atomic transition probability and that varies for each atomic level.

After some developments, we can derive the following relation :

$$\log \frac{W}{\lambda} = \log C + \log A + \log g_n f \lambda - \theta_{ex} \chi - \log \kappa_\nu \quad (2.34)$$

where  $g$  is the statistical weight,  $C$  is a constant for a given star and a given ion,  $\chi$  the excitation potential of the level,  $\theta_{ex} = 5040/T$  where  $T$  is the temperature (LTE) and  $A = N_X/N_H$  is the number abundance for the element  $X$  relative to hydrogen. The higher the excitation potential is, the deeper in the photosphere the line is formed and the higher is the temperature.

This relation links the equivalent width and the number abundance  $A$  of the considered element, the interesting quantity we look for in the next chapter.

For a given atmosphere model, all spectra lines behave similarly with abundance variation which is determined by the curve of growth. When varying the element abundance, the lines move along the common curve of growth. However different lines take different positions at the curve of growth depending on their atmospheric parameters, excitation energy and oscillator strength. Each curve of growth presents three phases : a linear part for weak lines where the EW is proportional to the abundance, a saturated part where the EW is proportional to the square root of the logarithm of the abundance and finally for strong lines where the wings of the line dominate, the EW is proportional to the square root of the abundance. An example of a curve of growth is shown in figure 2.5 for an iron line from Lemasle et al. (2007). The full line is the theoretical curve of growth for a typical line  $\lambda = 5000 \text{ \AA}$ ,  $\chi_{ex} = 3$ . The squares, crosses and *plus* symbols are measurement for lines classed by potential excitation ranges. The x-axis is proportional to the logarithm of  $A$ .

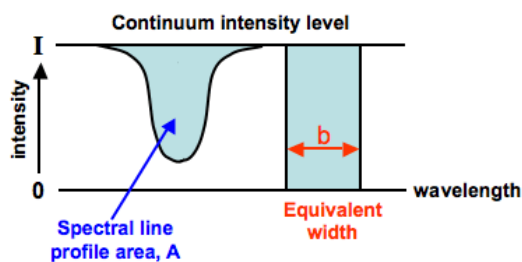


Figure 2.4: Definition of the equivalent width. The area  $A$  of a spectral line measured below the continuum level is related to a rectangular line profile with the same area and its equivalent width  $b$ . Source : <http://astronomy.swin.edu.au/cosmos/E/Equivalent+Width>

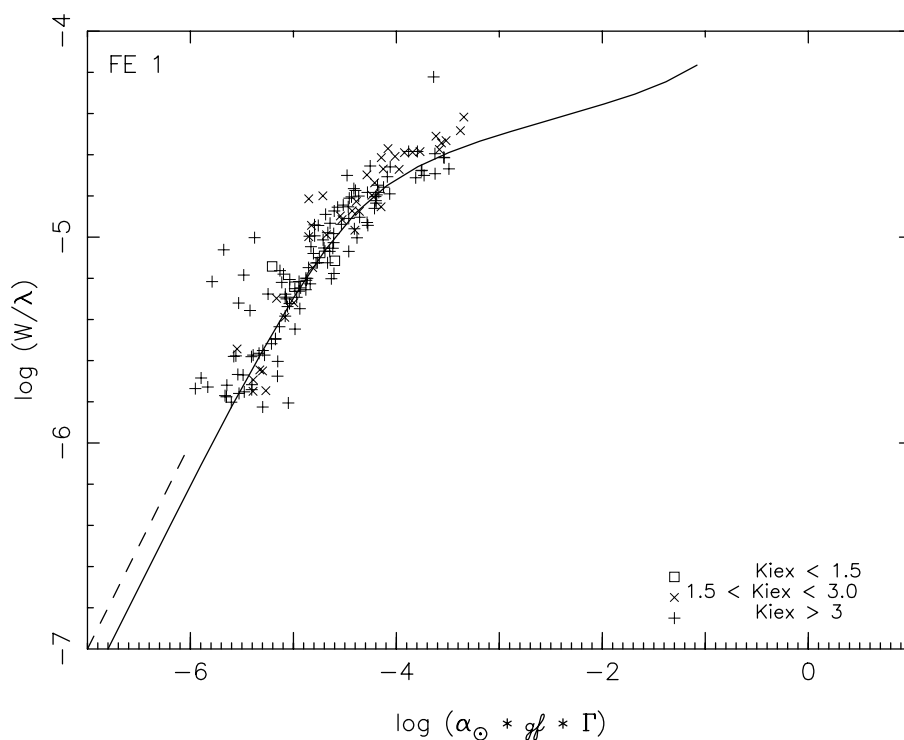


Figure 2.5: Lemasle et al. (2007) present in solid line the theoretical curve of growth for a typical line of Fe I at  $\lambda = 5000 \text{ \AA}$ ,  $\chi_{ex} = 3$ . The adopted atmospheric parameters are  $T_{\text{eff}} = 6180 \text{ K}$ ,  $\log g = 2.2$ ,  $v_{\text{turb}} = 4.0 \text{ km/s}$ , and  $[\text{Fe}/\text{H}] = -0.2 \text{ dex}$ . The dashed line corresponds to the  $[\text{Fe}/\text{H}] = 0$  location.



## 2.3 Model atmosphere

As determining abundances from strengths of spectral lines is a very complex problem due to the huge number of processes and parameters involved, we need to model the stellar atmospheres.

### 2.3.1 Definition

A model atmosphere is expressed as a table of values of physical parameters (source function, pressure, temperature) expressed at various optical depths. Under LTE, an atmospheric model is defined by the following parameters : the effective temperature  $T_{\text{eff}}$ , the surface gravity  $\log g$ , the metal abundances often expressed by the iron abundance  $[\text{Fe}/\text{H}]$  and the micro-turbulence velocity  $v_{\text{turb}}$ . The radius, luminosity  $L$  and the mass  $M$  of the star are expressed through the effective temperature and the surface gravity following :

$$T_{\text{eff}} = \left( \frac{L}{4\pi\sigma R_{\text{abs}}^2} \right)^{1/4} \quad g = g_{\odot} \frac{M}{R^2} \quad (2.35)$$

where  $\sigma$  is Stefan-Boltzmann constant,  $R_{\text{abs}}$  is the absolute stellar radius,  $g_{\odot}$  is the surface gravity of the sun and  $R$  is the stellar radius expressed in solar units. The expression of the effective temperature follows the Stefan-Boltzmann law expressing the bolometric flux. In that sense, the effective temperature can be expressed as the temperature of a black body presenting the same luminosity per surface. The expression of the surface gravity comes directly from the Newton gravitation law and corresponds to the gravitational acceleration experienced at the surface of the star. The surface gravity is generally given as the logarithm of its value expressed in  $\text{cm}/\text{s}^2$ .

In practice, models of atmosphere are computed for a fixed grid of stellar parameters and the searched model atmosphere is interpolated inside the grid.

### 2.3.2 Assumption and computation

Several hypothesis are needed to reduce the complexity of the problem of describing a stellar atmosphere :

- either homogeneous plane-parallel layers or homogeneous spherical shells making the geometry 1D
- a fixed chemical composition with depth
- statistical and hydrostatic equilibrium (no time dependence and no large scale motion as winds)

## Chapter 2. Stellar photospheres

---

- the mass of the atmosphere is negligible in comparison to the mass of the star
- energy conservation meaning that there is a radiative equilibrium in the outer layers
- energy is transported thanks to radiation and convection

The computation is an iterative process starting from a first guess of the temperature  $T_\tau$  and the gas pressure. The flux at the surface is derived through resolution of equations : the statistical equilibrium, the radiative transfer, the hydrostatic equilibrium. The structure is adjusted until reaching a convergence.

The plane-parallel model is a good approximation while the atmosphere is thin in comparison with the radius of the star. For giant stars the spherical model is more appropriated providing a better realistic description of the stellar photosphere. All the equations linked to the radiative transfer and to the construction of the atmosphere models have simpler expressions in 1D geometry than in 3D. Independently from each other, the creation of a model atmosphere and the calculation of a spectrum can be done either in 1D or in 3D geometry.

In an ideal case, computing models should be deriving the absorption coefficient at several points across each line as a function of the optical depth using transition probabilities and damping constants. However all of these data are not available and the number of lines to consider is very huge. Two techniques of simplifications exist: i) generate an opacity distribution function (ODF) for lines : the spectral range is divided into small intervals on which the ODF is calculated. ii) use a statistical opacity sampling (OS) of the absorption coefficient : chose a few but enough sampling points over the wavelength range. The former method is less costly but require some conditions.

### 2.3.3 Spectroscopic or photometric derivation of $T_{\text{eff}}$ , $\log g$ and $v_{\text{turb}}$

The three stellar parameters  $T_{\text{eff}}$ ,  $\log g$  and  $v_{\text{turb}}$  can be determined either from spectroscopy or from photometry. The former is well suited for high quality spectra presenting low noise and a large statistical number of measurable lines. In addition, the spectroscopic method are not well adapted for cool and metal-poor stars where NLTE effects are more important.

$T_{\text{eff}}$  Using spectroscopy the temperature is adjusted until obtaining no trend between the iron abundances and the excitation potentials of the lines. With different excitation potentials lines are formed at different depths inside the atmosphere. A wrong effective temperature would modify the temperature gradient implying an abundance gradient with excitation potential. This method is applicable under the condition that there is no intrinsic gradient of abundance with atmospheric depth.

A photometric alternative of the temperature determination is given by color temperatures

measurements. As an example Ramírez & Meléndez (2005) propose color indices calibrations for dwarf and giant stars.

$\log g$  The surface gravity can be derived requiring equal abundances from atoms of neutral elements and ionized elements. However the ionization balance depends also on the effective temperature. In general iron lines are used but often the number of Fe II lines is too low to infer a good estimation of the surface gravity.

As for  $T_{\text{eff}}$  a photometric calculation can be used to determine  $\log g$  based on the bolometric magnitudes.

$v_{\text{turb}}$  As the micro-turbulence velocity influences differently weak and strong lines it can be derived requiring no trend between the iron abundances and the equivalent widths of lines. The alternative comes not from photometry but from empirical relations.



## 3 The dwarf spheroidal galaxy Sextans

### 3.1 Observations with FLAMES/GIRAFFE

#### 3.1.1 Description of the Fibre Large Array Multi Elements Spectrograph (FLAMES)

The European Southern Observatory (ESO) VLT complex located in Paranal in Chile's Atacama desert is composed of four 8.2-m telescopes individually operating with a large collection of instruments. Each unit telescope (UT) offers four focus stations : one Cassegrain, two Nasmyth and a Coude for interferometry. A picture of the panorama of the observation site is shown in figure 3.1 and figure 3.2 presents the map of the instruments distribution among the four UTs. FLAMES is the multi-fibers intermediate and high resolution spectrograph mounted at the Nasmyth A focus of platform UT2 (Kueyen Telescope). A spectrograph operates fundamentally



Figure 3.1: Panorama of the ESO VLT observation site. Credit : G.Hüdepohl/ESO (atacamaphoto.com) Source : <http://www.eso.org/public/images/potw1139a/>

like a sophisticated prism: it decomposes the light into its component wavelengths called



Figure 3.2: The map of the current instruments distribution among the four VLT Unit Telescopes. Source : <http://www.eso.org/sci/facilities/paranal/instruments/overview.html>

a spectrum. The output spectrum is recorded on a CCD detector and finally saved in a computer file for further analysis. One of the major characteristics of a spectrograph, the resolution  $R$ , is defined as the minimum difference in wavelength  $\Delta\lambda$  that can be detected for a specific wavelength of light  $\lambda$  as given by the equation 3.1. It is determined by the dispersion characteristics of the prism-like device.

$$R = \frac{\lambda}{\Delta\lambda} \quad (3.1)$$

The spectrograph FLAMES and its fiber system were developed by the Observatoire de Paris-Meudon (P.I. F. Hammer) and Observatoire de Genève (P.I. A. Blecha) in collaboration with ESO. The integration of GIRAFFE started in spring 2001 in ESO-Garching.

FLAMES offers a field of view of 25 arcmin of diameter. The instrument is composed of three main sub-systems :

- the fiber positioner *OzPoz* hosting two plates as presented in figure 3.3. Dead time

### 3.1. Observations with FLAMES/GIRAFFE

---

between two observations is then reduced to less than 15 minutes taking the advantage of positioning the fibers on the second plate while the first one is in observing mode. The fibers are attached to the plate thanks to magnetic buttons. The minimum separation between two objects is of 10.5 arcseconds (arcsec) due to the size of the magnetic buttons. The position accuracy of the fibers is better than 0.1 arcsec.

- the intermediate-high resolution optical spectrograph, GIRAFFE, with three types of feeding fiber systems : MEDUSA, IFU, ARGUS. GIRAFFE is equipped with two gratings, one for intermediate resolution (5600-8600 in MEDUSA mode) and a second for high resolution (11642-30200 in MEDUSA mode). GIRAFFE proposes 30 fixed setups covering the whole visible range (3700 Å-9500 Å): 8 in intermediate resolution modes and 22 in high resolution with spectral bands varying from 167 to 1240 Å.  
The term GIRAFFE is not an acronym but its name comes from the first designs where the spectrographs were placed vertically.
- A link to the red arm of Ultraviolet and Visual Echelle Spectrograph (UVES) installed at the Nasmyth B focus of platform UT2 with 8 fibers of 1 arcsec entrance aperture each for a spectral resolution of 47000 and a wavelength coverage of 4200–11000 Å. Three standard UVES setups are proposed with central wavelengths of 5200, 5800, and 8600 Å and spectral band of 2000 Å. 7 fibers are dedicated to objects and/or sky spectra (if needed) and generally one fiber for simultaneous calibration allowing an accurate radial velocity measurements.

One advantage of this configuration is the possibility to observe simultaneously with the two spectrographs GIRAFFE and UVES without being constrained to have the same exposure time. In comparison with GIRAFFE, UVES proposes a larger spectral band at higher spectral resolution but only for a reduced number of fibers.

The fiber system of GIRAFFE is composed of the three following parts :

- 2 MEDUSA slits (MEDUSA 1 and MEDUSA 2) one per plate : up to 132 single fibers (including sky fibers) that can be used simultaneously. One set of MEDUSA fibers exists for each plate allowing the positioning of the fibers on the second plate while the first one is observing. The fiber aperture is 1.2 arcsec on the sky.
- 2 Integral Field Unit (IFU) slits : they are composed of rectangular array of 20 micro-lenses of 0.52 arcsec each, giving an aperture of 2 arcsec x 3 arcsec. 15 IFUs are dedicated for the objects and 15 others for the sky measurements.
- 1 ARGUS slit : a large IFU of 22 x 14 micro-lenses is mounted at the center of one of the 2 plates with two available magnification scales 1:1 and 1:1.67.

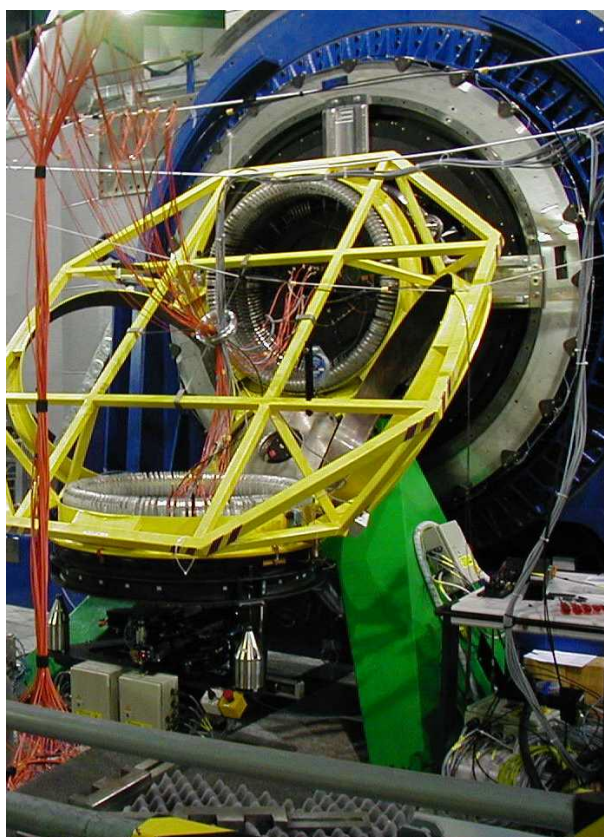


Figure 3.3: Picture of the OzPoz fiber positioner. Source : <http://www.eso.org/sci/facilities/paranal/instruments/flames/inst/OzPoz.html>

The captor used to transform the incoming photons in electric currents through photoelectric effect is a CCD. GIRAFFE is equipped with a 2K x 4K EEV CCD ( $15 \mu\text{m}$  pixels) with a scale of 0.3 arcsec/pixel in MEDUSA, IFUs and ARGUS direct mode, and a scale of 0.15 arcsec/pixel in the enlarged ARGUS mode. From a schematic point of view, the light coming from one of the slits goes through the order sorting filter. Before reaching the grating the light is reflected into a double pass collimator. The light is re-imaged on the CCD after formation of an intermediate spectrum. Scanning the grating along its rotation axis allows to obtain different wavelengths. The schematic layout of the GIRAFFE spectrograph is presented in figure 3.4 and figure 3.5 shows a picture of it. The spectrograph apertures of 1.2 arcsec on the sky corresponds to 6 pixels on the detector. The required spectral ranges are obtained choosing the corresponding filters.



### 3.1. Observations with FLAMES/GIRAFFE

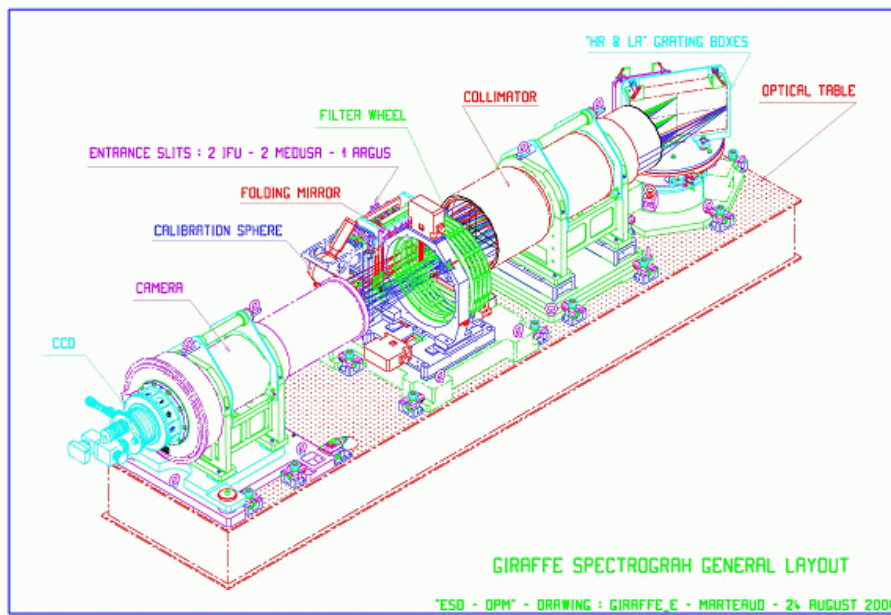


Figure 3.4: Schematic layout of the GIRAFFE spectrograph. Source : <http://www.eso.org/sci/facilities/paranal/instruments/flames/inst/Giraffe.html>

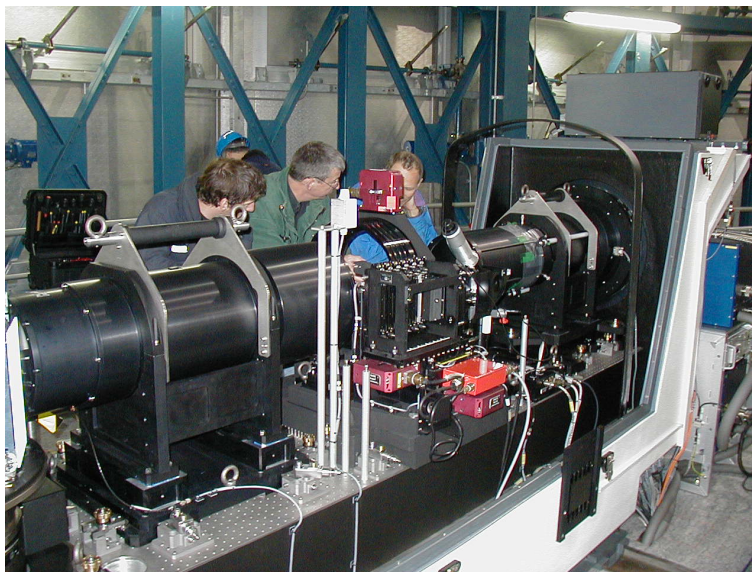


Figure 3.5: Picture of the GIRAFFE spectrograph. Source : [http://www.eso.org/sci/facilities/paranal/instruments/flames/img/giraffe\\_picture\\_3.jpg](http://www.eso.org/sci/facilities/paranal/instruments/flames/img/giraffe_picture_3.jpg)

### 3.1.2 Data sample

Based on ESO Program 171.B-0588(A) we obtained 26 science exposures from FLAMES/GIRAFFE. They have been observed in service mode during several epochs in the year 2004 for a total time of 30h17min. The spectrograph was used in MEDUSA mode providing the opportunity to observe simultaneously up to 132 separate objects. Three high resolution setups HR10, HR13 and HR14 were chosen to cover a sufficient large wavelength range in order to measure expected atomic absorption lines of the following elements Mg, Ca, Sc, Ti, Cr, Mn, Co, Ni, Ba and Eu. The table 3.1 gives the characteristics of these three setups : the wavelength coverage, the central resolution and the total exposure time.

Table 3.1: Characteristics of the three FLAMES/GIRAFFE gratings.

Setup	HR10	HR13	HR14
$\lambda$ Coverage [Å]	5339-5619	6120-6405	6308-6701
Central Resolution $R$	19800	22500	17740
Total Exposure Time	36080 sec	43566 sec	29400 sec

The table 3.2 presents the observational characteristics of the 26 science exposures (given in *fits* format) : 8 have been observed in setup HR10, 11 in HR13 and 7 in HR14. The observation dates are encoded in the file names in the first column. The following columns express respectively the Medusa plate number (M1 for Medusa1 and M2 for Medusa2), the name of the setup, the central wavelength of the setup  $\lambda_c$  in Å, the exposure time (Exp. T) in seconds, the right ascension RA and the declination Dec of the observation fields center and the presence of the thorium-argon simultaneous calibration fibers called *SimCal*. Each exposure was composed of :

- 5 fibers allowed to simultaneous wavelength calibration except for setup HR14
- several fibers dedicated to sky spectra : 16 for HR10 and 19 for HR13 and HR14
- all the remaining fibers (108-109) are dedicated to stellar spectra

The initial sample counts 110 stars but after an attentive check of the stars list of each exposure, we find that three stars have one or two missing spectrum(spectra) : stars S05-70 and S05-78 do not have a HR10 spectrum and star S08-274 has only a HR10 spectrum. We have then an homogeneous sample of 107 stars observed in each exposures over the three setups and three other stars with missing spectra. The table 3.3 presents the distribution of the fibers for each setup and each Medusa plate. The third column counts the homogeneous sample of 107 stars and the fourth column concerns the three stars presenting some missing spectra.

With GIRAFFE the spectra are recorded in 2D format (2148 x 4096 pixels), they are parallel in dispersion along the long side of the detector (y-axis of 4096 pixels) and parallel to the

### 3.1. Observations with FLAMES/GIRAFFE

Table 3.2: Observations log

Filename	Slit	Setup	$\lambda_c$ [Å]	Exp. T [sec]	RA	Dec	SimCal
GIRAF2004-04-10T23:47:25.903	M1	HR10	5488	4799.9129	10:12:58.04	-01:38:06.79	ThAr
GIRAF2004-04-11T01:11:34.070	M1	HR10	5488	4379.9125	10:12:58.04	-01:38:07.04	ThAr
GIRAF2004-05-17T01:11:02.626	M1	HR10	5488	4379.9821	10:12:58.02	-01:38:06.14	ThAr
GIRAF2004-05-20T23:22:45.336	M2	HR10	5488	4379.9739	10:12:58.05	-01:38:06.68	ThAr
GIRAF2004-05-21T23:21:49.302	M2	HR10	5488	4379.9784	10:12:58.06	-01:38:06.68	ThAr
GIRAF2004-12-19T06:13:28.694	M2	HR10	5488	4999.9979	10:12:58.07	-01:38:07.15	ThAr
GIRAF2004-12-20T06:36:05.814	M1	HR10	5488	4379.9984	10:12:58.07	-01:38:07.01	ThAr
GIRAF2004-12-12T07:06:21.690	M1	HR10	5488	4379.9981	10:12:58.06	-01:38:07.15	ThAr
GIRAF2004-03-23T01:54:32.804	M1	HR13	6273	4499.9833	10:12:58.04	-01:38:06.83	ThAr
GIRAF2004-03-23T01:34:40.159	M1	HR13	6273	430.6750	10:12:58.04	-01:38:06.83	ThAr
GIRAF2004-03-23T00:07:20.071	M2	HR13	6273	4499.9827	10:12:58.05	-01:38:06.76	ThAr
GIRAF2004-03-23T03:20:48.069	M2	HR13	6273	4499.9823	10:12:58.04	-01:38:06.47	ThAr
GIRAF2004-03-23T04:46:56.455	M1	HR13	6273	4499.9827	10:12:58.02	-01:38:06.18	ThAr
GIRAF2004-03-24T02:24:39.869	M2	HR13	6273	5099.9831	10:12:58.06	-01:38:06.83	ThAr
GIRAF2004-03-24T04:01:02.982	M1	HR13	6273	4499.9801	10:12:58.02	-01:38:06.22	ThAr
GIRAF2004-03-25T02:01:10.081	M1	HR13	6273	4499.9759	10:12:58.05	-01:38:06.86	ThAr
GIRAF2004-03-25T04:13:50.550	M1	HR13	6273	4499.9819	10:12:58.03	-01:38:06.14	ThAr
GIRAF2004-03-25T23:49:36.111	M2	HR13	6273	2034.9102	10:12:58.05	-01:38:06.65	ThAr
GIRAF2004-03-26T00:25:28.294	M2	HR13	6273	4499.9811	10:12:58.05	-01:38:06.76	ThAr
GIRAF2004-03-22T00:06:38.062	M2	HR14	6515	4499.9822	10:12:58.06	-01:38:06.68	none
GIRAF2004-03-22T01:32:33.077	M1	HR14	6515	4499.9827	10:12:58.04	-01:38:06.79	none
GIRAF2004-03-22T02:57:40.958	M2	HR14	6515	4499.9817	10:12:58.06	-01:38:06.90	none
GIRAF2004-03-22T04:23:50.994	M1	HR14	6515	4499.9800	10:12:58.04	-01:38:06.29	none
GIRAF2004-03-26T01:51:18.437	M1	HR14	6515	4199.9799	10:12:58.04	-01:38:06.94	none
GIRAF2004-03-27T02:42:36.053	M1	HR14	6515	3599.9800	10:12:58.05	-01:38:06.72	none
GIRAF2004-03-26T03:12:19.859	M2	HR14	6515	3599.9791	10:12:58.05	-01:38:06.54	none

slit on the short side (x-axis of 2148 pixels). Figure 3.6 presents the schematic layout of the MEDUSA spectral format. The blue lines indicate the location of the object fibers and the red dotted lines the simultaneous calibration fibers. The x-axis corresponds to the increasing fiber number in the slit and the y-axis to the wavelength range.

Due to instrument configuration, there is a wavelength shift between the fibers located at the edge and fibers at the center of the slit. The central fibers have a slightly redder wavelength coverage than fibers at the CCD edges. Then drawing lines of constant wavelength show arcs. This effect can be observed in one of our raw science exposure on figure 3.7 particularly with a bright emission line around pixel 3500 on y-axis.

Table 3.3: Distribution of the fibers for the three setups and the two Medusa plates.

Setup	Medusa plate	Common stars	Add. stars	Sky fibers	SimCal fibers	Total fibers
HR10	Medusa1	107	1	16	5	129
HR10	Medusa2	107	1	16	5	129
HR13	Medusa1	107	1	19	5	132
HR13	Medusa2	107	2	19	5	133
HR14	Medusa1	107	1	19	0	127
HR14	Medusa2	107	2	19	0	128

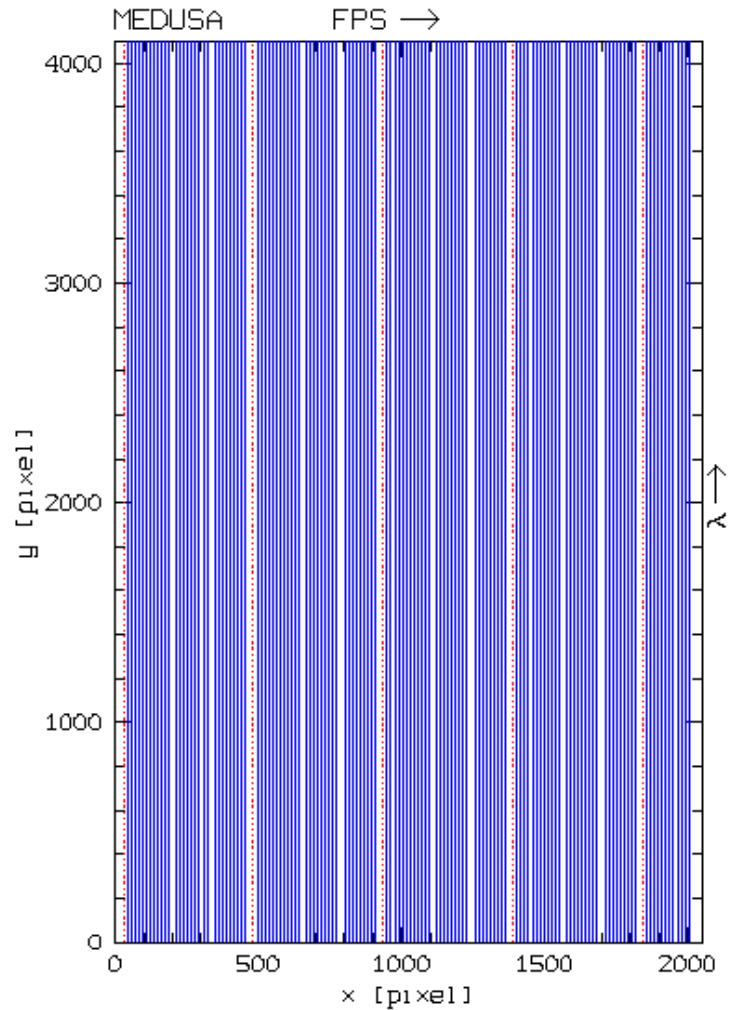


Figure 3.6: Schematic layout of the MEDUSA spectral format. The blue lines indicate the location of the object fibers and the red dotted lines the simultaneous calibration fibers. The x-axis corresponds to the increasing fibers number in the slit and the y-axis to the wavelength range. Source : [http://www.eso.org/observing/dfo/quality/GIRAFFE/pipeline/pipe\\_gen.html](http://www.eso.org/observing/dfo/quality/GIRAFFE/pipeline/pipe_gen.html)

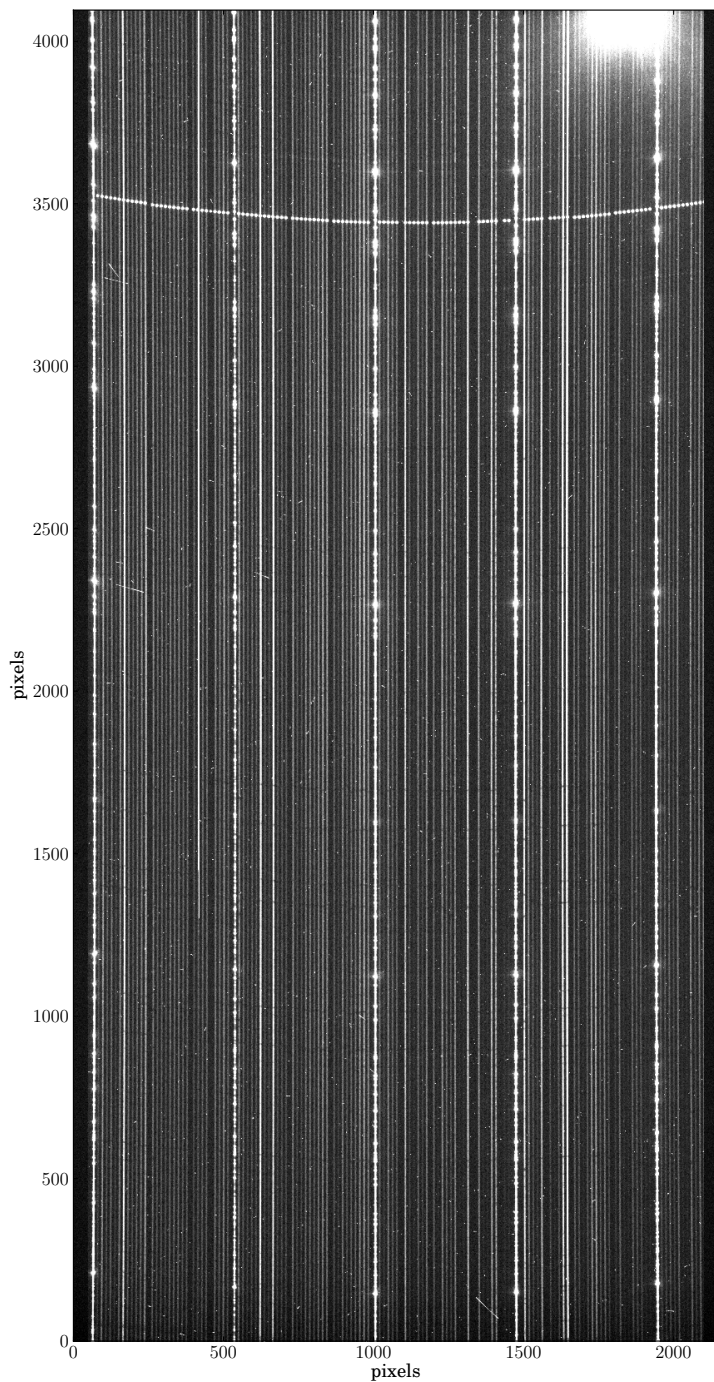


Figure 3.7: Example of a raw science exposure frame in setup HR10

### 3.2 Data reduction process

Before being able to extract radial velocity or chemical composition information from the stellar spectra a cleaning treatment called *reduction* is needed. This process consists in cleaning the raw data removing all extra information that has been added to the first signal coming from the stars. To each science exposure correspond several calibration files needed in the reduction process : we have 3 bias frames, 5 dark frames, 5 flat-field frames, and 1 arc lamp frame per science exposure. The definition and the role of these calibration files are given through the steps of the reduction process.

If we express in equation the different components of the raw light  $R$  observed on the telescope detector we obtain :

$$R = B + D + F \cdot (S_{star} + S_{sky}) \quad (3.2)$$

where  $S_{star}$  is the desired signal from the star and  $S_{sky}$  is the polluted light due to the sky background. The three other signal sources depend on the characteristics of the instrument and the CCD. There are two additional term : the bias frame  $B$  and the dark frame  $D$  due to different types of noise, and a multiplicative term the flat-filed frame  $F$  expressing the response quality of the fibers.

The first goal of the reduction process is to inverse the equation 3.2 in order to obtain the observed spectrum  $S_{obs}$  ( $= S_{star} + S_{sky}$ ) performing a good estimation of the bias, dark and flat-field frames.

We achieved the basic data reduction using the ESO GIRAFFE Pipeline version 2.8.9 using the Data File Organiser GASGANO. The first part of the reduction process is summarized through the following steps :

1. Subtract the master bias

Due to electronics in CCD, a residual signal is always present even with the shutter closed and for a zero integration time. These electronic artefacts are called the bias  $B$ . Three bias frames are recorded with the shutter closed and for an exposure time equals to zero. As being subject to noise the three bias frames are combined into a master bias frame  $B_{master}$  in order to improve the signal-to-noise ratio. An example of a master bias frame is given in figure 3.8. The master biases frames are then subtracted from the raw science exposures.

2. Subtract the master dark

Even if the CCD is cooled to very low temperature (around 150 K), a dark current exists due to thermal excitation of the electrons in the CCD. This dark current is then strongly dependent on the temperature. 5 dark frames  $D$  are obtained with the shutter closed and for the same integration time as the scientific observations. For the same reasons as

for the biases, the dark frames are combined into a master dark frame  $D_{master}$  being previously de-biased (corrected from the bias). Figure 3.9 shows an example of a master dark frame. The de-biased science exposures are then dark-subtracted using the master dark frame.

3. Locate the fibers on the detector

The third calibration frame called flat-field frame  $F$  serves two roles : i) report the transmission efficiency of each fiber and ii) locate the fibers on the detector in prevision of their extraction.

Being not identical the fibers present different levels of transmission efficiency and even the CCD pixels efficiency vary in function of the wavelength. These transmission inhomogeneities can be taken into account by generating a flat-field frame. To this end the source needs to be completely uniform in wavelength and composed of a pure continuum spectrum without absorption or emission lines. For GIRAFFE this illumination is made by a tungsten lamp. As usual in order to reduce the noise, 5 flat-field frames are recorded and combined into a master flat-field frame  $F_{master}$  after being all de-biased and dark-subtracted. An example of a master flat-field frame is given in figure 3.10.

In the context of multi-fibres spectroscopy, flat-filed frames are also used to accurately localize the fibers in prevision of their extraction. The tungsten lamp provides the trace of all fibers at each pixel on the CCD. A gaussian profile is fitted to adjust the position of the fibers recording their center and width at each pixel along the dispersion axis.

4. Extract the spectra and the flat-fields

Extract means here converting a 2D frame of 2148 x 4096 pixels into a 2D frame of 132 x 4096 where after extraction each pixel of the x-axis corresponds to one fiber. When we speak here about extracting spectra, these spectra correspond to  $R - B_{master} - D_{master}$  frames. The GIRAFFE ESO pipeline offers two methods of extraction : a summation or optimal extraction. The former makes a simple average of the fluxes vertically. The latter is more complex with the aim of reducing the noise by weighting the flux and removing directly the cosmic rays. The second one is chosen to improve the signal-to-noise. Figures 3.11 and 3.12 show extracted frames for science and flat-field frames.

5. Divide the extracted spectra by the extracted flat-fields to correct for fiber-to-fiber transmission inhomogeneities

Ideally the science frame should be divided by the flat-field frame pixel by pixel on the 2D image before extraction. In reality it is technically not possible to perfectly illuminate the fiber profile without a drop of intensity towards the edges of the fibers. This is why the division by the flat field frame takes place after the extraction. Extracting the flat-filed spectra allows to average the pixel-to-pixel variations of wavelength sensitivity.

Moreover the extracted flat-field spectra are normalized to compensate for the fiber relative transmission.

#### 6. Wavelength calibration

The next step of reduction consists in the wavelength calibration of the spectra. The wavelength calibration frame (or arc frame or lamp frame) is obtained by a thorium-argon lamp illuminating all the fibers. A spectrum composed of well-known wavelength emission lines is produced by ionizing gas through high voltage in a cathodic lamp. The wavelength calibration frame is extracted after being de-biased and dark-subtracted. An example of a lamp frame is given in figure 3.13. Figures 3.14 and 3.15 show the same lamp frame after respectively extraction and wavelength calibration. In each fiber the emission lines are identified thanks to a catalog and their positions are noticed. A dispersion solution is computed comparing the observed lines and expected positions from GIRAFFE. Using this dispersion solution the spectra are wavelength calibrated. After this step the emission lines appears as straight lines being aligned fiber to fiber. As the wavelength calibration frame are normally recorded during the day, it is possible to allocate 5 fibers of the science exposure to simultaneous calibration fibers illuminated by the same thorium-argon lamp. The new dispersion solution derived from the simultaneous calibrations frames is used to correct from wavelength shifts due to mechanical vibrations occurred during science frame recording.

The outputs of the ESO pipeline consist in 2D images of de-biased dark-subtracted flat-fielded extracted wavelength calibrated science frames as one example is given in figure 3.16. The x-axis represent the individual fibers and the y-axis the wavelength range. They can be expressed by the equation 3.3 :

$$S_{obs} = S_{star} + S_{sky} = \frac{\text{extracted } (R - B_{master} - D_{master})}{\text{extracted } (F_{master})} \quad (3.3)$$



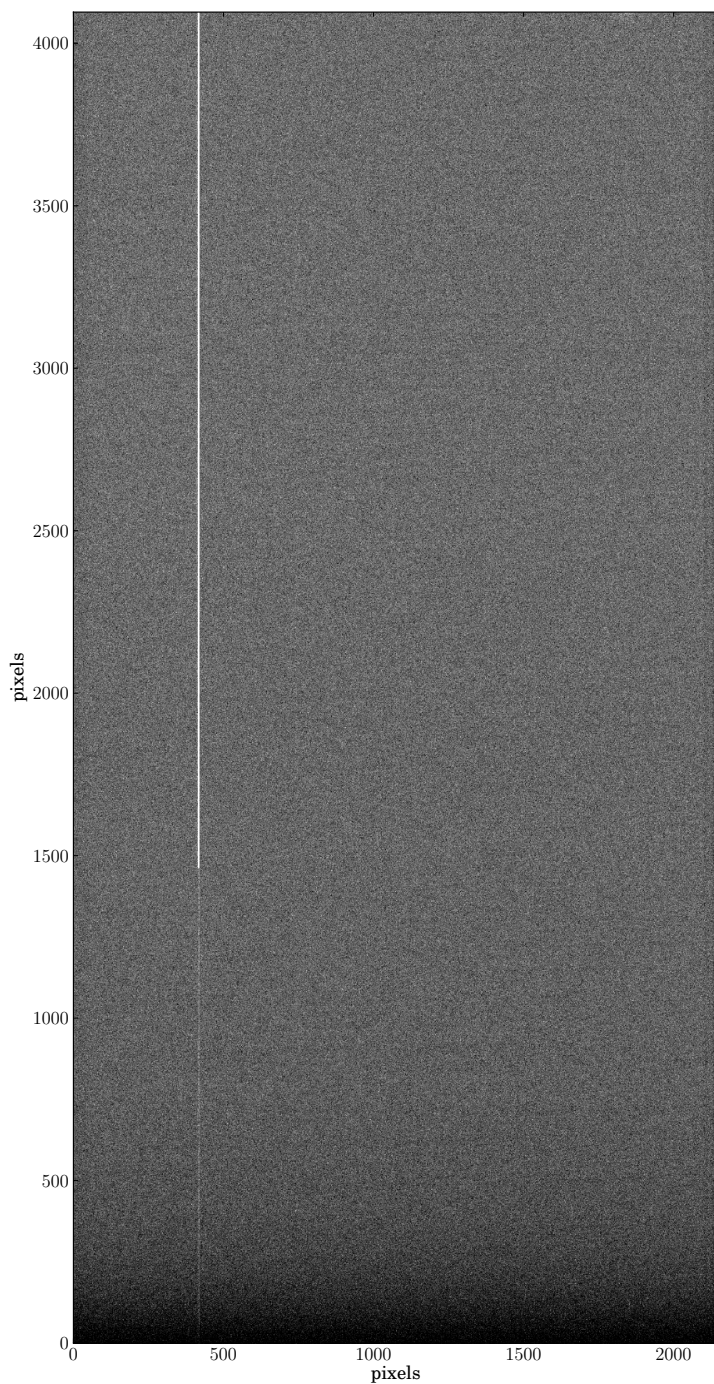


Figure 3.8: Example of master bias frame in setup HR10.

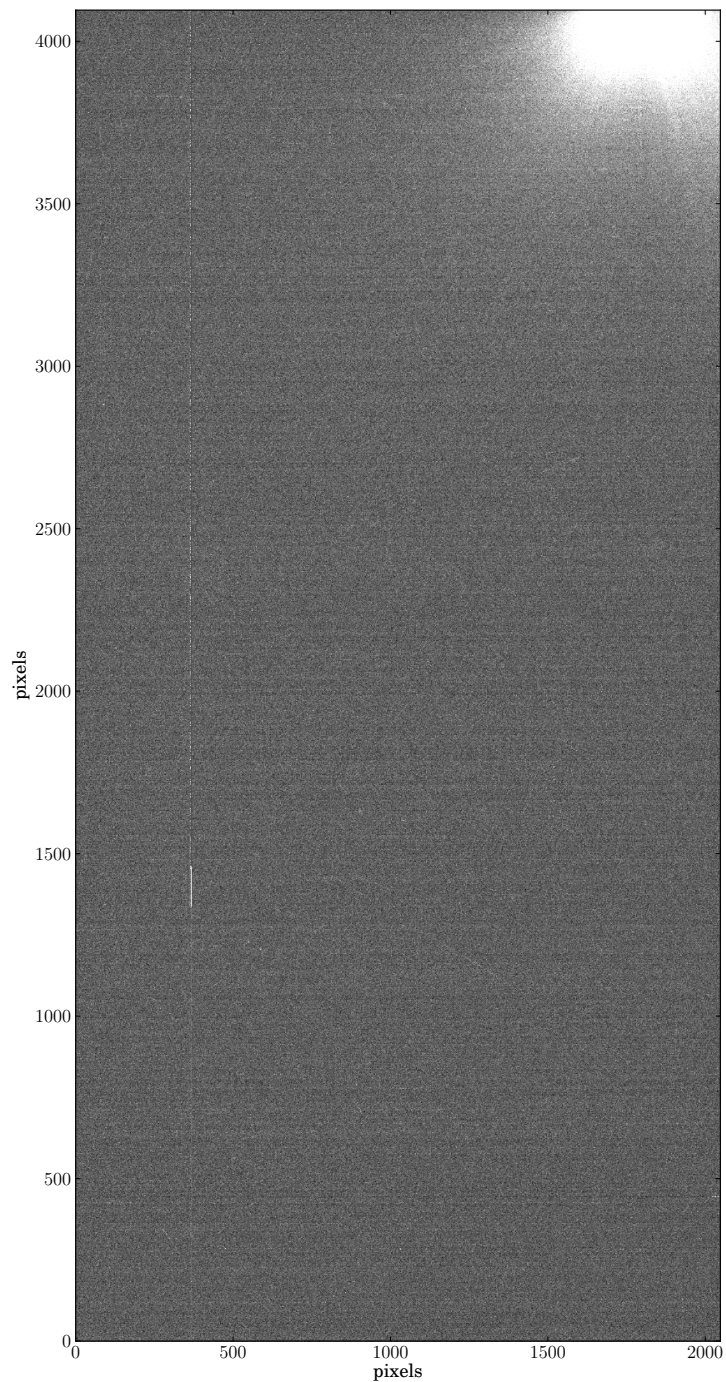


Figure 3.9: Example of master dark frame in setup HR10.

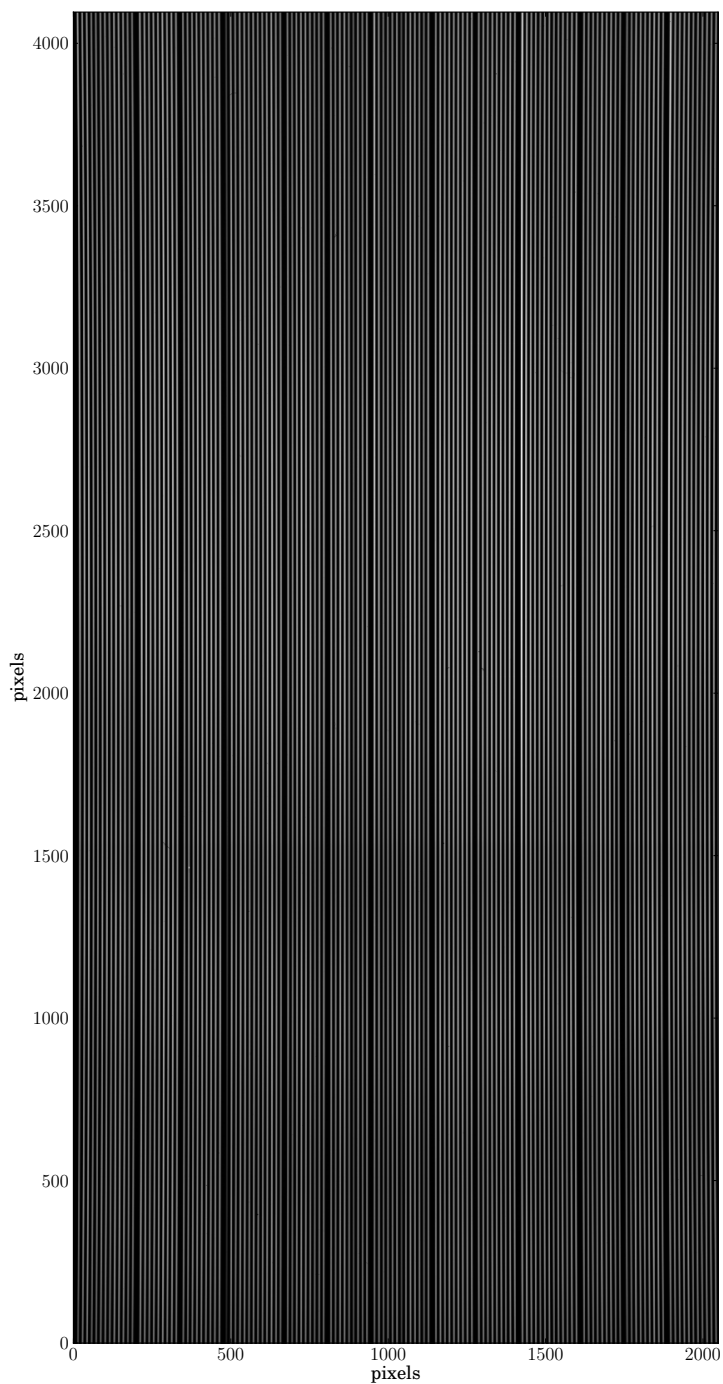


Figure 3.10: Example of master flat frame in setup HR10.

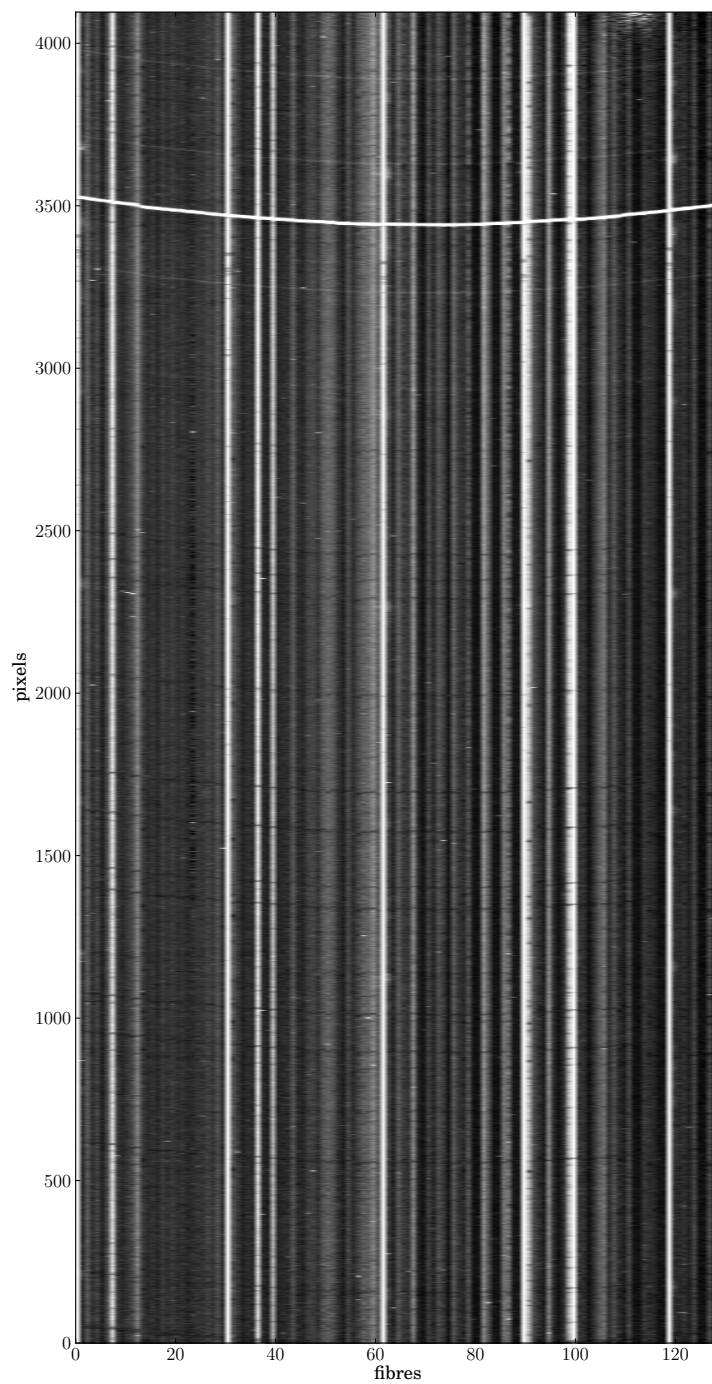


Figure 3.11: Example of extracted de-biased dark-subtracted science frame in setup HR10.

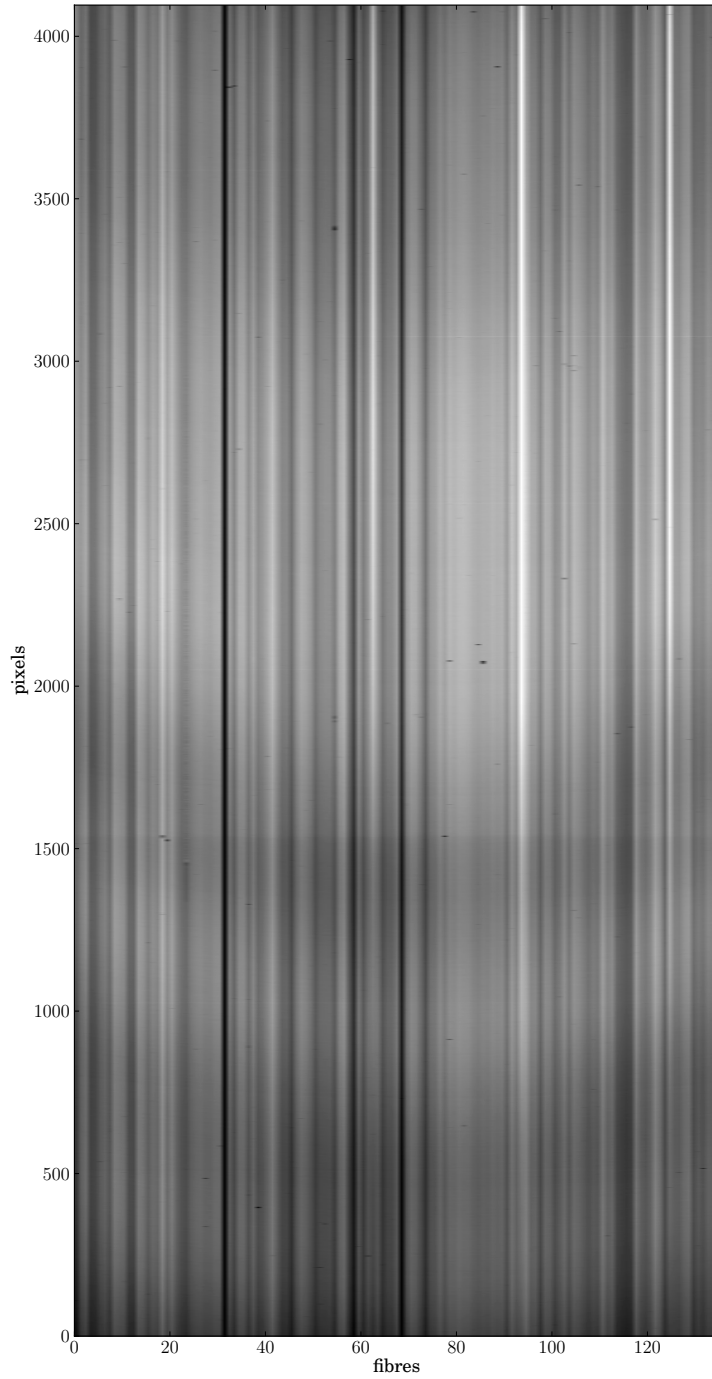


Figure 3.12: Example of extracted de-biased dark-subtracted flat-field frame in setup HR10.

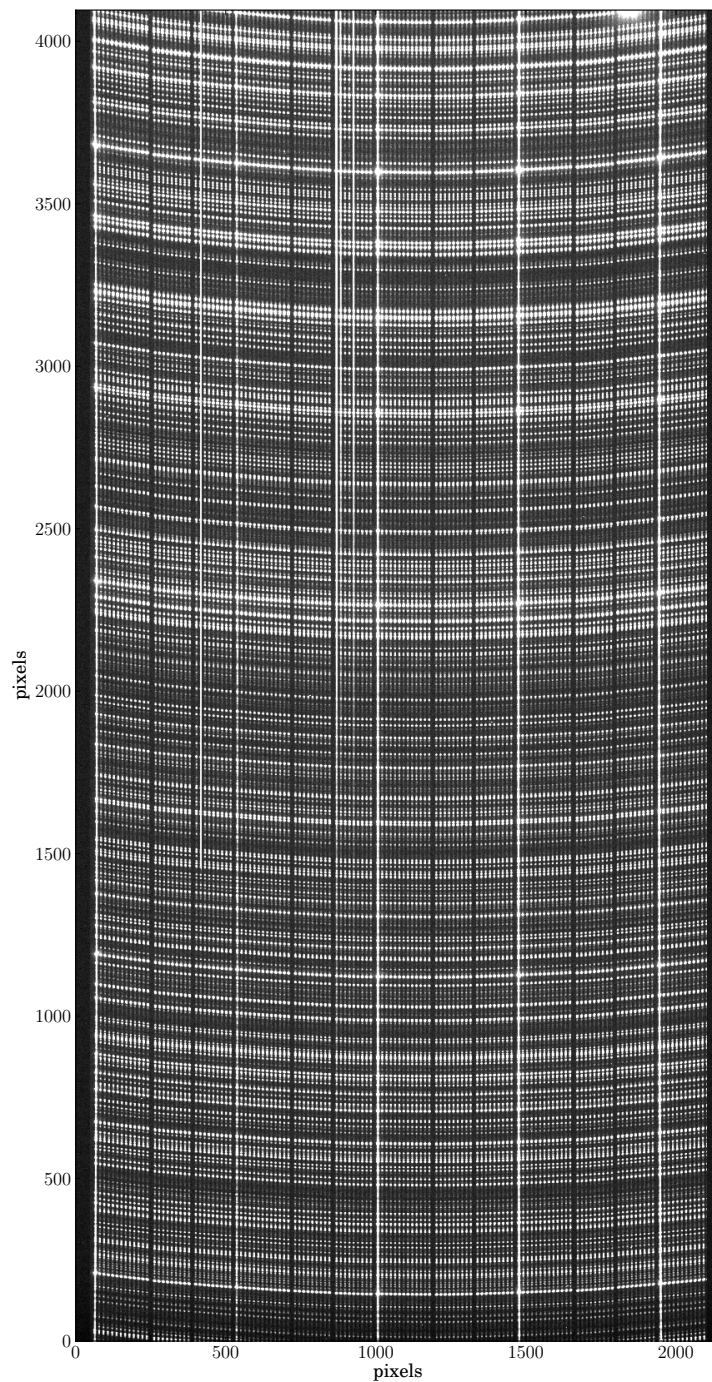


Figure 3.13: Example of an arc lamp frame in setup HR10.

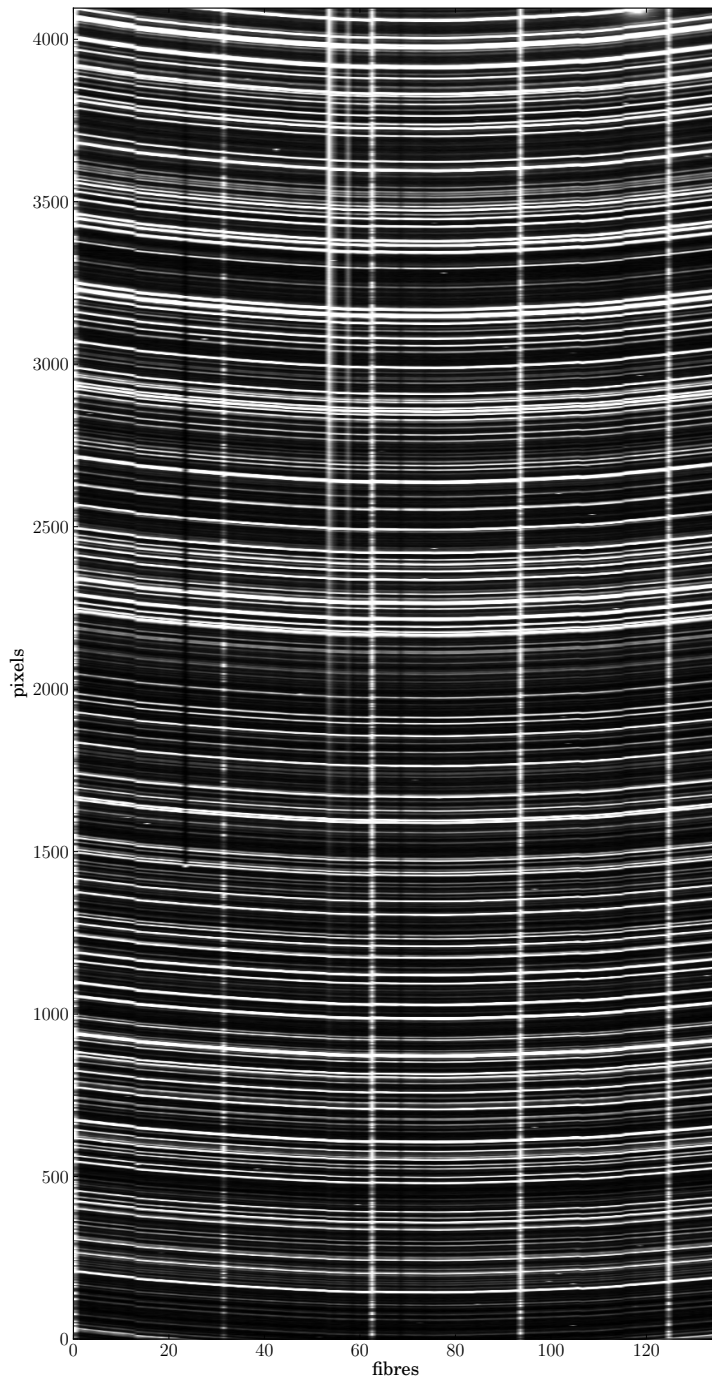


Figure 3.14: Example of an extracted arc lamp frame in setup HR10.

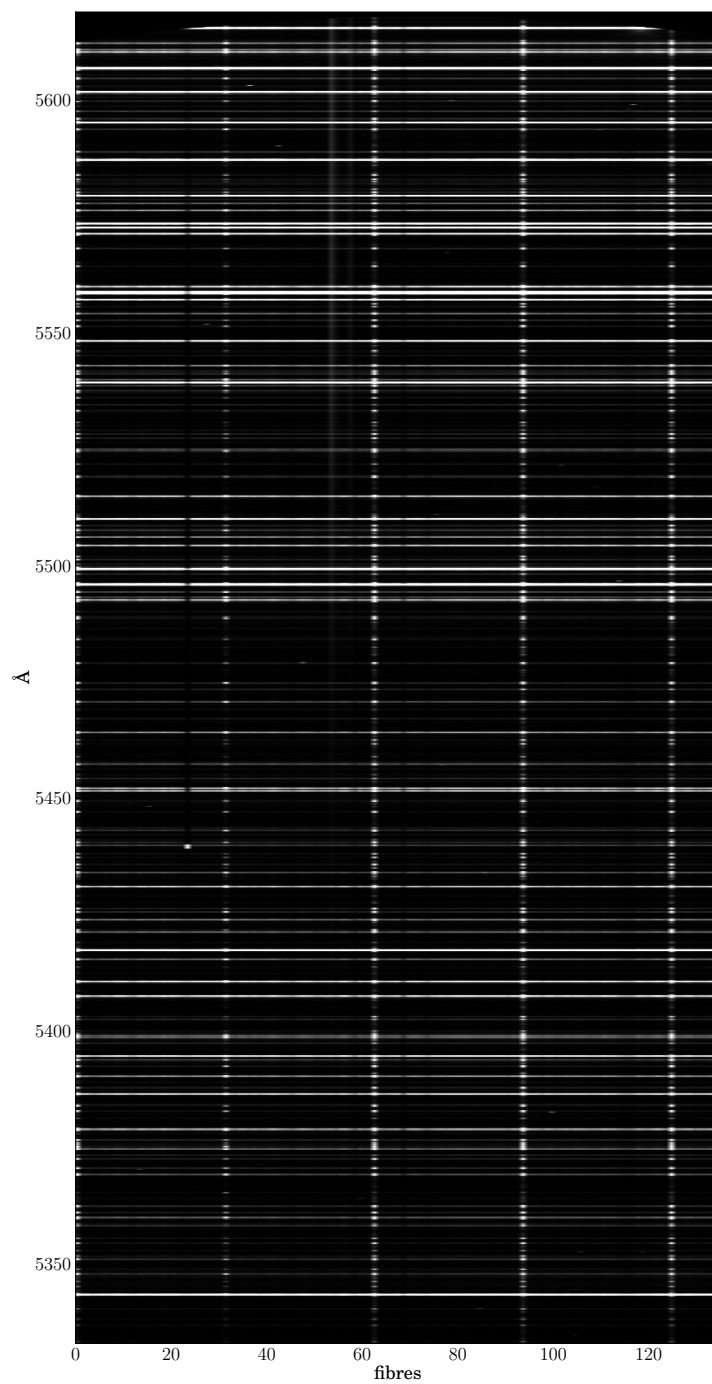


Figure 3.15: Example of an extracted arc lamp frame in setup HR10 after wavelength calibration.



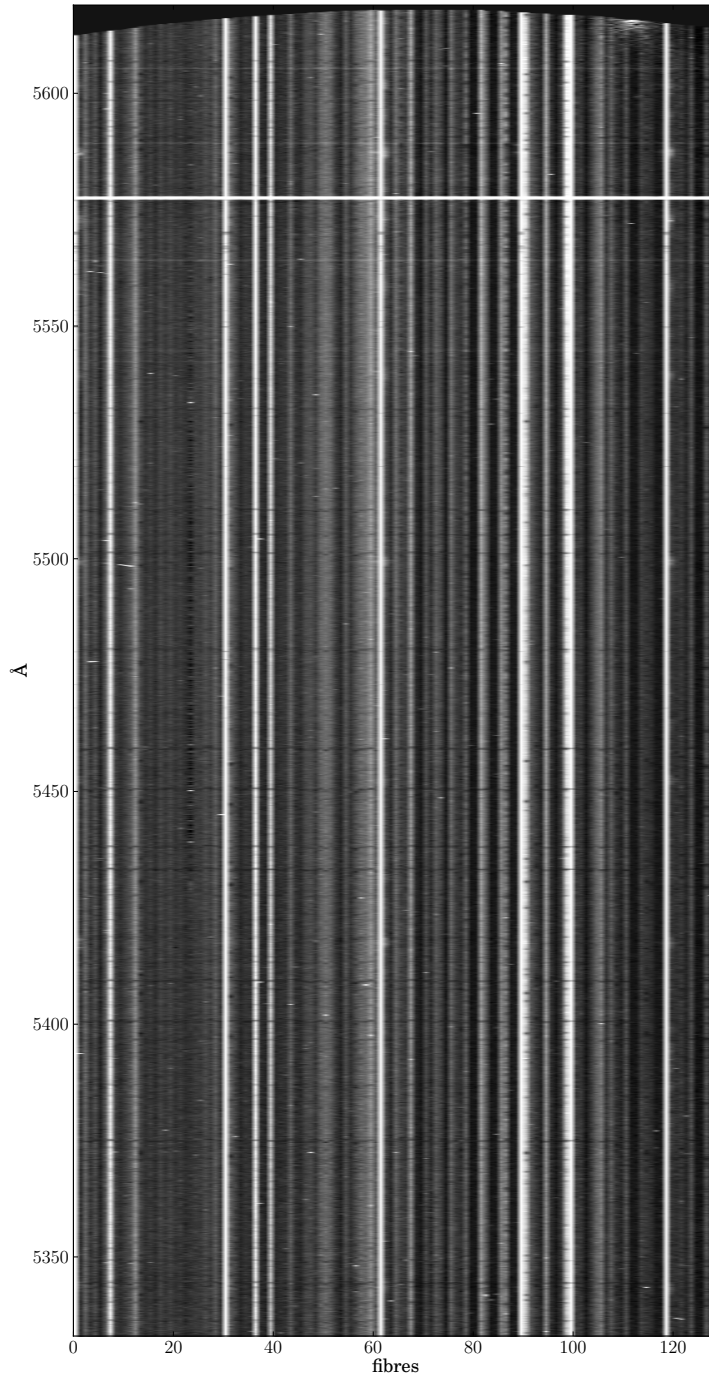


Figure 3.16: Example of a de-biased dark-subtracted flat-fielded wavelength calibrated science frame in setup HR10 corresponding to the final state of the ESO pipeline reduction process.

A few remarks about this first part of the reduction process need to be mentioned :

- Cosmic rays as source noise  
Another source of noise could come from the cosmic rays hitting the CCD and producing saturated signals. As their appearance is random the solution to remove them resides in combining exposures and removing outlier pixel values. This operation is done further in the reduction process when combining 1D spectra.
- Bad pixels map  
The CCD is not perfect and may comport bad pixels due to manufacturing defects or intensive use. If pixels saturate because of a too high dark current they are considered as *hot* pixels and on the contrary as *dead* pixels if their sensitivity is very poor. During the read-out operation these defects can affect a whole column. During the reduction process a bad pixel map is computed to flag their position in order to skip them.
- Contamination from scattered light  
Scattered light can also occur inside the spectrograph because areas between fiber projections are not completely dark and should provoke internal reflections. It is known that the *Bruce* type CCD used in GIRAFFE until May 2008 presents a contaminating feature called *glow* in the upper right corner due to charge injection caused by a manufacturing defect on the CCD. The intensity of this feature is proportional to the exposure time and also depends on the temperature. This is why the dark frames subtraction is needed to remove at best this glow pattern from the science exposures.  
This glow pattern is observed only in 3 of our 26 science exposures. It is clearly visible on the raw science frame in figure 3.7 and on the master dark frame in figure 3.9.
- Light pollution from simultaneous calibration fibers at high wavelengths  
For the reddest setups (mainly exceeding 6500 Å) it is known that thorium-argon simultaneous calibrations fibers show very strong saturated argon emission lines implying visible ghosts on the neighbor fibers over a large part of the CCD. Unfortunately this pollution can not be removed by any filter. These ghosts are especially problematic if the observed objects are faint with a low signal-to-noise ratios. Therefore if an accurate radial velocity measurement is not required it is often preferable to switch off the simultaneous calibrations lamps for setups having a redder coverage.  
In our case, concerning the setup HR14, no simultaneous calibration fibers were used in order to prevent pollution from argon lines. Nevertheless we noticed that the calibration fibers present in the two other setups HR10 and HR13 have somehow polluted their closest neighbor stellar spectra. This effect concerns 25 stars, and we did not consider the polluted spectra (in HR10 and/or in HR13) in our abundances determination. These stars are indicated as *polluted spectra* in table A.1 and the detailed list of their polluted setups are given in table A.4. One example of a HR13 spectrum polluted by simultaneous

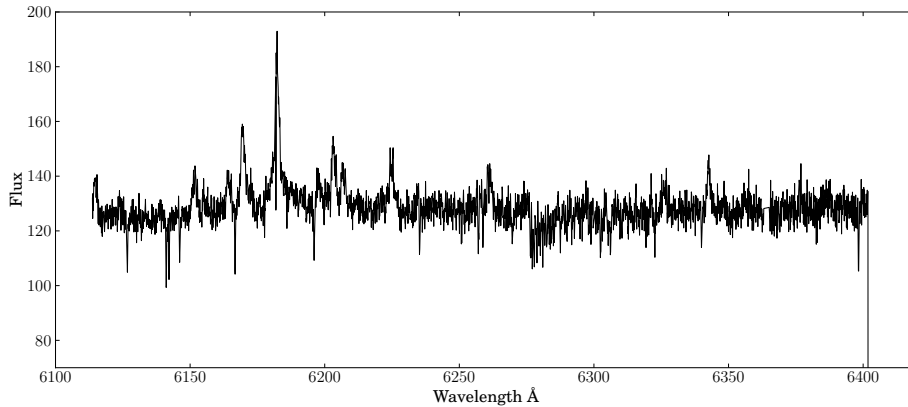


Figure 3.17: Example of polluted spectra in setup HR13 with emission lines due to proximity to simultaneous calibration fibers. This corresponds to the 1D spectrum of star S11-97 in setup HR13.

calibration fiber is presented in figure 3.17. Some emission lines are clearly visible particularly in the first half of this spectrum.

Some last steps are required in order to finally recover the star signal :

#### 7. Subtract the sky

Before reaching the telescope detector, the star light passes through the Earth atmosphere which is one of the main contributor to an additional light pollution called the sky background. Indeed radiations are emitted by the Earth atmosphere also during the night (desexcitation of molecules and atoms, thermal continuum, etc.). Other fainter contributors to the sky background could be the sunlight scattered or reflected by the dust particles around the Earth, the Galactic starlight scattered or reflected by interstellar dust and light coming from non-resolved objects as distant stars or galaxies. This is why the sky spectra need to be acquired in a sky zone free of stars and close to the direction of observations in order to cover the same portion of atmosphere. Due to the time-dependence, they are preferentially taken simultaneously to the science observations with the same exposure time.

For setup HR10, 16 fibers were dedicated to sky spectra and 19 fibers for HR13 and HR14. For the sky subtraction we used a FORTRAN routine (M. Irwin priv. comm.) that creates an average sky spectrum from the sky fibers. This average sky spectrum is then subtracted from each object spectrum after being rescaled to match the sky features in each fiber. Before this subtraction, some sky spectra belonging to three different science exposures taken in HR10 were rejected because carrying the previously discussed glow pattern.

8. Extract 1D files for each star

From 2D images of extracted sky-subtracted spectra we create using the Image Reduction and Analysis Facility (IRAF) task *scopy* individual files containing 1D spectrum for each star. Apart from exceptions (stars with missing spectra S05-70, S05-78, S08-274), we end up with 8 spectra in HR10, 11 in HR13 and 7 in HR14 for each star.

9. Correct from barycentric velocities

As the observations were recorded at different epochs we first need to correct them from barycentric velocities before combining 1D spectra. These corrections take into account the motion of the sun around the solar system barycenter. We apply the barycentric velocity corrections derived by the ESO reduction pipeline.

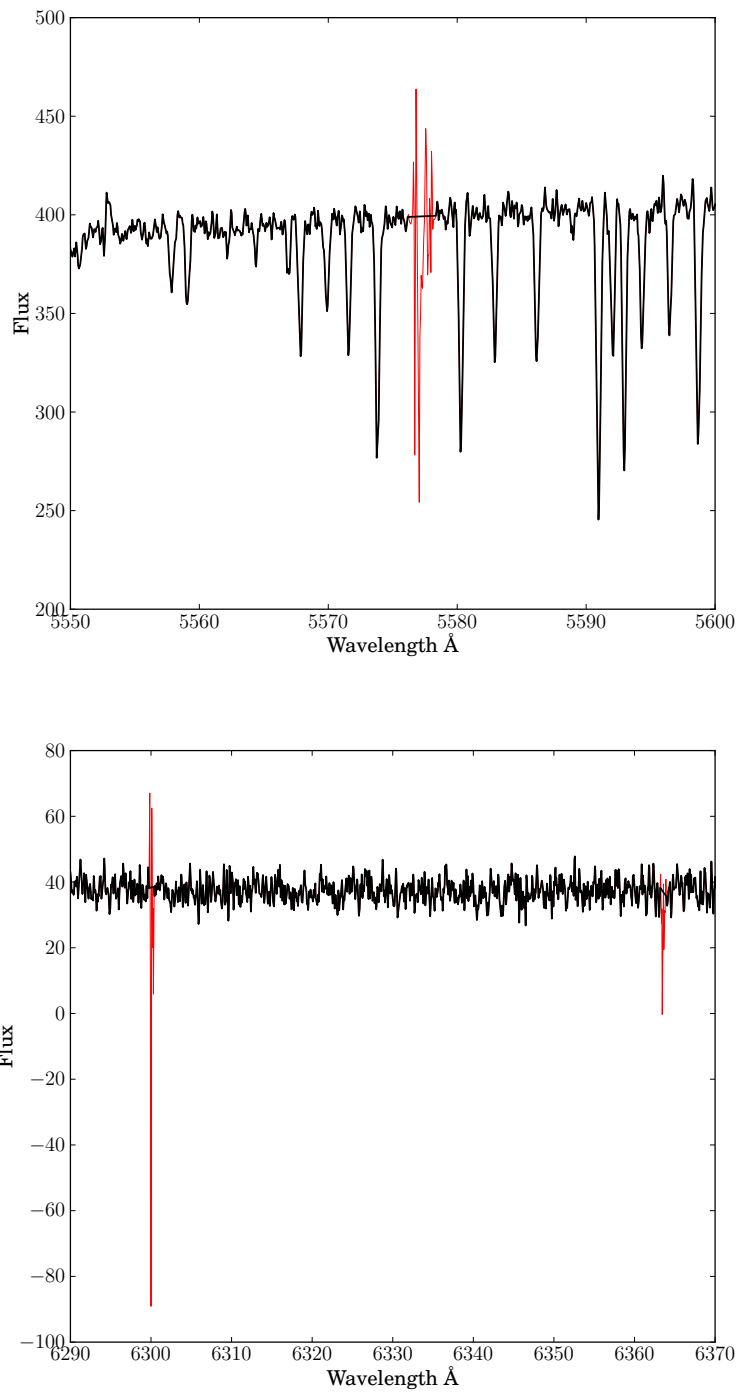
10. Combine spectra

The final combination of spectra is performed with the IRAF task *scombine*. In the co-addition of individual spectra of the same star we used a flux weighted average with median sigma clipping in order to remove possible cosmic rays.

11. Remove telluric absorptions

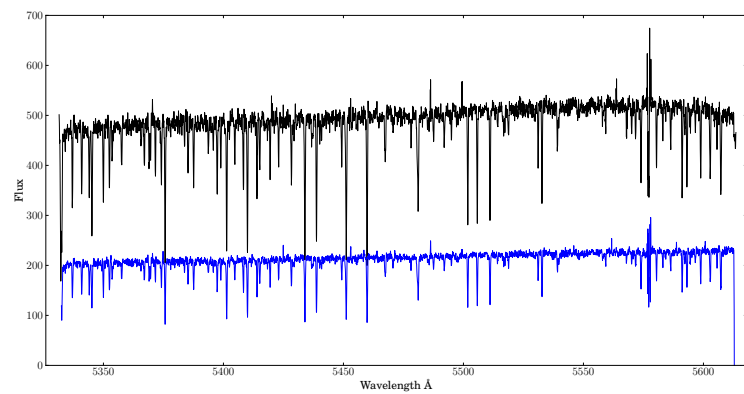
The last step is the correction from the telluric absorptions. Spectra present residual features remaining from the sky subtraction. Molecules present in the Earth atmosphere absorb the stellar light and it translates into absorption bands in the stellar spectra. The major known contributor is oxygen around three regions covered by our spectra corresponding to lines at 5577.338 Å, 6300.304 Å, 6363.78 Å. We replaced these small affected parts of spectra (width of about 2-3 Å) with estimated continuum values. Figure 3.18 presents star S08-3 spectra in setup HR10 and star S05-60 in setup HR13 before and after removing the telluric absorption features indicated in red.

**Old versus new reduction** During the first months of the thesis we worked on data previously reduced with an old version of the ESO Pipeline. We decided to re-do the complete reduction procedure because final spectra seemed to suffer from sinusoidal artefacts. We also take the advantage of using an improved and more recent version of the ESO reduction pipeline. Comparing the previously reduced spectra with the newly one we can see that the latter are more stable. Figure 3.19 presents in black the previously reduced spectra for star S05-10 respectively in each setup and in blue the newly reduced spectra. The flux difference come from the methods used to extract and combine spectra. All the results presented in this work concerned spectra obtained after the new reduction process described above.

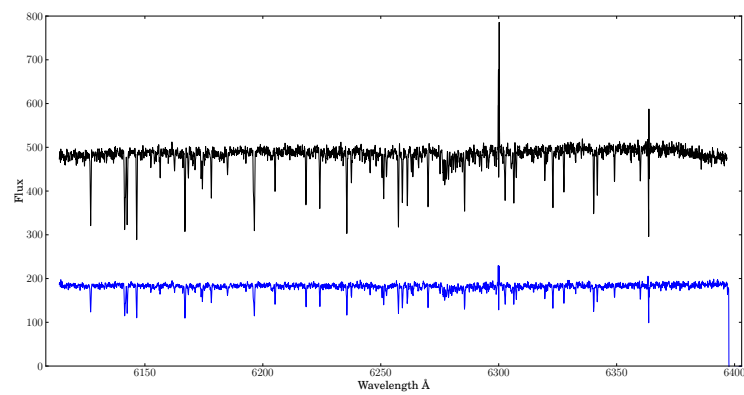


(b) Example of telluric absorption lines in HR13 spectrum of star S05-60

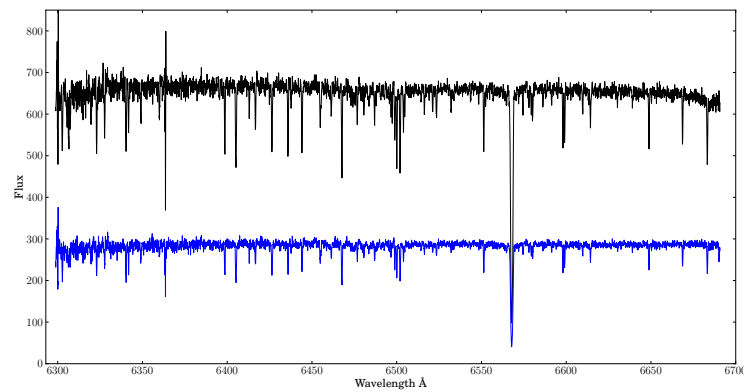
Figure 3.18: Example of telluric absorption lines in HR10 spectrum of star S08-3 and in HR13 spectrum of star S05-60. The initial spectrum is plotted in red and the cleaned spectrum is over-plotted in black.



(a) Reduced spectra for star S05-10 in setup HR10 after the old reduction and the new ESO reduction process.



(b) Reduced spectra for star S05-10 in setup HR13 after the old reduction and the new ESO reduction process.



(c) Reduced spectra for star S05-10 in setup HR14 after the old reduction and the new ESO reduction process.

Figure 3.19: Black spectra are the reduced spectrum for star S05-10 after the old reduction process and the blue ones after the new ESO reduction process. From top to bottom the panels correspond to HR10, HR13 and HR14 setups.

### 3.3 Selection of stars : our sample

Our 110 targets are stars located in the central 25 arcmin field of the Sextans dSph. 58 stars of our sample are RGBs previously identified as Sextans members thanks to the analysis of their intermediate resolution spectra in the calcium triplet (CaT) region (Battaglia et al. 2011), and the 52 other stars were chosen according to their position in the galaxy CMD along the red giant branch. The spatial location of the stars is presented in figure 3.20. The gray circles show the targets observed by the intermediate resolution Ca II triplet survey (Battaglia et al. 2011), the blue circles correspond to the probable members of that sample, and the green circles are the targets of our HR sample. In comparison our stars are very centrally concentrated. The black ellipse represents the tidal radius of Sextans as given by Irwin & Hatzidimitriou (1995). The tidal radius represents the distance from the center at which stars become equally influenced by the external gravitation than the dwarf galaxy itself. The stellar density at that distance should correspond to the field density. Figure 3.21 displays the distribution of the Sextans  $V$  versus  $V - I$  color magnitude diagram along the the red giant branch. The blue and green circles follow the same color code as in the previous figure 3.20. The black dots correspond to Sextans photometry from Lee et al. (2003).

### 3.4 Determination of radial velocities

#### 3.4.1 Doppler-Fizeau effect

The Doppler-Fizeau effect explains the observed shift in wavelength due to the relative motion of a light source to an observer. As we are facing a non-relativistic case (the source velocity is small relatively to the speed of light, of the order of a few hundreds km/s), the wavelength shift is given by the expression:

$$\frac{\lambda - \lambda_0}{\lambda_0} = \frac{\Delta\lambda}{\lambda_0} \simeq \frac{v_{rad}}{c} \quad (3.4)$$

where  $\lambda_0$  corresponds to the wavelength emitted at the source,  $\lambda$  the wavelength received by the observer,  $v_{rad} = v_s \cos\theta$  is the radial component of the source velocity  $v_s$  along the line-of-sight.  $\theta$  is the angle between the source velocity  $\vec{v}_s$  and the line-of-sight connecting the observer and the source. When the star is moving away from the observer the wavelength is red-shifted and  $\lambda > \lambda_0$ .

Being dynamically bounded the stars members of a dwarf galaxy display similar radial velocities from our point of view as observers on Earth.

The determination of stellar radial velocity is essential and has two roles : i) determine the membership to the dwarf galaxy and ii) transpose the stellar spectra into a reference frame of zero velocities in order to identify elemental absorption lines whose wavelengths has been

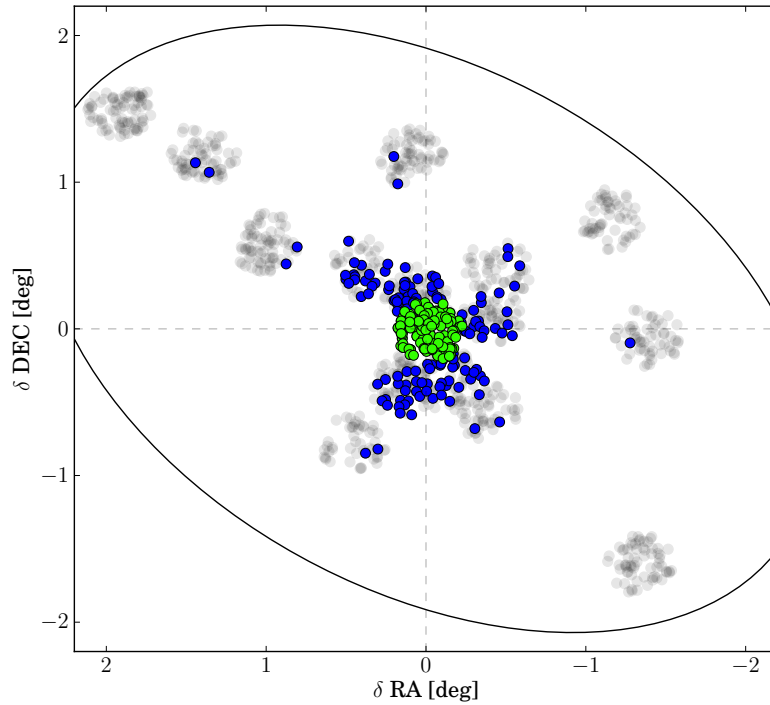


Figure 3.20: Spatial distribution of the spectroscopic observations of the dSph Sextans. The grey circles show the stars previously observed in the VLT/FLAMES Intermediate Resolution DART CaT survey (Battaglia et al. 2011). The blue circles correspond to the probable members of this sample, and the green circles are the stars of our High Resolution sample which is very centrally-concentrated (see Table A.1 for the coordinates). The black ellipse represents the tidal radius of Sextans as given by Irwin & Hatzidimitriou (1995).

measured in a laboratory rest frame.

Particularly for Sextans situated in the background of a dense halo stars region ( $l = 243.5$  deg,  $b = +42.3$  deg; Mateo (1998)), confirming the membership is a necessary step because Sextans observations fields contain a lot of contaminants from the Milky Way. This is why in this study the membership criterion is based on a  $3\text{-}\sigma$  radial velocity clipping argument.

### 3.4.2 DAOSPEC : a tool to derive radial velocities

Radial velocities are derived from the 1D spectra using the program DAOSPEC (Stetson & Pancino 2008) which cross-correlates all the detected lines with an input line list. DAOSPEC is



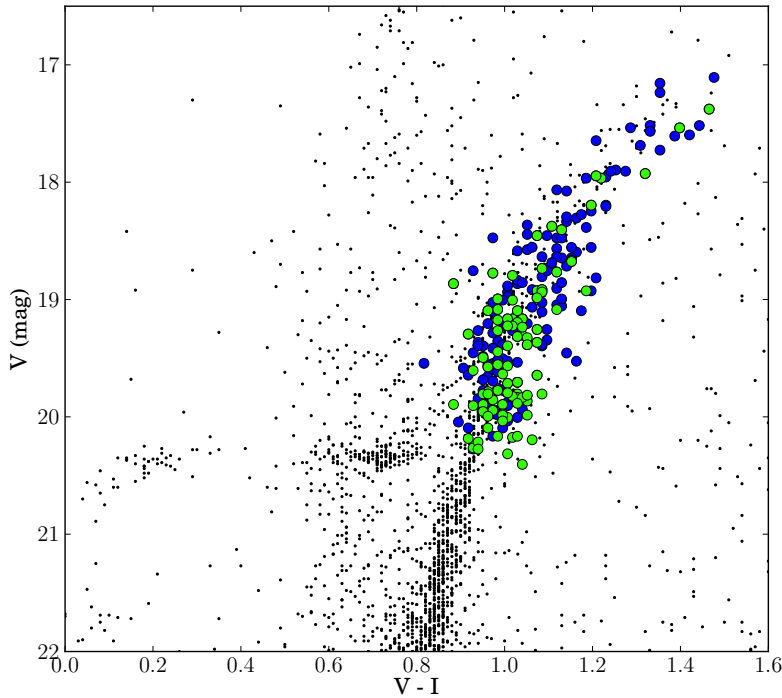


Figure 3.21: Color Magnitude Diagram of the Sextans stars. As in Figure 3.20, the blue circles are the probable members of the Intermediate Resolution DART CaT survey (Battaglia et al. 2011), and the green circles correspond to this study. The black dots correspond to Sextans photometry taken by CFH12K CCD camera at CFHT (Lee et al. 2003).

a Fortran code designed to work on extracted 1D spectra linearly binned in wavelength.

The different tasks of DAOSPEC are : automatically detect absorption lines by iterative gaussian fitting, fit the continuum, measure equivalent widths, identify lines through cross-correlation with an input laboratory line list in order to estimate the radial velocity. The program requires a line list of laboratory rest wavelengths and several input parameters as :

- an initial estimate of the spectral resolution : the FWHM expressed in pixel unit (see equation 3.1 ).  
This parameter is modified in the course on basis of measured line widths. The model of lines used by DAOSPEC is a saturated gaussian profile.
- the order of a Legendre polynomial used to fit the continuum level.  
This order can be seen as the inverse of the variation scale, for an order of 5 it corresponds to a variation of scale of  $\frac{1}{5}$ . The continuum fitting task can be removed from the

procedure when dealing with normalized spectra.

- the wavelength range on which DAOSPEC operates.
- the factor of the velocity limit  
Radial velocities are derived iteratively for each line and outliers are discarded following a  $k$ - $\sigma$  clipping. This factor corresponds to this  $k$  variable.
- the expected radial velocity range could be given in order to save time and avoid a bad initial guess.
- scaling or not the spectral resolution with wavelength.  
DAOSPEC offers the possibility either to use a constant resolution or to take into account its evolution with wavelength.

Our laboratory line list was based on the list of Tafelmeyer et al. (2010). The order of the polynomial fit of the continuum is kept at 12 for all spectra. The wavelength ranges are chosen according to our setups coverage : [5333.5; 5610.0] Å for HR10, [6115.0; 6395.0] Å for HR13 and [6303.0 ; 6688.0] Å for HR14. The estimated values of FWHM are 6.88, 7.28 and 9.27 in pixel units respectively for HR10, HR13 and HR14. Using IRAF task *splot* we first estimate the FWHM (through gaussian fitting) of a dozen of lines in each setup for star S08-3. We average them and convert them in pixel units to obtain these FWHM values. The evolution of resolution in function of the wavelength has been taken into account during processing DAOSPEC.

We run DAOSPEC on our 326 spectra (3 spectra per star exception apart). For the first run no real constraints on the expected radial velocity interval are given ( $v_{\min} = -300$ ,  $v_{\max} = 300$  km/s) with a 3-sigma clipping. Then all spectra, respectively shifted by their obtained radial velocity, are checked by comparing them to a rest frame spectrum. The stars are classified in three groups : a) satisfying radial velocities in the three setups, b) satisfying radial velocity in setup HR10 only, c) no satisfying radial velocities. We apply different issues for group b) and c). For spectra of group b), we impose the expected radial velocity interval to be [ $v_{\text{rad,HR10}} - 5$ ;  $v_{\text{rad,HR10}} + 5$ ] km/s with a 2-sigma clipping. For the last group of spectra we impose a velocity interval of 10 km/s centered on the best value determined manually after comparison with a rest frame spectrum. In order to reduce the obtained velocity dispersion, we iterate DAOSPEC reducing the width of the expected interval from 10 to 8, 6 and 4 km/s. At each new iteration the center of the interval corresponds to the value obtained in the previous iteration.

Table A.5 gives for each star the final radial velocities and their respective errors for each setup and also in average.

### 3.4.3 Distribution of the radial velocities

The distribution of radial velocities is presented in figure 3.22. Applying a  $3\text{-}\sigma$  rejection based on the mean radial velocity derived by Battaglia et al. (2011) :  $v_{\text{sys, helio, Bat11}} = 226.0 \pm 0.6$  km/s,  $\sigma_{\text{Bat11}} = 8.4 \pm 0.4$  km/s we ruled out 12 stars. These non-member stars are S05-100, S07-83, S08-102, S08-266, S08-269, S08-285, S08-322, S08-327, S08-337, S08-45, S08-89, S08-99. They are quoted as *Non-member (v)* in Table A.1. They could be MW contaminants, foreground interlopers, or could have poor quality spectra (e.g. lines indistinguishable from the noise) no allowing a correct derivation of radial velocities. Our mean velocity and dispersion  $v_{\text{sys, helio}} = 224.9 \pm 1.9$  km/s,  $\sigma = 7.7 \pm 0.5$  km/s are in good agreements with the previous results from Battaglia et al. (2011).

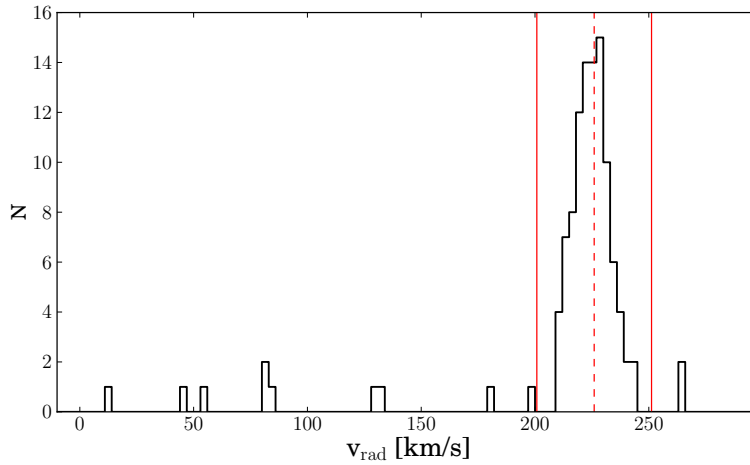


Figure 3.22: Radial velocity distribution of our stars (black solid line). The dashed red line correspond to the mean radial velocity from Battaglia et al. (2011) based on 174 probable members  $v_{\text{sys, helio, Bat11}} = 226.0 \pm 0.6$  km/s. The two solid red lines represent the  $\pm 3\sigma$  interval within which the membership zone is defined.

### 3.4.4 Binaries

As the data in the three setups were obtained at different dates (a month difference between HR10 and HR13/HR14), variation of radial velocities with time is a hint for binary stars. Due to rotation of stars in a binary system radial velocities will be altered according to their orbital period.

Our knowledge about binaries is far from well understood. Several studies have shown that binary system are more common than single star except for massive stars (see, e.g., Abt & Levy (1976, 1978); Kobulnicky & Fryer (2007); Eggleton & Tokovinin (2008); Sana et al. (2012)).

Gao et al. (2014) analyzing F, G and K stars from the SDSS determined the fraction of binary stars having orbital periods of 1000 days or shorter to be at  $43.0\% \pm 2.0\%$ . They show that this fraction decreases with increasing effective temperature and metallicity.

To test the variation of radial velocities we observe if the radial velocities taking into account their errors are consistent over the three setups. If at least one of the interval  $[\nu_{\text{rad,HR}} - \sigma_{\nu_{\text{rad,HR}}}, \nu_{\text{rad,HR}} + \sigma_{\nu_{\text{rad,HR}}}]$  is inconsistent with another setup (no intersection), the star is defined as a probable binary. Following this argument 13 stars have been cataloged as probable binaries : S05-104, S07-115, S07-16, S08-131, S08-184, S08-232, S08-252, S08-282, S08-309, S08-316, S08-317, S08-322, S08-332. Figure 3.23 shows for these 13 probable binaries the three intervals of radial velocities for each setup. HR10 is represented in magenta, HR13 in green and HR14 in blue. We do not investigate much in their binary characteristics.

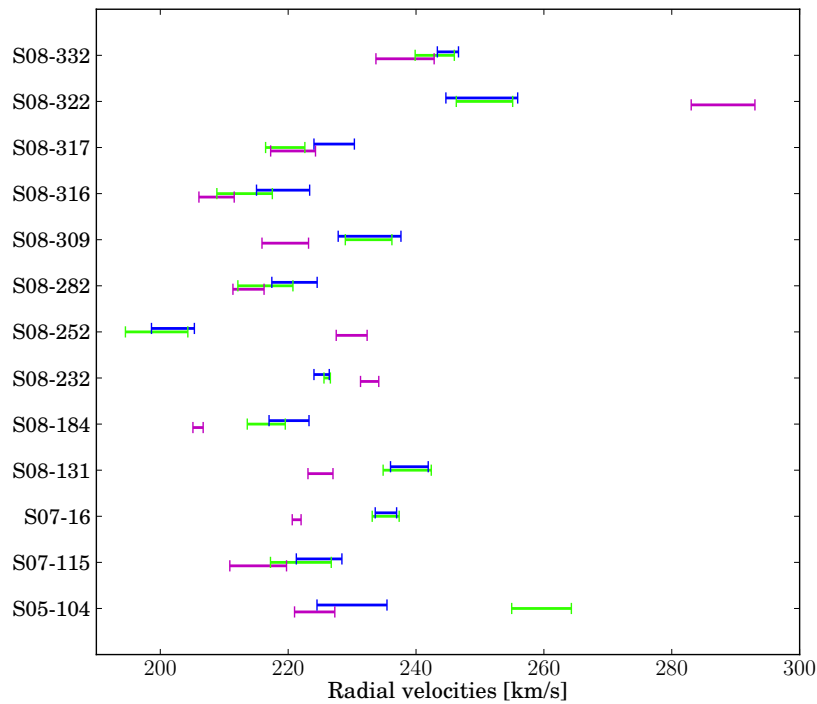


Figure 3.23: Radial velocity intervals for the 13 probable binaries. HR10 is represented in magenta, HR13 in green and HR14 in blue.

### 3.5 Carbon stars

Inspecting carefully spectra we notice specific carbon features in 6 stars : S08-232, S08-306, S08-55, S08-72, S11-111, S11-114. These spectral features are due to strong CN and C<sub>2</sub> molecular bands. Figure 3.24 compare the spectrum of S08-111 having a medium-low signal-to-noise ratio (S/N) (upper panel) with the spectrum of S08-306 cataloged as a carbon-star (lower panel) in HR10 setup. These typical molecular features are well visible in the carbon-star spectrum and are not comparable to noise. Figure 3.25 presents selected portions of spectrum of the carbon star S08-306 and the *normal* star S08-3 around specific molecular carbon lines (CN and C<sub>2</sub>). These carbon stars are discarded from the rest of the study because they need specific treatment and analysis. They will be analyzed by Shetrone et al. (in prep.)

This means that for the rest of the study we work with a sample of 92 stars. Starting from the initial sample of 110 stars, 12 were cataloged as non members from the radial velocity criterion and 6 carbon stars were rejected.

Carbon stars are chemically peculiar stars exhibiting high enhancement in carbon. Recent studies show that the fraction of carbon stars is increasing at very low metallicities : 32-39% of stars with  $[Fe/H] < -3$  (Yong et al. 2013; Aoki et al. 2013; Lee et al. 2013) and 9-21% of stars with  $[Fe/H] < -2.0$  (e.g., Norris et al. (1997); Rossi et al. (1999); Christlieb (2003); Marsteller et al. (2005); Lucatello et al. (2006); Cohen et al. (2005); Frebel et al. (2006); Carollo et al. (2012); Lee et al. (2013)). The origin of the carbon enhancement is still debated and two hypothesis are proposed : i) either the enhancement is due to the star birth composition (the star should form from gas clouds already imprinted with a large over-abundance of carbon : Bromm & Loeb (2003); Norris et al. (2013); Gilmore et al. (2013)) or ii) the stellar atmosphere has been polluted through accretion from an AGB companion in a binary system (Lucatello et al. 2005).

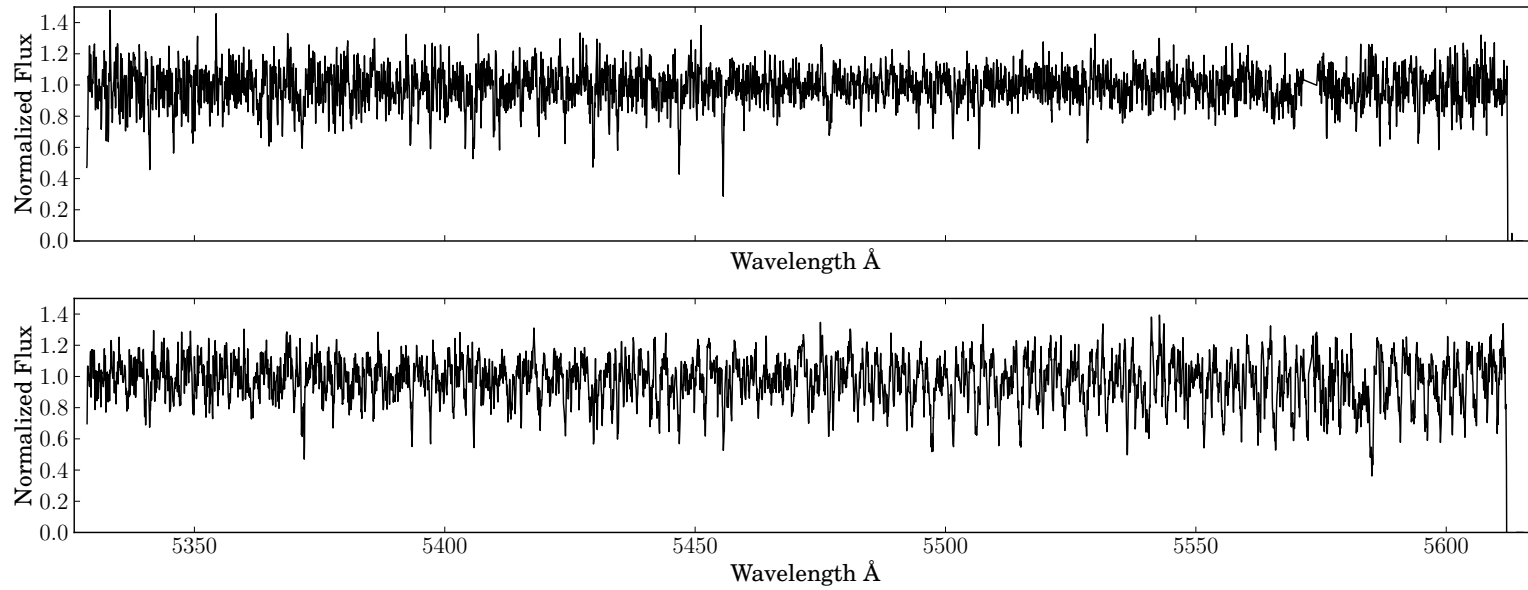


Figure 3.24: The upper panel shows the HR10 spectrum of star S08-111 having a S/N of 14 and the lower panel presents the HR10 spectrum of the carbon-star S08-306. The spectral molecular features observed in the lower spectrum are real and can not be confused with presence of noise.

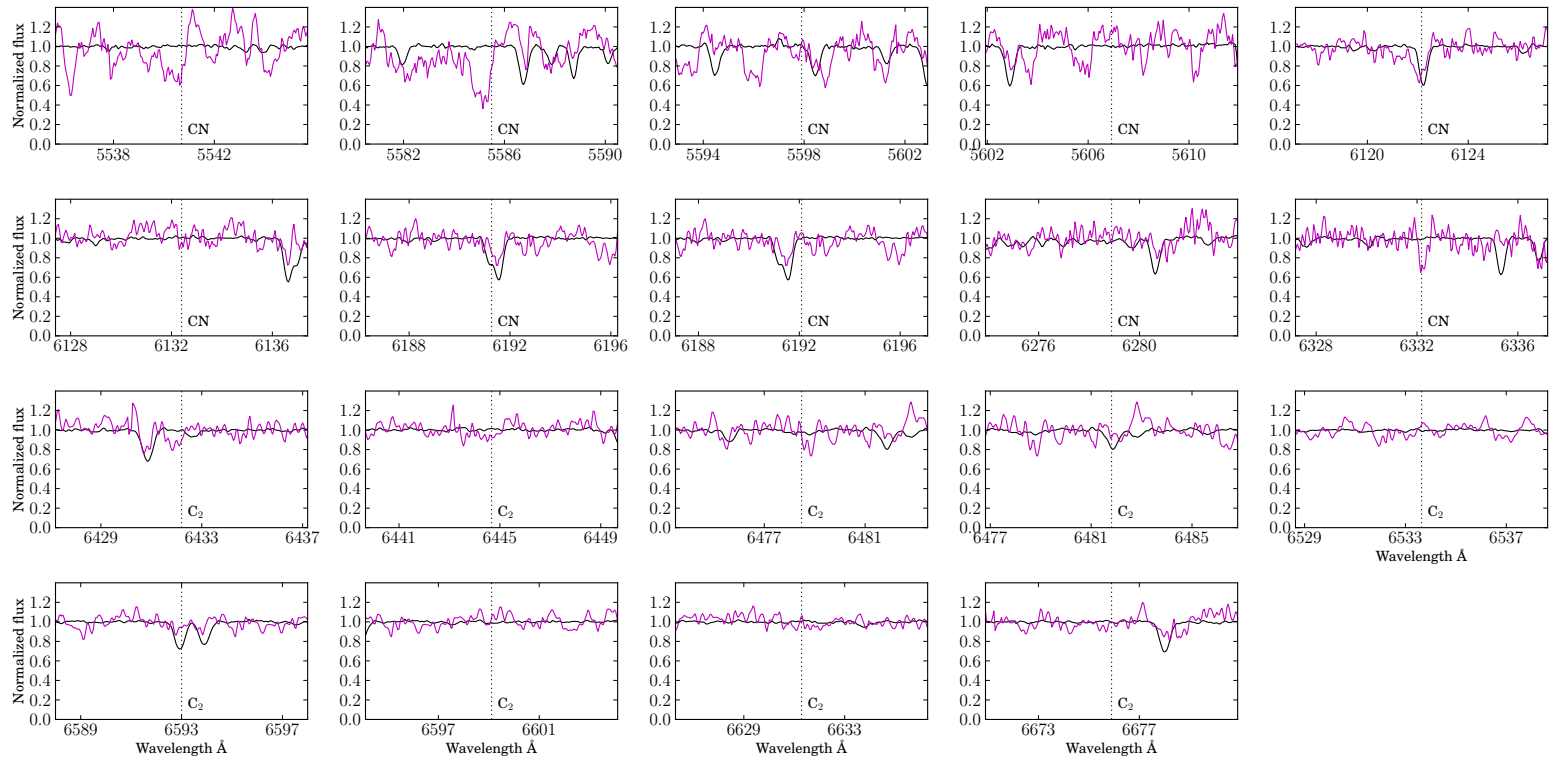


Figure 3.25: In black are plotted spectra from S08-3 and in magenta spectra from the carbon-star S08-306 around several molecular carbon lines (CN and C<sub>2</sub>) covering the three setups.

### 3.6 Normalization of spectra

The operation of normalization consists in dividing the spectrum by its continuum in order to have a signal centered around 1. The continuum corresponds to the stellar signal exempt of lines. As abundances are derived by synthesis, our spectra required to be normalized in order to be comparable with synthetic spectra.

The challenging part of the normalization resides in the continuum determination. As a first test we used the continua created by DAOSPEC to normalize our spectra. Unfortunately we noted that the continua are in general overestimated and that this bad trend is getting worst with decreasing signal-to-noise ratios.

As a second test, we used a FORTRAN routine from (M. Irwin priv. comm.) which produces better continua even for low signal-to-noise spectra. This routine consists in a an iterative process of spectrum filtering. The routine detects lines through asymmetric k-sigma clipping and the lines are masked to obtained the continuum spectrum. A linear and median filter scales are used by the routine. The value of the median filter is given by the user and the linear filter is defined as 1/3 of the median filter value. The user specifies also the number of iteration and the values of the k-sigma clipping. We take 300 for the median filter, 10 for the number of iteration and [-2, 3] for the asymmetric k-sigma clipping.

A comparative example of continuum derived by the two methods is given in figure 3.26. The spectra of star S08-242 (S/N = 38) are plotted in black. The DAOSPEC continua are over-plotted in cyan and continua from the FORTRAN routine are presented in red. The cyan continua are over-estimated and the red continua are correctly placed considering the noise.

Giving more satisfying continuum placement the second method is adopted and all the spectra are normalized.

The normalized spectra are finally shifted in wavelength to be transposed in a rest frame according to the radial velocities previously derived by DAOSPEC. This operation is done by the task *dopcor* in IRAF. Figure 3.27 shows the different steps : the initial spectrum in black and its determined continuum are presented in red in the first panel, the normalized spectra in the middle panel and finally the shifted spectrum in the bottom panel for the case of star S05-10 in setup HR10. Some iron lines are indicated by vertical dotted lines in the two last panels to check the correct alignment with the spectral lines.



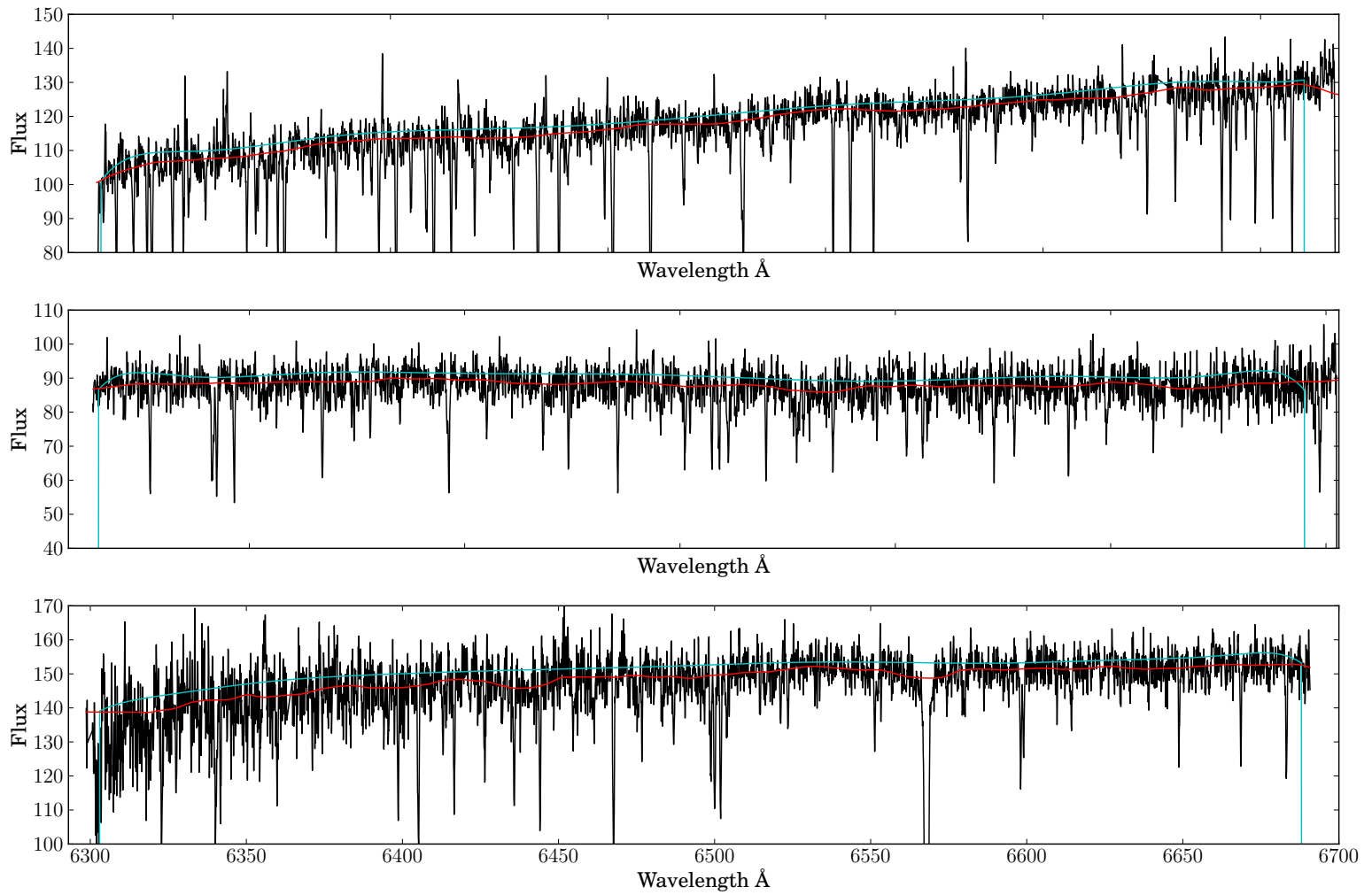


Figure 3.26: The spectra of S08-242 are plotted in black. Their continuum derived by DAOSPEC are shown in cyan and the continuum derived by the FORTRAN routine are presented in red.

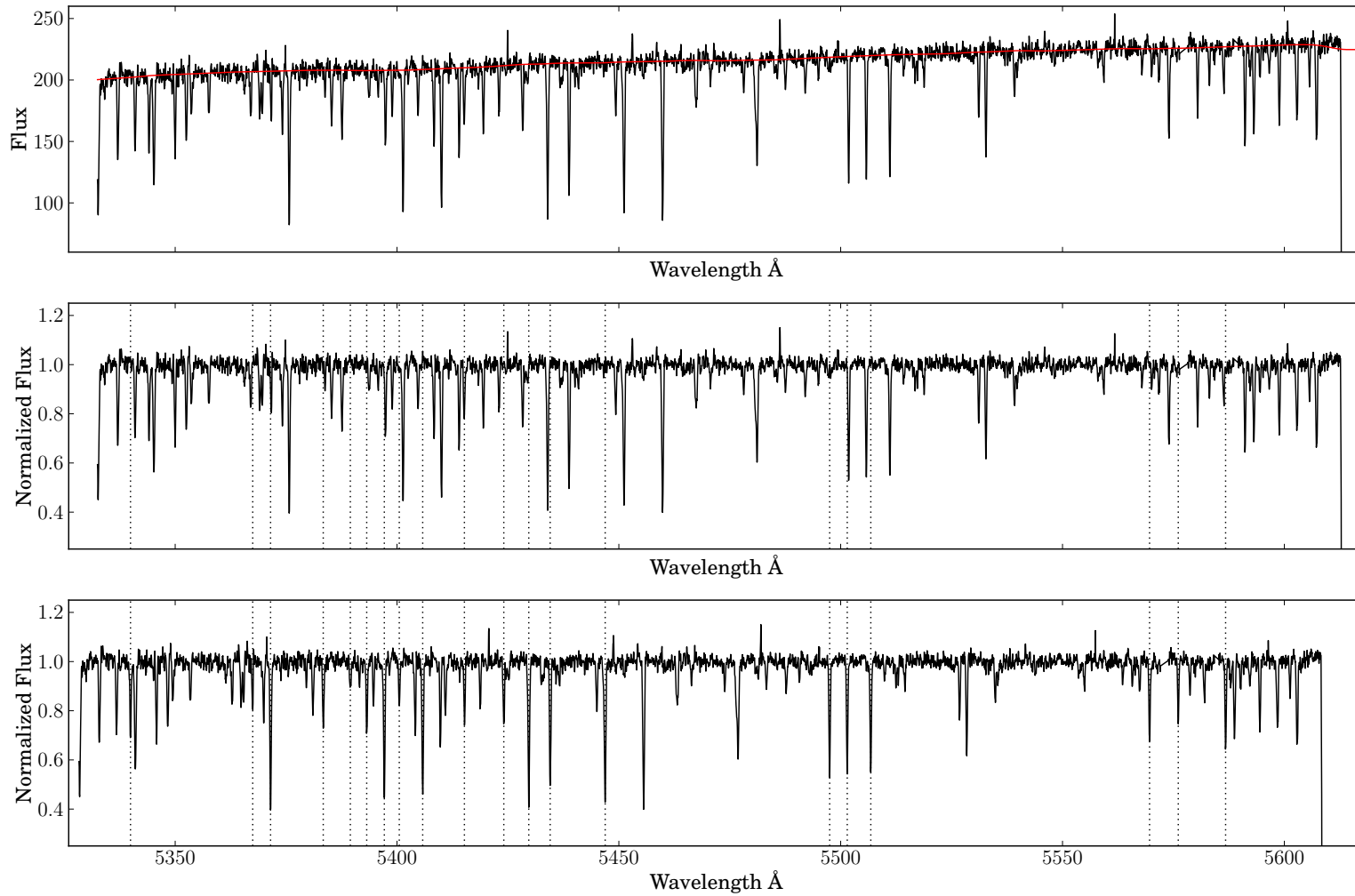


Figure 3.27: Top panel : the HR10 spectrum of star S05-10 in black and its continuum in red. Middle panel : the same spectrum after normalization. Bottom panel : the normalized spectrum after the wavelength shift according to the measured radial velocity. In middle and bottom panels several iron lines are indicated by vertical dotted lines.

### 3.7 Estimation of the signal-to-noise ratios

The signal-to-noise ratio is a measurement of the quality of a spectrum. It depends on many parameters : the number of incoming stellar photons which follows a Poisson probability distribution, the integration time, the sky photons, the readout noise, the number of dark electrons, and the quantum efficiency of the CCD pixels. The signal-to-noise ratio is proportional to the square root of the integration time.

The signal-to-noise ratio of each spectrum is estimated in continuum regions in each setup using the IRAF task *splot* : [5456.6, 5458.94] Å , [6193.47, 6197.74] Å and [6520.0, 6524.4] Å in HR10, HR13, and HR14, respectively. These three regions are represented by blue shaded area in figure 3.28 on the spectra of star S08-3. The results are presented in the table A.3 and are ranging in average from 5 to 120 with a majority between 10 and 25. The distribution of the signal-to-noise ratios in each setup and in average are presented on figure 3.29.

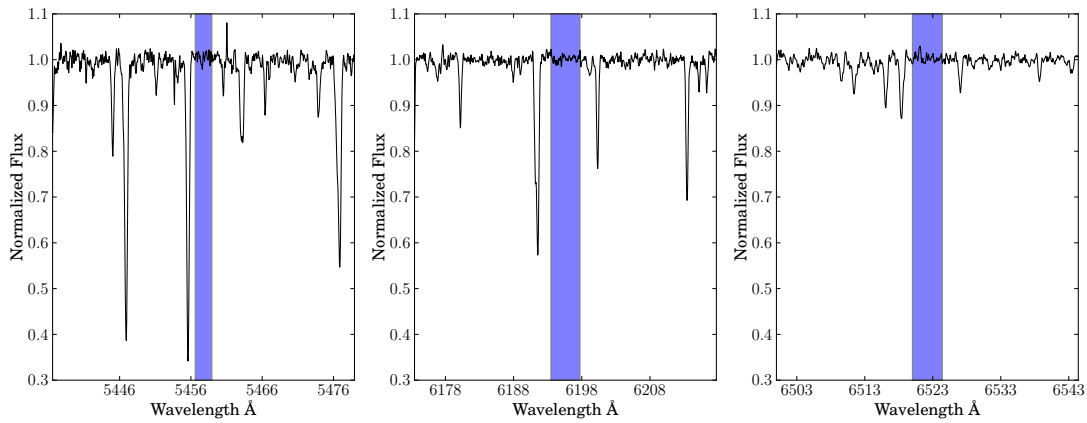


Figure 3.28: Parts of the spectra of S08-3 are represented in the three panels and the shaded areas correspond to the zones used to define the signal-to-noise ratios.

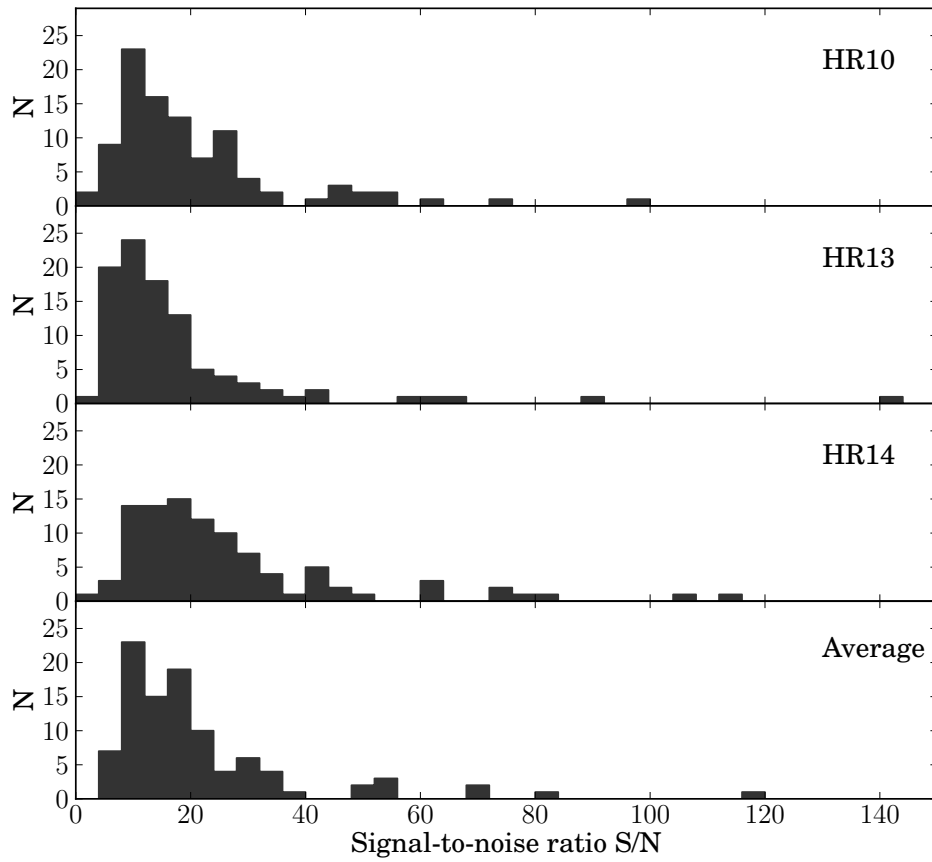


Figure 3.29: The three first panels show the histogram of the signal-to-noise ratios obtained respectively in each setup (HR10, HR13 and HR14) and their average values are presented in the fourth panel.

### 3.8 Determination of stellar parameters

Taking into account the rather low signal-to-noise of our spectra, the stellar parameters  $T_{\text{eff}}$ ,  $\log g$ , and  $v_{\text{turb}}$  are derived from Sextans photometry based on ESO 2.2m Wide Field Imager (WFI)  $V$  and  $I$ -band magnitudes, as well as on the  $J$ ,  $H$ , and  $K$  photometry gathered in the Wide Field Camera (WFCAM) from the Large area Survey (LAS) on the United Kingdom Infra-Red Telescope (UKIRT). The magnitudes are presented in Table A.1. We adopted the reddening law of  $E_{BV} = 0.0477$  (Schlegel et al. 1998). The magnitudes  $J$ ,  $H$ , and  $K$  are converted to Two Micron All Sky Survey (2MASS) system (Hewett et al. 2006).

#### 3.8.1 Effective temperature

For each star four color temperatures  $T_{VI}$ ,  $T_{VJ}$ ,  $T_{VH}$ , and  $T_{VK}$  are obtained following the calibration of Ramírez & Meléndez (2005) :

$$T_{\text{eff}} = \frac{5040}{a_0 + a_1 X + a_2 X^2 + a_3 X[\text{Fe}/\text{H}] + a_4 [\text{Fe}/\text{H}] + a_5 [\text{Fe}/\text{H}]^2} \quad (3.5)$$

where  $X$  is a color and  $a_i$  are the calibration coefficients. If the metallicity estimate from the Ca II Triplet was available, we used it as initial iron abundance ( $[\text{Fe}/\text{H}]$  CaT), otherwise we took the mean metallicity of the Sextans stellar population derived by Battaglia et al. (2011)  $[\text{Fe}/\text{H}]_{\text{average}} = -1.9$ , as a first guess. The final effective temperature is the average of the four color temperatures. The four color temperatures and the first guess metallicities are given in Table A.1.

#### 3.8.2 Surface gravity

The surface gravities were calculated with the following standard relation :

$$\log g_* = \log g_{\odot} + \log \frac{M_*}{M_{\odot}} + 4 \times \log \frac{T_{\text{eff},*}}{T_{\text{eff},\odot}} + 0.4 \times (M_{\text{Bol}} - M_{\text{Bol},\odot}) \quad (3.6)$$

where the adopted surface gravity, effective temperature and bolometric magnitude for the sun are respectively  $\log g_{\odot} = 4.44$ ,  $T_{\text{eff},\odot} = 5790$  K,  $M_{\text{Bol},\odot} = 4.75$ . We took a stellar mass was  $M_* = 0.8M_{\odot}$  and a distance of 90 kpc (Tafelmeyer et al. 2010; Battaglia et al. 2011). The bolometric corrections for giants are derived following Alonso et al. (1999). The absorption  $A_V = 3.24E_{BV}$  from Cardelli et al. (1989) is used.

### 3.8.3 Microturbulence velocity

The micro-turbulence velocities were derived according to the empirical relation of Anthony-Twarog et al. (2013) :

$$v_{\text{turb}} = 2.0 - 0.2 \times \log g \quad (3.7)$$

This relation was obtained by Anthony-Twarog et al. (2013) on a sample of 332 red giants members of the open cluster NGC 6819 following Carretta et al. (2004) and McWilliam & Bernstein (2008). They chose to derive the micro-turbulence velocity assuming a simple relation dependent only on the surface gravity. They argued that this method was more stable than adopting individual values of micro-turbulence velocity by eliminating trends in the abundances of Fe I with expected line strengths.

Before adopting this empirical definition of the micro-turbulence velocities we tried unsuccessfully to derive them simultaneously with the metallicity by synthesis based on a  $\chi^2$  minimization procedure with two parameters. The results were not satisfying because of large degeneracies in micro-turbulence velocity range (more pronounced at low S/N).

### 3.8.4 Final stellar parameters

The effective temperatures, the surface gravities, the micro-turbulence velocities and first guessed metallicities are provided in Table A.2. Our sample displays large ranges of stellar parameters : more than 1000 K in effective temperatures (from 4150 to 5250 K), between 0.5 and 2.5 in surface gravities and from 1.5 to 1.9 km/s for micro-turbulence velocities.

Figure 3.30 and 3.31 show the relations between the effective temperatures, the surface gravities and the micro-turbulence velocities obtained for all the members.

### 3.8. Determination of stellar parameters

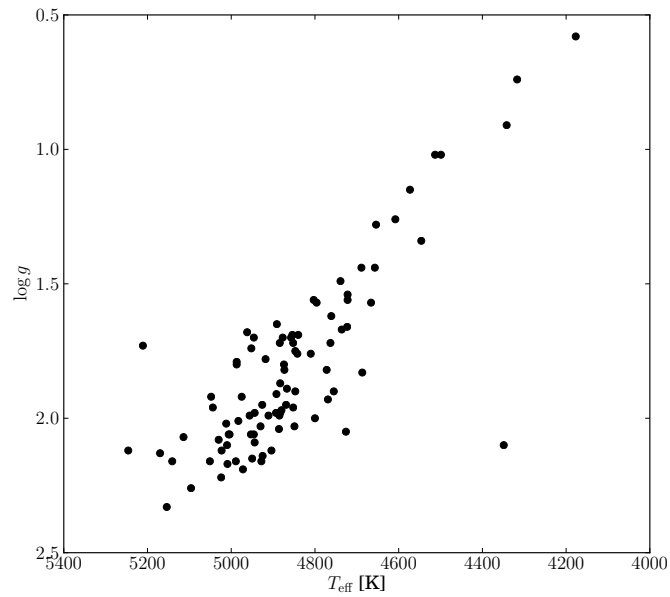


Figure 3.30: The surface gravities of our members are presented in function of the effective temperatures. The two axis are reversed in order to have a similar plot to the color magnitude diagram.

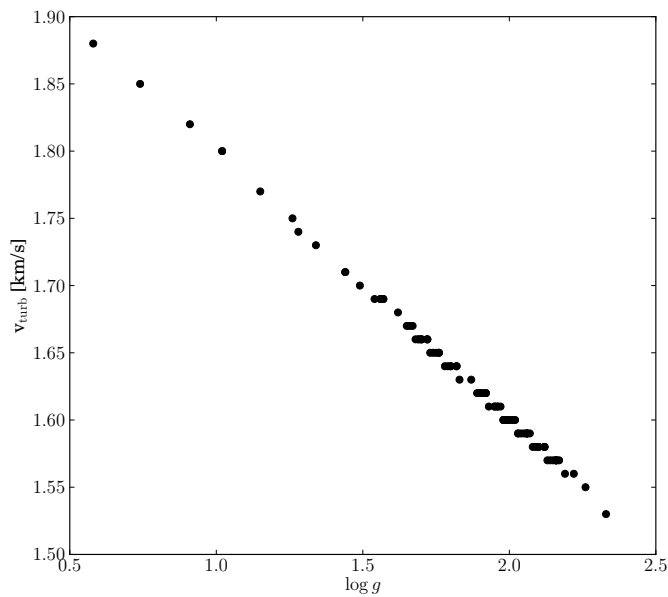


Figure 3.31: The micro-turbulence velocities of our members are plotted in function of the surface gravities. The relation is clearly linear following the formula used to derive of the micro-turbulence velocities from surface gravities.

## 3.9 Metallicity determination method

### 3.9.1 Notation

The fraction of metals (all elements heavier than helium) contained in an object is expressed by  $Z$  in comparison with  $X$  and  $Y$  the respective fractions of hydrogen and helium. The metallicity or metal content  $[M/H]$  defines the total abundance of metals. As a misuse of language the metallicity is often replaced by the iron abundance  $[Fe/H] = \log(N_{Fe}/N_H)_* - \log(N_{Fe}/N_H)_\odot$  where  $N_{Fe}$ ,  $N_H$  are number of iron and hydrogen atoms per unit of volume and  $*$  and  $\odot$  symbols refer respectively to the considered star and the sun. The iron abundance is related to the total metal content by a multiplicative constant :  $[M/H] = A [Fe/H]$  where  $A$  is between 0.9 and 1.

Iron was chosen because it is abundant in stellar atmospheres and iron lines are easily measurable in visible spectra. In intermediate resolution spectroscopy  $[Fe/H]$  can be estimated from Ca II triplet lines while in high resolution spectroscopy a typical number of 70 Fe I lines and 15 Fe II lines are available for a more robust determination.

The abundances of other elements follow the same definition of the iron abundance simply replacing in the formula Fe by the considered element. Concerning abundance ratios they are given by :  $[E/Fe] = [E/H] - [Fe/H]$  for an element E.

We clarify that in this thesis the term *metallicity* always refers to  $[Fe/H]$  as generally (abusively) used.

The solar metallicity and abundances used as references come from Grevesse & Sauval (1998) and are indicated in tables A.8, A.9 and A.10.

### 3.9.2 Two methods of deriving abundances

Two techniques are generally used to derive abundances. This first called the classical technique is based on equivalent width measurements and the second one is the synthesis method.

#### Classical method

In this method the stellar parameters are spectroscopically estimated based on diagnostics plots (spectroscopic stellar parameters as seen in the end of chapter 2). The effective temperatures and micro-turbulence velocities are adjusted requiring respectively no trend of iron abundances with excitation potentials and with equivalent widths. The surface gravities are defined requiring an ionization equilibrium for iron lines. The initial guess of stellar parameters could come from photometry.

The equivalent widths of lines are derived from gaussian fits. Therefore this method is suitable for lines corresponding to the linear part of the curve of growth. This is why the lines are



often restricted to  $20 \leq EQW \leq 250$  mÅ. This technique is applicable for spectra having high signal-to-noise ratios. One advantage of this method is that equivalent width measurements are independent of the spectral resolution.

#### Synthesis method

The spectral synthesis method is preferred when dealing with weak or strong lines, blended lines and spectra with low signal-to-noise ratios. This method consists in a spectral fitting technique. The goal is to find the best fit between an observed spectra and a library of synthetic spectra.

The challenge in this method resides in making comparable spectra to allow a correct fitting. This means to achieve a good normalization of the observed spectra and to convolve the synthetic spectra in order to obtain the same spectral resolution as the observed spectra.

In this study, we use the synthesis technique to derive the metallicity and elemental abundances considering the rather low signal-to-noise ratios displayed by our spectra.

#### 3.9.3 Description of the synthesis method

For each star we have determined the effective temperature, the surface gravity and the micro-turbulence velocity. The next stellar parameter to be determined is the metallicity [Fe/H].

#### Library of synthetic spectra and model atmospheres

A library of synthetic spectra designed to cover the stellar parameters of our stars sample and the HR10, HR13 and HR14 wavelength ranges was created with MOOG (Snedden 1973) (August 2010 Version) by Pierre North. The nominal resolution was  $R = 40000$ , and the spectra were generated over a temperature range of  $4200 \leq T_{\text{eff}} \leq 5300$  with a step of 50 K, surface gravity range of  $0.5 \leq \log g \leq 2.5$  with a step of 0.1, micro-turbulence range of  $1.4 \leq v_{\text{turb}} \leq 2.0$  with a step of 0.2, and metallicity of  $-4.0 \leq [\text{Fe}/\text{H}] \leq -0.5$  with a step of 0.1 dex. The wavelength step of synthetic spectra is 0.02 Å and they are normalized to 1.

We adopted the Model Atmospheres in Radiative and Convective Scheme (MARCS) 1D spherical atmosphere models with standard abundances downloaded from the MARCS web site (Gustafsson et al. 2008) (marcs.astro.uu.se). We assumed standard values of  $[\alpha/\text{Fe}]$ , following the Galactic disk and halo, namely +0.4 for  $[\text{Fe}/\text{H}] \leq -1.5$ , +0.3 for  $[\text{Fe}/\text{H}] = -0.75$ , +0.2 for  $[\text{Fe}/\text{H}] = -0.54$ , +0.1 for  $[\text{Fe}/\text{H}] = -0.25$  and +0.0 for  $[\text{Fe}/\text{H}] \geq 0.0$ . The interpolations between the atmosphere models are done using Thomas Masseron's `interpol_modeles` code available on the same web site.

For each star of known  $T_{\text{eff}}$ ,  $\log g$  and  $v_{\text{turb}}$  we select in this library the closest synthetic spectra corresponding to the closest  $T_{\text{eff}}$  within 50 K,  $\log g$  within 0.1 and we interpolated them to get

the  $v_{\text{turb}}$ . For each observed spectrum, we have then a set of 36 synthetic spectra with fixed  $T_{\text{eff}}$ ,  $\log g$  and  $v_{\text{turb}}$  and varying in  $[\text{Fe}/\text{H}]$  from  $-4.0$  to  $-0.5$  with a step of  $0.1$  dex.

#### Macroscopic broadening : macro-turbulence and rotation

As presented in chapter 2, several macroscopic mechanisms are responsible for the broadening of spectral lines. The dominant one in our spectra is the instrumental broadening which is of the order of  $15.2$  km/s,  $13.3$  km/s and  $16.9$  km/s corresponding respectively to the spectral resolution of HR10, HR13 and HR14 setups. Applying these instrumental broadening turned out not to be sufficient and macro-turbulence as possibly rotation needed to be considered. The combination of these two macroscopic effects are estimated by comparing Fe I lines of observed spectra and of their best fitted synthetic spectra slightly broadened (previously corrected from instrumental broadening). Ideally the macro-turbulence and rotation broadening should be derived star by star but the low signal-to-noise ratios of the majority of stars do not allow this determination. This is why we used only the four brightest stars (S08-3, S08-6, S05-10, S08-38) of our sample displaying the highest signal-to-noise ratios. We found that a subsequent convolution by  $9.0$  km/s,  $7.9$  km/s and  $7.6$  km/s for the HR10, HR13 and HR14 setups respectively, give the best agreement between the spectra.

#### Re-binning and convolution of the synthetic spectra

Several steps of modification of the synthetic spectra are needed to make them comparable to the observed spectra :

- cut the synthetic spectra to the same wavelength limits as the observed spectra
- re-bin the synthetic spectra to have the same wavelength step (from  $\Delta\lambda = 0.02 \text{ \AA}$  to  $\Delta\lambda = 0.05 \text{ \AA}$ )
- convolve the synthetic spectra taking into account the instrumental broadening
- convolve the synthetic spectra according to the macroscopic broadening

The convolution operations are done using the *scipy* function *scipy.ndimage.gaussianfilter1D* consisting in passing a 1D gaussian filter through the spectrum.

Figure 3.32 shows the impact of this two-step convolution on a synthetic spectrum around two iron lines.

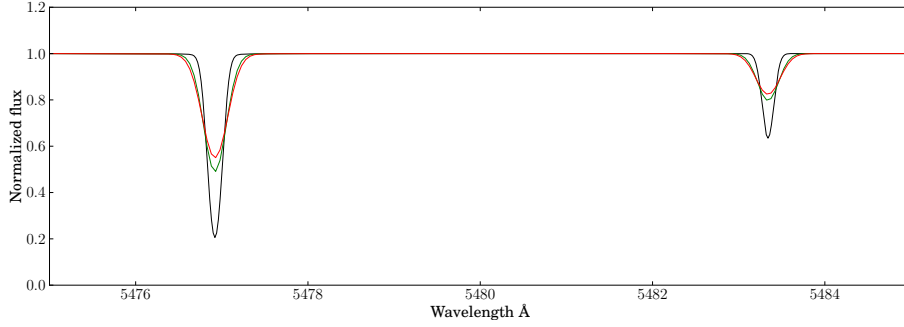


Figure 3.32: The black line shows a part of synthetic spectrum corresponding to the following stellar parameters  $T_{\text{eff}} = 4200$  K,  $\log g = 0.6$ ,  $[\text{Fe}/\text{H}] = -2.0$  dex and  $v_{\text{turb}} = 2.0$  km/s. The green line is the result of the convolution of the black synthetic spectrum with a gaussian function to take into account the instrumental broadening. The red line corresponds to the resulting synthetic spectrum after the second convolution taking into account the macro-turbulence and the rotation broadening.

#### $\chi^2$ minimization procedure around Fe I lines

**$\chi^2$  formula** The abundances were derived by synthesis based on a  $\chi^2$  minimization procedure around Fe I lines. The formula used for the  $\chi^2$  is the following :

$$\chi^2 = \sum_{i=1}^N \frac{(y_{\text{obs},i} - y_{\text{syn},i})^2}{y_{\text{syn},i}} \quad (3.8)$$

where  $i$  is the pixel index and  $y$  the flux of this pixel either in the observed ( $y_{\text{obs},i}$ ) spectrum or in the model synthetic ( $y_{\text{syn},i}$ ) one. A  $\chi^2$  value is attributed to each considered Fe I line along the spectrum. They are summed by setup and multiplied by the median  $m_{\text{HR}}$  of the continuum in each setup (as a weight). Finally the total  $\chi^2$  corresponding to the compatibility between an observed spectrum and a synthetic spectrum in three setups is defined by :

$$\chi_{\text{tot}}^2 = \left( \sum_{\text{HR10}} \chi_{\text{FeI line}}^2 \right) m_{\text{HR10}} + \left( \sum_{\text{HR13}} \chi_{\text{FeI line}}^2 \right) m_{\text{HR13}} + \left( \sum_{\text{HR14}} \chi_{\text{FeI line}}^2 \right) m_{\text{HR14}} \quad (3.9)$$

Normally the exact formula of the  $\chi^2$  should be defined with the square of measurement errors  $\sigma_i$  as denominator. In that case, we need flux errors at each pixel. However a correct determination of these errors is a very complicated task because many sources of noise need to be taken into account as seen in the reduction process. However these errors can be estimated as the square root of flux values  $\sigma_i \approx \sqrt{y_i}$ . This explains the flux value in the denominator of the formula we used for the  $\chi^2$ .

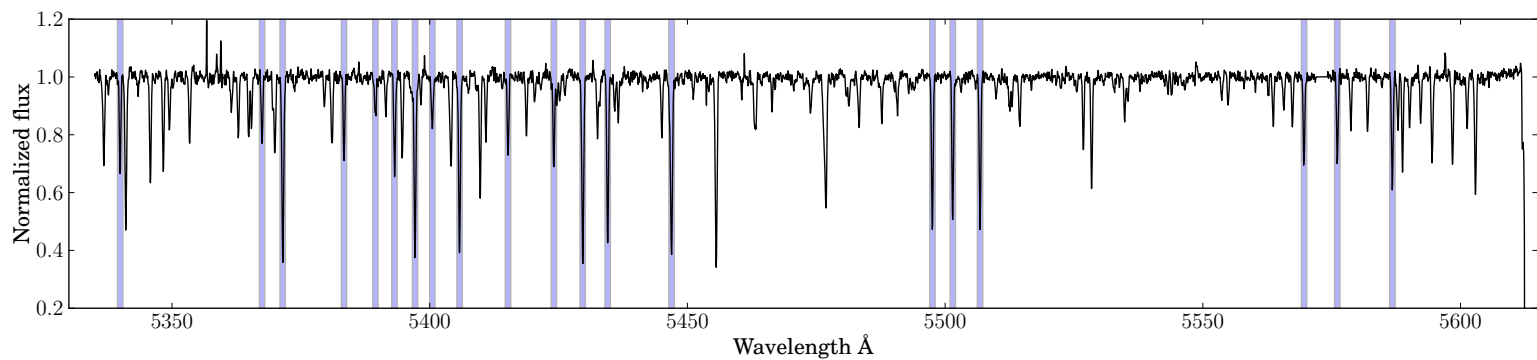
We may have chosen a variation of the  $\chi^2$  formula replacing the synthetic spectrum by the

observed spectrum in the denominator. This modification would add noise contribution in the division. After testing this variation, we observed that the impact was not significantly different on results for high signal-to-noise ratios spectra but worst for S/N around 20 and below because displaying flatter  $\chi^2$  curves. Considering the distribution of our signal-to-noise ratios the first version of the  $\chi^2$  is preferred giving better determined minima.

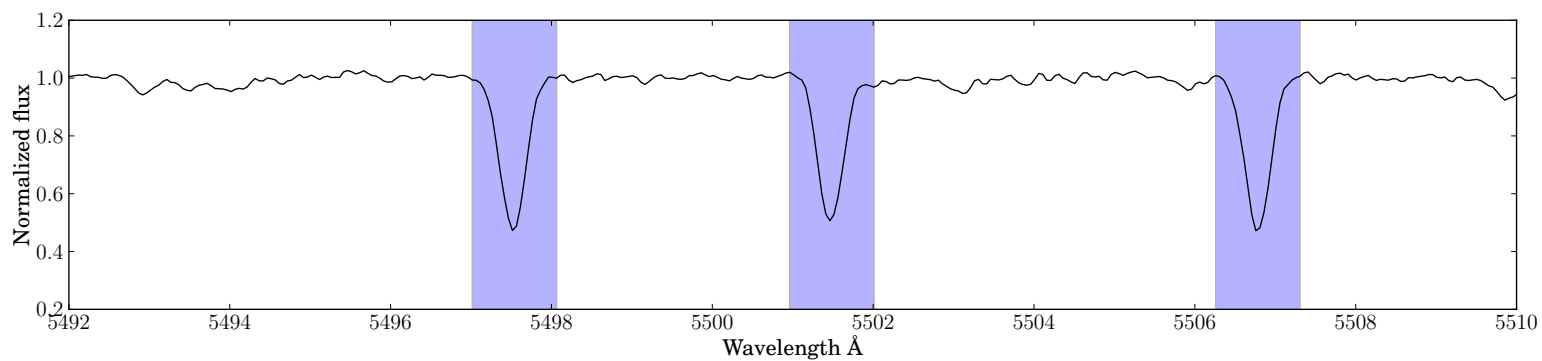
**List of iron lines** We started from the Fe I line list of Tafelmeyer et al. (2010) and discarded the faintest lines which could be affected by the noise and those which could be blended. The final list counts 50 Fe I lines in total : 20 lines in HR10, 21 lines in HR13 and 9 lines in HR14. As setups HR13 and HR14 have a small overlapping region, we chose to consider the common lines in HR13 and not in HR14 taking advantage of a higher resolution. The lines are listed in table A.6 with their characteristic excitation potentials, oscillator strengths and  $C_6$  damping constants.

For stars presenting polluted spectra, Fe I lines belonging to the corresponding polluted setup are discarded from the  $\chi^2$  minimization. The number of used Fe I lines in the [Fe/H] determination are given in table A.8.

**Spectral windows centered on lines** The match between the synthetic and observed spectra was estimated in spectral windows centered on the lines, with a width of 22 pixels in HR10 and HR13 (1.05 Å), and 28 pixels (1.35 Å) in H14. The width of these windows were calculated as  $1.75 \times \text{FWHM}$ , where FWHM is defined by the spectral resolution of each setup. The factor 1.75 has been chosen to adapt windows to lines presenting larger wings. Figures 3.33, 3.34 and 3.35 present along each setup the position of the defined intervals around the Fe I lines. Zoomed portions of the same figures are shown in the second panels of each figure.

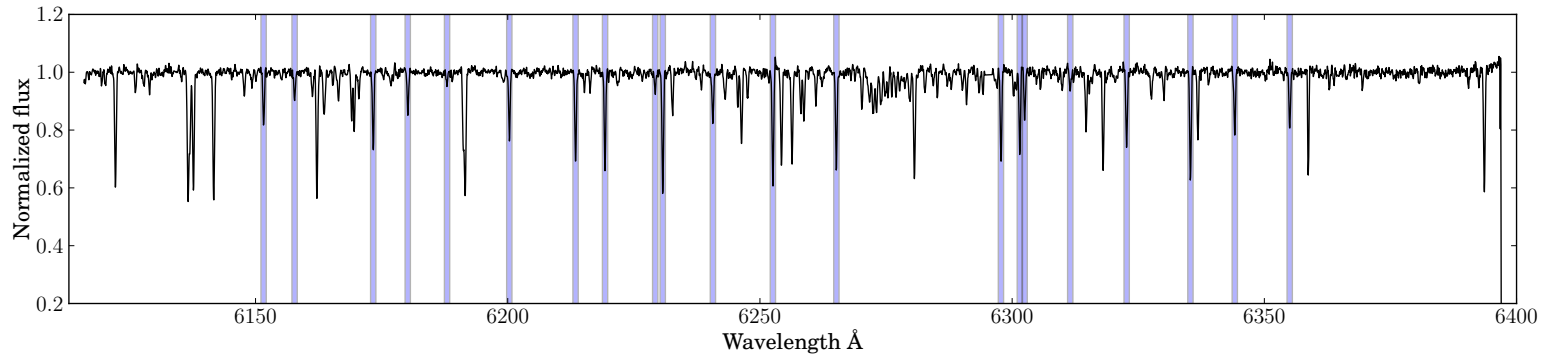


(a) Location of selected intervals around Fe I lines in setup HR10

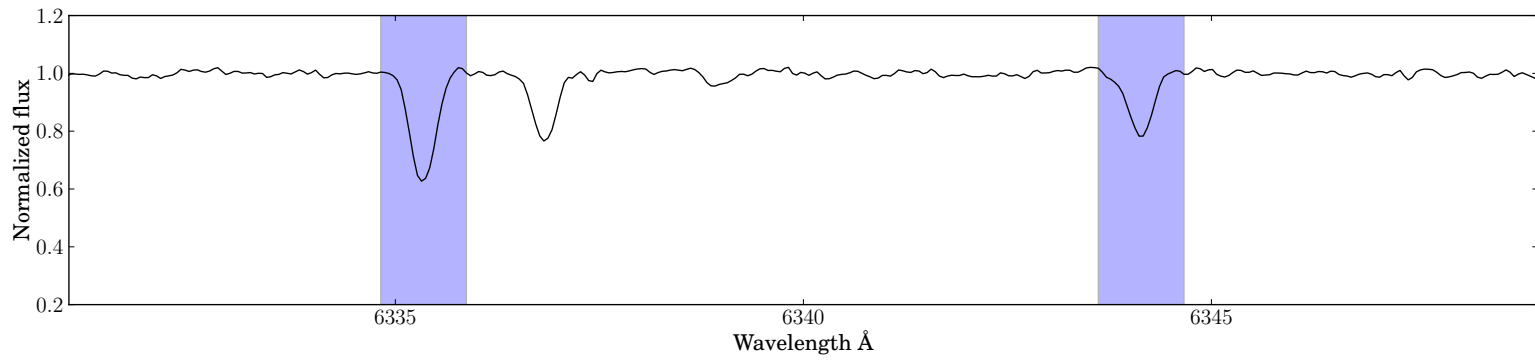


(b) Zoomed version of (a)

Figure 3.33: The black line corresponds to the observed spectrum of star S08-3 in setup HR10. The shaded blue areas are the selected intervals around Fe I lines where the  $\chi^2$  are calculated.

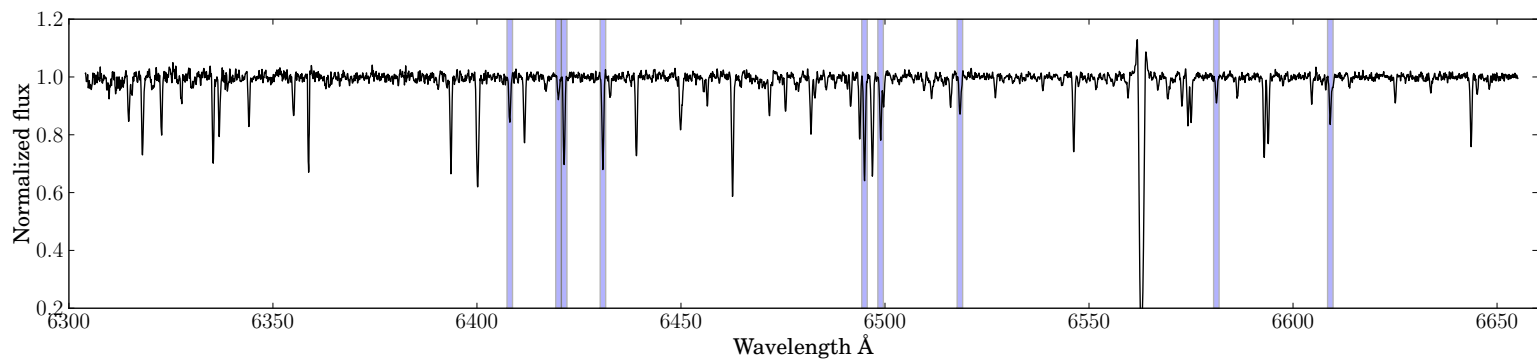


(a) Location of selected intervals around Fe I lines in setup HR13

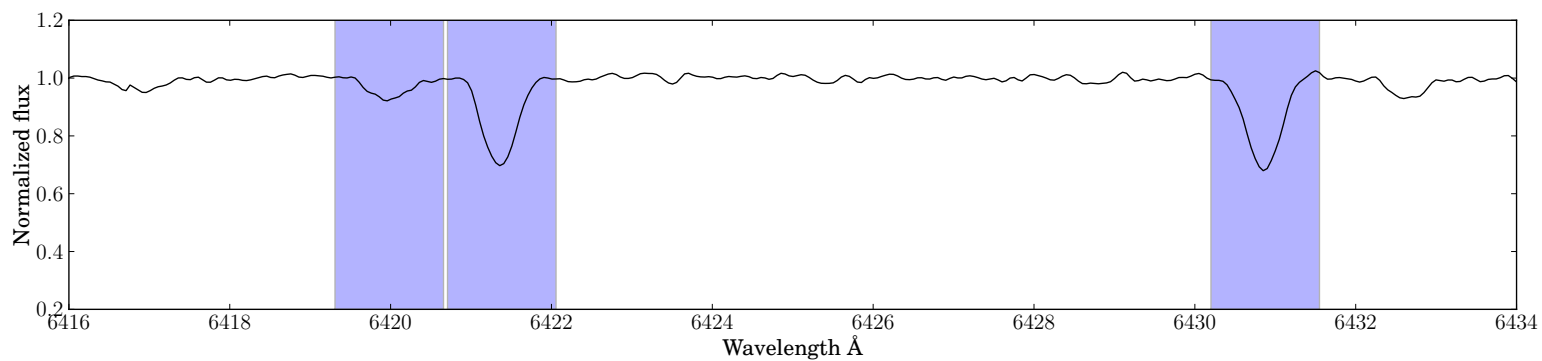


(b) Zoomed version of (a)

Figure 3.34: The black line corresponds to the observed spectrum of star S08-3 in setup HR13. The shaded blue areas are the selected intervals around Fe I lines where the  $\chi^2$  are calculated.



(a) Location of selected intervals around Fe I lines in setup HR14

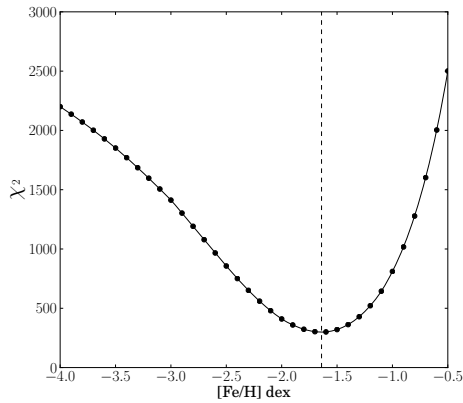


(b) Zoomed version of (a)

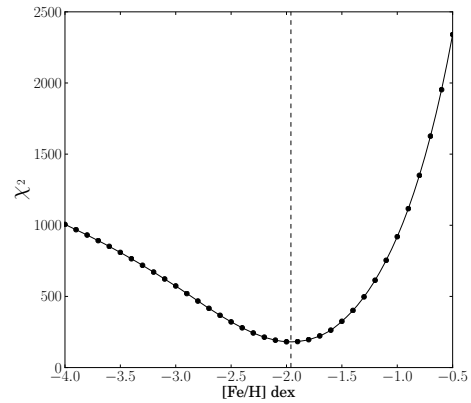
Figure 3.35: The black line corresponds to the observed spectrum of star S08-3 in setup HR14. The shaded blue areas are the selected intervals around Fe I lines where the  $\chi^2$  are calculated.

**Minimization of  $\chi^2$**  The  $\chi^2$  values are calculated for  $[\text{Fe}/\text{H}]$  varying from  $-4.0$  to  $-0.5$  in steps of  $0.1$  dex. We interpolate them to obtain a thinner step of  $0.01$  dex in  $[\text{Fe}/\text{H}]$  and the minimization is applied by brute force using the *scipy.optimize.brute* on the interpolated results. Figure 3.36 presents three examples of  $\chi^2$  curves in a decreasing quality order. The left part of the  $\chi^2$  curve becomes flatter when the lines become smaller and hardly distinguishable from the noise.

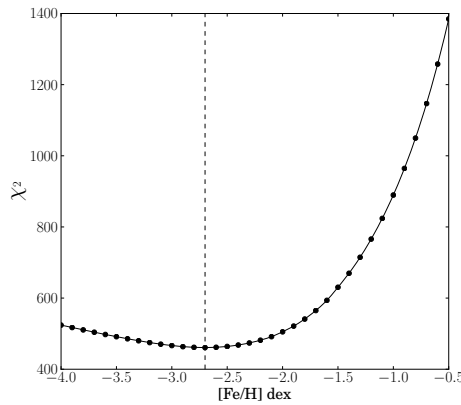
The final  $[\text{Fe}/\text{H}]$  are listed in table A.7.



(a) Curve of  $\chi^2$  for  $[\text{Fe}/\text{H}]$  determination for star S05-47



(b) Curve of  $\chi^2$  for  $[\text{Fe}/\text{H}]$  determination for star S08-250



(c) Curve of  $\chi^2$  for  $[\text{Fe}/\text{H}]$  determination for star S08-292

Figure 3.36: Curve of  $\chi^2$  for  $[\text{Fe}/\text{H}]$  determination for stars S05-47, S08-250 and S08-292. The values obtained before interpolation are represented by the black circles. The black solid line connects the interpolated values and the position of the minimum after interpolation is indicated by the vertical dashed line.



### 3.10 Error budget on [Fe/H]

The metallicity uncertainties are defined by the quadratic addition of the systematic errors and the random errors :  $\text{err}_{\text{tot}} = \sqrt{\text{err}_{\text{sys}}^2 + \text{err}_{\text{rand}}^2}$ . The total errors on [Fe/H] are displayed in table A.7 and the detailed systematic and random errors can be found in table A.8.

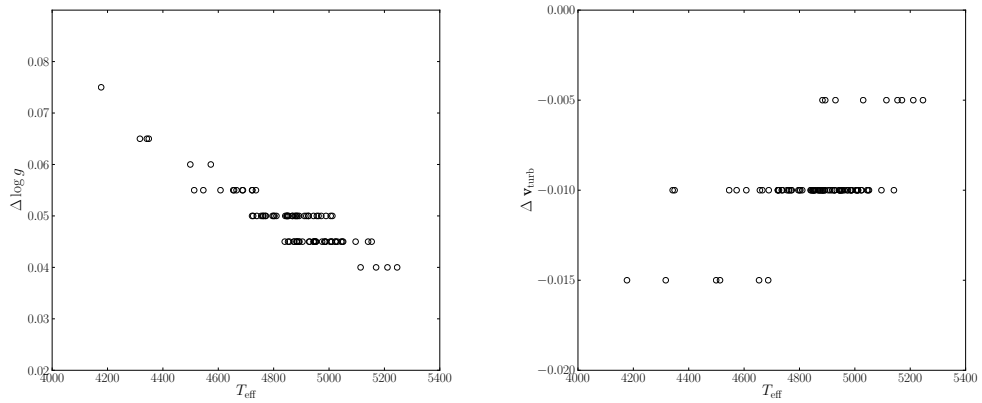
#### 3.10.1 Systematic errors

Taking into account a typical variation of  $\pm 100$  K of the effective temperatures, we re-derived the stellar parameters  $\log g$ ,  $v_{\text{turb}}$  and [Fe/H] for each star. The systematic error is defined by the mean of the two differences :

$$\text{err}_{\text{sys}} = \frac{([\text{Fe}/\text{H}]_{T+100} - [\text{Fe}/\text{H}]_T) + ([\text{Fe}/\text{H}]_T - [\text{Fe}/\text{H}]_{T-100})}{2} \quad (3.10)$$

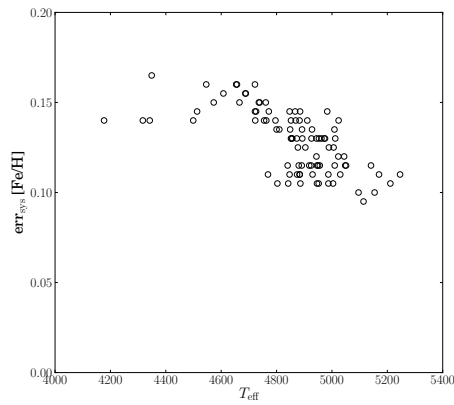
Figure 3.37 presents the differences in surface gravities, micro-turbulence velocities and metallicities implied by the variation of  $\pm 100$  K in effective temperatures. Concerning the surface gravities, the systematic errors range from 0.04 to 0.075 with a majority around 0.05. The systematic errors on micro-turbulence velocities are centered around 0.01 km/s. The systematic errors on [Fe/H] range from 0.1 to 0.17 dex with an increasing trend with decreasing effective temperatures.

We also test the impact of distance uncertainties on the determination of surface gravities. Considering an error of 5 kpc on the estimated distance to Sextans we obtain an error of 0.05 on  $\log g$ . This corresponds to the same order of magnitudes as systematic errors obtained from a typical variation of 100 K in effective temperatures.



(a) Systematic errors on surface gravities

(b) Systematic errors on micro-turbulence velocities



(c) Systematic errors on metallicities

Figure 3.37: Systematic errors on surface gravities (a), micro-turbulence velocities (b) and metallicities (c) due to a variation of  $\pm 100$  K of the effective temperatures. The systematic errors are presented in function of the effective temperatures.

### 3.10.2 Random errors

Depending on the atmospheric parameters and the metallicity of the stars the results evolve differently with variations of signal-to-noise ratios. The impact of the noise is bigger for low metallicities, high effective temperatures and surface gravities because lines are smaller. Our sample spans more than 1 dex in [Fe/H] and 1000 K in  $T_{\text{eff}}$ .

We estimated the random errors on the metallicities by Monte Carlo simulations. For each star, at given  $T_{\text{eff}}$ ,  $\log g$ ,  $v_{\text{turb}}$ , and [Fe/H], we generated 1000 spectra considering only iron lines with the same stellar parameters and signal-to-noise ratio as the observed spectrum. The spectra are generated by MOOG (Sneden 1973) using the same atmosphere models used to create the previous library. In addition these spectra are convolved taking into account the different sources of broadening in order to make them similar to observed spectra. The noise was added thanks to the IRAF task *iraf.noao.artdata.mknoise* with Poisson noise through a gain of  $(S/N)^2$  and a readout noise defined as  $(S/N)^{-1}$ .

MOOG (Sneden 1973) is a FORTRAN code designed to perform a variety of LTE line analysis and spectrum synthesis with the aim to help to the stellar chemical composition determination. The basic equations of the stellar line analysis in LTE are used following the formulation of Edmonds (1969). Much of the MOOG code (Sneden 1973) is written as in a general way the WIDTH and SYNTH codes of R. L. Kurucz (<http://kurucz.harvard.edu/>).

The metallicities are then determined with these simulated noisy spectra using the same procedure as described above except that the possible [Fe/H] are reduced to an interval of 1 dex centered on the expected value with a step of 0.1 dex. As previously the minimum is obtained on interpolated values with a step of 0.01 dex.

The distribution of the 1000 final [Fe/H] (binned with a step of 0.01 dex) is fitted by a gaussian and the adopted random error is the standard deviation of this gaussian function. Figures 3.38 and 3.39 show the distribution of the 1000 [Fe/H] for star S08-38 and S08-292.

Figure 3.40 show the final random errors on [Fe/H] obtained in function of the signal-to-noise ratios. There is an exponential increase of the random errors on [Fe/H] with decreasing signal-to-noise ratios.

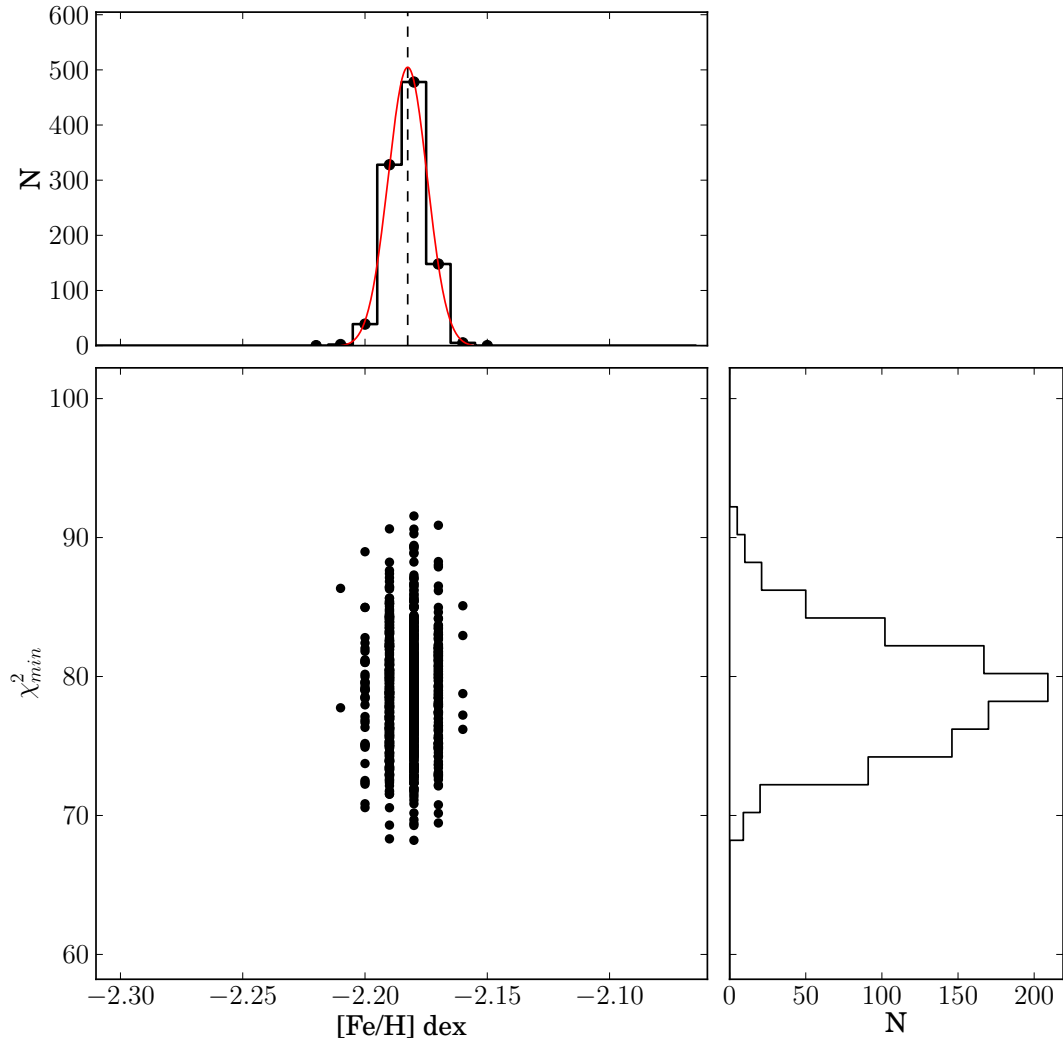


Figure 3.38: Top panel : the black solid line is the re-binned histogram of the distribution of 1000 final  $[Fe/H]$  obtained by Monte Carlo simulated spectra for star S08-38. The red solid line is the best fitted gaussian function used to determine the random error corresponding to the standard deviation. Bottom left : The points represent the 1000 couples of  $(\chi_{min}^2, [Fe/H])$ . Bottom right : the solid black line shows the histogram of the  $\chi_{min}^2$  values.

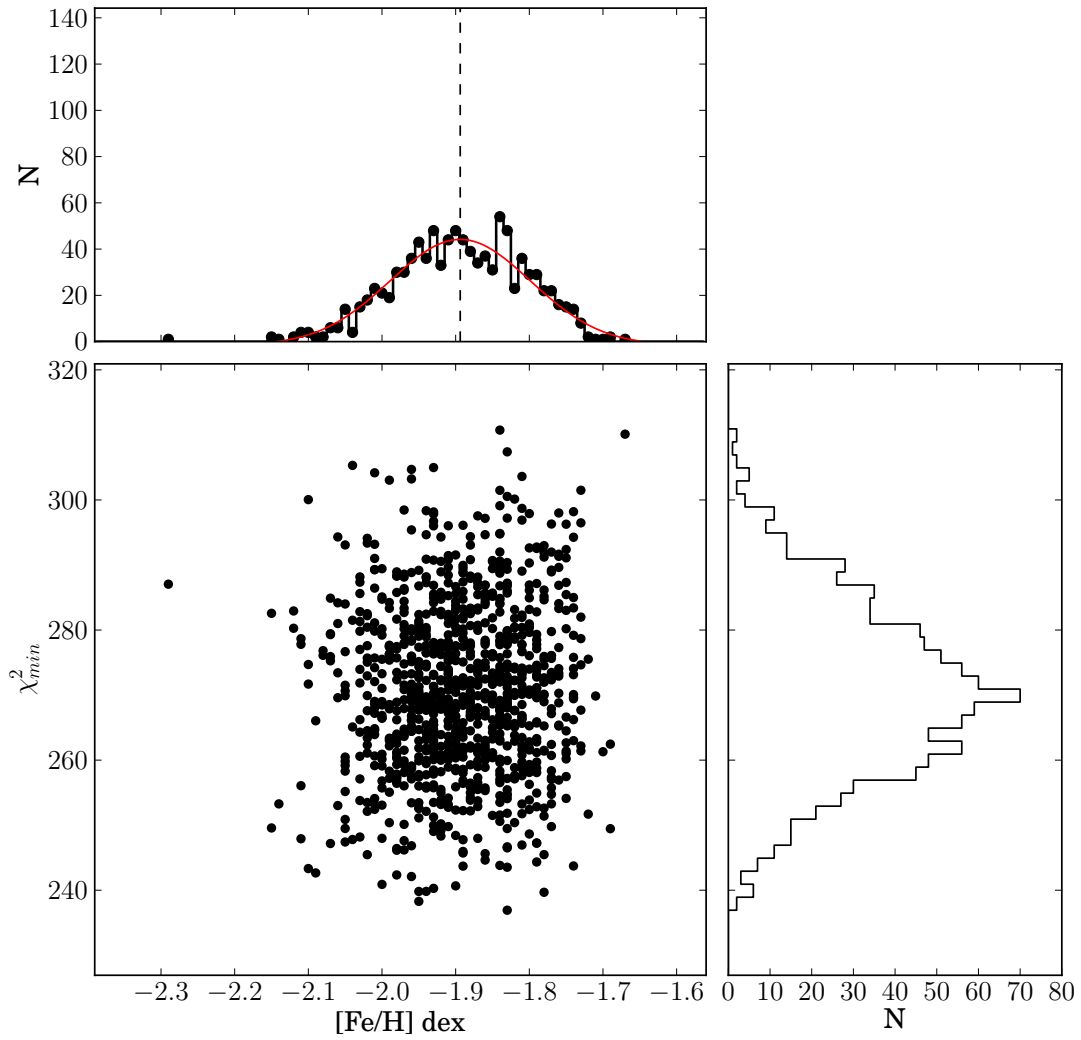


Figure 3.39: Same as in Figure 3.38 but for star S08-292.

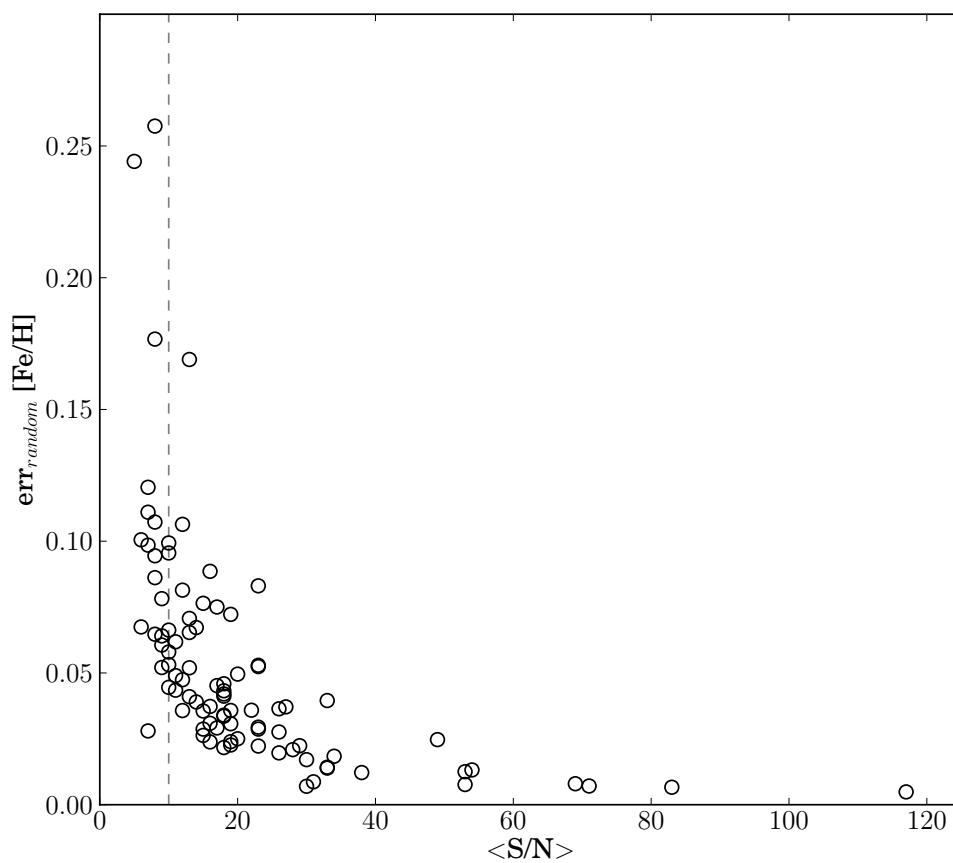


Figure 3.40: Random errors for [Fe/H] in function of average signal-to-noise ratios. The vertical dashed line at  $S/N = 10$  is indicated because from abundances ratios figures we decide not take into account stars having  $S/N \leq 10$ .

### 3.11 Remarks on [Fe/H] determination

#### Deviation in $T_{\text{eff}}$ and $\log g$ between derived values and closest values adopted in the library of synthetic spectra

The maximal differences for  $T_{\text{eff}}$  and  $\log g$  between the stellar parameters and the values adopted selecting spectra in the library are respectively of 25 K and 0.05 as presented in figure 3.41. The differences are smaller than the considered systematic errors.

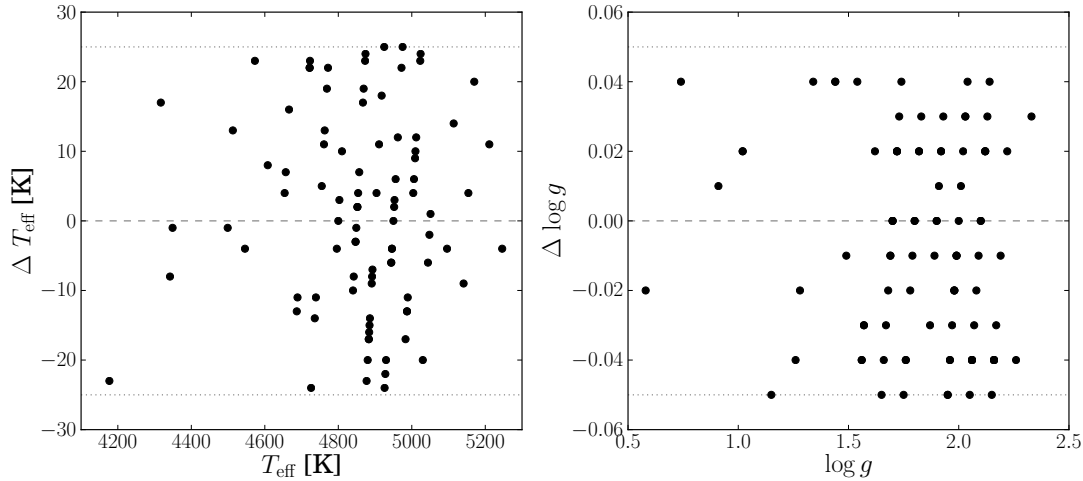


Figure 3.41: The left plot shows the difference between the  $T_{\text{eff}}$  and the closest values adopted in the library. The right plot is similar but concerns  $\log g$ .

#### Insert the final [Fe/H] in the color temperature definition

As the color temperatures depend on metallicities we test the impact of replacing the first guessed [Fe/H] by our final [Fe/H]. We compare then the new derived  $T_{\text{eff}}$ ,  $\log g$  and  $v_{\text{turb}}$  with the previous values. These differences are presented in figure 3.42 in function of metallicity variations. The index  $CaT$  for [Fe/H] in x-axis refers to first guessed metallicities. The black points correspond to stars present in the DART survey having an estimated [Fe/H] from CaT and magenta points to new observed stars with a fixed initial guessed [Fe/H] of -1.9 dex. The  $T_{\text{eff}}$  are more affected by the variation in [Fe/H] than  $\log g$  and  $v_{\text{turb}}$  presenting very small variations. The maximal difference is of the order of 45 K in effective temperatures and the magenta points display the largest variations. The general trend is the following : the more the [Fe/H] variation is large the more the  $T_{\text{eff}}$  variation increases. According to Ramírez & Meléndez (2005) the calibrations of color temperatures vary following three [Fe/H] intervals :  $[\text{Fe}/\text{H}] < -2.5$  dex,  $-2.5 \leq [\text{Fe}/\text{H}] \leq -1.5$  dex and  $[\text{Fe}/\text{H}] \geq -1.5$  dex. If the final [Fe/H] is

sufficiently different from the initial guessed  $[\text{Fe}/\text{H}]$  the star could fall into a different  $[\text{Fe}/\text{H}]$  interval with a different expression of the color temperature explaining the points out of the general trend passing through (0,0).

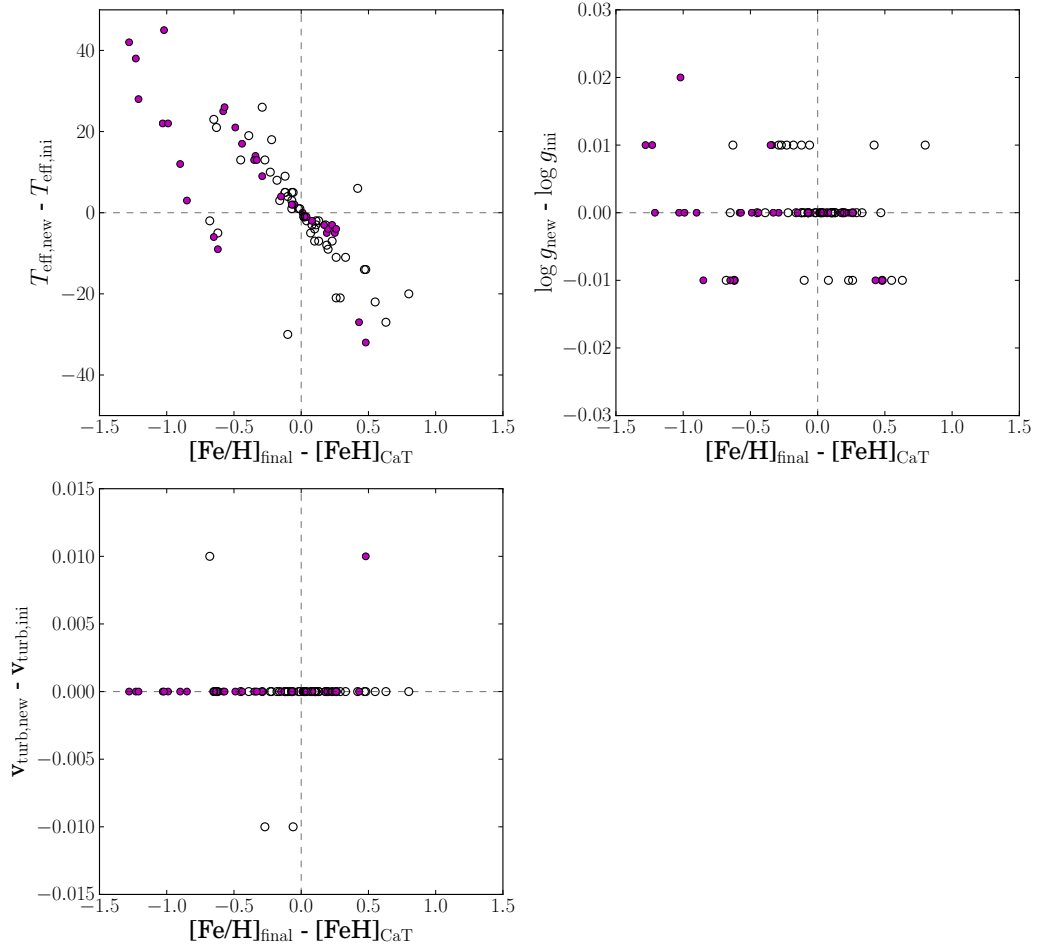


Figure 3.42: Top left : Difference between the new effective temperatures derived using the final  $[\text{Fe}/\text{H}]$  and the initial values derived using the first guessed  $[\text{Fe}/\text{H}]$  (either the CaT value or the mean value of -1.9 dex). The x-axis corresponds to the difference in  $[\text{Fe}/\text{H}]$  between the final values and the initial guessed. The black points correspond to stars present in the DART survey then having an estimated  $[\text{Fe}/\text{H}]$  from CaT and magenta points to all other new stars. Top right : Idem as the previous figure but for surface gravities. Bottom left : idem but for micro-turbulence velocities.



### 3.12 Abundances determination method

Once  $T_{\text{eff}}$ ,  $\log g$ ,  $v_{\text{turb}}$ , and  $[\text{Fe}/\text{H}]$  are determined, we derived the abundances of the rest of the elements ( $[\text{X}/\text{H}]$ ) one by one. For each star we created a set of MOOG synthetic spectra directly at the resolution of the observed spectra with the corresponding stellar parameters and a range of abundances  $[\text{X}/\text{H}]$  for the considered element X. The final abundances are obtained in a two steps process: i) a  $\chi^2$  minimization on a large range of possible abundances, scanning a grid of 6 dex in  $[\text{X}/\text{H}]$  in 0.5 dex steps, which provided a first estimate of the abundance ii) a second set of  $\chi^2$  minimization on a refined grid, 2 dex wide in 0.05 dex steps, around this first estimated  $[\text{X}/\text{H}]$ . Finally the  $\chi^2$  curves are interpolated to reach a step of 0.01 dex on which the final minimization is done to obtain the final abundance  $[\text{X}/\text{H}]$ .

Thanks to the wavelength coverage of our spectra we were able to derive abundances for 10 elements : Mg, Ca, Sc, Ti, Cr, Mn, Co, Ni, Ba, and Eu. A certain number of lines per element are observable in our spectra : 1 for Mg I, 13 for Ca I, 3 for Sc II, 4 for Ti I and Ti II, 3 for Cr I, 4 for Mn I, 1 for Co I, 6 for Ni I, 2 for Ba II and 1 for Eu II. As for  $[\text{Fe}/\text{H}]$  determination, if lines are located in polluted spectrum they are not taken into account in the abundance determination. From the sample of 92 Sextans members, we reject 5 stars (S05-72, S08-321, S08-111, S08-301, S08-293) because not completely located along the red giant branch on the CMD and displaying unexpected abundances. These stars are mentioned as *Non-member (c)* in Table A.1. We end up with a sample of 87 stars. We had another constraint on the line list in order to avoid too faint lines : we kept only lines that have been detected by DAOSPEC and that present an equivalent width (measured by DAOSPEC) larger than 20 mÅ.

Hyperfine structure (HFS) has been taken into account for odd atomic number isotopes : Sc II (Prochaska et al. 2000), Mn I (from Kurucz database<sup>1</sup> same as used in North et al. (2012)), Co I (Prochaska et al. 2000), Ba II (Prochaska et al. 2000), Eu II (Lawler et al. (2001) same as used in Van der Swaelmen et al. (2013)).

The complete line list with wavelengths, excitation potentials, oscillator strengths and  $C_6$  constants is presented in the Table A.6. The hyperfine components are indicated in italic and their corresponding equivalent lines are followed by the text (*equi*). The final abundances are given in Tables A.8, A.9, A.10 and A.11. The used solar abundances from Grevesse & Sauval (1998) are given in the first line of these four tables.

Figures 3.43 and 3.44 present examples of  $\chi^2$  curves for  $[\text{Mg}/\text{H}]$  determination for star S05-47 and for  $[\text{Ba}/\text{H}]$  determination for star S08-250.

Figure 3.45 shows parts of observed spectrum in setup HR10 of three stars S08-6, S08-242 and S05-67 with their best fitted synthetic spectrum. The observed spectra are in black and the synthetic ones in red. The lines used in the abundance determination are indicated next to the corresponding lines. These three stars are ordered in decreasing signal-to-noise ratios :  $S/N = 83$  for S08-6,  $S/N = 38$  for S08-242 and  $S/N = 23$  for S05-67.

<sup>1</sup>available at <http://kurucz.harvard.edu/linelists.html>

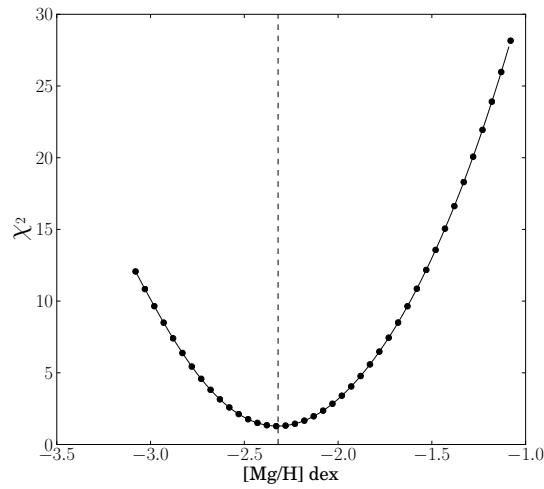


Figure 3.43: Curve of  $\chi^2$  for [Mg/H] determination for star S05-47. The values obtained before interpolation are represented by the black circles. The black solid line connects the interpolated values and the position of the minimum after interpolation is indicated by the vertical dashed line.

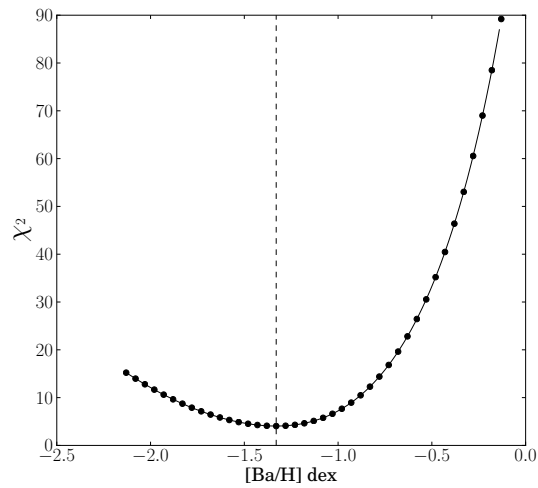
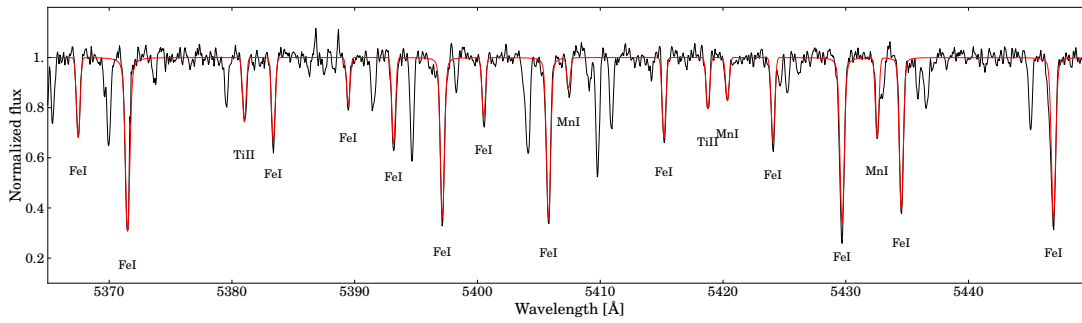
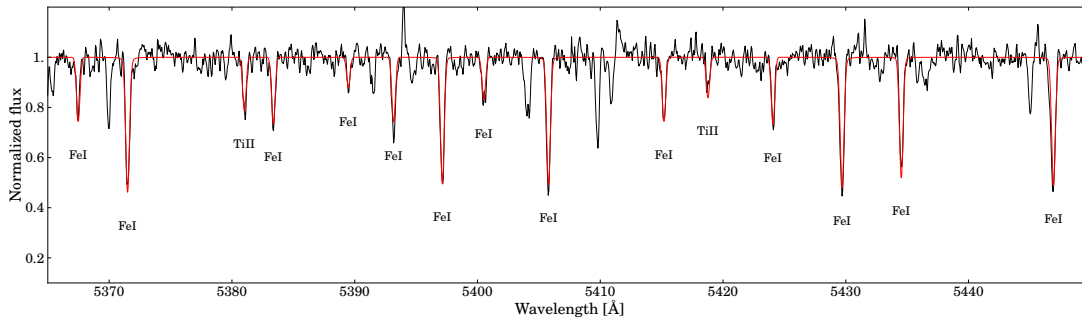


Figure 3.44: Curve of  $\chi^2$  for [Ba/H] determination for star S08-250. The values obtained before interpolation are represented by the black circles. The black solid line connects the interpolated values and the position of the minimum after interpolation is indicated by the vertical dashed line.

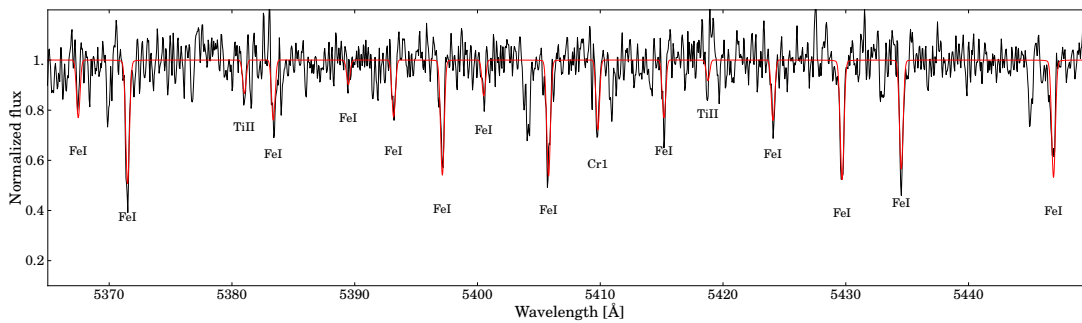
### 3.12. Abundances determination method



(a) Spectrum of star S08-6 ( $S/N = 83$ ) in part of setup HR10 with its best corresponding synthetic spectrum



(b) Spectrum of star S08-242 ( $S/N = 38$ ) in part of setup HR10 with its best corresponding synthetic spectrum



(c) Spectrum of star S05-67 ( $S/N = 23$ ) in part of setup HR10 with its best corresponding synthetic spectrum

Figure 3.45: Parts of observed spectrum in setup HR10 of 3 stars S08-6 in a), S08-242 in b) and S05-67 in c) with their best fitted synthetic spectrum. The observed spectra are in black and the synthetic ones in red. The lines used in abundance determination are indicated next to the corresponding wavelengths.

### 3.13 Error budget on [X/H]

As for the error budget on [Fe/H], the methods used here are very similar.

#### 3.13.1 Systematic errors

The idea is the same as previously : we derive [X/H] from two set of stellar parameters corresponding to a variation of  $\pm 100$  K on effective temperatures. Comparing the obtained [X/H] with the initial one the systematic error is defined as follows :

$$\text{err}_{\text{sys}} = \frac{([\text{X}/\text{H}]_{T+100} - [\text{X}/\text{H}]_T) + ([\text{X}/\text{H}]_T - [\text{X}/\text{H}]_{T-100})}{2} \quad (3.11)$$

The systematic errors for the 10 elements are presented in figure 3.46 in function of the effective temperatures. They are ranging from maximum of 0.05 dex for Mg, Sc, Ti2 and Eu to around 0.2 dex for Cr and Mn at minimum. Other elements display in between systematic errors.

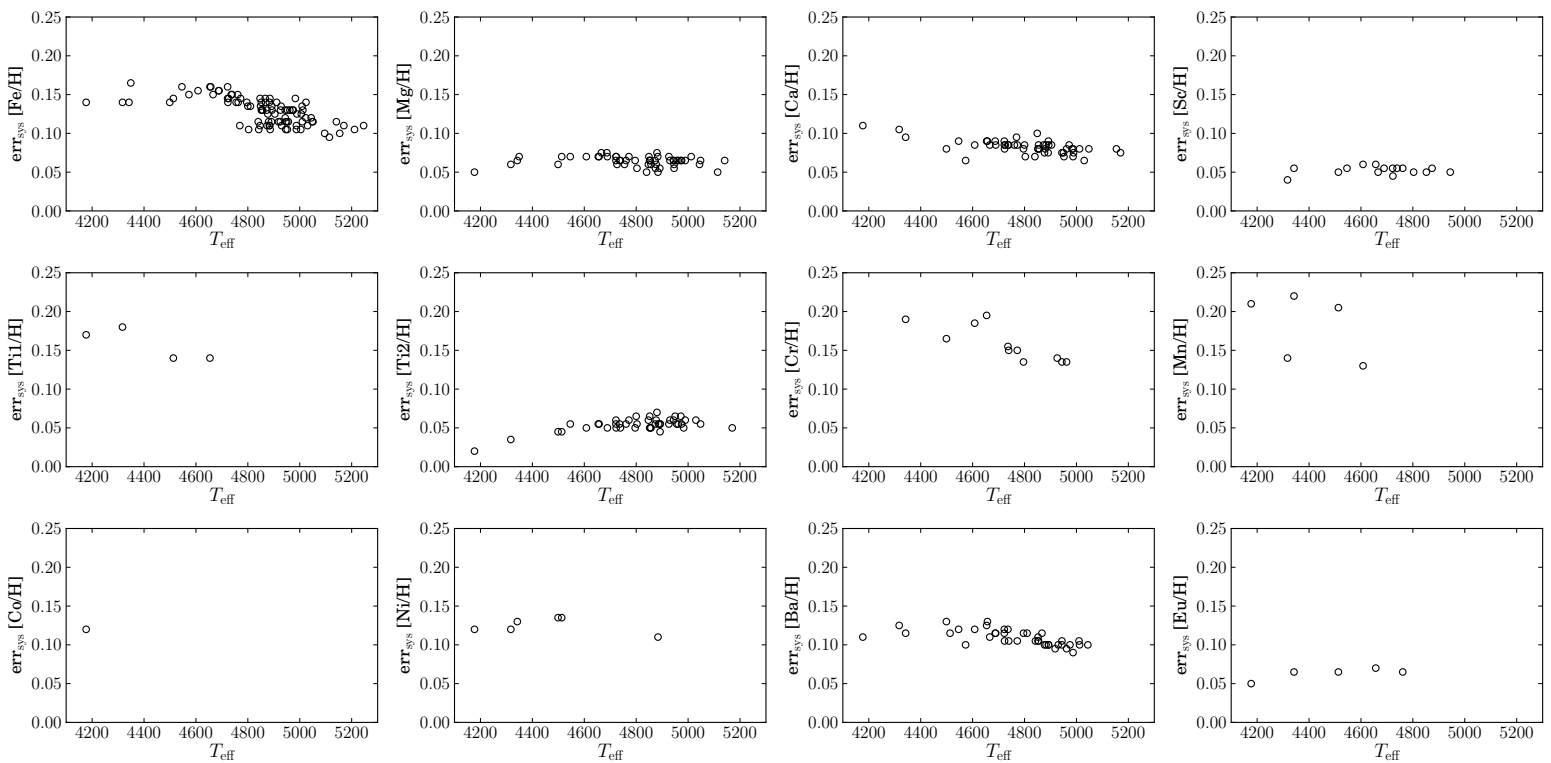


Figure 3.46: Systematic errors on  $[X/H]$  due to a variation of  $\pm 100$  K of the effective temperatures are presented in function of the initial effective temperatures.

### 3.13.2 Random errors

The process is very close to the calculation of random errors on  $[\text{Fe}/\text{H}]$ . However two differences remain : i) the spectra created with MOOG display the abundances of the 10 elements together and ii) the abundance interval proposed is 2 dex wide with a step of 0.05 around the expected value.

Two examples of distribution of abundances for  $[\text{Ca}/\text{H}]$  and  $[\text{Ti}/\text{H}]$  are given in figures 3.47 and 3.48 for star S08-38.

The random errors obtained for the  $[\text{X}/\text{H}]$  concerning all elements are presented in figure 3.49 in function of the signal-to-noise ratios.

Based on the random errors we decided to keep only stars having  $S/N \geq 10$  because smaller signal-to-noise values do not allow reliable abundances.

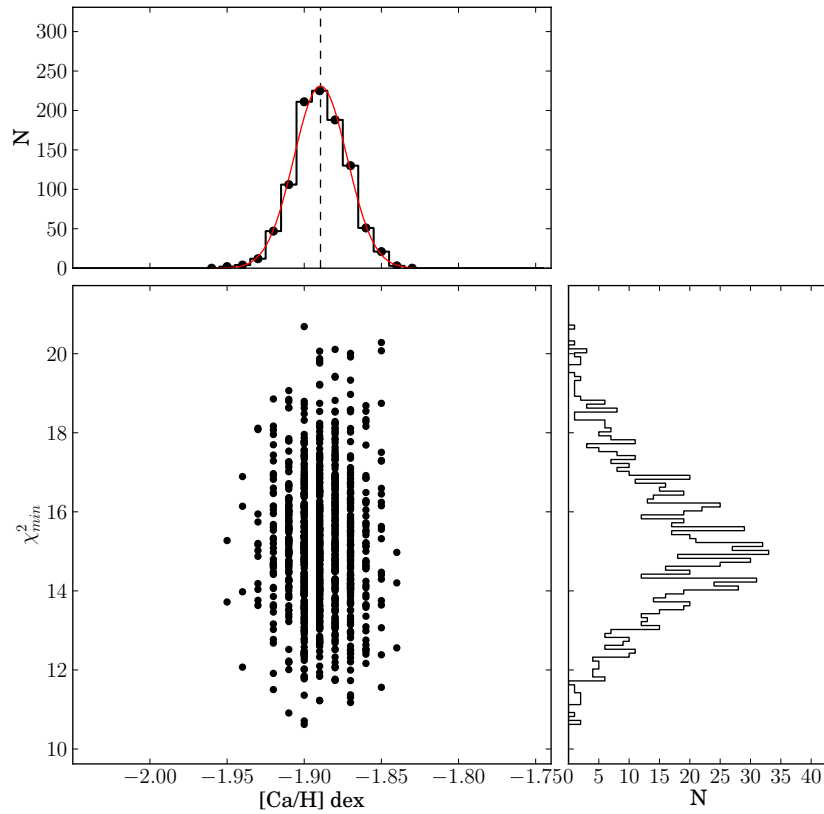


Figure 3.47: Top panel : the black solid line is the re-binned histogram of the distribution of 1000 final  $[\text{Fe}/\text{H}]$  obtained by Monte Carlo simulated spectra for star S08-38. The red solid line is the best fitted gaussian function used to determine the random error corresponding to the standard deviation. Bottom left : The points represents the 1000 couples of  $(\chi_{min}^2, [\text{Ca}/\text{H}])$ . Bottom right : the solid black line shows the histogram of the  $\chi_{min}^2$  values.

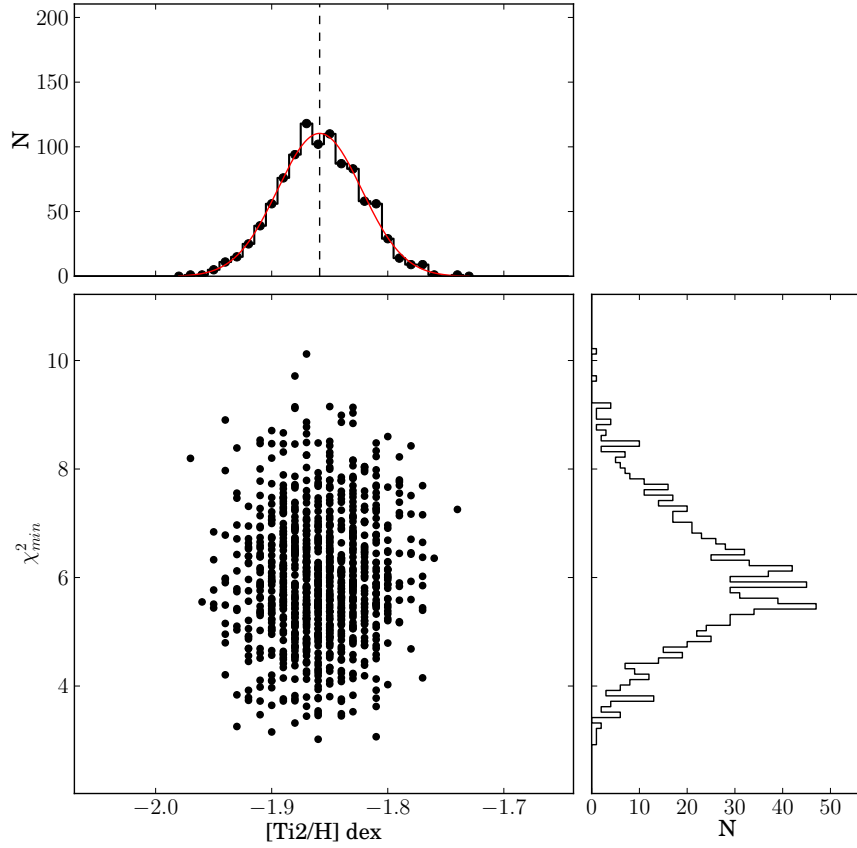


Figure 3.48: Top panel : the black solid line is the re-binned histogram of the distribution of 1000 final [Fe/H] obtained by Monte Carlo simulated spectra for star S08-38. The red solid line is the best fitted gaussian function used to determine the random error corresponding to the standard deviation. Bottom left : The points represents the 1000 couples of  $(\chi_{min}^2, [\text{Ti2}/\text{H}])$ . Bottom right : the solid black line shows the histogram of the  $\chi_{min}^2$  values.

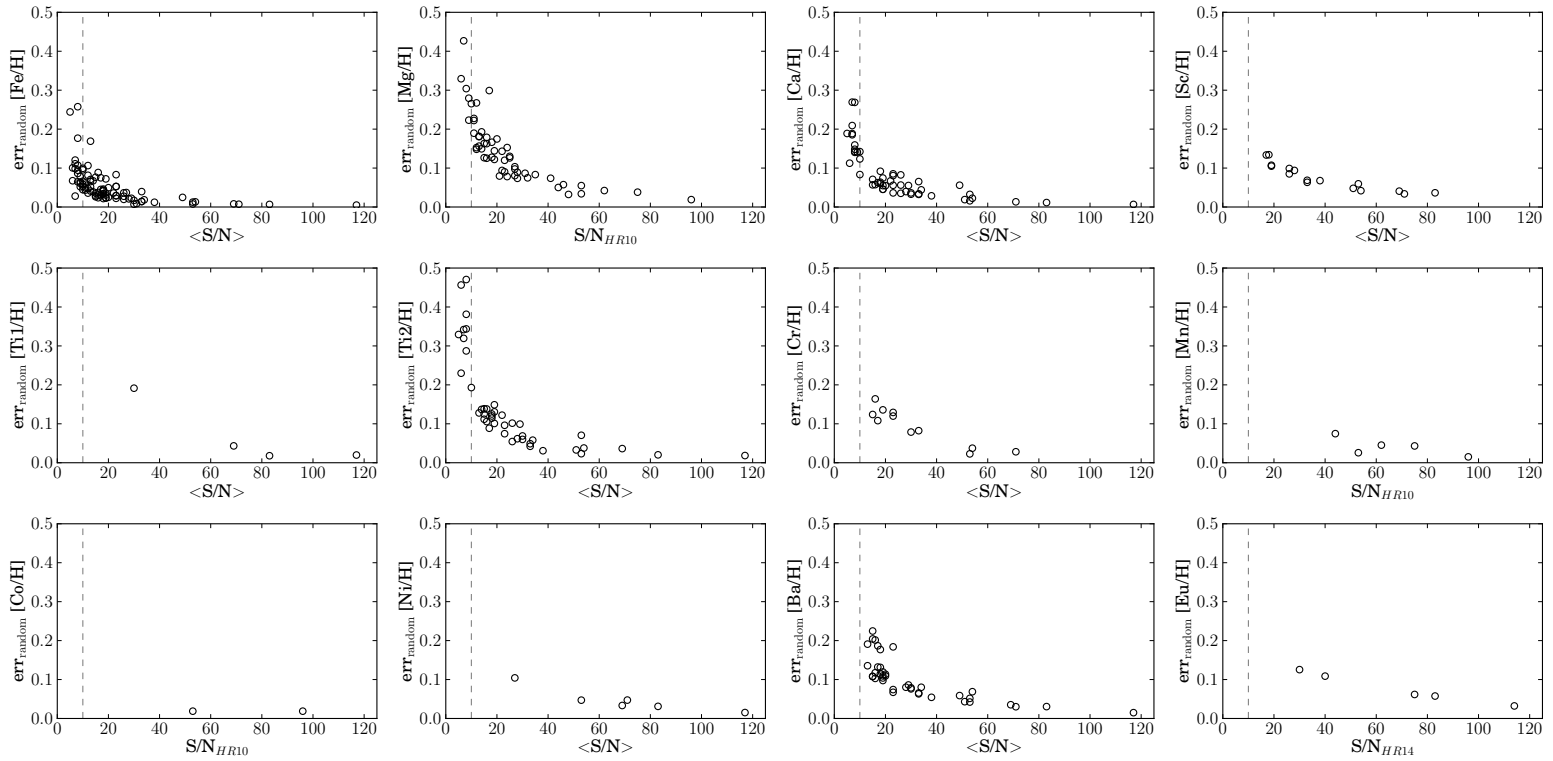


Figure 3.49: Random errors for  $[X/H]$  in function of signal-to-noise ratios. The vertical dashed line at  $S/N = 10$  is shown because we decide not to take into account stars having  $S/N \leq 10$ .



## 3.14 Analysis of the results

### 3.14.1 S08-3 as a benchmark star

Star S08-3 is the brightest star of our sample. As such, its abundances were derived from the individual line equivalent widths by Pascale Jablonka as 10 other high signal-to-noise ratios stars of our sample. S08-3 had also been observed with the High Resolution Echelle Spectrometer (HIRES) at the Keck I telescope at a resolution of  $R \sim 34000$  and analyzed by Shetrone et al. (2001) using also the classical method.

There are 10 elements in common between the three analysis of this star and figure 3.50 presents their comparison. The blue stars are from Shetrone et al. (2001), the magenta squares from Pascale Jablonka and the green circles from this work. Some abundances are missing : Sc II was determined by Pascale Jablonka only, Shetrone et al. (2001) did not present abundances of Ti I and Eu II and we were not able to determine reliable abundance of Cr I. Comparing the differences between the three studies we obtain a minimum of 0.01 dex, a maximum of 0.3 dex and a median of 0.08 dex. Globally the three studies agree well together within the error bars except for chromium.

Figure 3.51 show the best fit between the observed spectrum over the three setups of star S08-3 and the synthetic spectrum in red displaying all the final abundances we obtained. All the lines used in abundances determination are indicated with the name of the corresponding elements.

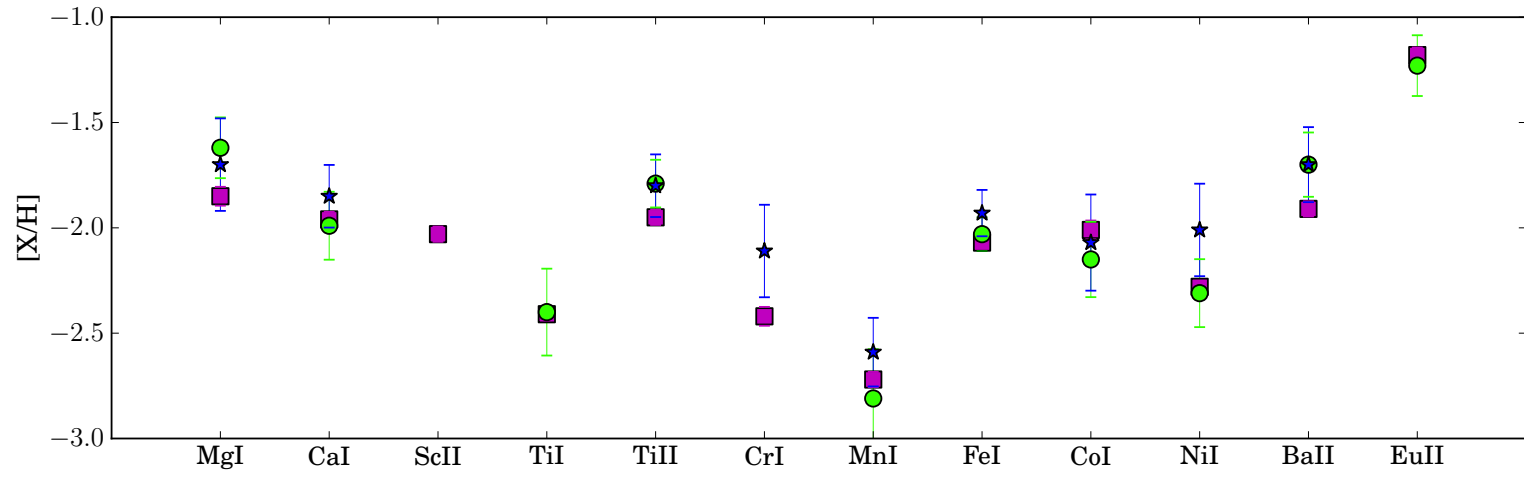


Figure 3.50: Abundance distribution of the star S08-3. The green circles correspond to this study, the blue stars come from Shetrone et al. (2001) and the magenta squares are from Pascale Jablonka.

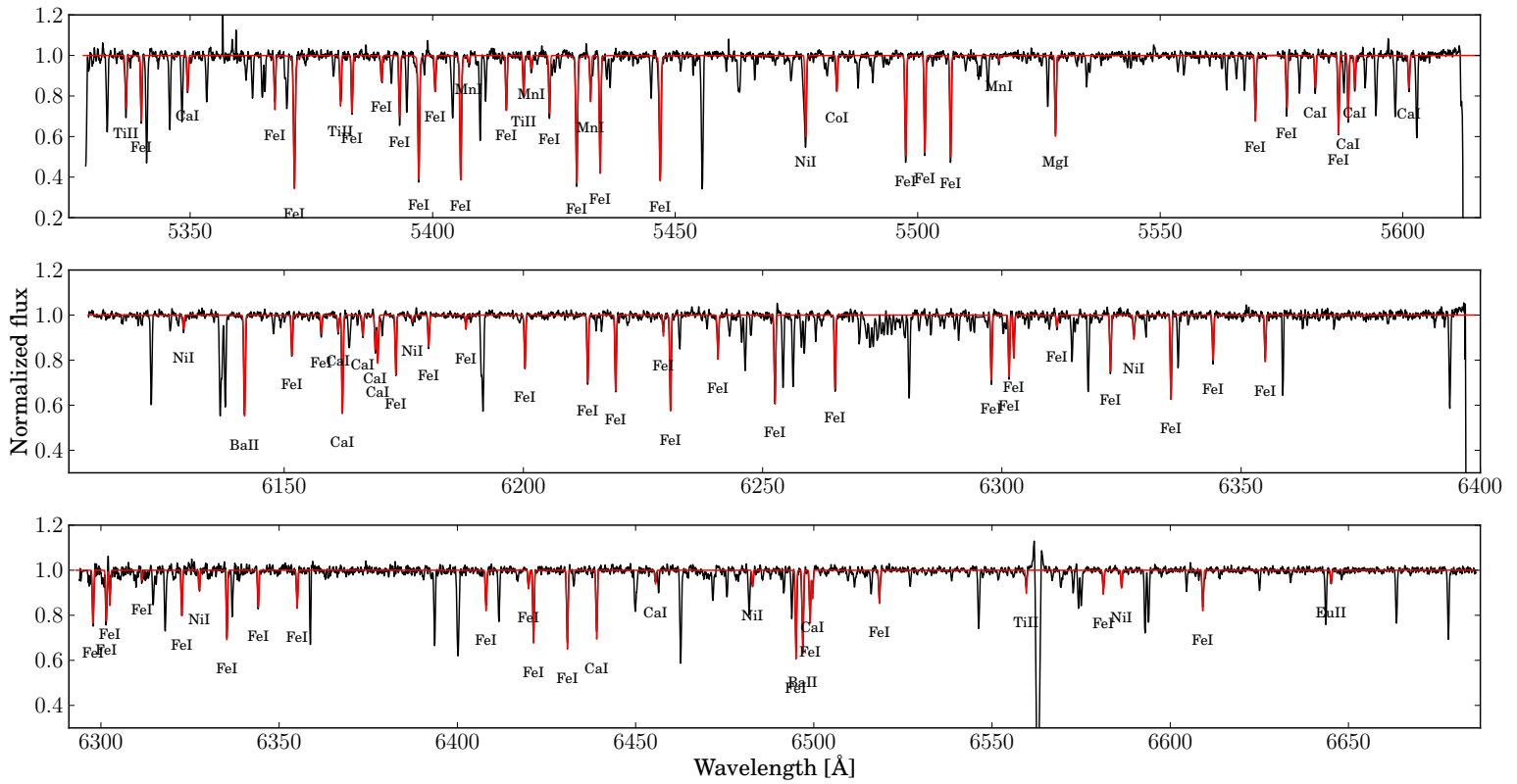


Figure 3.51: The complete spectrum of star S08-3 over the three setups is presented in black and in red is over-plotted its best fitted synthetic spectrum. All the lines used in abundances determination are indicated with the name of the corresponding elements.

### 3.14.2 Sub-sample of brightest stars: comparison with results from classical method

A sub-sample of 11 bright stars having high signal-to-noise ratios were analyzed by Pascale Jablonka following the classical method. We describe below the classical method to understand in what way our results can be compared. The absorption lines were selected from a line list based on the list of Letarte et al. (2010), supplemented with lines from Cayrel et al. (2004). The equivalent widths were measured in an automated way using DAOSPEC. The MARCS spherical atmospheric models used were the same as for the synthesis method. The atmospheric parameters  $T_{\text{eff}}$  and  $\log g$  were also derived from the photometry. Only  $v_{\text{turb}}$  was tuned by requesting a null slope (within the fit uncertainties resulting from the measurement errors) in the relation between the abundances and equivalent widths of the individual Fe I lines. The abundance analysis calculations were performed using the LTE code CALRAI first developed by Spite (1967) (see also Cayrel et al. (1991) for the atomic part), and continuously updated over the years. CALRAI was used in all previous DART publications (Letarte et al. 2010; Tafelmeyer et al. 2010).

Tables A.12 and A.13 present the stellar parameters and the final abundances for these 11 stars derived by the classical method.

Figure 3.52 summarizes the comparison between the two analysis by comparing the iron abundances. The circles are size-coded with their signal-to-noise ratios. The dashed lines are placed at  $\pm 0.1$  dex of the line  $x = y$ . The agreement is good with a mean difference of 0.1 dex and a standard deviation of 0.09 dex. The index EQW refers to classical method and SYNTH to synthesis method. We tried to understand in more details the origins of the differences between the two analysis.

**Outlier star S05-60** The outlier star is S05-60 for which the difference in micro-turbulence velocities is maximal (0.3 km/s). In addition its photometric temperature has been modified during the [Fe/H] determination by classical method. This star displays also the smallest signal-to-noise ratio of the sub-sample. If we do not take into account this outlier star we obtain a better agreement with a mean difference of 0.08 dex and a standard deviation of 0.06 dex.

**The two brightest stars S08-3 and S08-6** The brightest star S08-3 gives very close results :  $[\text{Fe}/\text{H}]_{\text{EQW}} = -2.07$  dex and  $[\text{Fe}/\text{H}]_{\text{SYNTH}} = -2.03$  dex.

However the second bright star S08-6 shows a difference of 0.1 dex two times bigger than for S08-3 :  $[\text{Fe}/\text{H}]_{\text{EQW}} = -1.5$  dex and  $[\text{Fe}/\text{H}]_{\text{SYNTH}} = -1.6$  dex. This difference can be reduced to 0.03 dex taking in synthesis method exactly the same Fe I line list as used in the classical method. For S08-6 we obtain this time :  $[\text{Fe}/\text{H}] = -1.53$  dex. This example demonstrates that

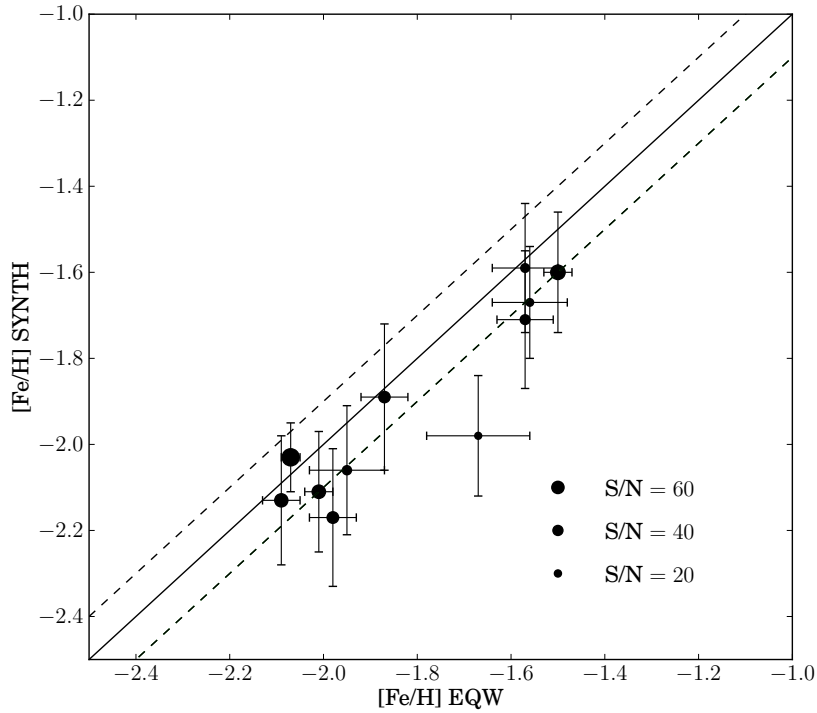
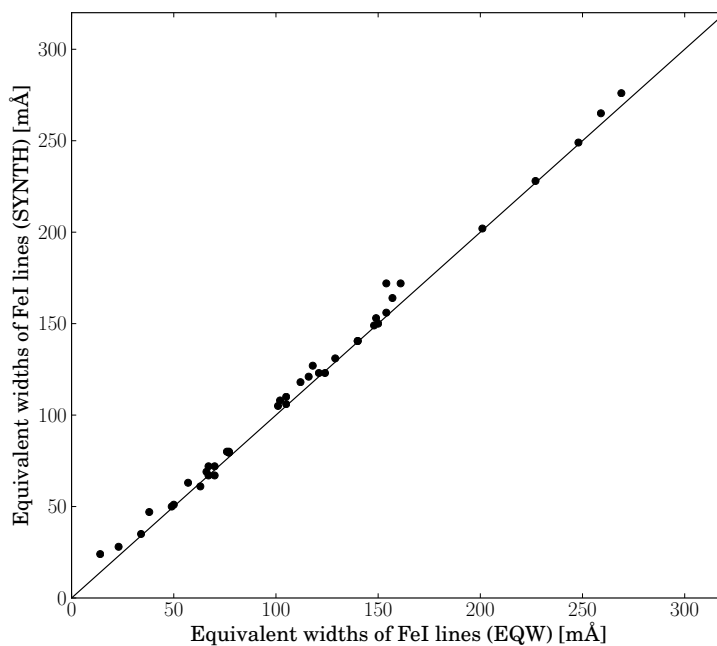


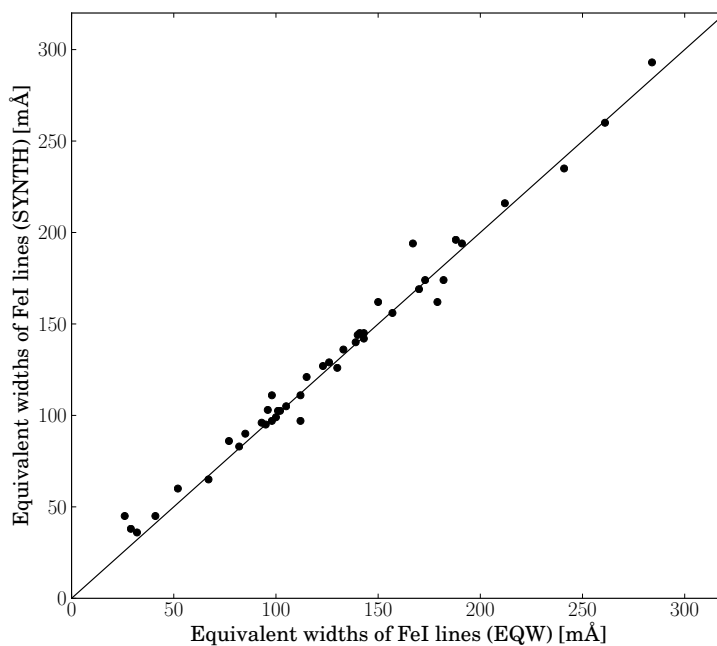
Figure 3.52: Comparison with  $[\text{Fe}/\text{H}]$  obtained from classical method (EQW) for a sub-sample of 11 brightest stars. The circles are size-coded with their signal-to-noise ratios. The dashed lines are placed at  $\pm 0.1$  dex of the line  $x = y$ .

the line list has also an impact on the final  $[\text{Fe}/\text{H}]$ .

In order to test the reliability of the continuum placement in the two methods we compared the Fe I equivalent widths for S08-6 and S08-3. We used DAOSPEC to derive equivalent widths on our normalized spectra. The results presented in the two plots in figure 3.53 show a clear agreement between the equivalent widths for these two stars.



(a) Equivalent widths of iron lines for star S08-3



(b) Equivalent widths of iron lines for star S08-6

Figure 3.53: Comparison of iron equivalent widths for stars S08-3 in a) and S08-6 in b) derived from classical and synthesis methods

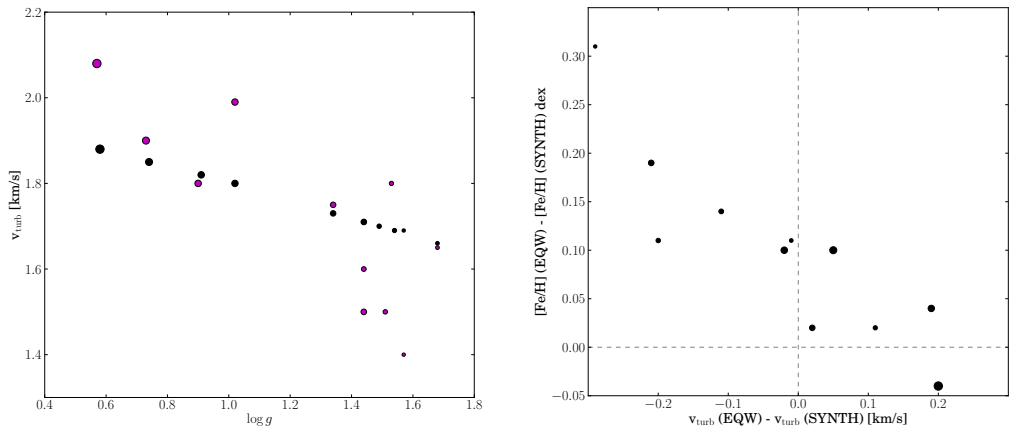
**Differences in micro-turbulence velocities** The micro-turbulence velocities are defined in a different way : in classical method they are tuned requesting a zero slope comparing Fe I abundances and equivalent widths, in synthesis they obey to an empirical relation depending on the surface gravities. The first plot of the figure 3.54 shows the relation between  $v_{\text{turb}}$  and  $\log g$  for the two analysis. The black points from the synthesis range from 1.7 to 1.9 km/s while magenta points from the classical method display a larger interval in  $v_{\text{turb}}$ . The stars for which the differences in  $v_{\text{turb}}$  is maximal display either the lowest  $v_{\text{turb}}$  or the highest  $v_{\text{turb}}$  from classical analysis. This is visible in last plot of figure 3.54. The second plot in the same figure presents the difference in  $[\text{Fe}/\text{H}]$  in function of the difference in  $v_{\text{turb}}$ . It shows that a difference in  $v_{\text{turb}}$  bigger than 0.1 km/s could imply a  $\Delta[\text{Fe}/\text{H}] \geq 0.1$  dex. Then for stars presenting a large difference in  $v_{\text{turb}}$  their variation in  $[\text{Fe}/\text{H}]$  could be induced by different micro-turbulence velocities.

Following this idea we select stars having  $v_{\text{turb}}$  difference smaller than 0.1 km/s and test if the  $[\text{Fe}/\text{H}]$  difference could be due to variation in  $T_{\text{eff}}$  or  $\log g$ . We previously said that they are the same for the two analysis, however in synthesis we take their closest values in the synthetic library then a difference exists. Figure 3.55 presents in first plot the 6 stars having  $v_{\text{turb}}$  difference smaller than 0.1 km/s. The two following plots show their  $[\text{Fe}/\text{H}]$  differences in function of the  $T_{\text{eff}}$  and  $\log g$  variations. Given these plots there is no clear trend linked with differences in  $T_{\text{eff}}$  or  $\log g$  for these 6 stars.

To sum up the remaining differences in  $[\text{Fe}/\text{H}]$  could come from a different line list and variation on micro-turbulence velocities. We show that there is no significant difference for the placement of the continuum for S08-3 and S08-6, but this has not been tested on the other stars. Maybe it could also be another source of metallicity variation at smaller signal-to-noise ratios.

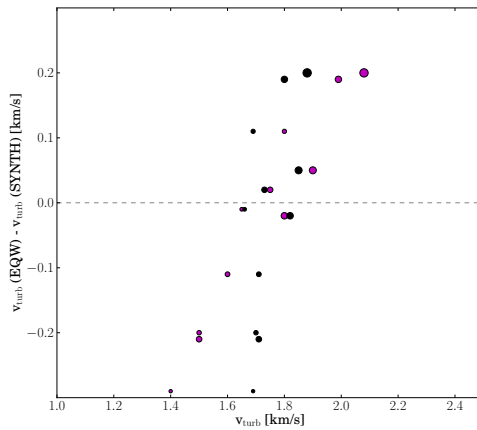
Figure 3.56 presents similarly to figure 3.52 the comparison between the two analysis methods for the 10 elemental abundances. The same results are expressed by histograms of the difference between abundances in figure 3.57. Except for barium which presents relatively dispersed abundances the other elements present close values. The histograms are generally centered around 0 except cases as for europium presenting a very few number of stars.

The comparison with the classical results for this sub-sample helped to the validation of our synthesis procedure.



(a) Relation between micro-turbulence velocities and surface gravities

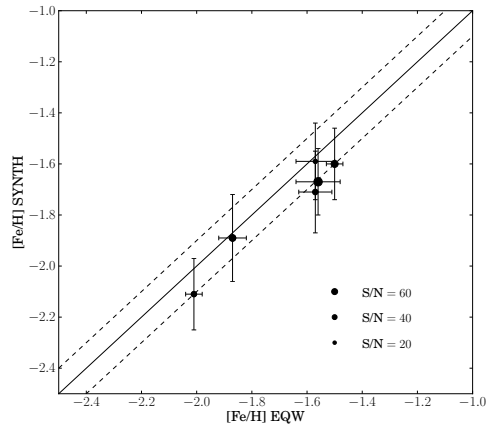
(b) Differences between metallicities obtained by 2 methods in function of the differences of their micro-turbulence velocities



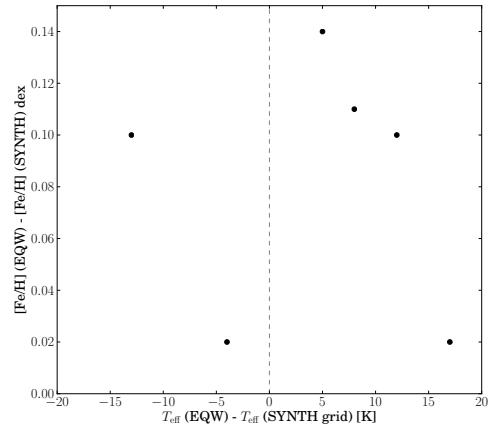
(c) Differences between micro-turbulence velocities obtained by 2 methods in function of the micro-turbulence velocities derived by EQW method.

Figure 3.54: Relations linked with the variation of micro-turbulence velocities for the subsample of 11 brightest stars.

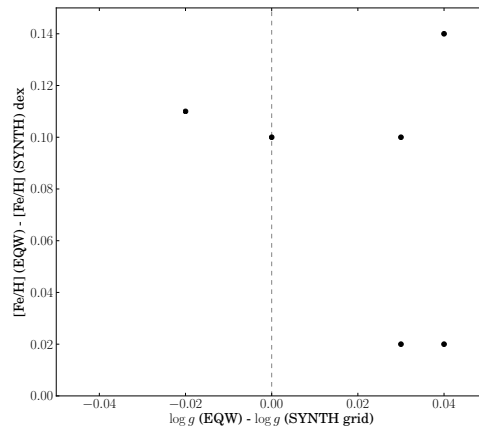




(a) Comparison with  $[\text{Fe}/\text{H}]$  obtained from EQW method for stars presenting a  $\Delta v_{\text{turb}} < 0.1$



(b) Differences between metallicities obtained by 2 methods in function of the differences of their effective temperatures



(c) Differences between metallicities obtained by 2 methods in function of the differences of their surface gravities

Figure 3.55: Dependence between variations of  $[\text{Fe}/\text{H}]$  with differences of  $T_{\text{eff}}$  and  $\log g$  for stars presenting a  $\Delta v_{\text{turb}} < 0.1$  among the sub-sample of 11 brightest stars

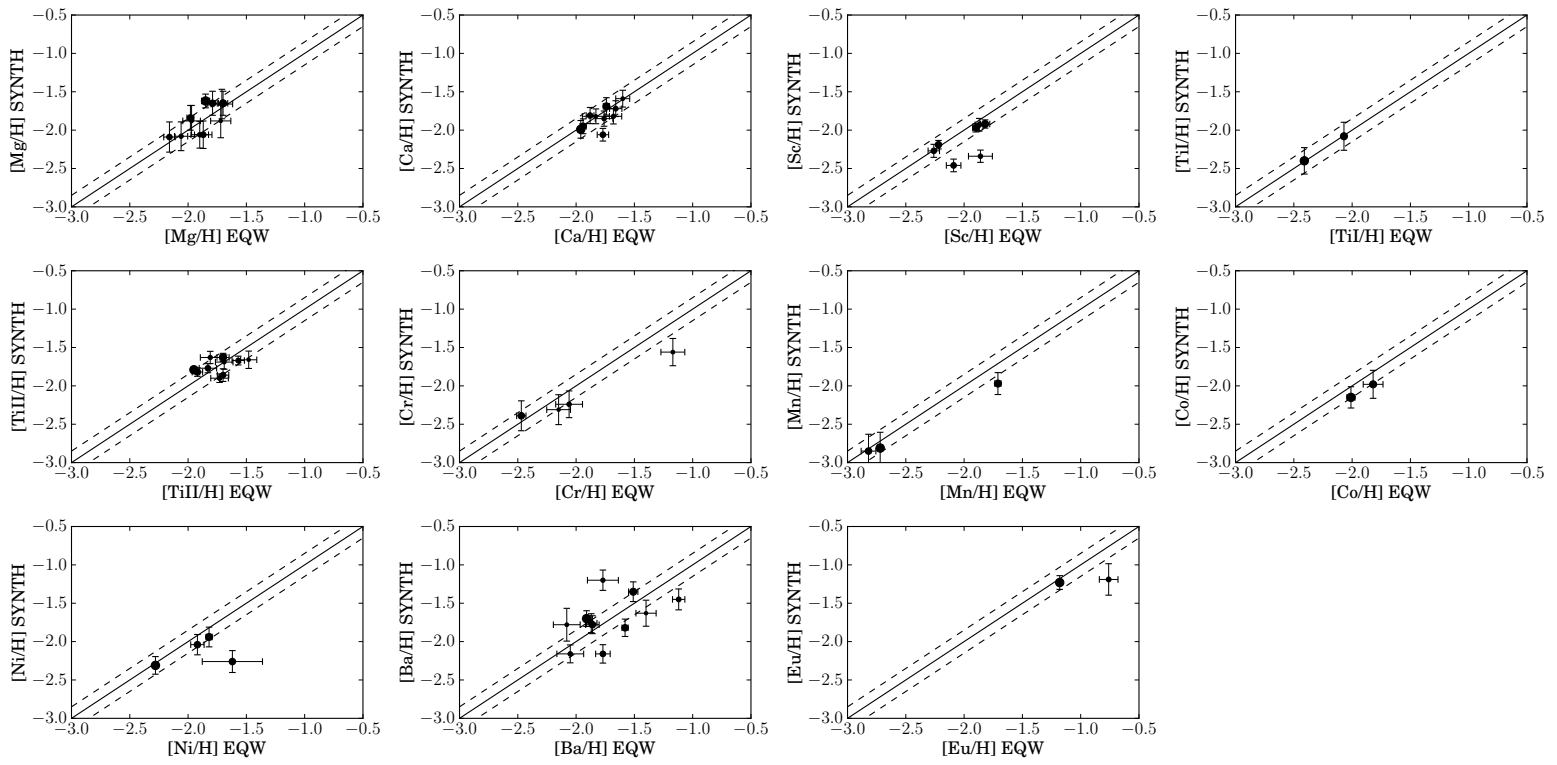


Figure 3.56: Comparison between abundances  $[X/H]$  derived by EQW and synthesis method for a sample of highest S/N stars.

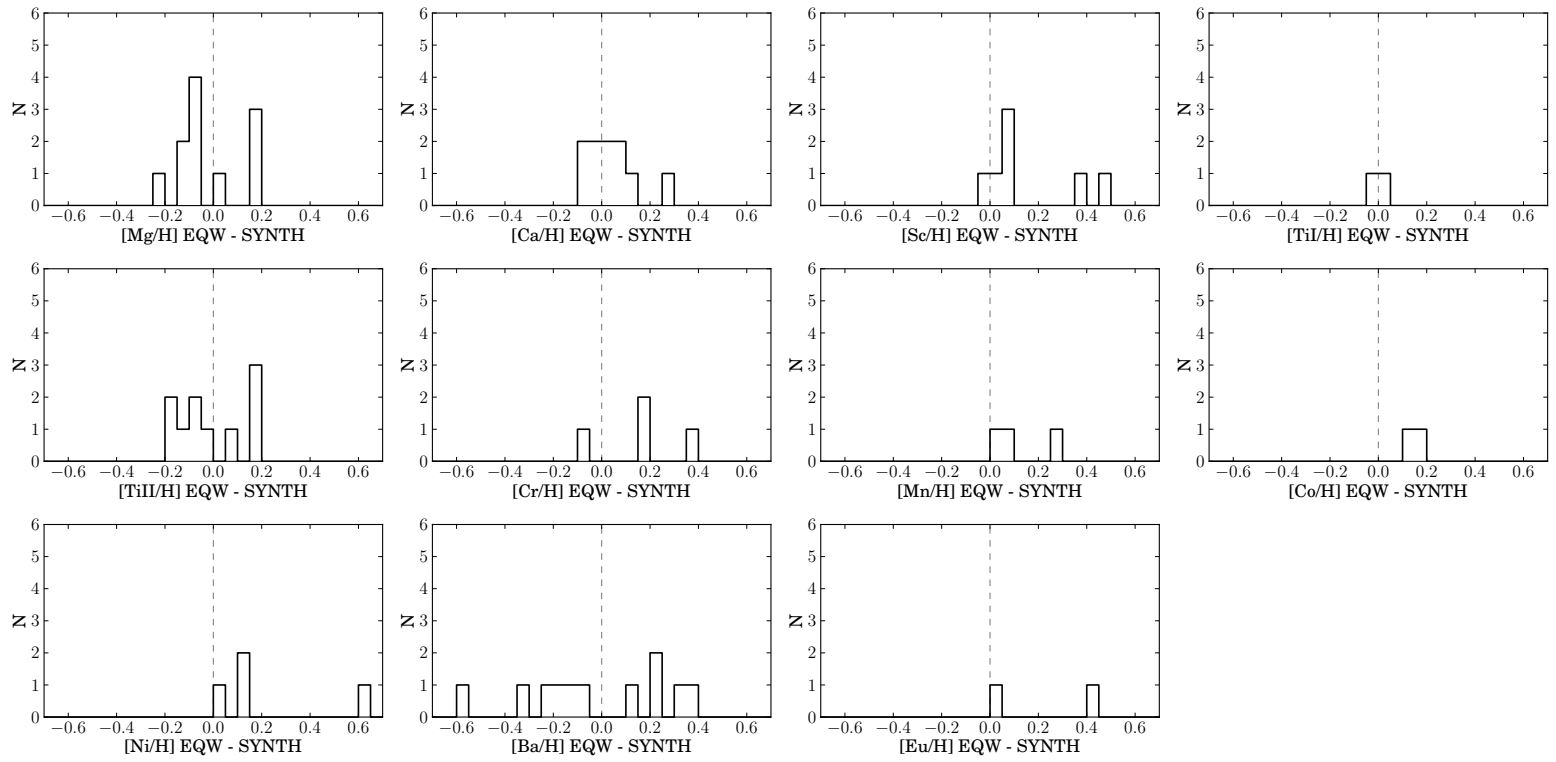


Figure 3.57: Histogram of differences between abundances  $[X/H]$  derived by EQW and synthesis method for a sample of highest S/N stars.

### 3.14.3 Metallicity distribution function and comparison with Ca II Triplet survey

The metallicity distribution function of Sextans is presented in figure 3.58. The blue line corresponds to the members of the intermediate resolution DART CaT survey (Battaglia et al. 2011) and the green line is the metallicity distribution function of our members. Our distribution peaks around -1.8 dex and is almost completely included in the CaT distribution showing a good agreement between the two samples. If we keep only the stars previously observed in the CaT survey, we obtain the filled green area which seems to peak at the same [Fe/H] as the CaT distribution. Our distribution is in average more metal-rich than the CaT sample. The explanation resides in the location of the stars (see Figure 3.20) and the existence of a radial gradient in Sextans (Lee et al. 2009; Battaglia et al. 2011). Our field is small and centrally-concentrated (diameter of 25 arcmin), while the DART survey is composed of 16 fields of same diameter located between the center and the tidal radius of Sextans (160 arcmin Irwin & Hatzidimitriou (1995)).

Considering the 34 common stars between the two samples, we compare their metallicities in figure 3.59. The points are size-coded in function of the signal-to-noise ratios. The mean of the difference is well centered with a value of -0.006 dex. However the standard dispersion of 0.28 dex is large. The agreement within errors bars is very good except for 5 outliers indicated in red : S08-292, S08-75, S05-67, S08-246 and S08-59 (listed according to x-axis). We tried to explain these discrepancies.

S08-292 with a signal-to-noise of 10 did not have a very well defined  $\chi^2$  curve. Spectra of star S08-75 have been polluted by simultaneous calibration fibers in HR10 and HR13 therefore only 9 instead of 50 lines of Fe I were used to derive [Fe/H]. After inspecting continua of S05-67 we could suspect a slight under-estimation of the placement of the continuum in HR10 which would over-estimate the metallicity as observed here. S08-59 is suspected to be an horizontal branch star according to its location on the color-magnitude diagram. Without the 5 outliers the standard deviation is almost divided by 2 with a value of 0.14 dex and the mean delta stays very close to zero with a value of 0.006 dex.

For the rest of the analysis, we did not take into account these 5 outliers.

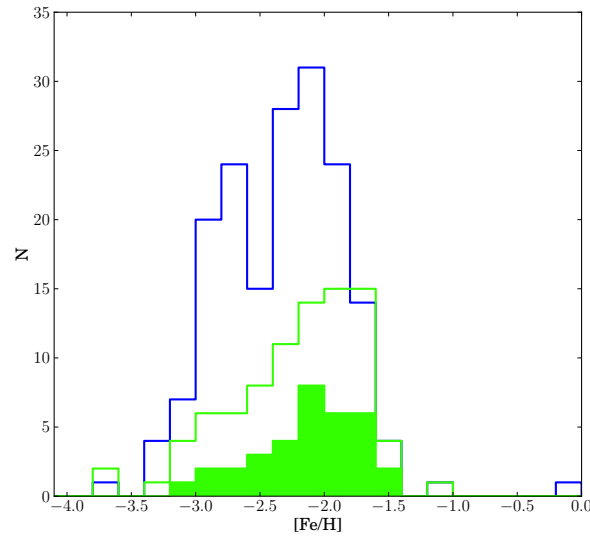


Figure 3.58: Metallicity Distribution Function of the Sextans stars. Following the same color code as in Figures 3.20 and 3.21, the blue solid line corresponds to the probable members of the Intermediate Resolution DART CaT survey (Battaglia et al. 2011) and the green solid line represent our members. The filled green area corresponds to the sub-sample of our members previously studied by the Intermediate Resolution DART CaT survey and also defined as members by them.

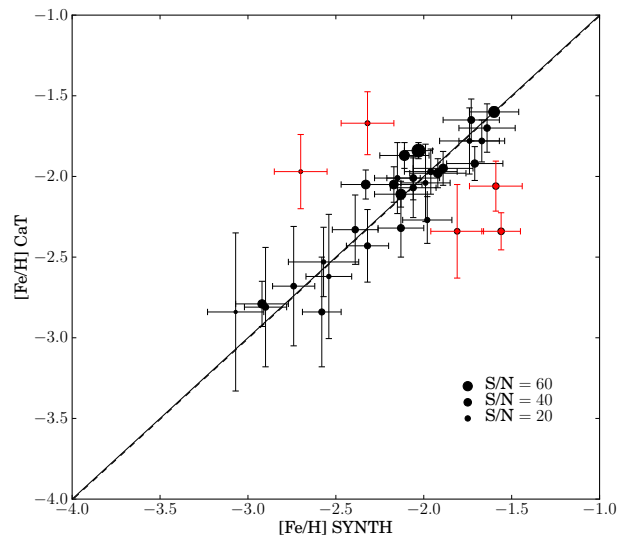


Figure 3.59: Comparison of  $[\text{Fe}/\text{H}]$  between our values (SYNTH) and values derived from CaT (EQW). Five outliers are indicated in red and all the symbols are size-coded with signal-to-noise ratios.

### 3.14.4 Alpha-elements

#### Sextans

Three alpha-elements have been studied in our sample : Mg I (1 line), Ca I (13 lines), Ti I (4 lines) and Ti II (4 lines).

**[Ti I/Fe] versus [Ti II/Fe]** The Ti I lines are very faint and [Ti I/Fe] abundances are derived only in 4 stars. We compared the ratios of [Ti I/Fe] with [Ti II/Fe] for these 4 stars presenting the highest S/N. As S05-47 has very large error bar in [Ti I/Fe] and only one line used, we consider it as poorly reliable. Taking into account only the 3 other stars (S08-3, S08-6 and S08-38) : [Ti I/Fe] is always smaller than [Ti II/Fe] with a mean difference of 0.49 dex. It would have been interesting to measure [Fe II/H] in order to derive [Ti II/Fe II] to compare with [Ti I/Fe] and determine the ionization balance. Unfortunately too few lines of Fe II are observable in our wavelength coverage.

Similarly, Letarte et al. (2010) show in Fornax stars a clear offset of [Ti I/Fe] versus [Ti II/Fe] with a mean difference of 0.4 dex presenting always lower values for [Ti I/Fe]. They propose that this difference could be due to : i) significant NLTE effects (Ti I lines are more sensitive to departure from ionization equilibrium due to their lower excitation potential in comparison with Ti II lines), ii) bias in effective temperature shifting ionization equilibrium in the same way. More recently, Lemasle et al. (2012) observed also for Carina stars systematically lower values for [Ti I/Fe] than for [Ti II/Fe]. The same arguments as in Letarte et al. (2010) are given. Despite the small number of stars in our sample having both [Ti I/Fe] and [Ti II/Fe], our data present a similar discrepancies as observed in Fornax and Carina stars. We could then invoke the same explanation for our results. As the faint Ti I lines can be observed only in a very few number of stars and to ensure homogeneity we decided to keep only the abundances of Ti II lines in the abundance ratios as generally done in other dwarfs.

**Distribution of  $[\alpha/\text{Fe}]$  in function of  $[\text{Fe}/\text{H}]$**  The distribution of  $[\alpha/\text{Fe}]$  in function of  $[\text{Fe}/\text{H}]$  are presented in Figure 3.60 for Sextans and the Milky Way stars. The grey circles present the MW stars from Venn et al. (2004), Cayrel et al. (2004), François et al. (2007), Gratton et al. (2003), Cohen et al. (2006), Cohen et al. (2008), Cohen et al. (2013), Honda et al. (2004), Reddy et al. (2006), Yong et al. (2013), Lai et al. (2007), Spite et al. (2005), Aoki et al. (2005), Aoki et al. (2007), Barklem et al. (2005), Ishigaki et al. (2013). All the green symbols correspond to Sextans stars : circles are stars from this study, squares from Shetrone et al. (2003) but re-analysed by Pascale Jablonka using the classical method, stars from Aoki et al. (2009), down triangles from Kirby et al. (2010), right triangles from Tafelmeyer et al. (2010) and diamond from Honda et al. (2011)). All the Sextans results plotted in the abundance ratios come from high resolution

spectroscopy except stars from Kirby et al. (2010). Therefore we kept only stars from Kirby et al. (2010) having an error on  $[\text{Fe}/\text{H}] \leq 0.12$  dex to assure good quality data. Concerning star S15-19 analyzed by both Aoki et al. (2009) and Honda et al. (2011) (identified as a carbon EMP, we keep abundances from the most recent study in our plots.

Our study largely increased the number stars displaying  $[\alpha/\text{Fe}]$  in Sextans : 44 stars in  $[\text{Mg}/\text{Fe}]$ , 35 in  $[\text{Ca}/\text{Fe}]$  and 32 in  $[\text{Ti}/\text{Fe}]$ .

The considered stars in Sextans (all the HR studies and high quality data of medium resolution study from Kirby et al. (2010)) display a large and populated range in metallicities from -3.3 to -1.5 dex allowing the study of the abundances evolution.

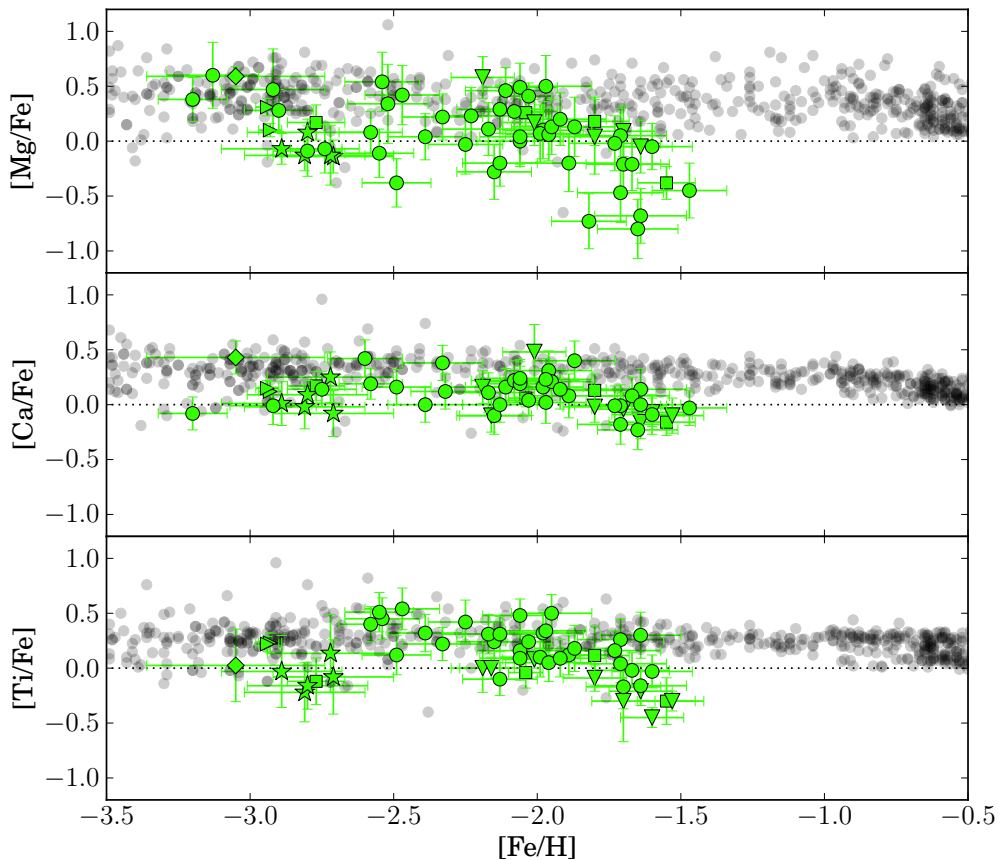


Figure 3.60: The distribution  $[\alpha/\text{Fe}]$  for Sextans (green symbols) and Milky Way stars (grey circles). See the references and the description of the symbols in the text. Top panel :  $[\text{Mg}/\text{Fe}]$ . Middle panel :  $[\text{Ca}/\text{Fe}]$ . Bottom panel :  $[\text{Ti}/\text{Fe}]$ .

**3 outliers in [Mg/Fe]** Concerning magnesium abundance ratios three stars of our sample are considered as outliers and highly uncertain (displaying also the largest error bars). Stars S08-282, S08-280 and S05-47 (according to x-axis increasing order) present very low abundances :  $[Mg/Fe] < -0.5$ . In order to test the reliability of their rather low  $[Mg/Fe]$  we compare their Mg line with the line of a star presenting similar stellar parameters but a higher value of  $[Mg/Fe]$ . For star S08-282 with stellar parameters [5044 K, 1.96, 1.61 km/s, -1.82 dex] respectively for  $T_{\text{eff}}$ ,  $\log g$ ,  $v_{\text{turb}}$  and  $[Fe/H]$  we find S05-84 as a similar star with [5048 K, 1.92, 1.62 km/s, -1.96 dex]. In the same way S08-242 with [4657 K, 1.44, 1.71 km/s, -1.71 dex] has close stellar parameters to S05-47 [4654 K, 1.28, 1.74 km/s, -1.64 dex]. Unfortunately we did not find a similar star to S08-280 in our sample. Figure 3.61 shows in the two first panels spectrum of the outlier star in black with the spectrum of the similar star around the Mg line for S08-282 and S05-47. The third panel represents the spectrum of S08-280 in black and its best fitted synthetic spectrum in red around Mg line.

The Mg line in S08-282 is very faint in comparison to its similar stars S05-84 (first panel of figure 3.61), but it is also hardly distinguishable from the noise. We can add that no reliable calcium abundance was measured for this star and that its signal-to-noise ratio in HR10 is 16. This value could be treated as a lower limit.

S05-47 shows in the second panel of figure 3.61 a well defined line but effectively smaller than the Mg line of S08-242. Star S05-47 seems strange because presents also a low  $[Ti/Fe]$  (-0.16 dex) but a not so low  $[Ca/Fe]$  (0.14 dex) in comparison with other stars at same  $[Fe/H]$ .

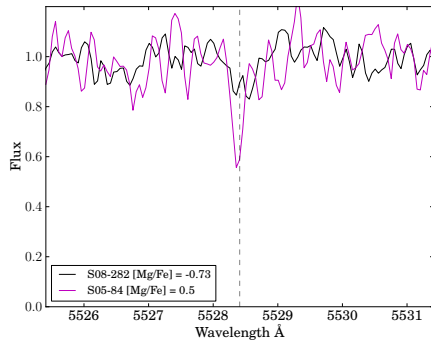
The third panel of figure 3.61 gives the comparison between the spectrum of S08-280 in black and its best fitted synthetic spectrum in red around Mg line. As seen for S08-282 the noise is important in this spectrum (signal-to-noise ratio of 15 in HR10). The  $[Mg/Fe]$  could be used as a lower limit. However this star displays the lowest value in  $[Ca/Fe]$ .

Due to the uncertainties, these three outliers are not taken into account in the next considerations about magnesium abundances.

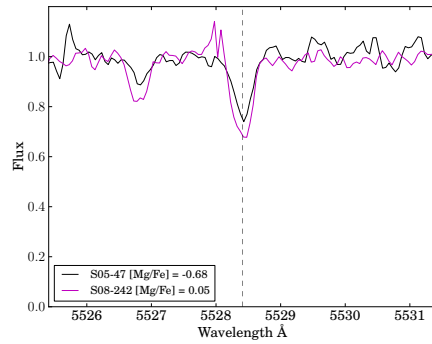
**Global similar behavior for  $\alpha$  elements** A similar global behavior of  $[\alpha/Fe]$  versus  $[Fe/H]$  is observed for Sextans stars : a plateau phase at low  $[Fe/H]$  with rather constant value of  $[\alpha/Fe]$  (0.14 dex in average for  $[Mg/Fe]$ , 0.13 dex for  $[Ca/Fe]$  and 0.17 dex for  $[Ti/Fe]$ ) followed by a decrease of  $[\alpha/Fe]$  with increasing metallicity. In Sextans this decrease occurs around  $[Fe/H] = -2.0$  dex and corresponds to the knee location when the contributions of the SNeIa dominate the ISM over the SNeII. SNeIa ejecting more iron than  $\alpha$ -elements into the ISM imply  $[\alpha/Fe]$  to decrease in next generation of stars (e.g., Venn et al. (2004), Tolstoy et al. (2009)).

Comparing Sextans with the Milky Way for stars having  $[Fe/H] < -2.0$  dex we noted that the interval of points in  $[\alpha/Fe]$  cover the same range. This leads to the conclusion that at very early times the conditions of the chemical enrichment were the same for the dwarf and the MW halo stars. As  $\alpha$ -elements are mainly produced by SNeII, similar  $[\alpha/Fe]$  is a hint that the IMF

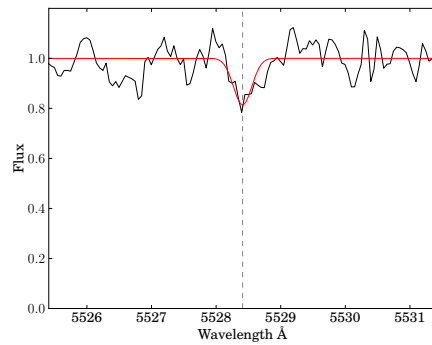




(a) In black spectrum of S08-282 and in magenta spectrum of S05-84 around Mg line indicated by the vertical dashed line.



(b) In black spectrum of S05-47 and in magenta spectrum of S08-242 around Mg line indicated by the vertical dashed line.



(c) Spectrum of S08-280 in black and its best fitted synthetic spectrum in red around Mg line indicated by the dashed vertical line.

Figure 3.61: Comparison of Mg line for the three outliers in  $[Mg/Fe]$

was probably similar at that time in these systems.

From a sample of Sculptor, Carina, Fornax and Sagittarius stars Tolstoy et al. (2009) already observed that stars on the metal-poor side of their knee tend to be indistinguishable from those of the Milky Way halo. They conclude that the first billion years of chemical enrichment in dwarf galaxies and in the MW halo gave rise to the similar enrichment features. Even if Sextans has a larger probability to present lower  $[\alpha/Fe]$  than the MW because of its lower mass (producing then fewer SNeII and/or less massive SNeII) as revealed by the average values, the intervals cover the same  $[\alpha/Fe]$  range at low metallicities.

**Small differences between [Mg/Fe], [Ca/Fe] and [Ti/Fe]** Although all the  $[\alpha/\text{Fe}]$  present decreasing trends for  $[\text{Fe}/\text{H}] > -2.0$  dex, the decreasing slopes seem to be different for [Mg/Fe], [Ca/Fe] and [Ti/Fe] (see Figure 3.62). The points are more dispersed in Mg than in Ti and in Ca.

According to literature, Mg is mainly produced in hydrostatic burning phase of massive stars (SNeII). Ca and Ti are mainly produced in explosive burning phases (SNeII). However some fractions of Ca and very little Mg are produced in SNeIa. Some isotopes of Ca and Ti can be produced in rare varieties of SNeIa. Then as some fraction of Ca and a smaller fraction of Ti could be produced also in SNeIa, it may explain the less pronounced decrease of [Ca/Fe] and [Ti/Fe] versus [Fe/H] (for  $[\text{Fe}/\text{H}] > -2.0$  dex) in comparison with [Mg/Fe].

This is also why in general [Mg/Fe] is preferably used to determined the location of the knee in order to trace as close as possible the ratio [SNeII/SNeIa] reflecting the star formation time-scale.

A less pronounced decreasing behavior in [Ca/Fe] (and [Ti/Fe]) in comparison with [Mg/Fe] has been observed several times : by Shetrone et al. (2003) and by Venn et al. (2004) for several dSphs stars, by Fulbright et al. (2007) for galactic bulge stars, and Letarte et al. (2010) in Fornax stars. Various explanations are given but always related to differences in nucleosynthesis. Venn et al. (2004) suggest a similar idea as presented by Tolstoy et al. (2003) : the upper IMF is truncated for low mass dwarf galaxies (presenting slower chemical evolution). They explained the differences in [Ca,Ti/Fe] behavior compared to [Mg/Fe] by a lack of hypernovae. In Letarte et al. (2010) where SNeIa (producing fractions of Ca and Ti) considerably contribute to the enrichment of Fornax they invoke the sensitivity of the SNeIa ejecta to the metallicity of the progenitors (Timmes et al. 2003; Röpke et al. 2006). Tolstoy et al. (2009) explain that the differences between trends of [Mg/Fe] and [Ca/Fe], [Ti/Fe] with [Fe/H] come from the fact that Ca and Ti are mostly produced during SNeII explosion while Mg is produced during hydrostatic burning phases. Then Mg being not affected by the explosion conditions.

Taking into account the short SF in Sextans the differences observed in the decreasing trends between  $\alpha$ -elements could be simply due to the number of lines used to determined the abundances. The less dispersed trend is for calcium for which we consider up to 13 lines, in comparison with 4 lines for titanium and 1 line for magnesium.

#### Comparison with other dwarfs

Figure 3.62 is the same figure as 3.60 at which we add  $[\alpha/\text{Fe}]$  from other dwarf galaxies for comparison : Sculptor in blue circles from Tolstoy et al. (2009), and blue triangles from Geisler et al. (2005), Shetrone et al. (2003); Fornax in red circles from Letarte et al. (2010); Carina in yellow circles from Lemasle et al. (2012) (we represent only the old population with an age  $\geq 8$  Gyr), Shetrone et al. (2003), and triangles from Venn et al. (2012), Ursa Minor in violet stars from Sadakane et al. (2004), Cohen & Huang (2010b); Draco in violet triangles from Cohen &

Huang (2009), Fulbright et al. (2004); Ursa Major in black up triangles from Frebel et al. (2010); Coma Berenices in black stars from Frebel et al. (2010) ; Leo IV in black squares from Simon et al. (2010) ; Hercules in black down triangles from Koch et al. (2008), Adén et al. (2011), Koch et al. (2012) ; Segue I in black right triangles from Norris et al. (2010), Frebel et al. (2014) ; Boötes in black diamonds from Norris et al. (2010), Feltzing et al. (2009), Ishigaki et al. (2014), Lai et al. (2011).

The dark green lines are the least squares polynomial fits of the Sextans stars for  $[\text{Fe}/\text{H}] > -2.0$  dex (decreasing trend). The 3 Mg outliers were not use to compute the fit. They are located between  $3-4 \sigma$  of the fit. Same fits are done for Sculptor stars having  $[\text{Fe}/\text{H}] > -1.8$  dex

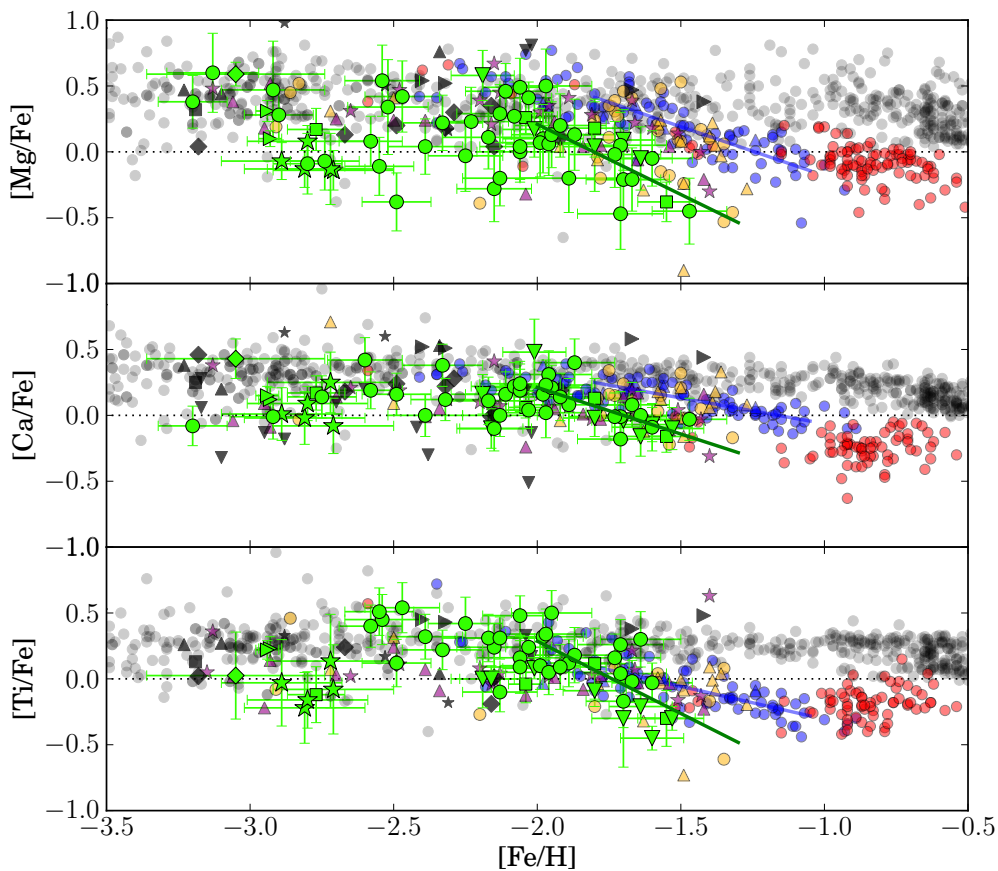


Figure 3.62: The distribution of  $[\alpha/\text{Fe}]$  for Sextans (green symbols), the Milky Way (gray circles) and other dwarf galaxies stars : Sculptor blue symbols, Fornax red circles, Carina yellow symbols, Ursa Minor violets stars and Draco violet triangles, and black symbols for UFDs. See the references and a detailed description of the symbols in the text. Top panel :  $[\text{Mg}/\text{Fe}]$ . Middle panel :  $[\text{Ca}/\text{Fe}]$ . Bottom panel :  $[\text{Ti}/\text{Fe}]$ . The fitted decreasing trends are highlighted by solid lines in dark green for Sextans and in blue for Sculptor in each panel.

The position of this knee is expected to be different for dwarf spheroidal galaxies because of the wide variety of star formation histories. All of the dSphs present a lower star formation efficiency than the MW because the SNeIa start to contribute at a lower  $[\text{Fe}/\text{H}]$  than the knee of the MW.

Tolstoy et al. (2009) show that the position of the knee correlates with the total luminosity of the galaxy, and the mean metallicity of the galaxy. They suggest that the presently most luminous galaxies are those that must have formed more stars at the earliest times and/or retained metals more efficiently than the less luminous systems.

More recently (de Boer et al. 2014a) proposed in the same way that  $\alpha$ -knee are correlated with the mass of the system. For example the (first) knee in Carina ( $M_{\text{dyn}} \approx 3.4 \cdot 10^6 M_{\odot}$ ) takes place at  $[\text{Fe}/\text{H}] \approx -2.5$  dex, while the knee in the more massive Sculptor ( $M_{\text{dyn}} \approx 1.4 \cdot 10^7 M_{\odot}$ ) is found at  $[\text{Fe}/\text{H}] \approx -1.8$  dex (Walker & Peñarrubia 2011; McConnachie 2012).

For the moment, only a few dSphs have their knee robustly determined : Sagittarius around -1.27 dex (de Boer et al. 2014a), and Sculptor around -1.8 dex (Tolstoy et al. 2009; Starkenburg et al. 2013). According to Forbes & Bridges (2010) the knee in Sagittarius corresponds to an age of  $\approx 11$  Gyr, roughly 1.5 Gyr after their proposed start of star formation in agreement with theories of galaxy formation (e.g. Raiteri et al. (1996); Matteucci & Recchi (2001)).

Sculptor seems to be a good example of isolated system evolution harboring two distinct ancient stellar components (both 10 Gyr old) : one metal-rich and one metal-poor (Tolstoy et al. 2004). The chemical evolution of Sculptor seems to be simple with a early burst of SF (13-14 Gyr ago) and slowly continuously until 6-7 Gyr ago and presenting no signs of recent tidal interactions.

Two knees are expected for Carina because of its bursty star formation. Lemasle et al. (2012) indicate that the first knee may be between -2.7 and -2.3 dex, however the second knee is not clearly visible. Lemasle et al. (2012) proposed the following interpretation of the complex star formation in Carina : a fairly *normal* chemical evolution for the oldest star formation episode ( $> 10$  Gyr) from  $[\text{Fe}/\text{H}] \sim -3.0$  to  $-1.5$  dex with  $[\text{Mg}/\text{Fe}]$  decreasing to lower values with a large scatter after a knee around  $[\text{Fe}/\text{H}] \sim -2.3$  dex. The second episode of star formation does not follow the same pattern (no obvious second knee) because most of the stars younger than 8 Gyr old seem to be formed from gas not strongly polluted by SNeIa. These stars cover metallicities from -1.8 to -1.2 dex but display mainly high  $[\text{Mg}/\text{Fe}]$  around 0.3 dex. This lack of SNeIa enrichment could be explained by short star formation episodes (SNeII are able to remove the ISM of the galaxy before the onset of the SNeIa). The overlap of Mg-poor and Mg-rich stars means that the most metal poor stars in the intermediate age group, are at lower  $[\text{Fe}/\text{H}]$  than the most metal rich stars in the old group. This requires that either star formation in this second episode started with a new reservoir of gas (at  $[\text{Fe}/\text{H}] \leq -2$  dex,  $[\text{Mg}/\text{Fe}] \sim 0.3$  dex) or additional more metal poor gas was added to gas that was enriched by the first star formation episode to be able to start forming stars at lower  $[\text{Fe}/\text{H}]$ . In any scenario it is difficult to explain it in such a low mass system without implication of external processes. The presence

of high values of  $[\text{Mg}/\text{Fe}]$  over a large range of  $[\text{Fe}/\text{H}]$  could be interpreted by SNe feedback : after one episode of star formation the ISM is removed by SNe then the new gas required for the next SF originates from external processes (merging or accretion). The modelization of the chemical evolution of Carina by Revaz et al. (2009) show good predictions for the large scatter in  $[\alpha/\text{Fe}]$  and low  $[\text{Mg}/\text{Fe}]$  value but a less good match for the SFH. The discrepancies could come from the fact that the model assumes a dwarf in isolation with a fixed reservoir of gas, while Carina enrichment was probably driven by external interactions. Moreover from its estimated position on the orbit around the MW (close to its apocentre) Carina should have been orbiting MW for a considerable time leading possible tidal interactions.

Concerning Fornax, Hendricks et al. (2014) determined with HR data a knee around  $[\text{Fe}/\text{H}] = -1.9$  dex. This low value of  $[\text{Fe}/\text{H}]$  for the knee is unexpected considering the large mass of Fornax  $M_{\text{dyn}} \approx 1.6 \cdot 10^8 M_{\odot}$  Walker et al. (2006) and its high mean metallicity. The most puzzling point come from the comparison between Fornax and Sculptor : they present similar  $\alpha$ -knee location, respectively -1.9 dex and -1.8 dex, however Sculptor is about 10 times less massive than Fornax and has an average metallicity lower by more than 0.6 dex.

This is the first time we have a sufficient number of stars in Sextans with alpha abundances to estimate the location of the knee around -2.0 dex.

The Sextans knee is located at a smaller metallicity than Sculptor knee indicating that star formation was less efficient in Sextans than in Sculptor. At same  $[\text{Fe}/\text{H}]$ , Sculptor displays higher  $[\alpha/\text{Fe}]$  than Sextans. These considerations support the theory saying that being less massive than Sculptor, Sextans produced fewer SNe and/or less massive SNe hence reaching lower abundances. The slopes of their decreasing parts are similar, following the same time-scale after the onset of the SNeIa.

In comparison with the old population of Carina (age  $\geq 8$  Gyr), Sextans show similar abundances and cover comparable areas in abundances ratios figure. This is in agreement with the idea that having similar low mass their should follow a close chemical evolution. It seems that the oldest population of Sextans and Carina could gather similar evolution but then differ for their intermediate age stellar populations.

Figure 3.63 represent as in Hendricks et al. (2014) the knee locations in function of the absolute magnitudes (McConnachie 2012) for several dwarfs. Adopting a knee at  $[\text{Fe}/\text{H}] \simeq -2.0$  dex we observe that Sextans follows the linear relation without surprise. As the absolute magnitude <sup>2</sup> correlates with the galaxy mass, the position of the knee depends also on the mass of the system. The general idea is the following : the more massive a galaxy is, the more efficient its SF and the higher the  $[\text{Fe}/\text{H}]$  of the knee in its  $[\alpha/\text{Fe}]$  vs  $[\text{Fe}/\text{H}]$  diagram.

<sup>2</sup>Here the magnitudes are taken in band  $V$  which is sensitive to current SF. Note that  $M_V$  can be over-estimated considering galaxies which are still forming stars.

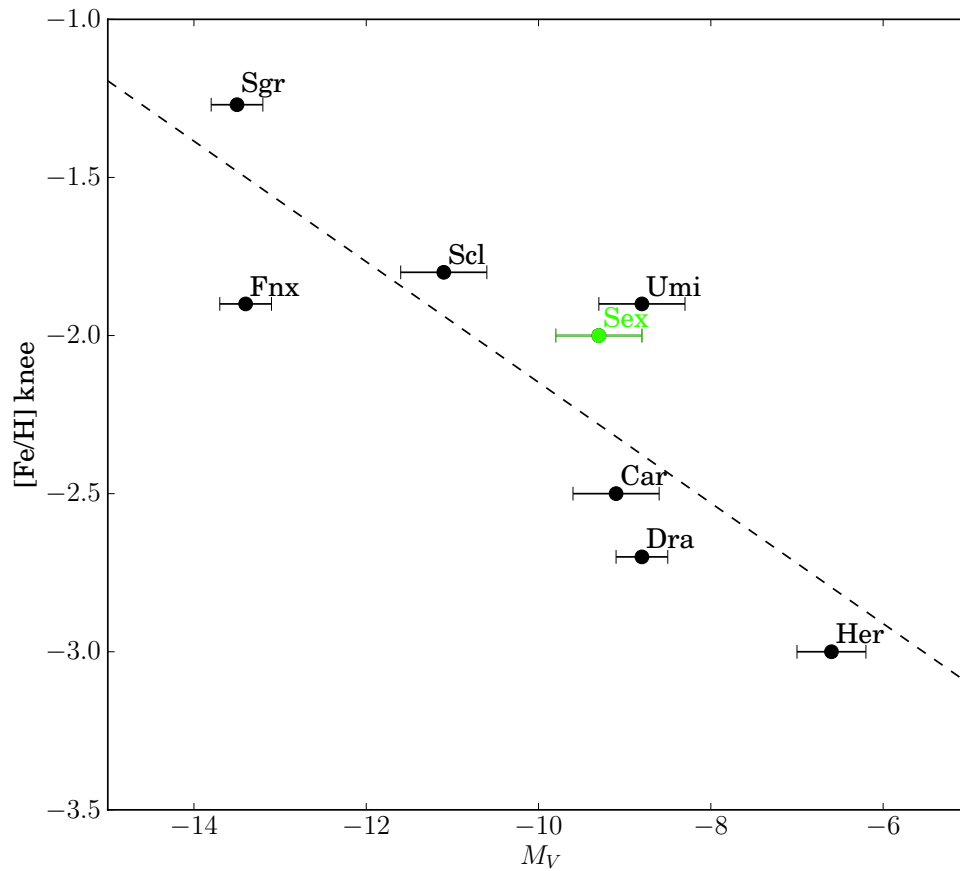


Figure 3.63: Position of the knee in the  $[\text{Mg}/\text{Fe}]$  distribution of several dwarf galaxies as a function of absolute magnitude. Absolute magnitudes  $M_V$  have been adopted from McConnachie (2012). The estimations of the knee positions are from previous studies : Tolstoy et al. (2009) for Sculptor, Cohen & Huang (2009) for Draco, Cohen & Huang (2010b) for Ursa Minor, Vargas et al. (2013) for Hercules, Hendricks et al. (2014) for Fornax, Lemasle et al. (2012) for Carina and de Boer et al. (2014a) for Sagittarius. The dashed line corresponds to the best fitting linear relation taking into account all plotted dwarfs.

**No intrinsic dispersion in  $[\alpha/\text{Fe}]$  for our central stars** Sextans is interesting because its range of mass places it at the turning point between a homogeneous and inhomogeneous ISM (Revaz et al. 2009). The idea is then to test the presence of a real scatter in  $[\alpha/\text{Fe}]$  in Sextans. A real/intrinsic scatter means large range  $[\alpha/\text{Fe}]$  due to an ineffective mixing of SNe ejecta characteristic of low mass galaxies.

According to Letarte et al. (2010) Sculptor and Fornax exhibit a small dispersion in  $[\text{Mg}/\text{Fe}]$  which is only due to measurement errors. Carina shows hints of scatter in  $[\text{Mg}/\text{Fe}]$  but for this particular case the explanation may lie in its bursty star formation history (Lemasle et al. 2012).

From the least square polynomial fit on Sextans stars having  $[\text{Fe}/\text{H}] > -2.0$  dex, we derived the standard deviation and calculate the mean of the errors. Table 3.4 gives the values for Sextans. For Mg and Ca the scatter is clearly smaller than the mean of the errors and for Ti they have similar values. From these results we can conclude that the dispersion is not intrinsic but come from the errors. Doing the same for Sculptor for stars having  $[\text{Fe}/\text{H}] > -1.8$  dex, we obtained the results in table 3.5. For Sculptor the deviation is either smaller than the mean of errors (Mg, Ti) or they display similar values (Ca). This confirms previous results that in Sculptor the small dispersion is only also due to measurement errors.

Battaglia et al. (2011) show the presence of a radial metallicity gradient in Sextans considering observation until the tidal radius (see figure 8 in Battaglia et al. (2011)). For a projected radius  $R < 0.8$  deg stars cover the whole range of  $[\text{Fe}/\text{H}]$ , while for  $R > 0.8$  deg all stars are metal-poor  $[\text{Fe}/\text{H}] < -2.2$  dex. We know from photometry that center stars display ages between 10-14 Gyr and the stars in the outskirts are old stars with a age of the order  $\sim 14$  Gyr. Our centrally-centered sample represents then the last phase of the chemical evolution. The observation of no intrinsic dispersion in  $[\alpha/\text{Fe}]$  show that Sextans exhibit an homogeneous ISM in its center despite its low mass. However in order to have a global understanding of the role of the dwarf mass and the presence of a scatter in abundances we should consider stars from the whole dwarf galaxy and not only from the center.

Recently Nichols et al. (2014) test through simulations the impact of tidal interactions between the MW and typical dSphs similar to Fornax, Sculptor, Sextans and Carina. For similar Sextans dSphs they find that the star formation is quenched around perigalacticon for cases which experienced 2 or 3 perigalacticon passages. A second effect is that stars are stripped at larger radii. The metallicity gradient is then gradually erased with increasing number of interactions and the stellar density profile is smoothed out. The decrease of the metallicity gradient is due to lack of young stars in the center. After comparison the metallicity gradient observed in Sextans could correspond to the one perigalacticon passage model. We could then imagine the following evolution for Sextans : stars are forming when entering the potential well of the MW, due to tidal interactions the stars formation is quenched in the outskirts when passing around the perigalacticon but star formation continue in the center leading to an homogeneous ISM.

### Chapter 3. The dwarf spheroidal galaxy Sextans

---

Table 3.4: Standard deviations and means of errors on  $[\alpha/\text{Fe}]$  for Mg, Ca and Ti for Sextans stars with  $[\text{Fe}/\text{H}] > -2.0$  dex.

Abundance ratios	Standard deviation dex	Mean of errors dex
[Mg/Fe]	0.160	0.240
[Ca/Fe]	0.110	0.170
[Ti/Fe]	0.175	0.178

Table 3.5: Standard deviations and means of errors on  $[\alpha/\text{Fe}]$  for Mg, Ca and Ti for Sculptor stars with  $[\text{Fe}/\text{H}] > -1.8$  dex.

Abundance ratios	Standard deviation dex	Mean of errors dex
[Mg/Fe]	0.139	0.193
[Ca/Fe]	0.079	0.078
[Ti/Fe]	0.110	0.128

#### 3.14.5 Iron-peak elements

The next five studied elements are iron-peak elements : Sc II (3 lines), Cr I (3 lines), Mn I (4 lines), Co I (1 line) and Ni I (6 lines). The number of stars for which abundances are determined is smaller than for  $\alpha$  elements : 16 stars for Sc, 10 stars for Cr, 5 stars for Mn, 2 stars for Co and 6 stars for Ni. This is mainly due to weakness of the lines requiring sufficient signal-to-noise.

**Sc** Scandium abundances in Sextans stars are presented in figure 3.64 (top panel) with Milky Way stars and in figure 3.65 (top panel) with other dwarf galaxies stars. For Sextans stars having  $[\text{Fe}/\text{H}] < -2.5$  dex they overlap well the dispersed MW stars. At higher metallicity, they are slightly under-abundant than the MW stars and seem to follow a similar decreasing trend as Sculptor stars.

As being only produced by SNeII and not from SNeIa, the evolution of Sc follows the same trend as  $\alpha$ -elements (plateau followed by a decline). Indeed the start of the decrease corresponds to the  $\alpha$ -knee around -2.0 dex. This is in agreement with results of Battistini & Bensby (2015) studying a homogeneous and statistically significant sample of MW stars and showing that their trend of scandium with metallicity is similar to alpha-elements (compatible production from SNeII).

**Cr** Chromium and manganese distribution are presented in figures 3.66 and 3.67.

The metal-poor stars in Sextans display slightly lower  $[\text{Cr}/\text{Fe}]$  than the MW stars at same metallicity but similar abundances at higher metallicities.

Bergemann & Cescutti (2010) confirm that the increasing trend of  $[\text{Cr}/\text{Fe}]$  with metallicity observed for MW stars is clearly an artifact due to neglecting NLTE effects in line formation of



Cr for metal-poor stars. The departure from LTE is due to sensitivity of atomic level populations of Cr in the atmosphere of late-type stars to the non-local UV radiation field (over ionization from the low excitation odd Cr I levels with large quantum-mechanical photo-ionization cross-sections). The NLTE corrections are positive and increase with decreasing [Fe/H] and gravity. They are of the order of +0.1 dex at solar metallicities and up to +0.5 dex for metal-poor stars. Taking into account these NLTE effects they show that MW stars display in reality a relative constant trend over the whole metallicity range. This constant trend of corrected [Cr/Fe] over range in [Fe/H] is consistent with the nucleosynthesis theory predicting that Cr and Fe are co-produced in explosive Si-burning phase in SNe. 60% of the solar Cr and Fe are predicted by models to be produced in SNeIa while the rest in SNeII. Cr is under-produced relatively to Fe in SNeIa but it is compensated by over-production in solar SNeII. Then a NLTE correction for Cr need to be applied to Sextans stars in order to see if the trend changes. None of the [Cr/Fe] abundances presented on Figures 3.66 and 3.67 have been corrected from NLTE effects.

**Mn** The distribution of manganese in Sextans follows the same behavior as the MW stars. As Mn can be produced by both types of SNe they are created by SNeII until the knee and then produced by SNeIa.

Woolley & Weaver (1995) show that yields of Mn should increase with metallicity as observed by Feltzing et al. (2007). However the metallicity dependence of SNeIa yields is still an open question. Several studies suggest that SNeIa yields of Mn increase with metallicity (Shetrone et al. 2003; Ohkubo et al. 2006; Cescutti et al. 2008; Badenes et al. 2008). Following this idea Mn abundances could be used as tracer of progenitor metallicity.

North et al. (2012) derived HFS-corrected Mn abundances for Sculptor, Fornax and Carina. For strong lines (typically of 200 mÅ) the corrections could reach 1.6 dex. The corrections depend on the equivalent width but also on the stellar parameters (especially on the micro-turbulent velocities). The three studied dSphs exhibit all sub-solar [Mn/Fe] ratios as expected from their low metallicity. In Sculptor, the evolution of [Mn/Fe] with [Fe/H] display a plateau at low [Fe/H] followed by a decrease at higher [Fe/H]. This decreasing trend has already been observed previously in the GC Omega Centauri. In Fornax, [Mn/Fe] does not vary in any significant way with [Fe/H]. Comparing [Mn/ $\alpha$ ] in function of [Fe/H] they show a clear systematic offset between the MW and the dSphs reflecting the different SFHs. The variation in [Mn/ $\alpha$ ] can be interpreted in terms of the balance between the metal-dependent yields of type II and type Ia supernovae. Computing simple chemical evolution models assuming either constant or variable SNeIa yields North et al. (2012) show that the metallicity dependence of SNeIa yields are required to reproduce the observations of [Mn/Fe] in dwarfs. They conclude that the consecutive increase and decrease of [Mn/Fe] with [Fe/H] are the consequence of the increasing yields of SNeII with metallicity in combination with initially low SNeIa yields that subsequently rise with metallicity.

The observed light increasing trend in our values could be explained by this metallicity dependence of SNeIa yields. This is the first time we have for a dSph manganese abundances covering a so large range in  $[\text{Fe}/\text{H}]$  despite our small number of points.

**Co** We add two stars to the four previous cobalt abundance measurements in Sextans. The results are presented on figures 3.68 and 3.69. Sextans stars follow the MW but the too small statistics do not allow to conclude a trend. There could be a hint for a decreasing behavior. Battistini & Bensby (2015) show that the MW  $[\text{Co}/\text{Fe}]$  trend is flat for solar and super solar metallicities and then there is an increase in  $[\text{Co}/\text{Fe}]$  for decreasing metallicity. A chemical evolution model of Timmes et al. (1995) suggests that the trend in  $[\text{Co}/\text{Fe}]$  with respect to  $[\text{Fe}/\text{H}]$  can be explained by the dependence of Co ejection on mass/metallicity of massive stars and by the production of Fe through SNeIa.

**Ni** Figures 3.64 and 3.65 show in bottom panel the distribution of  $[\text{Ni}/\text{Fe}]$  for Sextans stars with MW stars and other dwarf galaxies for comparison.

The Sextans stars globally overlap the MW stars at low metallicity and then decrease at higher metallicity. This feature has been already observed in Sculptor dSph (Tolstoy et al. 2009). In Fornax, Lemasle et al. (2014) observed that Ni follows the MW in the metal-poor stars but become under-abundant for  $[\text{Fe}/\text{H}] > -1.5$  dex. Timmes et al. (2003) and Travaglio et al. (2005) show that Ni yields of **SNeII (SNeII)**a are more important at low  $[\text{Fe}/\text{H}]$ . For the MW, the constant solar trend of  $[\text{Ni}/\text{Fe}]$  with  $[\text{Fe}/\text{H}]$  can be explained by a long continuous SF :  $[\text{Ni}/\text{Fe}]$  is mainly produced by SNeII for  $[\text{Fe}/\text{H}] < -1.0$  dex and then in majority by SNeIa for  $[\text{Fe}/\text{H}] > -1.0$  dex. Considering the long star forming dSph Fornax, as the  $[\text{Ni}/\text{Fe}]$  decrease is observed at a higher  $[\text{Fe}/\text{H}]$  (more than 0.4 dex) than the  $[\alpha/\text{Fe}]$  knee, this could be interpreted as a hint that Ni yields of SNeIa a less important than Ni yields of SNeII. On the contrary for Sculptor and Sextans having a shorter SF in comparison with Fornax and the MW, the decrease could be due to less numerous SNeIa due to lower SFR in less massive systems.

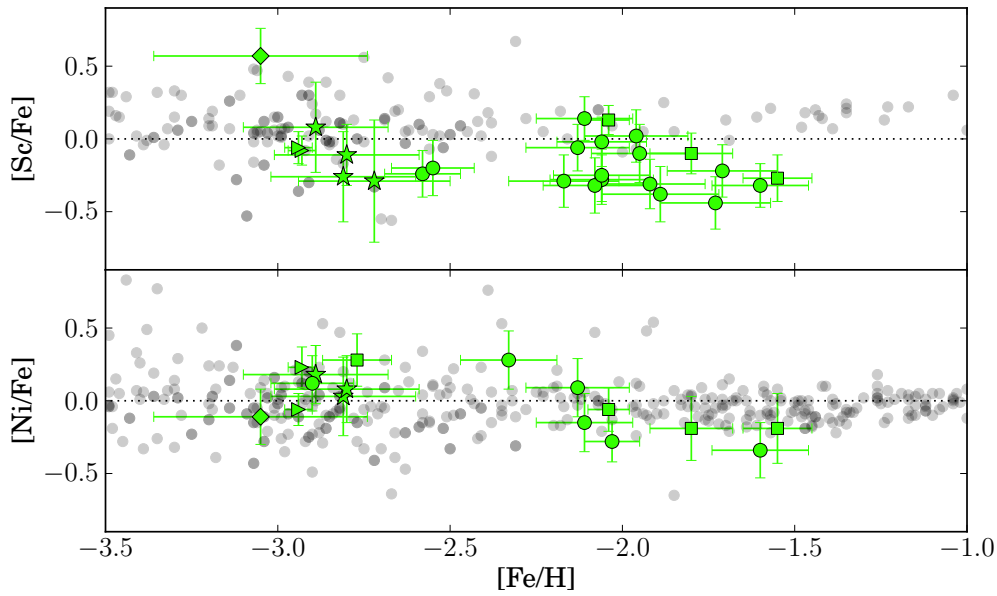


Figure 3.64: The distribution of  $[\text{Sc}/\text{Fe}]$  (top panel),  $[\text{Ni}/\text{Fe}]$  (bottom panel) for Sextans and Milky Way stars. The symbols are the same as in Figure 3.60.

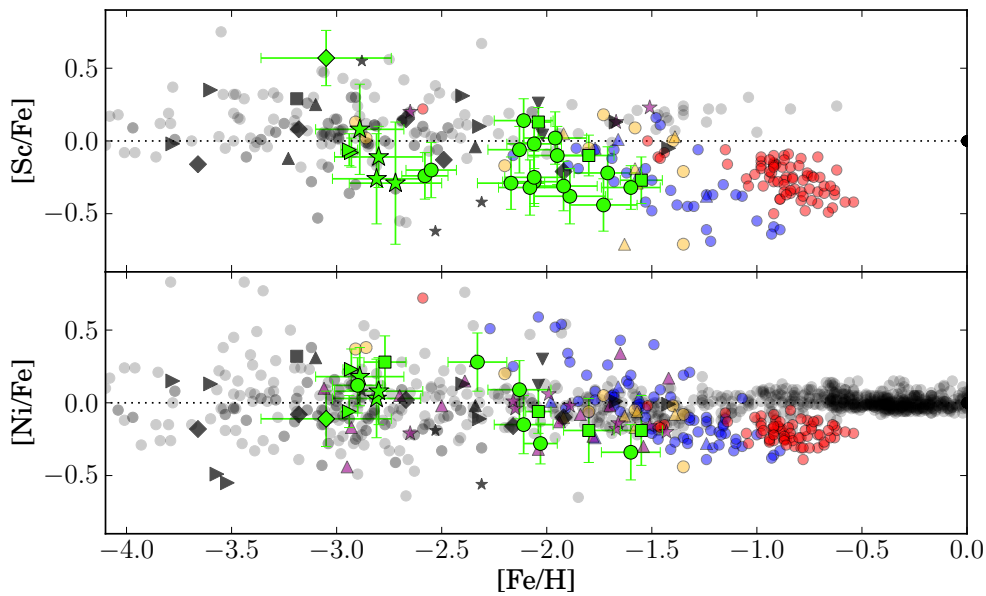


Figure 3.65: The distribution of  $[\text{Sc}/\text{Fe}]$  (top panel) and  $[\text{Ni}/\text{Fe}]$  (bottom panel) for Sextans, the Milky Way and other dwarf galaxy stars. The symbols are the same as in Figure 3.62.

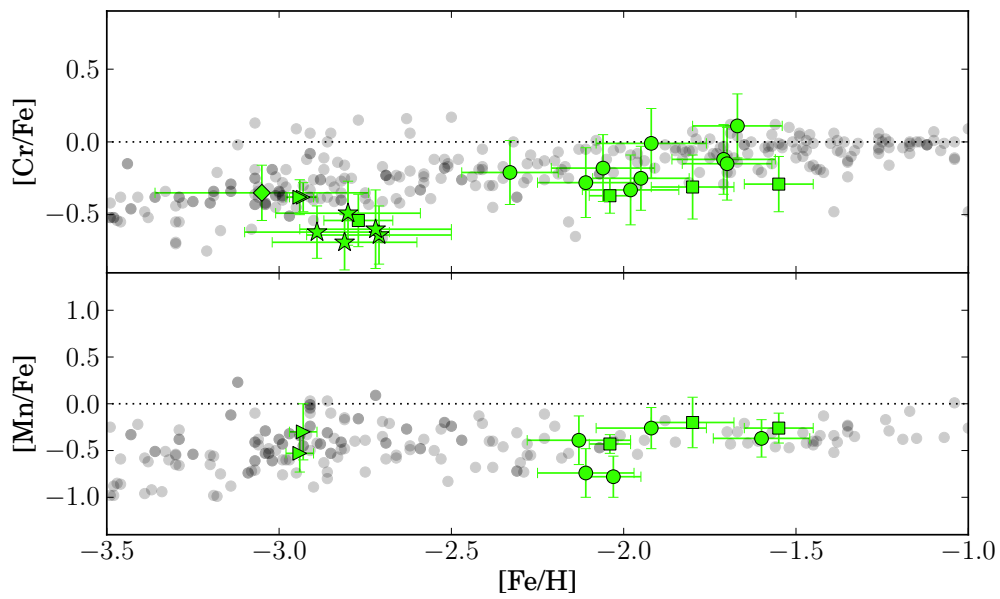


Figure 3.66: The distribution of  $[\text{Cr}/\text{Fe}]$  (top panel),  $[\text{Mn}/\text{Fe}]$  (bottom panel) for Sextans and Milky Way stars. The symbols are the same as in Figure 3.60.

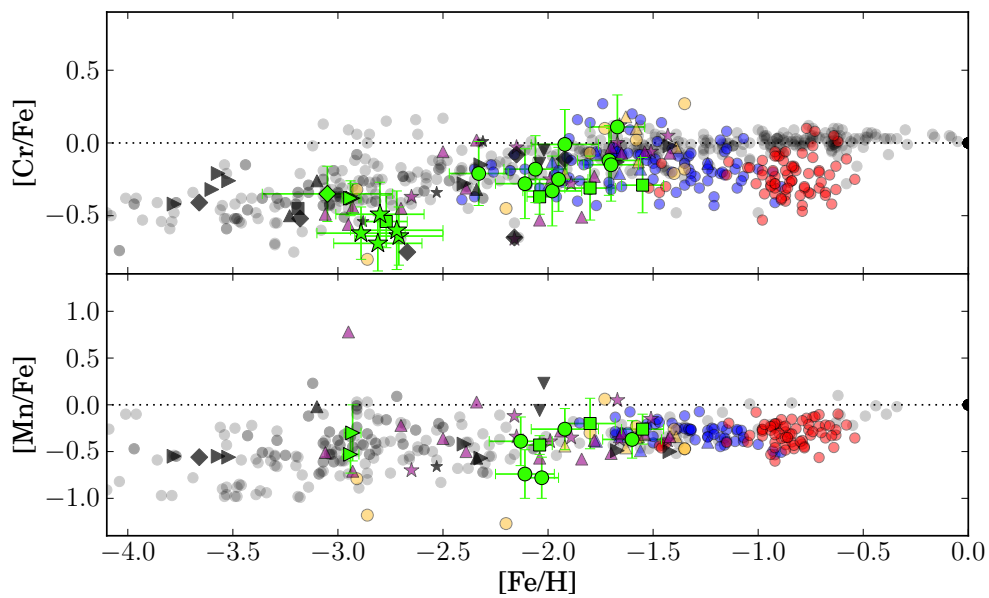


Figure 3.67: The distribution of  $[\text{Cr}/\text{Fe}]$  (top panel) and  $[\text{Mn}/\text{Fe}]$  (bottom panel) for Sextans, the Milky Way and other dwarf galaxies stars. The symbols are the same as in Figure 3.62.

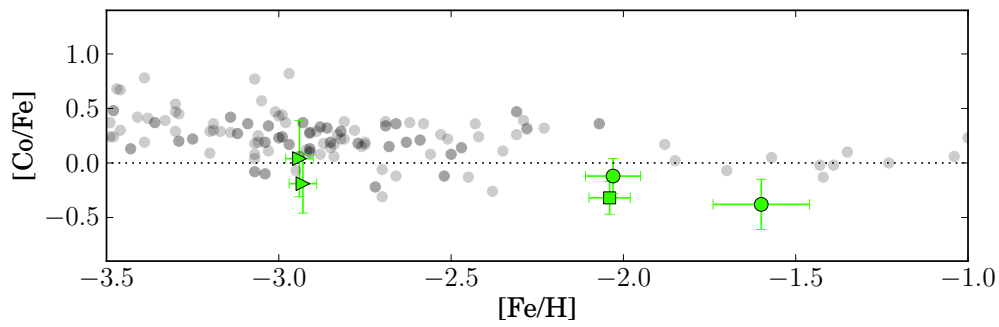


Figure 3.68: The distribution of [Co/Fe] for Sextans and Milky Way stars. The symbols are the same as in Figure 3.60.

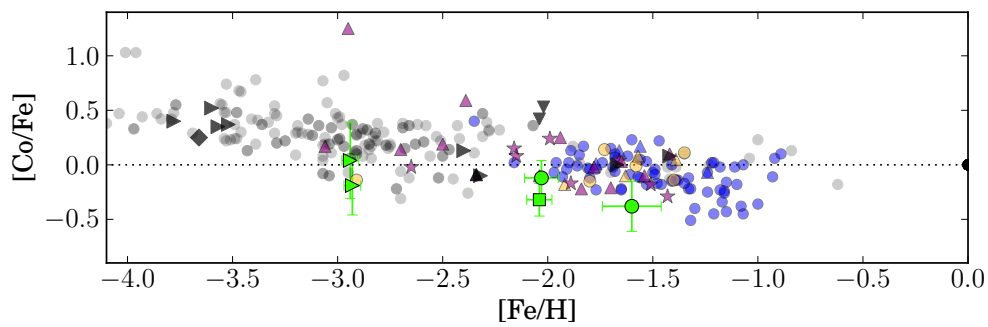


Figure 3.69: The distribution of [Co/Fe] for Sextans, the Milky Way and other dwarf galaxies stars. The symbols are the same as in Figure 3.62.

### 3.14.6 Neutron-capture elements

Two neutron-capture process elements have been studied : Ba II (2 lines) measured for 37 stars and Eu II (1 line) obtained in 5 stars. Figures 3.70 and 3.71 present the evolution of [Ba/Fe], [Eu/Fe] and [Ba/Eu] in function of [Fe/H]. The Sextans stars closely follow the same trend as the MW stars in the three panels.

**[Ba/Fe]** In [Ba/Fe] distribution we find two regimes for Sextans : a large scatter of abundances for  $-3.3 \leq [\text{Fe}/\text{H}] \leq -2.3$  dex and a narrow constant behavior around solar abundances for  $[\text{Fe}/\text{H}] \geq -2.3$  dex .

The dispersion in [Ba/Fe] of the MW stars at low metallicities is interpreted as the stochastic sampling of the barium from SNeII products (main r-process). The decrease of the scatter and the increase trend towards higher metallicities corresponds to the start of the AGBs contribution to barium (main s-process). The flat behavior of [Ba/Fe] at higher metallicities in the MW is the sign that the timescale and yields of Ba from AGBs and Fe from SNeIa are similar. The small dispersion show that the gas was well mixed.

The abundances ratios [Ba/Fe] of Sculptor and Carina follow the MW trend while Fornax present higher value than in MW for  $[\text{Fe}/\text{H}] > -1.0$  dex. This could be explained by a dominance of s-process at late times in Fornax (Lemasle et al. 2014).

**[Eu/Fe]** Concerning [Eu/Fe], the general decrease trend at higher metallicities could be interpreted as similar to the decrease of  $\alpha$ -elements but with super-solar values. This could be understood by the fact that Eu is an almost pure r-process element presumably produced in SNeII which is also the main producer of alpha-elements through hydrostatic and explosive nucleosynthesis. Fornax abundances follow the MW values but for  $[\text{Fe}/\text{H}] > -1.0$  dex they follow the upper side of the MW trend (Lemasle et al. 2014). Sculptor and Carina stars also follow the MW stars (Venn et al. 2012; Tolstoy et al. 2009). The small number of points for Sextans well follow the upper part of MW stars.

**[Ba/Eu]** [Ba/Eu] is generally used to trace the r-process and to disentangle s- from r-process. As Ba is mainly produced by r-process in low metallicities and by s-process at higher metallicities and Eu is almost a pure r-process element, the ratio [Ba/Eu] represents the relative contribution of Ba from s-process to Ba from r-process. The rise in s-process can thus be estimated from [Ba/Eu]. The low values at early time are due to the fact that Ba and Eu are both produced by r-process at low metallicities (Snedden et al. 2008). The start of the rise in s-process in the Milky Way occurs around  $[\text{Fe}/\text{H}] = -2.5$  dex (McWilliam 1998; Burris et al. 2000; François et al. 2007). In Sculptor this turnover, corresponding to the metallicity reached by the system at the time when the s-process produced in AGBs start to contribute, has been

observed at  $[\text{Fe}/\text{H}] = -1.8$  dex (Tolstoy et al. 2009). This corresponds also to the same location as Sculptor  $\alpha$ -knee. The rise in s-process in Fornax has been estimated at  $[\text{Fe}/\text{H}] = -1.5$  dex by Lemasle et al. (2014), and at  $[\text{Fe}/\text{H}] = -0.8$  dex for LMC (Pompéia et al. 2008; Van der Swaelmen et al. 2013). Venn et al. (2012) propose that the rise of s-process starts around  $-2.0$  dex in Carina. For Sextans only 5 points were determined and they are located in the area of the  $\alpha$ -knee in  $[\text{Fe}/\text{H}]$  where we could expect a variation. However from their location we can conclude that Ba is a purely produced by r-process in Sextans. In addition it should be also interesting to have measurements of light neutron-capture elements in order to compare with Ba and to test the metallicity dependence of the AGBs yields (if any). As an example Venn et al. (2012) show that metal-poor AGBs contribute much to Carina enrichment. Lemasle et al. (2014) give the same interpretation in Fornax studying  $[\text{Ba}/\text{Y}]$  ratios.

**Hypothesis of an universal r-process enrichment** The abundances  $[\text{Ba}/\text{Fe}]$  are very interesting because showing a completely different enrichment behavior between on one side dSphs (Sextans, Sculptor, and Carina) that overlap very well the MW and on the other side the UFDs with noticeably under-abundance values. As the main difference between dSphs and UFDs is their mass, the hypothesis is that the main source of r-process elements can be linked to the galaxy stellar mass content. In the sense that the probability of producing Ba seem to correlate with the number of massive stars formed in the galaxy. For systems with higher mass that a threshold mass they are enrich by the same main source of r-process elements. Then this threshold mass should lie in between UFDs and dSphs. We can conclude that the r-process enrichment seems to be universal at least for a certain range system mass. The source of r-process elements is still debated but the recent alternative proposed as binary neutron star (NS-NS) mergers (Wanajo et al. 2014; Just et al. 2014) may satisfy the threshold mass hypothesis. They show that these objects successfully produce all r-process elements. Moreover, Tsujimoto & Shigeyama (2014) show that neutron star mergers are rare events with high yields of r-process elements. This means that there is a high probability they occur in more massive systems.

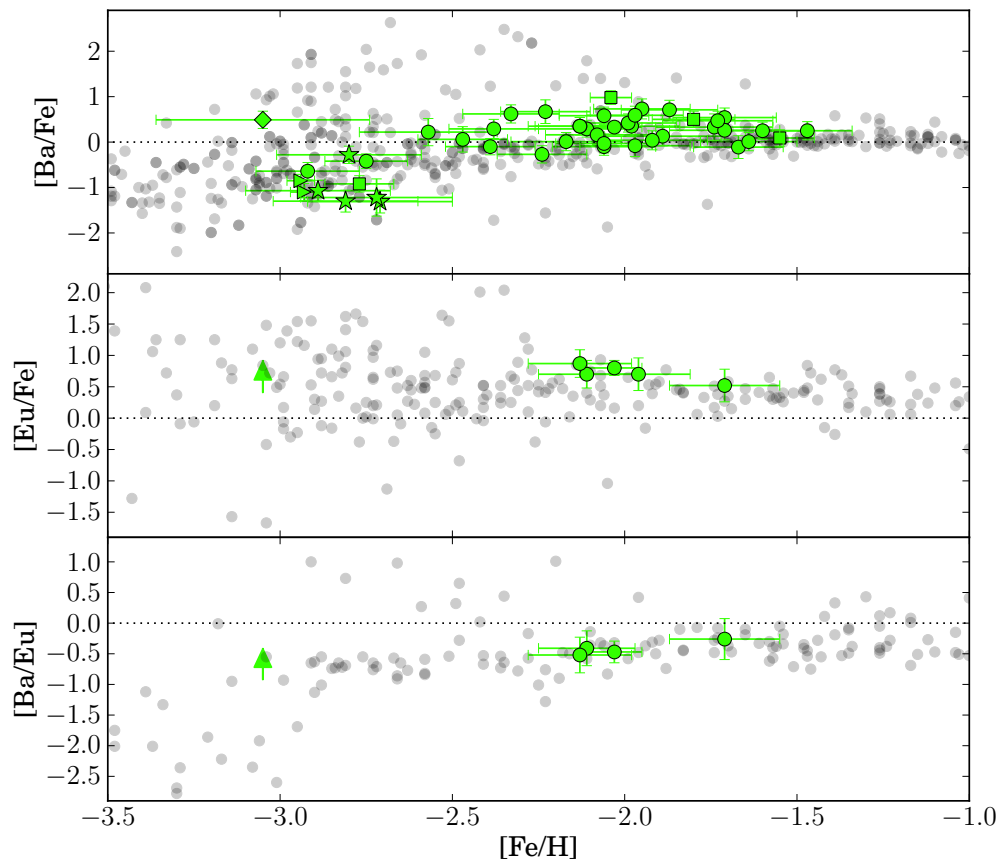


Figure 3.70: The distribution of  $[\text{Ba}/\text{Fe}]$  (top panel),  $[\text{Eu}/\text{Fe}]$  (middle panel) and  $[\text{Ba}/\text{Eu}]$  (bottom panel) for Sextans and Milky Way stars. The symbols are the same as in Figure 3.60.



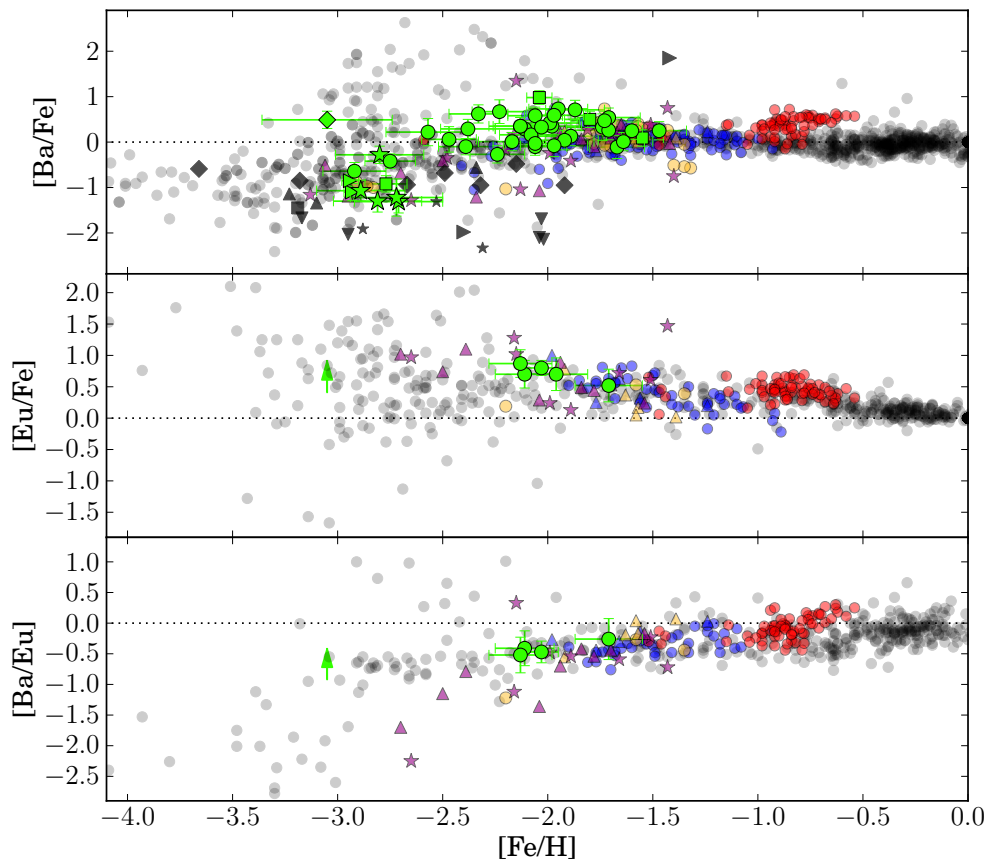


Figure 3.71: The distribution of  $[Ba/Fe]$  (top panel),  $[Eu/Fe]$  (middle panel) and  $[Ba/Eu]$  (bottom panel) for Sextans, the Milky Way and other dwarf galaxies stars. The symbols are the same as in Figure 3.62.



## 4 Conclusion

Combined with the previous high resolution spectroscopic studies in Sextans this work allowed the first picture of the chemical evolution in Sextans. The studied central field containing the last generation of stars displays a large range of metallicities from  $[\text{Fe}/\text{H}] = -1.0$  dex to  $-3.5$  dex. Thanks to a large number of abundances obtained for  $\alpha$ -elements the position of the knee was determined around  $[\text{Fe}/\text{H}] = -2.0$  dex corresponding to the domination of SNeIa over SNeII in the chemical evolution. A lower knee than in Fornax and Sculptor suggests that star formation was less efficient in Sextans in agreement with their estimated masses. The absence of intrinsic scatter in  $[\alpha/\text{Fe}]$  shows that in the center of Sextans the interstellar medium has been homogeneously enriched through star formation. Sextans probably suffered from some tidal interactions with the Milky Way along its orbit causing maybe the quenching of star formation in its outskirts. The star formation was probably much less or not affected in the center and could continue until reaching the observed homogeneous medium. This scenario could explain the metallicity gradient observed in the whole dwarf galaxy. From neutron-capture elements results, Sextans as other dSphs show that above a certain galaxy stellar mass the r-process enrichment seems to be universal for any system implying that the nucleosynthesis source should be the same. Thanks to these results new observational data (abundances) are brought to better constrain theoretical models of nucleosynthesis sites. For further investigations it would be interesting to observe stars of the outer parts of Sextans with high resolution spectroscopy in order to test the presence of inhomogeneities and trace a precise gradient. In that sense an application for observing time (PI Pierre North) has been accepted by ESO for studying  $\sim 60$  Sextans stars in an off centered field (about half a degree away from the center) using FLAMES-GIRAFFE during 25 hours. This study shows that high resolution and high signal-to-noise spectra are needed to obtain reliable abundances.



# **A An appendix**

Table A.1: Position, photometry and radial velocities of our targets. V and I magnitudes are from ESO/WFI and J, H and K magnitudes from UKIDSS. The radial velocities were determined using cross-correlation with an input line list thanks to the program DAOSPEC (Stetson & Pancino 2008). The radial velocities given here are the average between the three radial velocities obtained in each grating, therefore we put a tilde before the radial velocities in the cases of probable binaries. In the last column we comment on particularities noticed for some stars of our sample : non-member, binary, polluted spectra (by a calibration lamp), carbon star, or incomplete spectra. For the rest of the study we left aside the non-members and carbon stars.

ID	RA hms	Dec dms	V mag	I mag	J mag	H mag	K mag	$v_{r,mean}$ km/s	Comments
S05-10	+10 12 39.0	-01 29 58.9	17.915	16.740	15.696	15.072	14.987	234.40 ± 0.67	
S05-47	+10 12 27.0	-01 30 21.2	18.373	17.380	16.469	15.917	15.867	229.83 ± 1.20	
S05-60	+10 13 17.1	-01 26 38.0	18.925	17.963	17.134	16.659	16.543	241.55 ± 1.99	
S05-67	+10 12 40.2	-01 29 07.6	19.253	18.290	17.398	16.869	16.801	232.12 ± 1.56	
S05-70	+10 12 44.3	-01 33 48.3	19.300	18.370	17.580	17.145	17.166	224.76 ± 2.30	<sup>1</sup>
S05-72	+10 13 09.9	-01 29 34.8	19.336	18.358	17.498	16.986	17.042	233.15 ± 1.87	Non-member (c), polluted spectra
S05-78	+10 13 18.9	-01 26 58.2	19.357	18.396	17.598	17.128	17.028	221.70 ± 2.96	<sup>2</sup>
S05-84	+10 13 37.2	-01 32 04.3	19.492	18.643	17.900	17.485	17.320	225.92 ± 2.25	
S05-86	+10 12 37.9	-01 28 23.1	19.561	18.655	17.821	17.299	16.906	221.72 ± 1.79	
S05-93	+10 12 59.5	-01 33 45.2	19.712	18.812	18.050	17.602	17.417	234.64 ± 1.55	
S05-94	+10 13 11.9	-01 29 46.6	19.797	18.831	18.042	17.485	17.292	224.61 ± 2.78	
S05-95	+10 13 34.9	-01 29 49.8	19.798	18.881	18.046	17.619	17.564	222.33 ± 2.07	
S05-98	+10 12 58.8	-01 28 25.8	19.832	18.906	18.063	17.579	17.395	228.65 ± 1.71	
S05-100	+10 12 32.6	-01 32 08.9	19.836	18.959	18.160	17.721	17.764	131.84 ± 1.63	Non-member (v), polluted spectra
S05-101	+10 12 31.1	-01 32 53.7	19.857	18.922	17.995	17.499	17.547	232.77 ± 2.57	
S05-104	+10 13 04.5	-01 26 10.7	19.889	19.036	18.303	17.898	17.536	~ 237.92 ± 2.62	binary
S05-111	+10 13 19.7	-01 33 25.8	19.940	19.071	18.318	17.782	17.664	220.24 ± 1.73	
S05-112	+10 13 33.0	-01 30 53.6	19.938	19.073	18.352	17.832	17.777	213.25 ± 2.52	
S05-115	+10 13 22.7	-01 33 41.6	19.952	19.095	18.219	17.885	17.698	218.83 ± 2.17	
S05-123	+10 13 21.1	-01 33 27.5	20.094	19.232	18.500	18.041	17.963	222.77 ± 2.06	

<sup>1</sup>Incomplete spectra (not present in HR10)

<sup>2</sup>Incomplete spectra (not present in HR10)

Table A.1: continued.

ID	RA hms	Dec dms	V mag	I mag	J mag	H mag	K mag	$v_{r,mean}$ km/s	Comments
S05-132	+10 12 43.0	-01 33 10.8	20.400	19.469	18.839	18.221	18.787	222.16 $\pm$ 2.58	polluted spectra
S05-133	+10 13 27.3	-01 30 56.5	20.309	19.413	18.593	18.406	18.420	224.42 $\pm$ 2.61	
S05-168	+10 12 14.0	-01 33 38.0	19.985	19.038	18.273	17.644	17.586	218.73 $\pm$ 2.20	
S07-16	+10 13 40.2	-01 33 39.6	17.958	16.873	15.891	15.344	15.237	$\sim$ 230.63 $\pm$ 0.93	binary, polluted spectra
S07-69	+10 13 38.6	-01 40 45.7	18.793	17.877	16.918	16.395	16.349	221.04 $\pm$ 1.47	
S07-76	+10 13 44.9	-01 36 30.7	19.081	18.202	17.412	16.970	16.828	213.71 $\pm$ 2.25	
S07-79	+10 13 41.4	-01 35 38.7	19.160	18.227	17.431	16.929	16.870	228.85 $\pm$ 1.84	polluted spectra
S07-81	+10 13 38.7	-01 39 12.9	19.173	18.294	17.472	17.009	17.032	237.95 $\pm$ 1.79	
S07-83	+10 13 37.6	-01 42 57.6	19.191	18.357	17.556	17.093	17.100	199.79 $\pm$ 1.75	
S07-110	+10 13 40.9	-01 43 52.8	19.891	19.099	18.470	17.979	17.616	224.13 $\pm$ 2.32	Non-member (v)
S07-112	+10 13 37.8	-01 38 15.4	19.989	19.128	18.500	18.009	17.966	238.63 $\pm$ 1.96	
S07-115	+10 13 43.0	-01 37 13.5	20.165	19.282	18.528	18.107	17.977	$\sim$ 220.71 $\pm$ 2.47	
S08-3	+10 12 41.8	-01 45 27.2	17.368	16.059	14.937	14.277	14.180	225.63 $\pm$ 0.39	binary
S08-6	+10 12 37.3	-01 49 04.3	17.526	16.278	15.366	14.602	14.627	227.29 $\pm$ 0.53	
S08-38	+10 13 27.3	-01 34 04.8	17.942	16.861	15.899	15.337	15.229	234.90 $\pm$ 0.80	
S08-45	+10 12 24.1	-01 45 00.0	18.072	17.221	16.446	15.966	15.900	82.71 $\pm$ 0.70	Non-member (v)
S08-55	+10 13 37.4	-01 44 31.9	18.772	17.897	17.013	16.550	16.537	227.93 $\pm$ 1.90	carbon star
S08-59	+10 12 45.4	-01 47 55.9	18.865	18.072	17.341	16.839	16.962	225.47 $\pm$ 1.90	Non-member (v)
S08-71	+10 12 26.9	-01 44 31.7	19.218	18.325	17.460	17.040	16.906	213.23 $\pm$ 2.18	
S08-72	+10 13 26.0	-01 45 24.9	19.307	18.392	17.488	17.011	16.812	222.86 $\pm$ 2.22	
S08-75	+10 13 28.5	-01 45 10.4	19.377	18.441	17.623	17.132	16.994	226.18 $\pm$ 1.97	carbon star
S08-89	+10 12 26.7	-01 45 05.0	19.716	18.665	17.732	17.207	17.056	263.49 $\pm$ 1.53	polluted spectra
S08-98	+10 12 37.7	-01 44 14.8	19.811	18.867	18.168	17.558	17.583	227.81 $\pm$ 1.66	Non-member (v)
S08-99	+10 13 02.1	-01 46 08.9	19.883	18.851	17.927	17.468	17.241	128.75 $\pm$ 2.18	Non-member (v)
S08-102	+10 12 21.2	-01 44 52.8	19.934	19.063	18.302	17.722	17.725	181.40 $\pm$ 1.88	Non-member (v), polluted spectra
S08-111	+10 12 32.1	-01 46 00.0	20.225	19.365	18.527	18.043	17.968	223.71 $\pm$ 2.27	Non-member (c)
S08-113	+10 12 25.9	-01 47 33.0	20.257	19.426	18.664	18.270	17.722	225.84 $\pm$ 1.75	Non-member (v)
S08-131	+10 12 12.0	-01 36 02.4	19.075	18.075	17.192	16.694	16.548	$\sim$ 234.21 $\pm$ 1.72	

Table A.1: continued.

ID	RA hms	Dec dms	V mag	I mag	J mag	H mag	K mag	$v_{r,mean}$ km/s	Comments
S08-151	+10 12 08.9	-01 35 46.7	19.997	19.102	18.253	17.701	17.689	229.75 $\pm$ 1.91	
S08-183	+10 12 47.9	-01 29 38.7	18.992	18.112	17.370	16.836	16.775	223.09 $\pm$ 1.81	polluted spectra
S08-184	+10 12 42.8	-01 30 08.3	18.995	18.088	17.264	16.785	16.756	$\sim$ 214.21 $\pm$ 1.46	binary
S08-199	+10 12 59.4	-01 28 03.3	19.570	18.711	17.942	17.500	17.255	222.44 $\pm$ 2.31	
S08-202	+10 13 12.4	-01 29 17.0	19.635	18.684	17.966	17.454	17.306	241.07 $\pm$ 1.96	polluted spectra
S08-203	+10 12 51.9	-01 30 00.9	19.699	18.777	17.973	17.422	17.406	230.03 $\pm$ 1.80	
S08-222	+10 13 00.6	-01 30 35.5	20.166	19.255	18.389	17.974	18.315	218.09 $\pm$ 2.11	
S08-225	+10 12 37.3	-01 26 43.3	20.183	19.358	18.552	18.062	17.729	220.23 $\pm$ 2.10	
S08-232	+10 13 03.1	-01 42 13.9	18.448	17.492	16.539	15.899	15.836	$\sim$ 228.03 $\pm$ 0.64	binary, carbon star
S08-239	+10 12 35.9	-01 41 15.2	18.672	17.641	16.604	16.049	16.095	217.65 $\pm$ 0.88	
S08-241	+10 12 49.3	-01 42 18.0	18.726	17.757	16.824	16.299	16.250	216.65 $\pm$ 1.58	
S08-242	+10 13 10.2	-01 42 07.0	18.765	17.763	16.859	16.281	16.296	231.07 $\pm$ 1.51	
S08-245	+10 13 40.2	-01 38 48.3	18.912	17.945	17.160	16.582	16.555	244.62 $\pm$ 2.10	
S08-246	+10 13 25.9	-01 36 10.8	18.926	17.964	17.072	16.572	16.437	210.54 $\pm$ 1.31	
S08-250	+10 13 16.7	-01 39 56.5	19.093	18.227	17.255	16.645	16.616	220.38 $\pm$ 1.11	
S08-252	+10 13 18.2	-01 35 15.6	19.159	18.249	17.430	16.942	16.836	$\sim$ 210.45 $\pm$ 2.13	binary
S08-253	+10 12 56.3	-01 39 21.0	19.162	18.256	17.409	16.833	16.876	224.59 $\pm$ 1.45	
S08-257	+10 12 35.1	-01 39 40.2	19.187	18.270	17.330	16.893	16.971	230.25 $\pm$ 1.97	
S08-258	+10 12 38.8	-01 41 44.9	19.219	18.313	17.471	16.914	16.940	228.22 $\pm$ 2.08	
S08-259	+10 12 25.9	-01 32 38.9	19.226	18.299	17.380	16.850	16.692	231.87 $\pm$ 1.69	
S08-261	+10 13 08.9	-01 36 04.6	19.259	18.379	17.595	17.135	17.064	211.54 $\pm$ 2.19	polluted spectra
S08-264	+10 12 40.9	-01 32 01.1	19.317	18.384	17.600	17.038	16.995	216.49 $\pm$ 1.98	
S08-266	+10 13 20.8	-01 35 57.5	19.302	18.314	17.474	16.961	16.864	44.33 $\pm$ 0.79	Non-member (v), polluted spectra
S08-267	+10 13 07.5	-01 41 12.8	19.287	18.466	17.608	17.148	17.006	219.38 $\pm$ 1.95	polluted spectra
S08-269	+10 12 25.2	-01 33 52.9	19.396	18.385	17.561	16.991	16.834	13.27 $\pm$ 1.20	Non-member (v)
S08-274	+10 12 29.9	-01 34 31.8	19.386	18.486	17.593	17.139	17.210	209.01 $\pm$ 2.90	<sup>3</sup>

<sup>3</sup>Incomplete spectra (not present in HR13 and HR14)



Table A.1: continued.

ID	RA hms	Dec dms	V mag	I mag	J mag	H mag	K mag	$v_{r,mean}$ km/s	Comments
S08-280	+10 12 20.7	-01 37 39.3	19.554	18.669	17.856	17.319	17.231	228.92 $\pm$ 1.95	
S08-282	+10 13 02.0	-01 36 58.5	19.596	18.770	18.027	17.531	17.371	$\sim$ 217.08 $\pm$ 2.03	binary
S08-284	+10 13 11.2	-01 35 01.8	19.633	18.740	18.021	17.354	17.262	233.68 $\pm$ 1.85	polluted spectra
S08-285	+10 13 05.6	-01 31 27.8	19.651	18.544	17.612	17.014	16.874	80.82 $\pm$ 0.86	Non-member (v), polluted spectra
S08-289	+10 13 01.8	-01 35 24.1	19.766	18.890	18.091	17.633	17.526	218.45 $\pm$ 1.81	polluted spectra
S08-291	+10 13 06.6	-01 34 19.3	19.779	18.921	18.085	17.699	17.520	220.77 $\pm$ 2.08	
S08-292	+10 13 26.2	-01 31 50.1	19.827	18.902	18.205	17.615	17.435	228.02 $\pm$ 2.10	
S08-293	+10 12 43.1	-01 40 14.8	19.779	18.934	18.649	17.478	17.547	231.06 $\pm$ 1.95	Non-member (c), polluted spectra
S08-295	+10 13 01.4	-01 36 24.1	19.801	18.951	18.198	17.772	17.883	225.42 $\pm$ 2.31	polluted spectra
S08-298	+10 12 30.7	-01 42 07.5	19.823	18.914	18.109	17.507	17.530	226.51 $\pm$ 1.65	
S08-301	+10 13 26.4	-01 36 36.0	19.833	18.969	18.149	17.729	17.420	215.38 $\pm$ 2.27	Non-member (c)
S08-303	+10 13 09.6	-01 37 32.9	19.850	18.975	18.133	17.613	17.541	222.13 $\pm$ 1.51	polluted spectra
S08-306	+10 12 40.6	-01 35 47.5	19.880	18.958	18.609	17.658	17.220	219.45 $\pm$ 2.09	carbon star
S08-307	+10 12 50.6	-01 34 56.6	19.889	18.996	18.088	17.802	17.765	217.88 $\pm$ 2.38	
S08-309	+10 13 08.2	-01 35 53.4	19.895	19.073	18.226	17.915	17.594	$\sim$ 228.29 $\pm$ 2.37	binary, bad spectra
S08-316	+10 12 50.5	-01 33 32.9	19.967	19.078	18.179	17.819	17.717	$\sim$ 213.73 $\pm$ 2.20	binary
S08-317	+10 13 06.2	-01 33 10.3	19.976	19.090	18.368	17.913	17.843	$\sim$ 222.50 $\pm$ 1.88	binary, polluted spectra
S08-321	+10 12 59.1	-01 34 42.6	20.016	19.183	18.434	17.868	17.830	217.62 $\pm$ 1.81	Non-member (c)
S08-322	+10 13 11.2	-01 42 36.2	20.023	19.139	18.355	17.922	17.813	$\sim$ 263.00 $\pm$ 2.90	Non-member (v), binary
S08-323	+10 13 03.3	-01 37 22.5	20.030	19.138	18.321	17.858	17.911	213.50 $\pm$ 1.87	
S08-327	+10 12 23.0	-01 37 46.7	20.072	19.061	18.045	17.540	17.419	84.10 $\pm$ 1.52	Non-member (v)
S08-331	+10 12 33.8	-01 31 58.9	20.155	19.242	18.466	17.909	17.969	228.48 $\pm$ 2.46	polluted spectra
S08-332	+10 12 31.8	-01 32 49.4	20.187	19.235	18.473	17.850	18.252	$\sim$ 242.07 $\pm$ 1.91	binary, polluted spectra
S08-336	+10 12 54.5	-01 35 49.2	20.211	19.373	18.650	18.139	0.000	236.45 $\pm$ 2.42	polluted spectra
S08-337	+10 12 22.8	-01 39 22.0	20.213	19.214	18.235	17.690	17.556	54.23 $\pm$ 2.12	Non-member (v)
S08-339	+10 13 00.7	-01 41 05.7	20.865	19.345	18.591	18.300	18.219	229.11 $\pm$ 2.16	
S08-341	+10 13 14.1	-01 33 48.4	20.271	19.430	18.645	18.115	18.151	213.76 $\pm$ 1.72	
S11-97	+10 12 27.8	-01 48 05.1	18.189	17.125	16.204	15.653	15.542	219.63 $\pm$ 1.68	polluted spectra

Table A.1: continued.

ID	RA hms	Dec dms	V mag	I mag	J mag	H mag	K mag	$v_{r,mean}$ km/s	Comments
S11-100	+10 13 05.9	-01 44 51.4	18.397	17.387	16.450	15.886	15.792	223.71 $\pm$ 0.82	polluted spectra
S11-111	+10 12 44.7	-01 42 48.8	18.924	17.855	16.854	16.319	16.246	232.38 $\pm$ 2.07	carbon star
S11-113	+10 12 53.8	-01 45 27.0	18.976	18.025	17.158	16.583	16.495	226.69 $\pm$ 0.80	
S11-114	+10 13 04.8	-01 45 10.8	19.088	18.172	17.216	16.683	16.578	215.55 $\pm$ 2.60	carbon star
S11-127	+10 13 27.1	-01 47 27.4	19.441	18.563	17.679	17.236	17.130	230.20 $\pm$ 1.93	
S11-137	+10 12 18.3	-01 40 22.3	19.695	18.782	17.824	17.308	17.010	222.03 $\pm$ 1.86	
S11-139	+10 12 53.7	-01 45 02.8	19.787	18.890	18.178	17.631	17.751	225.85 $\pm$ 1.82	
S11-141	+10 13 21.7	-01 47 44.3	19.799	18.938	18.172	17.710	17.551	228.30 $\pm$ 2.62	polluted spectra

Table A.2: The first columns are dedicated to parameters derived from photometry for our sample members : the four color temperatures, the bolometric corrections, the bolometric magnitudes. The last column gives a first estimate of metallicity : either the value derived from the Intermediate Resolution DART Ca II triplet survey if the star was previously observed or a fixed value corresponding to the average [Fe/H] given by Battaglia et al. (2011) -1.9 dex.

ID	$T_{(V-I)}$ K	$T_{(V-J)}$ K	$T_{(V-H)}$ K	$T_{(V-K)}$ K	$BC_V$ mag	$M_{bol}$ mag	[Fe/H] CaT dex
S05-10	4337	4350	4315	4366	-0.57	-2.57	-1.88±0.08
S05-47	4628	4667	4626	4694	-0.41	-1.96	-1.75±0.15
S05-60	4711	4832	4811	4830	-0.37	-1.36	-2.24±0.15
S05-67	4716	4764	4700	4764	-0.39	-1.06	-2.36±0.30
S05-70	4763	4907	4934	5069	-0.32	-0.94	-1.90
S05-78	4727	4894	4856	4892	-0.36	-0.92	-2.47±0.19
S05-84	4955	5104	5092	5042	-0.28	-0.71	-1.90
S05-86	4817	4888	4790	4591	-0.37	-0.73	-1.90
S05-93	4831	4995	4969	4911	-0.31	-0.52	-1.90
S05-94	4687	4869	4754	4708	-0.37	-0.50	-1.90
S05-95	4792	4861	4902	4965	-0.33	-0.45	-1.90
S05-98	4853	4966	4843	4812	-0.38	-0.47	-3.44±1.88
S05-101	4753	4721	4725	4878	-0.37	-0.43	-1.90
S05-104	4945	5113	5095	4865	-0.29	-0.32	-1.90
S05-111	4904	5067	4919	4923	-0.30	-0.29	-1.82±0.28
S05-112	4927	5150	4990	5052	-0.32	-0.30	-2.85±0.55
S05-115	4935	4878	5018	4954	-0.31	-0.28	-1.90
S05-123	4932	5123	5051	5096	-0.29	-0.12	-2.25±0.47
S05-132	4761	5181	4949	5725	-0.26	0.22	-1.90
S05-133	4847	4903	5244	5390	-0.30	0.09	-2.72±0.74
S05-168	4727	4939	4735	4797	-0.36	-0.29	-1.90
S07-16	4480	4502	4490	4524	-0.50	-2.46	-2.06±0.09
S07-69	4799	4716	4683	4759	-0.38	-1.51	-2.05±0.14
S07-76	4882	4992	4970	4942	-0.33	-1.17	-2.67±0.37
S07-79	4762	4908	4848	4911	-0.34	-1.10	-2.05±0.23
S07-81	4882	4947	4923	5057	-0.33	-1.08	-2.67±0.30
S07-110	5110	5428	5195	4946	-0.25	-0.28	-1.90
S07-112	4925	5295	5136	5207	-0.26	-0.19	-1.90
S07-115	4871	5032	5033	5021	-0.30	-0.05	-1.90
S08-3	4176	4179	4152	4199	-0.69	-3.24	-1.85±0.05
S08-6	4228	4399	4263	4376	-0.58	-2.98	-1.62±0.03
S08-38	4490	4531	4498	4532	-0.49	-2.47	-2.11±0.08

Table A.2: continued.

ID	$T_{(V-I)}$ K	$T_{(V-J)}$ K	$T_{(V-H)}$ K	$T_{(V-K)}$ K	$BC_V$ mag	$M_{bol}$ mag	[Fe/H] CaT dex
S08-59	5116	5256	5104	5370	-0.26	-1.32	-2.36±0.12
S08-71	4863	4883	4901	4889	-0.36	-1.06	-2.84±0.39
S08-75	4745	4857	4824	4813	-0.35	-0.89	-1.69±0.20
S08-98	4733	5043	4829	4965	-0.33	-0.43	-1.90
S08-113	5002	5098	5083	4703	-0.30	0.04	-1.84±0.38
S08-131	4611	4684	4688	4679	-0.41	-1.25	-1.63±0.31
S08-151	4843	4885	4783	4884	-0.34	-0.26	-1.90
S08-183	4876	5066	4926	4981	-0.30	-1.23	-1.80±0.14
S08-184	4821	4906	4874	4965	-0.33	-1.26	-2.10±0.29
S08-199	4933	5054	5012	4899	-0.30	-0.66	-2.03±0.25
S08-202	4717	4990	4892	4871	-0.33	-0.62	-1.85±0.23
S08-203	4785	4917	4797	4887	-0.36	-0.58	-2.64±0.41
S08-222	4827	4859	4928	5422	-0.31	-0.06	-2.41±0.51
S08-225	5022	5059	4949	4772	-0.31	-0.05	-2.11±0.83
S08-239	4566	4495	4490	4631	-0.47	-1.72	-1.97±0.11
S08-241	4687	4683	4656	4729	-0.40	-1.60	-2.05±0.11
S08-242	4618	4676	4606	4728	-0.41	-1.57	-1.94±0.11
S08-245	4714	4910	4750	4836	-0.38	-1.39	-2.87±0.35
S08-246	4702	4741	4719	4724	-0.39	-1.38	-2.07±0.15
S08-250	4914	4767	4637	4725	-0.37	-1.20	-1.98±0.14
S08-252	4824	4925	4865	4892	-0.34	-1.10	-2.32±0.22
S08-253	4833	4901	4761	4919	-0.35	-1.11	-2.33±0.18
S08-257	4817	4767	4796	4981	-0.37	-1.10	-2.91±0.39
S08-258	4823	4890	4779	4918	-0.34	-1.04	-2.09±0.18
S08-259	4771	4747	4695	4681	-0.39	-1.08	-1.94±0.33
S08-261	4905	5043	4974	5026	-0.33	-1.00	-3.01±0.47
S08-264	4767	4939	4802	4881	-0.35	-0.95	-2.16±0.39
S08-267	5044	5006	4952	4945	-0.31	-0.95	-2.45±0.22
S08-274	4831	4807	4839	5018	-0.33	-0.87	-1.90
S08-280	4866	4951	4840	4875	-0.33	-0.69	-1.90
S08-282	5016	5153	5023	4983	-0.28	-0.61	-1.90
S08-284	4847	5101	4794	4827	-0.33	-0.61	-1.90
S08-289	4888	4977	4949	4963	-0.31	-0.46	-1.90
S08-291	4932	4941	5004	4948	-0.31	-0.45	-1.90
S08-292	4778	5080	4859	4817	-0.33	-0.42	-2.02±0.24
S08-295	4953	5087	5088	5327	-0.26	-0.38	-1.90

Table A.2: continued.

ID	$T_{(V-I)}$ K	$T_{(V-J)}$ K	$T_{(V-H)}$ K	$T_{(V-K)}$ K	$BC_V$ mag	$M_{bol}$ mag	[Fe/H] CaT dex
S08-298	4810	4934	4765	4897	-0.34	-0.44	-1.90
S08-303	4890	4921	4839	4888	-0.33	-0.40	-1.90
S08-307	4847	4780	5007	5086	-0.31	-0.35	-1.90
S08-309	5026	4970	5112	4915	-0.29	-0.32	-1.90
S08-316	4857	4805	4933	4952	-0.33	-0.28	-1.90
S08-317	4861	5078	5030	5073	-0.29	-0.23	-1.73±0.38
S08-323	4850	4926	4918	5084	-0.31	-0.20	-1.90
S08-331	4801	4966	4839	5008	-0.32	-0.09	-1.90
S08-332	4716	4936	4770	5277	-0.32	-0.05	-1.90
S08-336	4984	5169	4026	0	-0.38	-0.09	-1.90
S08-339	4011	4281	4528	4577	-0.56	0.38	-1.90
S08-341	4982	5076	4940	5096	-0.30	0.05	-2.19±0.78
S11-97	4540	4616	4550	4585	-0.47	-2.20	-2.80±0.14
S11-100	4607	4631	4577	4617	-0.44	-1.96	-2.02±0.09
S11-113	4712	4776	4681	4717	-0.38	-1.33	-1.66±0.13
S11-127	4883	4849	4870	4888	-0.33	-0.81	-1.90
S11-137	4801	4712	4675	4561	-0.40	-0.63	-1.90
S11-139	4838	5092	4941	5176	-0.29	-0.42	-1.90
S11-141	4925	5053	4995	4958	-0.30	-0.42	-1.90

**Appendix A. An appendix**

---

Table A.3: The four columns are estimations of the signal-to-noise ratios S/N of spectra in each grating and also in average.

ID	S/N <sub>HR10</sub>	S/N <sub>HR13</sub>	S/N <sub>HR14</sub>	S/N <sub>av</sub>
S05-10	75	64	75	71
S05-47	31	25	33	30
S05-60	22	14	21	19
S05-67	22	15	31	23
S05-70	0	16	25	20
S05-78	0	10	16	13
S05-84	11	7	12	10
S05-86	13	9	22	15
S05-93	20	10	17	16
S05-94	11	9	17	12
S05-95	9	5	9	8
S05-98	9	11	18	13
S05-101	8	4	8	7
S05-104	10	8	18	12
S05-111	15	10	18	14
S05-112	6	4	10	7
S05-115	17	8	13	13
S05-123	10	6	11	9
S05-132	8	5	11	8
S05-133	9	5	10	8
S05-168	5	4	10	6
S07-16	48	32	79	53
S07-69	28	29	41	33
S07-76	25	15	30	23
S07-79	24	9	22	18
S07-81	26	18	25	23
S07-110	7	5	10	7
S07-112	10	6	14	10
S07-115	8	5	12	8
S08-3	96	141	114	117
S08-6	53	89	106	83
S08-38	62	62	83	69
S08-59	27	25	40	31
S08-71	24	22	35	27

Table A.3: continued.

ID	$S/N_{HR10}$	$S/N_{HR13}$	$S/N_{HR14}$	$S/N_{av}$
S08-75	15	12	23	17
S08-98	17	14	22	18
S08-113	7	8	9	8
S08-131	19	14	24	19
S08-151	6	4	12	7
S08-183	25	22	23	23
S08-184	23	14	30	22
S08-199	18	8	23	16
S08-202	17	11	21	16
S08-203	14	9	17	13
S08-222	11	7	15	11
S08-225	5	4	6	5
S08-239	53	40	60	51
S08-241	46	41	72	53
S08-242	41	32	40	38
S08-245	28	17	33	26
S08-246	27	19	44	30
S08-250	27	22	30	26
S08-252	23	24	39	29
S08-253	35	23	45	34
S08-257	21	29	48	33
S08-258	27	17	41	28
S08-259	16	17	23	19
S08-261	24	20	26	23
S08-264	14	17	24	18
S08-267	29	17	32	26
S08-274	18	0	0	18
S08-280	15	16	17	16
S08-282	16	13	26	18
S08-284	19	12	25	19
S08-289	14	15	22	17
S08-291	13	12	16	14
S08-292	8	8	13	10
S08-295	12	19	27	19
S08-298	15	12	18	15
S08-303	14	13	26	18

Table A.3: continued.

ID	$S/N_{HR10}$	$S/N_{HR13}$	$S/N_{HR14}$	$S/N_{av}$
S08-307	16	12	17	15
S08-309	4	8	15	9
S08-316	4	5	8	6
S08-317	12	9	18	13
S08-323	13	12	21	15
S08-331	11	6	11	9
S08-332	10	4	16	10
S08-336	11	6	12	10
S08-339	12	8	13	11
S08-341	16	5	5	9
S11-97	49	37	60	49
S11-100	44	56	61	54
S11-113	32	26	42	33
S11-127	9	8	14	10
S11-137	12	16	25	18
S11-139	19	13	28	20
S11-141	10	6	9	8



---

Table A.4: The list of stars concerned by the pollution due to simultaneous calibration fibres. The terms in second and third column indicate which setup suffered from pollution.

ID	HR10 polluted	HR13 polluted
S05-100	No	Yes
S05-132	Yes	No
S05-72	No	Yes
S07-16	No	Yes
S07-81	Yes	Yes
S08-102	No	Yes
S08-183	No	Yes
S08-202	Yes	Yes
S08-261	Yes	No
S08-266	Yes	No
S08-267	Yes	No
S08-284	Yes	No
S08-285	No	Yes
S08-289	No	Yes
S08-293	No	Yes
S08-295	No	Yes
S08-303	Yes	No
S08-317	Yes	No
S08-331	Yes	No
S08-332	Yes	Yes
S08-336	No	Yes
S08-75	Yes	Yes
S11-100	No	Yes
S11-141	Yes	Yes
S11-97	Yes	Yes

## Appendix A. An appendix

Table A.5: The radial velocities measured by DAOPSEC in each setup HR10, HR13 and HR14 and the average values with errors. Probable binaries are indicated by a tilde symbol in front of the average radial velocities.

ID	$V_{r,HR10}$ km/s	$V_{r,HR13}$ km/s	$V_{r,HR14}$ km/s	$V_{r,mean}$ km/s
S05-10	234.55 ± 0.69	234.58 ± 1.41	234.08 ± 1.25	234.40 ± 0.67
S05-47	228.90 ± 0.98	229.94 ± 2.28	230.65 ± 2.58	229.83 ± 1.20
S05-60	240.23 ± 1.72	241.68 ± 3.57	242.76 ± 4.45	241.55 ± 1.99
S05-67	232.87 ± 2.01	232.37 ± 2.09	231.13 ± 3.68	232.12 ± 1.56
S05-70	0.00 ± 0.00	223.26 ± 2.33	226.26 ± 3.96	224.76 ± 2.30
S05-72	232.26 ± 2.47	231.43 ± 4.06	235.76 ± 3.00	233.15 ± 1.87
S05-78	0.00 ± 0.00	220.12 ± 3.46	223.28 ± 4.81	221.70 ± 2.96
S05-84	224.73 ± 3.35	227.27 ± 3.97	225.75 ± 4.31	225.92 ± 2.25
S05-86	219.65 ± 1.99	222.28 ± 3.17	223.24 ± 3.85	221.72 ± 1.79
S05-93	235.09 ± 1.83	233.82 ± 1.28	235.02 ± 4.09	234.64 ± 1.55
S05-94	223.38 ± 4.99	222.33 ± 4.70	228.14 ± 4.75	224.61 ± 2.78
S05-95	222.22 ± 2.52	223.87 ± 4.00	220.91 ± 4.03	222.33 ± 2.07
S05-98	227.19 ± 2.70	229.08 ± 3.08	229.68 ± 3.11	228.65 ± 1.71
S05-100	131.96 ± 1.26	131.51 ± 3.61	132.05 ± 3.03	131.84 ± 1.63
S05-101	230.06 ± 3.77	236.03 ± 4.64	232.21 ± 4.87	232.77 ± 2.57
S05-104	224.15 ± 3.15	259.63 ± 4.67	229.98 ± 5.47	~ 237.92 ± 2.62
S05-111	218.91 ± 1.71	220.10 ± 4.29	221.71 ± 2.36	220.24 ± 1.73
S05-112	214.09 ± 3.22	213.34 ± 5.61	212.33 ± 3.91	213.25 ± 2.52
S05-115	219.01 ± 2.60	217.93 ± 4.37	219.55 ± 4.07	218.83 ± 2.17
S05-123	220.07 ± 3.44	223.75 ± 4.15	224.50 ± 3.03	222.77 ± 2.06
S05-132	222.28 ± 4.46	222.78 ± 4.73	221.40 ± 4.20	222.16 ± 2.58
S05-133	222.48 ± 2.94	222.05 ± 5.14	228.73 ± 5.14	224.42 ± 2.61
S05-168	221.77 ± 4.70	215.15 ± 4.38	219.26 ± 1.55	218.73 ± 2.20
S07-16	221.33 ± 0.69	235.25 ± 2.11	235.29 ± 1.67	~ 230.63 ± 0.93
S07-69	220.45 ± 0.95	221.60 ± 1.52	221.09 ± 4.04	221.04 ± 1.47
S07-76	214.45 ± 3.79	211.78 ± 2.58	214.89 ± 4.97	213.71 ± 2.25
S07-79	229.30 ± 1.13	227.20 ± 3.54	230.04 ± 4.06	228.85 ± 1.84
S07-81	239.38 ± 2.59	234.95 ± 3.97	239.53 ± 2.55	237.95 ± 1.79
S07-83	199.41 ± 1.77	199.16 ± 2.62	200.81 ± 4.20	199.79 ± 1.75
S07-110	221.74 ± 4.13	226.34 ± 4.65	224.30 ± 3.09	224.13 ± 2.32
S07-112	239.10 ± 3.14	238.47 ± 3.47	238.34 ± 3.54	238.63 ± 1.96
S07-115	215.31 ± 4.43	221.99 ± 4.75	224.84 ± 3.56	~ 220.71 ± 2.47
S08-3	225.47 ± 0.56	225.76 ± 0.43	225.65 ± 0.92	225.63 ± 0.39

Table A.5: continued.

ID	$V_{r,HR10}$ km/s	$V_{r,HR13}$ km/s	$V_{r,HR14}$ km/s	$V_{r,mean}$ km/s
S08-6	226.26 ± 0.88	227.66 ± 1.05	227.95 ± 0.83	227.29 ± 0.53
S08-38	234.32 ± 0.77	234.89 ± 1.26	235.50 ± 1.88	234.90 ± 0.80
S08-45	82.61 ± 0.66	82.73 ± 0.83	82.77 ± 1.82	82.71 ± 0.70
S08-55	227.63 ± 2.47	230.00 ± 4.25	226.16 ± 2.87	227.93 ± 1.90
S08-59	225.38 ± 0.99	225.86 ± 4.05	225.19 ± 3.90	225.47 ± 1.90
S08-71	215.00 ± 2.23	214.32 ± 3.99	210.36 ± 4.68	213.23 ± 2.18
S08-72	226.51 ± 3.67	221.07 ± 3.67	221.00 ± 4.18	222.86 ± 2.22
S08-75	224.78 ± 1.34	228.19 ± 4.42	225.56 ± 3.68	226.18 ± 1.97
S08-89	263.56 ± 2.51	261.01 ± 2.21	265.90 ± 3.17	263.49 ± 1.53
S08-98	226.38 ± 1.08	229.67 ± 3.36	227.38 ± 3.53	227.81 ± 1.66
S08-99	127.67 ± 2.38	128.92 ± 4.07	129.66 ± 4.55	128.75 ± 2.18
S08-102	180.91 ± 1.47	180.31 ± 2.95	182.97 ± 4.58	181.40 ± 1.88
S08-111	224.31 ± 1.49	224.88 ± 4.57	221.94 ± 4.84	223.71 ± 2.27
S08-113	224.11 ± 2.34	225.55 ± 4.37	227.87 ± 1.72	225.84 ± 1.75
S08-131	225.06 ± 1.96	238.62 ± 3.76	238.96 ± 2.95	~ 234.21 ± 1.72
S08-151	228.95 ± 2.16	230.85 ± 3.42	229.45 ± 4.07	229.75 ± 1.91
S08-183	221.60 ± 1.61	222.50 ± 4.11	225.17 ± 3.18	223.09 ± 1.81
S08-184	205.91 ± 0.80	216.58 ± 2.97	220.14 ± 3.12	~ 214.21 ± 1.46
S08-199	220.51 ± 2.34	221.83 ± 4.42	224.99 ± 4.80	222.44 ± 2.31
S08-202	240.39 ± 2.29	240.42 ± 3.43	242.40 ± 4.18	241.07 ± 1.96
S08-203	228.56 ± 2.13	234.07 ± 4.05	227.46 ± 2.88	230.03 ± 1.80
S08-222	218.44 ± 3.08	217.71 ± 3.35	218.12 ± 4.39	218.09 ± 2.11
S08-225	221.97 ± 3.64	221.14 ± 3.44	217.56 ± 3.83	220.23 ± 2.10
S08-232	232.75 ± 1.43	226.10 ± 0.50	225.23 ± 1.20	~ 228.03 ± 0.64
S08-239	217.50 ± 0.84	217.63 ± 1.69	217.82 ± 1.85	217.65 ± 0.88
S08-241	215.83 ± 0.95	216.41 ± 2.71	217.72 ± 3.77	216.65 ± 1.58
S08-242	231.87 ± 1.23	229.89 ± 2.82	231.45 ± 3.31	231.07 ± 1.51
S08-245	243.91 ± 1.51	242.28 ± 3.33	247.65 ± 5.14	244.62 ± 2.10
S08-246	210.44 ± 1.62	210.85 ± 2.06	210.31 ± 2.92	210.54 ± 1.31
S08-250	220.12 ± 1.03	220.45 ± 0.91	220.56 ± 3.03	220.38 ± 1.11
S08-252	229.93 ± 2.42	199.43 ± 4.88	201.98 ± 3.35	~ 210.45 ± 2.13
S08-253	223.14 ± 1.96	223.62 ± 2.28	227.00 ± 3.14	224.59 ± 1.45
S08-257	230.17 ± 3.14	231.77 ± 2.38	228.82 ± 4.40	230.25 ± 1.97
S08-258	226.55 ± 2.76	226.49 ± 3.29	231.61 ± 4.54	228.22 ± 2.08
S08-259	230.34 ± 1.87	232.97 ± 3.29	232.31 ± 3.37	231.87 ± 1.69
S08-261	208.49 ± 2.05	211.77 ± 4.08	214.37 ± 4.72	211.54 ± 2.19

Table A.5: continued.

ID	$V_{r,HR10}$ km/s	$V_{r,HR13}$ km/s	$V_{r,HR14}$ km/s	$V_{r,mean}$ km/s
S08-264	215.82 ± 1.52	215.77 ± 3.51	217.89 ± 4.54	216.49 ± 1.98
S08-266	43.64 ± 1.19	45.07 ± 1.12	44.29 ± 1.69	44.33 ± 0.79
S08-267	216.96 ± 1.88	218.91 ± 3.59	222.28 ± 4.20	219.38 ± 1.95
S08-269	12.80 ± 1.93	13.39 ± 2.10	13.62 ± 2.20	13.27 ± 1.20
S08-274	209.01 ± 2.90	0.00 ± 0.00	0.00 ± 0.00	209.01 ± 2.90
S08-280	228.04 ± 2.07	229.06 ± 4.29	229.66 ± 3.42	228.92 ± 1.95
S08-282	213.80 ± 2.43	216.44 ± 4.31	220.99 ± 3.54	~ 217.08 ± 2.03
S08-284	233.08 ± 1.50	234.04 ± 3.94	233.91 ± 3.60	233.68 ± 1.85
S08-285	80.91 ± 1.07	80.39 ± 2.16	81.16 ± 0.89	80.82 ± 0.86
S08-289	217.91 ± 2.55	215.84 ± 3.09	221.61 ± 3.68	218.45 ± 1.81
S08-291	222.40 ± 1.35	221.97 ± 2.12	217.94 ± 5.71	220.77 ± 2.08
S08-292	226.03 ± 3.80	225.81 ± 3.51	232.21 ± 3.57	228.02 ± 2.10
S08-293	231.16 ± 1.64	231.41 ± 3.32	230.63 ± 4.51	231.06 ± 1.95
S08-295	227.97 ± 3.22	223.75 ± 5.20	224.55 ± 3.25	225.42 ± 2.31
S08-298	226.23 ± 2.59	226.73 ± 2.63	226.56 ± 3.31	226.51 ± 1.65
S08-301	214.84 ± 2.67	217.20 ± 4.86	214.09 ± 3.97	215.38 ± 2.27
S08-303	221.69 ± 1.65	223.58 ± 3.91	221.11 ± 1.55	222.13 ± 1.51
S08-306	220.50 ± 3.83	217.44 ± 3.57	220.41 ± 3.45	219.45 ± 2.09
S08-307	218.63 ± 2.36	221.76 ± 4.12	213.24 ± 5.36	217.88 ± 2.38
S08-309	219.55 ± 3.64	232.58 ± 3.64	232.73 ± 4.91	~ 228.29 ± 2.37
S08-316	208.80 ± 2.76	213.19 ± 4.34	219.21 ± 4.16	~ 213.73 ± 2.20
S08-317	220.77 ± 3.51	219.54 ± 3.07	227.20 ± 3.16	~ 222.50 ± 1.88
S08-321	217.69 ± 2.39	217.52 ± 3.38	217.65 ± 3.54	217.62 ± 1.81
S08-322	288.02 ± 4.98	250.71 ± 4.41	250.28 ± 5.61	~ 263.00 ± 2.90
S08-323	213.85 ± 2.60	213.76 ± 4.63	212.89 ± 1.78	213.50 ± 1.87
S08-327	83.73 ± 1.12	84.92 ± 2.43	83.64 ± 3.71	84.10 ± 1.52
S08-331	226.88 ± 3.22	229.67 ± 5.14	228.89 ± 4.23	228.48 ± 2.46
S08-332	238.28 ± 4.55	242.93 ± 3.06	244.99 ± 1.65	~ 242.07 ± 1.91
S08-336	233.03 ± 4.69	238.43 ± 4.69	237.88 ± 2.98	236.45 ± 2.42
S08-337	54.42 ± 2.60	52.89 ± 3.90	55.38 ± 4.29	54.23 ± 2.12
S08-339	231.26 ± 3.02	227.01 ± 4.64	229.05 ± 3.40	229.11 ± 2.16
S08-341	214.56 ± 3.12	215.04 ± 3.66	211.68 ± 1.86	213.76 ± 1.72
S11-97	218.61 ± 2.68	219.62 ± 2.65	220.65 ± 3.35	219.63 ± 1.68
S11-100	223.51 ± 1.25	224.08 ± 1.44	223.54 ± 1.57	223.71 ± 0.82
S11-111	229.99 ± 3.75	233.55 ± 4.01	233.59 ± 2.91	232.38 ± 2.07
S11-113	226.55 ± 0.96	227.27 ± 1.38	226.25 ± 1.70	226.69 ± 0.80

Table A.5: continued.

ID	$V_{r,HR10}$ km/s	$V_{r,HR13}$ km/s	$V_{r,HR14}$ km/s	$V_{r,mean}$ km/s
S11-114	214.97 ± 3.19	215.69 ± 4.93	215.98 ± 5.13	215.55 ± 2.60
S11-127	228.43 ± 3.19	228.39 ± 3.12	233.77 ± 3.71	230.20 ± 1.93
S11-137	220.65 ± 1.82	222.71 ± 3.67	222.73 ± 3.78	222.03 ± 1.86
S11-139	226.48 ± 1.63	226.79 ± 3.96	224.29 ± 3.39	225.85 ± 1.82
S11-141	230.19 ± 3.62	225.86 ± 4.65	228.86 ± 5.19	228.30 ± 2.62

## Appendix A. An appendix

---

Table A.6: The complete line list used to derive all the atomic abundances : wavelength, species, excitation potential, oscillator strength and C6 constant. The hyperfine components are indicated in *italic* and their corresponding equivalent lines are followed by the text (*equi*). The references for HFS are given in the text.

$\lambda$ Å	El	$\chi_{exc}$ eV	$\log(gf)$	$C_6$
5528.410	MgI	4.350	-0.360	1.63e-30
5349.470	CaI	2.710	-0.310	0.00e+00
5581.970	CaI	2.520	-0.710	0.00e+00
5588.750	CaI	2.520	0.210	0.00e+00
5590.110	CaI	2.520	-0.710	0.00e+00
5601.280	CaI	2.520	-0.690	0.00e+00
6161.300	CaI	2.520	-1.270	5.98e-31
6162.170	CaI	1.900	-0.090	0.00e+00
6166.440	CaI	2.520	-1.140	5.95e-31
6169.040	CaI	2.520	-0.800	5.95e-31
6169.560	CaI	2.520	-0.480	5.98e-31
6439.080	CaI	2.520	0.390	5.12e-32
6455.600	CaI	2.520	-1.290	5.09e-32
6499.650	CaI	2.520	-0.820	5.05e-32
5526.790	ScII (equi)	1.770	0.030	0.00e+00
5526.770	<i>ScII</i>	1.768	-2.665	0.00e+00
5526.775	<i>ScII</i>	1.768	-2.262	0.00e+00
5526.779	<i>ScII</i>	1.768	-2.050	0.00e+00
5526.779	<i>ScII</i>	1.768	-1.452	0.00e+00
5526.783	<i>ScII</i>	1.768	-1.940	0.00e+00
5526.783	<i>ScII</i>	1.768	-1.247	0.00e+00
5526.786	<i>ScII</i>	1.768	-1.181	0.00e+00
5526.787	<i>ScII</i>	1.768	-1.919	0.00e+00
5526.788	<i>ScII</i>	1.768	-1.185	0.00e+00
5526.789	<i>ScII</i>	1.768	-0.523	0.00e+00
5526.790	<i>ScII</i>	1.768	-2.028	0.00e+00
5526.790	<i>ScII</i>	1.768	-1.246	0.00e+00
5526.791	<i>ScII</i>	1.768	-0.644	0.00e+00
5526.792	<i>ScII</i>	1.768	-1.368	0.00e+00
5526.793	<i>ScII</i>	1.768	-1.551	0.00e+00
5526.793	<i>ScII</i>	1.768	-0.780	0.00e+00
5526.794	<i>ScII</i>	1.768	-0.936	0.00e+00
5526.795	<i>ScII</i>	1.768	-1.697	0.00e+00

Table A.6: continued.

$\lambda$ Å	El	$\chi_{exc}$ eV	$\log(gf)$	$C_6$
5526.795	<i>ScII</i>	1.768	-1.355	0.00e+00
5526.795	<i>ScII</i>	1.768	-1.121	0.00e+00
6309.900	ScII (equi)	1.500	-1.520	0.00e+00
6309.906	<i>ScII</i>	1.497	-1.950	0.00e+00
6309.924	<i>ScII</i>	1.497	-2.047	0.00e+00
6309.938	<i>ScII</i>	1.497	-2.172	0.00e+00
6604.600	ScII (equi)	1.360	-1.310	0.00e+00
6604.582	<i>ScII</i>	1.357	-2.676	0.00e+00
6604.590	<i>ScII</i>	1.357	-2.518	0.00e+00
6604.594	<i>ScII</i>	1.357	-2.106	0.00e+00
6604.596	<i>ScII</i>	1.357	-2.529	0.00e+00
6604.599	<i>ScII</i>	1.357	-2.504	0.00e+00
6604.602	<i>ScII</i>	1.357	-2.702	0.00e+00
6604.604	<i>ScII</i>	1.357	-3.200	0.00e+00
6604.607	<i>ScII</i>	1.357	-4.626	0.00e+00
6604.609	<i>ScII</i>	1.357	-2.878	0.00e+00
6604.611	<i>ScII</i>	1.357	-2.676	0.00e+00
6604.613	<i>ScII</i>	1.357	-2.518	0.00e+00
6604.615	<i>ScII</i>	1.357	-2.702	0.00e+00
6604.615	<i>ScII</i>	1.357	-2.529	0.00e+00
5490.160	TiI	1.460	-0.930	5.41e-32
6126.220	TiI	1.070	-1.430	2.06e-32
6258.100	TiI	1.440	-0.350	4.75e-32
6556.080	TiI	1.460	-1.070	2.74e-32
5336.770	TiII	1.580	-1.700	0.00e+00
5381.010	TiII	1.570	-1.780	0.00e+00
5418.770	TiII	1.580	-2.110	0.00e+00
6559.590	TiII	2.050	-2.020	0.00e+00
5345.800	CrI	1.000	-0.980	0.00e+00
5409.800	CrI	1.030	-0.720	3.92e-32
6330.090	CrI	0.940	-2.920	3.33e-32
5407.420	MnI (equi)	2.140	-1.740	6.44e-32
5407.325	<i>MnI</i>	2.14	-3.139	6.44e-32
5407.332	<i>MnI</i>	2.14	-3.394	6.44e-32
5407.333	<i>MnI</i>	2.14	-3.394	6.44e-32
5407.341	<i>MnI</i>	2.14	-3.075	6.44e-32

Table A.6: continued.

$\lambda$ Å	El	$\chi_{exc}$ eV	$\log(gf)$	$C_6$
5407.353	<i>MnI</i>	2.14	-3.196	6.44e-32
5407.354	<i>MnI</i>	2.14	-3.196	6.44e-32
5407.366	<i>MnI</i>	2.14	-2.900	6.44e-32
5407.382	<i>MnI</i>	2.14	-3.131	6.44e-32
5407.384	<i>MnI</i>	2.14	-3.131	6.44e-32
5407.400	<i>MnI</i>	2.14	-2.708	6.44e-32
5407.420	<i>MnI</i>	2.14	-3.162	6.44e-32
5407.422	<i>MnI</i>	2.14	-3.162	6.44e-32
5407.442	<i>MnI</i>	2.14	-2.523	6.44e-32
5407.468	<i>MnI</i>	2.14	-3.344	6.44e-32
5407.469	<i>MnI</i>	2.14	-3.344	6.44e-32
5407.494	<i>MnI</i>	2.14	-2.352	6.44e-32
5420.360	MnI (equi)	2.140	-1.460	6.40e-32
5420.256	<i>MnI</i>	2.14	-3.018	6.40e-32
5420.261	<i>MnI</i>	2.14	-2.988	6.40e-32
5420.270	<i>MnI</i>	2.14	-2.733	6.40e-32
5420.272	<i>MnI</i>	2.14	-3.766	6.40e-32
5420.281	<i>MnI</i>	2.14	-2.812	6.40e-32
5420.295	<i>MnI</i>	2.14	-2.511	6.40e-32
5420.298	<i>MnI</i>	2.14	-3.687	6.40e-32
5420.311	<i>MnI</i>	2.14	-2.745	6.40e-32
5420.329	<i>MnI</i>	2.14	-2.327	6.40e-32
5420.333	<i>MnI</i>	2.14	-3.812	6.40e-32
5420.351	<i>MnI</i>	2.14	-2.771	6.40e-32
5420.374	<i>MnI</i>	2.14	-2.169	6.40e-32
5420.379	<i>MnI</i>	2.14	-4.164	6.40e-32
5420.402	<i>MnI</i>	2.14	-2.947	6.40e-32
5420.429	<i>MnI</i>	2.14	-2.029	6.40e-32
5432.550	MnI (equi)	0.000	-3.790	1.40e-32
5432.506	<i>MnI</i>	0.00	-4.377	1.40e-32
5432.510	<i>MnI</i>	0.00	-5.155	1.40e-32
5432.535	<i>MnI</i>	0.00	-5.155	1.40e-32
5432.538	<i>MnI</i>	0.00	-4.640	1.40e-32
5432.541	<i>MnI</i>	0.00	-4.992	1.40e-32
5432.561	<i>MnI</i>	0.00	-4.992	1.40e-32
5432.564	<i>MnI</i>	0.00	-4.971	1.40e-32



Table A.6: continued.

$\lambda$ Å	El	$\chi_{exc}$ eV	$\log(gf)$	$C_6$
5432.566	<i>MnI</i>	0.00	-4.987	1.40e-32
5432.580	<i>MnI</i>	0.00	-4.987	1.40e-32
5432.583	<i>MnI</i>	0.00	-5.418	1.40e-32
5432.584	<i>MnI</i>	0.00	-5.089	1.40e-32
5432.594	<i>MnI</i>	0.00	-5.089	1.40e-32
5432.595	<i>MnI</i>	0.00	-6.117	1.40e-32
5432.596	<i>MnI</i>	0.00	-5.351	1.40e-32
5432.601	<i>MnI</i>	0.00	-5.351	1.40e-32
5516.770	MnI (equi)	2.180	-1.850	6.36e-32
5516.699	<i>MnI</i>	2.18	-3.273	6.36e-32
5516.709	<i>MnI</i>	2.18	-2.905	6.36e-32
5516.718	<i>MnI</i>	2.18	-2.905	6.36e-32
5516.728	<i>MnI</i>	2.18	-4.482	6.36e-32
5516.743	<i>MnI</i>	2.18	-2.773	6.36e-32
5516.757	<i>MnI</i>	2.18	-2.773	6.36e-32
5516.771	<i>MnI</i>	2.18	-2.947	6.36e-32
5516.790	<i>MnI</i>	2.18	-2.875	6.36e-32
5516.809	<i>MnI</i>	2.18	-2.875	6.36e-32
5516.828	<i>MnI</i>	2.18	-2.398	6.36e-32
5339.930	FeI	3.270	-0.680	3.79e-31
5367.480	FeI	4.420	0.550	5.89e-31
5371.500	FeI	0.960	-1.640	1.80e-32
5383.370	FeI	4.310	0.500	4.04e-31
5389.480	FeI	4.420	-0.400	5.69e-31
5393.170	FeI	3.240	-0.920	3.52e-31
5397.140	FeI	0.910	-1.990	1.75e-32
5400.510	FeI	4.370	-0.150	4.84e-31
5405.790	FeI	0.990	-1.850	1.82e-32
5415.190	FeI	4.390	0.510	4.99e-31
5424.070	FeI	4.320	0.520	3.91e-31
5429.700	FeI	0.960	-1.880	0.00e+00
5434.520	FeI	1.010	-2.120	0.00e+00
5446.920	FeI	0.990	-1.910	0.00e+00
5497.520	FeI	1.010	-2.850	0.00e+00
5501.480	FeI	0.960	-3.050	1.76e-32
5506.790	FeI	0.990	-2.790	1.80e-32

Table A.6: continued.

$\lambda$ Å	El	$\chi_{exc}$ eV	$\log(gf)$	$C_6$
5569.620	FeI	3.420	-0.540	0.00e+00
5576.090	FeI	3.430	-1.000	0.00e+00
5586.760	FeI	3.370	-0.140	0.00e+00
6151.620	FeI	2.180	-3.370	2.55e-32
6157.750	FeI	4.070	-1.260	0.00e+00
6173.340	FeI	2.220	-2.850	2.65e-32
6180.200	FeI	2.730	-2.780	0.00e+00
6187.990	FeI	3.940	-1.580	4.90e-31
6200.310	FeI	2.610	-2.440	0.00e+00
6213.430	FeI	2.220	-2.660	2.62e-32
6219.290	FeI	2.200	-2.440	2.58e-32
6229.230	FeI	2.840	-2.900	4.58e-32
6230.740	FeI	2.560	-1.280	4.39e-32
6240.660	FeI	2.220	-3.230	3.14e-32
6252.570	FeI	2.400	-1.760	3.84e-32
6265.130	FeI	2.180	-2.550	0.00e+00
6297.800	FeI	2.220	-2.740	2.58e-32
6301.500	FeI	3.650	-0.720	0.00e+00
6302.490	FeI	3.690	-1.150	0.00e+00
6311.510	FeI	2.830	-3.220	4.39e-32
6322.690	FeI	2.590	-2.430	0.00e+00
6335.330	FeI	2.200	-2.230	0.00e+00
6344.150	FeI	2.430	-2.920	0.00e+00
6355.040	FeI	2.840	-2.290	4.39e-32
6408.030	FeI	3.690	-1.000	0.00e+00
6419.960	FeI	4.730	-0.240	4.66e-31
6421.360	FeI	2.280	-2.010	3.86e-32
6430.860	FeI	2.180	-1.950	2.42e-32
6494.980	FeI	2.400	-1.270	0.00e+00
6498.940	FeI	0.960	-4.690	1.53e-32
6518.370	FeI	2.830	-2.460	4.14e-32
6581.220	FeI	1.480	-4.680	2.06e-32
6609.120	FeI	2.560	-2.660	4.11e-32
5483.340	CoI (equi)	1.710	-1.490	2.89e-32
5483.309	CoI	1.711	-2.120	2.89e-32
5483.334	CoI	1.711	-2.261	2.89e-32

Table A.6: continued.

$\lambda$ Å	El	$\chi_{exc}$ eV	$\log(gf)$	$C_6$
5483.344	<i>CoI</i>	1.711	-2.961	2.89e-32
5483.354	<i>CoI</i>	1.711	-2.425	2.89e-32
5483.363	<i>CoI</i>	1.711	-2.764	2.89e-32
5483.370	<i>CoI</i>	1.711	-2.623	2.89e-32
5483.372	<i>CoI</i>	1.711	-4.074	2.89e-32
5483.378	<i>CoI</i>	1.711	-2.710	2.89e-32
5483.383	<i>CoI</i>	1.711	-2.878	2.89e-32
5483.387	<i>CoI</i>	1.711	-3.664	2.89e-32
5483.389	<i>CoI</i>	1.711	-2.732	2.89e-32
5483.393	<i>CoI</i>	1.711	-3.266	2.89e-32
5483.397	<i>CoI</i>	1.711	-2.822	2.89e-32
5483.397	<i>CoI</i>	1.711	-3.442	2.89e-32
5483.402	<i>CoI</i>	1.711	-3.011	2.89e-32
5483.403	<i>CoI</i>	1.711	-3.317	2.89e-32
5483.407	<i>CoI</i>	1.711	-3.296	2.89e-32
5483.407	<i>CoI</i>	1.711	-3.266	2.89e-32
5476.920	<i>NiI</i>	1.830	-0.890	0.00e+00
6128.970	<i>NiI</i>	1.680	-3.390	0.00e+00
6176.820	<i>NiI</i>	4.090	-0.430	3.92e-31
6327.600	<i>NiI</i>	1.680	-3.090	0.00e+00
6482.800	<i>NiI</i>	1.940	-2.850	0.00e+00
6586.320	<i>NiI</i>	1.950	-2.790	0.00e+00
6141.730	<i>BaII</i> (equi)	0.700	-0.080	0.00e+00
6141.695	<i>BaII</i>	0.704	-3.631	0.00e+00
6141.695	<i>BaII</i>	0.704	-3.397	0.00e+00
6141.697	<i>BaII</i>	0.704	-2.485	0.00e+00
6141.697	<i>BaII</i>	0.704	-2.251	0.00e+00
6141.698	<i>BaII</i>	0.704	-3.455	0.00e+00
6141.698	<i>BaII</i>	0.704	-3.221	0.00e+00
6141.699	<i>BaII</i>	0.704	-1.676	0.00e+00
6141.699	<i>BaII</i>	0.704	-1.443	0.00e+00
6141.699	<i>BaII</i>	0.704	-2.388	0.00e+00
6141.699	<i>BaII</i>	0.704	-2.154	0.00e+00
6141.700	<i>BaII</i>	0.704	-1.690	0.00e+00
6141.700	<i>BaII</i>	0.704	-0.214	0.00e+00
6141.700	<i>BaII</i>	0.704	-1.172	0.00e+00

Table A.6: continued.

$\lambda$ Å	El	$\chi_{exc}$ eV	$\log(gf)$	$C_6$
6141.701	<i>BaII</i>	0.704	-1.882	0.00e+00
6141.701	<i>BaII</i>	0.704	-1.649	0.00e+00
6141.701	<i>BaII</i>	0.704	-2.500	0.00e+00
6141.701	<i>BaII</i>	0.704	-2.267	0.00e+00
6141.702	<i>BaII</i>	0.704	-1.899	0.00e+00
6141.702	<i>BaII</i>	0.704	-2.455	0.00e+00
6141.702	<i>BaII</i>	0.704	-2.133	0.00e+00
6141.703	<i>BaII</i>	0.704	-2.221	0.00e+00
6496.910	BaII (equi)	0.600	-0.380	0.00e+00
6496.900	<i>BaII</i>	0.604	-2.000	0.00e+00
6496.906	<i>BaII</i>	0.604	-2.764	0.00e+00
6496.907	<i>BaII</i>	0.604	-2.367	0.00e+00
6496.889	<i>BaII</i>	0.604	-3.066	0.00e+00
6496.910	<i>BaII</i>	0.604	-2.367	0.00e+00
6496.892	<i>BaII</i>	0.604	-2.367	0.00e+00
6496.896	<i>BaII</i>	0.604	-1.919	0.00e+00
6496.900	<i>BaII</i>	0.604	-1.482	0.00e+00
6496.906	<i>BaII</i>	0.604	-2.531	0.00e+00
6496.908	<i>BaII</i>	0.604	-2.133	0.00e+00
6496.888	<i>BaII</i>	0.604	-2.832	0.00e+00
6496.912	<i>BaII</i>	0.604	-2.133	0.00e+00
6496.891	<i>BaII</i>	0.604	-2.133	0.00e+00
6496.896	<i>BaII</i>	0.604	-1.686	0.00e+00
6496.900	<i>BaII</i>	0.604	-0.524	0.00e+00
6645.130	EuII (equi)	1.370	0.120	0.00e+00
6645.071	<i>EuII</i>	1.379	-0.838	0.00e+00
6645.072	<i>EuII</i>	1.379	-2.105	0.00e+00
6645.074	<i>EuII</i>	1.379	-0.799	0.00e+00
6645.074	<i>EuII</i>	1.379	-3.749	0.00e+00
6645.078	<i>EuII</i>	1.379	-2.144	0.00e+00
6645.085	<i>EuII</i>	1.379	-3.788	0.00e+00
6645.087	<i>EuII</i>	1.379	-0.875	0.00e+00
6645.089	<i>EuII</i>	1.379	-1.910	0.00e+00
6645.094	<i>EuII</i>	1.379	-3.431	0.00e+00
6645.096	<i>EuII</i>	1.379	-0.954	0.00e+00
6645.097	<i>EuII</i>	1.379	-0.914	0.00e+00

Table A.6: continued.

$\lambda$ Å	El	$\chi_{exc}$ eV	$\log(gf)$	$C_6$
6645.101	<i>EuII</i>	1.379	-1.865	0.00e+00
6645.104	<i>EuII</i>	1.379	-1.949	0.00e+00
6645.104	<i>EuII</i>	1.379	-1.036	0.00e+00
6645.107	<i>EuII</i>	1.379	-3.359	0.00e+00
6645.109	<i>EuII</i>	1.379	-1.121	0.00e+00
6645.110	<i>EuII</i>	1.379	-1.917	0.00e+00
6645.112	<i>EuII</i>	1.379	-3.470	0.00e+00
6645.113	<i>EuII</i>	1.379	-1.203	0.00e+00
6645.116	<i>EuII</i>	1.379	-2.112	0.00e+00
6645.116	<i>EuII</i>	1.379	-3.527	0.00e+00
6645.118	<i>EuII</i>	1.379	-0.993	0.00e+00
6645.126	<i>EuII</i>	1.379	-1.904	0.00e+00
6645.133	<i>EuII</i>	1.379	-3.398	0.00e+00
6645.137	<i>EuII</i>	1.379	-1.075	0.00e+00
6645.144	<i>EuII</i>	1.379	-1.956	0.00e+00
6645.150	<i>EuII</i>	1.379	-3.566	0.00e+00
6645.152	<i>EuII</i>	1.379	-1.160	0.00e+00
6645.158	<i>EuII</i>	1.379	-2.151	0.00e+00
6645.163	<i>EuII</i>	1.379	-1.242	0.00e+00

## Appendix A. An appendix

---

Table A.7: The four stellar parameters for the our members : the effective temperature, the surface gravity, the micro-turbulenc velocity and the metallicity.

ID	$T_{eff}$ K	$\log g$ cm/s <sup>2</sup>	$v_{turb}$ km/s	[Fe/H] dex
S05-10	4342	0.91	1.82	-2.11±0.14
S05-47	4654	1.28	1.74	-1.64±0.16
S05-60	4796	1.57	1.69	-1.98±0.14
S05-67	4736	1.67	1.67	-1.81±0.15
S05-70	4918	1.78	1.64	-2.24±0.13
S05-78	4842	1.76	1.65	-2.57±0.20
S05-84	5048	1.92	1.62	-1.96±0.13
S05-86	4772	1.82	1.64	-1.71±0.15
S05-93	4926	1.95	1.61	-1.70±0.13
S05-94	4755	1.90	1.62	-3.13±0.16
S05-95	4880	1.97	1.61	-2.48±0.14
S05-98	4869	1.95	1.61	-1.16±0.15
S05-101	4769	1.93	1.61	-2.93±0.16
S05-104	5004	2.06	1.59	-2.75±0.15
S05-111	4953	2.06	1.59	-1.64±0.14
S05-112	5030	2.08	1.58	-3.07±0.16
S05-115	4946	2.06	1.59	-2.52±0.14
S05-123	5051	2.16	1.57	-2.06±0.14
S05-132	5154	2.33	1.53	-3.79±0.20
S05-133	5096	2.26	1.55	-2.30±0.15
S05-168	4800	2.00	1.60	-3.18±0.15
S07-16	4499	1.02	1.80	-2.33±0.14
S07-69	4739	1.49	1.70	-2.06±0.15
S07-76	4946	1.70	1.66	-2.74±0.12
S07-79	4857	1.70	1.66	-2.15±0.13
S07-81	4952	1.74	1.65	-2.60±0.13
S07-110	5170	2.13	1.57	-1.67±0.15
S07-112	5141	2.16	1.57	-1.73±0.12
S07-115	4989	2.16	1.57	-1.89±0.14
S08-3	4177	0.58	1.88	-2.03±0.08
S08-6	4317	0.74	1.85	-1.60±0.14
S08-38	4513	1.02	1.80	-2.13±0.15
S08-59	5211	1.73	1.65	-1.56±0.11
S08-71	4884	1.72	1.66	-2.90±0.12

Table A.7: continued.

ID	$T_{eff}$ K	$\log g$ cm/s <sup>2</sup>	$v_{turb}$ km/s	[Fe/H] dex
S08-75	4810	1.76	1.65	-2.32±0.15
S08-98	4893	1.98	1.60	-1.97±0.14
S08-113	4972	2.19	1.56	-2.00±0.16
S08-131	4666	1.57	1.69	-2.08±0.15
S08-151	4849	2.03	1.59	-1.42±0.14
S08-183	4962	1.68	1.66	-1.67±0.13
S08-184	4891	1.65	1.67	-2.49±0.12
S08-199	4975	1.92	1.62	-1.99±0.14
S08-202	4867	1.89	1.62	-1.74±0.17
S08-203	4847	1.90	1.62	-2.54±0.13
S08-222	5009	2.17	1.57	-1.78±0.14
S08-225	4950	2.15	1.57	-2.73±0.27
S08-239	4546	1.34	1.73	-1.89±0.17
S08-241	4689	1.44	1.71	-2.17±0.16
S08-242	4657	1.44	1.71	-1.71±0.16
S08-245	4803	1.56	1.69	-2.58±0.11
S08-246	4722	1.54	1.69	-1.59±0.15
S08-250	4761	1.62	1.68	-1.96±0.15
S08-252	4877	1.70	1.66	-2.39±0.13
S08-253	4854	1.69	1.66	-2.13±0.13
S08-257	4840	1.69	1.66	-3.20±0.12
S08-258	4852	1.72	1.66	-2.06±0.13
S08-259	4723	1.66	1.67	-2.06±0.14
S08-261	4987	1.79	1.64	-2.75±0.12
S08-264	4847	1.75	1.65	-1.69±0.15
S08-267	4987	1.80	1.64	-2.32±0.12
S08-274	4874	1.80	1.64	-2.55±0.12
S08-280	4883	1.87	1.63	-1.65±0.14
S08-282	5044	1.96	1.61	-1.82±0.13
S08-284	4892	1.91	1.62	-1.64±0.14
S08-289	4944	1.98	1.60	-1.95±0.14
S08-291	4956	1.99	1.60	-2.25±0.13
S08-292	4883	1.98	1.60	-2.70±0.15
S08-295	5114	2.07	1.59	-2.80±0.12
S08-298	4852	1.96	1.61	-1.87±0.14
S08-303	4885	1.99	1.60	-1.86±0.15

Table A.7: continued.

ID	$T_{eff}$ K	$\log g$ cm/s <sup>2</sup>	$v_{turb}$ km/s	[Fe/H] dex
S08-307	4930	2.03	1.59	-2.47±0.13
S08-309	5006	2.06	1.59	-2.19±0.14
S08-316	4886	2.04	1.59	-2.39±0.15
S08-317	5010	2.10	1.58	-2.38±0.13
S08-323	4944	2.09	1.58	-2.23±0.13
S08-331	4904	2.12	1.58	-2.34±0.14
S08-332	4925	2.14	1.57	-2.89±0.15
S08-336	4726	2.05	1.59	-3.11±0.16
S08-339	4349	2.10	1.58	-2.92±0.18
S08-341	5024	2.22	1.56	-1.86±0.15
S11-97	4573	1.15	1.77	-2.92±0.15
S11-100	4608	1.26	1.75	-1.92±0.16
S11-113	4722	1.56	1.69	-1.73±0.16
S11-127	4873	1.82	1.64	-2.05±0.14
S11-137	4687	1.83	1.63	-1.97±0.16
S11-139	5012	2.02	1.60	-1.47±0.13
S11-141	4983	2.01	1.60	-3.78±0.30



Table A.8: Atomic abundances for Fe, Mg, and Ca. The considered solar abundances given in the first line are from Grevesse & Sauval (1998). The number of lines used to determined each abundance is indicated in brackets. The asterisks indicate stars having a signal-to-noise  $\leq 10$ .

ID	[Fe/H] $\pm$ err <sub>sys</sub> $\pm$ err <sub>rand</sub> (N) dex	[Mg/Fe] $\pm$ err <sub>sys</sub> $\pm$ err <sub>rand</sub> dex	[Ca/Fe] $\pm$ err <sub>sys</sub> $\pm$ err <sub>rand</sub> (N) dex
log $\epsilon(X)_\odot$	7.50	7.58	6.36
S05-10	-2.11 $\pm$ 0.14 $\pm$ 0.01 (50)	+0.46 $\pm$ 0.15 $\pm$ 0.04	+0.16 $\pm$ 0.17 $\pm$ 0.01 (12)
S05-47	-1.64 $\pm$ 0.16 $\pm$ 0.01 (50)	-0.68 $\pm$ 0.17 $\pm$ 0.09	+0.14 $\pm$ 0.18 $\pm$ 0.03 (11)
S05-60	-1.98 $\pm$ 0.14 $\pm$ 0.03 (50)	+0.10 $\pm$ 0.15 $\pm$ 0.15	+0.16 $\pm$ 0.16 $\pm$ 0.06 (7)
S05-67	-1.81 $\pm$ 0.15 $\pm$ 0.02 (50)	-0.24 $\pm$ 0.16 $\pm$ 0.10	+0.02 $\pm$ 0.17 $\pm$ 0.04 (11)
S05-70	-2.24 $\pm$ 0.12 $\pm$ 0.05 (30)		
S05-78	-2.57 $\pm$ 0.10 $\pm$ 0.17 (30)		
S05-84*	-1.96 $\pm$ 0.12 $\pm$ 0.06 (50)	+0.50 $\pm$ 0.13 $\pm$ 0.23	+0.27 $\pm$ 0.14 $\pm$ 0.15 (5)
S05-86	-1.71 $\pm$ 0.14 $\pm$ 0.03 (50)	-0.47 $\pm$ 0.16 $\pm$ 0.16	-0.18 $\pm$ 0.17 $\pm$ 0.06 (8)
S05-93	-1.70 $\pm$ 0.13 $\pm$ 0.03 (50)	-0.21 $\pm$ 0.15 $\pm$ 0.18	
S05-94	-3.13 $\pm$ 0.14 $\pm$ 0.08 (50)	+0.60 $\pm$ 0.15 $\pm$ 0.21	
S05-95*	-2.48 $\pm$ 0.12 $\pm$ 0.09 (50)	+1.57 $\pm$ 0.14 $\pm$ 0.29	+0.24 $\pm$ 0.14 $\pm$ 0.28 (3)
S05-98	-1.16 $\pm$ 0.14 $\pm$ 0.04 (50)		
S05-101*	-2.93 $\pm$ 0.11 $\pm$ 0.12 (50)		+1.00 $\pm$ 0.15 $\pm$ 0.29 (3)
S05-104	-2.75 $\pm$ 0.10 $\pm$ 0.11 (50)		
S05-111	-1.64 $\pm$ 0.13 $\pm$ 0.04 (50)		
S05-112*	-3.07 $\pm$ 0.11 $\pm$ 0.11 (50)		+1.20 $\pm$ 0.13 $\pm$ 0.24 (4)
S05-115	-2.52 $\pm$ 0.12 $\pm$ 0.07 (50)	+0.34 $\pm$ 0.13 $\pm$ 0.31	
S05-123*	-2.06 $\pm$ 0.12 $\pm$ 0.08 (50)		
S05-132*	-3.79 $\pm$ 0.10 $\pm$ 0.18 (30)		+1.50 $\pm$ 0.13 $\pm$ 0.23 (4)
S05-133*	-2.30 $\pm$ 0.10 $\pm$ 0.11 (50)		
S05-168*	-3.18 $\pm$ 0.14 $\pm$ 0.07 (50)		+1.86 $\pm$ 0.16 $\pm$ 0.13 (5)
S07-16	-2.33 $\pm$ 0.14 $\pm$ 0.01 (29)	+0.22 $\pm$ 0.15 $\pm$ 0.03	+0.38 $\pm$ 0.16 $\pm$ 0.02 (7)
S07-69	-2.06 $\pm$ 0.15 $\pm$ 0.01 (50)	-0.00 $\pm$ 0.16 $\pm$ 0.08	+0.21 $\pm$ 0.17 $\pm$ 0.04 (5)
S07-76	-2.74 $\pm$ 0.10 $\pm$ 0.05 (50)	-0.07 $\pm$ 0.12 $\pm$ 0.14	
S07-79	-2.15 $\pm$ 0.13 $\pm$ 0.03 (50)	-0.28 $\pm$ 0.14 $\pm$ 0.16	-0.10 $\pm$ 0.15 $\pm$ 0.07 (8)
S07-81	-2.60 $\pm$ 0.10 $\pm$ 0.08 (9)		+0.42 $\pm$ 0.13 $\pm$ 0.12 (2)
S07-110*	-1.67 $\pm$ 0.11 $\pm$ 0.10 (50)		-0.09 $\pm$ 0.13 $\pm$ 0.21 (6)
S07-112*	-1.73 $\pm$ 0.12 $\pm$ 0.04 (50)	+0.05 $\pm$ 0.13 $\pm$ 0.27	
S07-115*	-1.89 $\pm$ 0.12 $\pm$ 0.07 (50)	-0.49 $\pm$ 0.14 $\pm$ 0.31	+0.31 $\pm$ 0.15 $\pm$ 0.16 (7)
S08-3	-2.03 $\pm$ 0.07 $\pm$ 0.01 (50)	+0.41 $\pm$ 0.09 $\pm$ 0.02	+0.04 $\pm$ 0.14 $\pm$ 0.01 (11)
S08-6	-1.60 $\pm$ 0.14 $\pm$ 0.01 (50)	-0.05 $\pm$ 0.15 $\pm$ 0.03	-0.09 $\pm$ 0.17 $\pm$ 0.01 (12)
S08-38	-2.13 $\pm$ 0.14 $\pm$ 0.01 (50)	+0.29 $\pm$ 0.16 $\pm$ 0.04	
S08-59	-1.56 $\pm$ 0.10 $\pm$ 0.01 (50)		
S08-71	-2.90 $\pm$ 0.11 $\pm$ 0.04 (50)	+0.28 $\pm$ 0.12 $\pm$ 0.09	
S08-75	-2.32 $\pm$ 0.14 $\pm$ 0.07 (9)		
S08-98	-1.97 $\pm$ 0.13 $\pm$ 0.04 (50)		+0.02 $\pm$ 0.16 $\pm$ 0.10 (5)
S08-113*	-2.00 $\pm$ 0.13 $\pm$ 0.09 (50)	-0.24 $\pm$ 0.15 $\pm$ 0.44	+1.05 $\pm$ 0.16 $\pm$ 0.17 (7)

Table A.8: continued.

ID	[Fe/H] $\pm$ err <sub>sys</sub> $\pm$ err <sub>rand</sub> (N) dex	[Mg/Fe] $\pm$ err <sub>sys</sub> $\pm$ err <sub>rand</sub> dex	[Ca/Fe] $\pm$ err <sub>sys</sub> $\pm$ err <sub>rand</sub> (N) dex
log $\epsilon(X)_\odot$	7.50	7.58	6.36
S08-131	-2.08 $\pm$ 0.15 $\pm$ 0.02 (50)	+0.27 $\pm$ 0.17 $\pm$ 0.12	+0.22 $\pm$ 0.17 $\pm$ 0.05 (11)
S08-151*	-1.42 $\pm$ 0.14 $\pm$ 0.03 (50)	+0.17 $\pm$ 0.15 $\pm$ 0.33	+0.37 $\pm$ 0.17 $\pm$ 0.19 (3)
S08-183	-1.67 $\pm$ 0.13 $\pm$ 0.03 (29)	-0.21 $\pm$ 0.15 $\pm$ 0.13	+0.08 $\pm$ 0.15 $\pm$ 0.06 (5)
S08-184	-2.49 $\pm$ 0.12 $\pm$ 0.04 (50)	-0.38 $\pm$ 0.13 $\pm$ 0.13	+0.16 $\pm$ 0.14 $\pm$ 0.08 (7)
S08-199	-1.99 $\pm$ 0.13 $\pm$ 0.04 (50)	+0.07 $\pm$ 0.15 $\pm$ 0.17	
S08-202	-1.74 $\pm$ 0.14 $\pm$ 0.09 (9)		
S08-203	-2.54 $\pm$ 0.11 $\pm$ 0.07 (50)	+0.54 $\pm$ 0.13 $\pm$ 0.20	
S08-222	-1.78 $\pm$ 0.14 $\pm$ 0.05 (50)		
S08-225*	-2.73 $\pm$ 0.12 $\pm$ 0.24 (50)		+1.15 $\pm$ 0.14 $\pm$ 0.31 (7)
S08-239	-1.89 $\pm$ 0.16 $\pm$ 0.06 (50)	-0.20 $\pm$ 0.17 $\pm$ 0.08	+0.08 $\pm$ 0.18 $\pm$ 0.07 (11)
S08-241	-2.17 $\pm$ 0.15 $\pm$ 0.01 (50)	+0.11 $\pm$ 0.17 $\pm$ 0.06	+0.11 $\pm$ 0.18 $\pm$ 0.03 (7)
S08-242	-1.71 $\pm$ 0.16 $\pm$ 0.01 (50)	+0.05 $\pm$ 0.17 $\pm$ 0.07	-0.01 $\pm$ 0.18 $\pm$ 0.03 (10)
S08-245	-2.58 $\pm$ 0.10 $\pm$ 0.03 (50)	+0.08 $\pm$ 0.12 $\pm$ 0.09	+0.19 $\pm$ 0.13 $\pm$ 0.06 (6)
S08-246	-1.59 $\pm$ 0.14 $\pm$ 0.02 (50)	-0.49 $\pm$ 0.16 $\pm$ 0.10	-0.23 $\pm$ 0.17 $\pm$ 0.04 (12)
S08-250	-1.96 $\pm$ 0.15 $\pm$ 0.02 (50)	+0.06 $\pm$ 0.16 $\pm$ 0.08	+0.31 $\pm$ 0.17 $\pm$ 0.04 (7)
S08-252	-2.39 $\pm$ 0.12 $\pm$ 0.02 (50)	+0.04 $\pm$ 0.14 $\pm$ 0.09	-0.00 $\pm$ 0.15 $\pm$ 0.06 (4)
S08-253	-2.13 $\pm$ 0.13 $\pm$ 0.02 (50)	-0.20 $\pm$ 0.15 $\pm$ 0.08	-0.00 $\pm$ 0.16 $\pm$ 0.05 (6)
S08-257	-3.20 $\pm$ 0.12 $\pm$ 0.04 (50)	+0.38 $\pm$ 0.13 $\pm$ 0.09	-0.08 $\pm$ 0.13 $\pm$ 0.08 (5)
S08-258	-2.06 $\pm$ 0.13 $\pm$ 0.02 (50)	+0.49 $\pm$ 0.15 $\pm$ 0.11	+0.19 $\pm$ 0.15 $\pm$ 0.05 (10)
S08-259	-2.06 $\pm$ 0.14 $\pm$ 0.02 (50)	+0.04 $\pm$ 0.16 $\pm$ 0.13	+0.24 $\pm$ 0.16 $\pm$ 0.05 (10)
S08-261	-2.75 $\pm$ 0.10 $\pm$ 0.05 (30)		+0.14 $\pm$ 0.13 $\pm$ 0.10 (3)
S08-264	-1.69 $\pm$ 0.14 $\pm$ 0.02 (50)		
S08-267	-2.32 $\pm$ 0.11 $\pm$ 0.04 (30)		+0.12 $\pm$ 0.14 $\pm$ 0.09 (3)
S08-274	-2.55 $\pm$ 0.11 $\pm$ 0.04 (20)	-0.11 $\pm$ 0.12 $\pm$ 0.13	
S08-280	-1.65 $\pm$ 0.14 $\pm$ 0.02 (50)	-0.80 $\pm$ 0.16 $\pm$ 0.16	-0.23 $\pm$ 0.16 $\pm$ 0.06 (6)
S08-282	-1.82 $\pm$ 0.12 $\pm$ 0.04 (50)	-0.73 $\pm$ 0.13 $\pm$ 0.17	
S08-284	-1.64 $\pm$ 0.14 $\pm$ 0.04 (30)		-0.00 $\pm$ 0.16 $\pm$ 0.08 (6)
S08-289	-1.95 $\pm$ 0.13 $\pm$ 0.04 (29)	+0.13 $\pm$ 0.15 $\pm$ 0.16	+0.21 $\pm$ 0.15 $\pm$ 0.08 (5)
S08-291	-2.25 $\pm$ 0.12 $\pm$ 0.07 (50)	-0.03 $\pm$ 0.13 $\pm$ 0.19	
S08-292*	-2.70 $\pm$ 0.11 $\pm$ 0.10 (50)		
S08-295	-2.80 $\pm$ 0.10 $\pm$ 0.07 (29)	-0.09 $\pm$ 0.11 $\pm$ 0.16	
S08-298	-1.87 $\pm$ 0.14 $\pm$ 0.03 (50)	+0.13 $\pm$ 0.15 $\pm$ 0.17	+0.40 $\pm$ 0.16 $\pm$ 0.08 (8)
S08-303	-1.86 $\pm$ 0.14 $\pm$ 0.05 (30)		
S08-307	-2.47 $\pm$ 0.11 $\pm$ 0.08 (50)	+0.42 $\pm$ 0.13 $\pm$ 0.19	
S08-309*	-2.19 $\pm$ 0.12 $\pm$ 0.05 (30)		
S08-316*	-2.39 $\pm$ 0.10 $\pm$ 0.10 (50)		
S08-317	-2.38 $\pm$ 0.12 $\pm$ 0.05 (30)		
S08-323	-2.23 $\pm$ 0.12 $\pm$ 0.04 (50)	+0.23 $\pm$ 0.14 $\pm$ 0.18	
S08-331*	-2.34 $\pm$ 0.12 $\pm$ 0.06 (30)		+0.02 $\pm$ 0.15 $\pm$ 0.15 (4)
S08-332*	-2.89 $\pm$ 0.12 $\pm$ 0.10 (9)		

Table A.8: continued.

ID	[Fe/H] $\pm$ err <sub>sys</sub> $\pm$ err <sub>rand</sub> (N) dex	[Mg/Fe] $\pm$ err <sub>sys</sub> $\pm$ err <sub>rand</sub> dex	[Ca/Fe] $\pm$ err <sub>sys</sub> $\pm$ err <sub>rand</sub> (N) dex
log $\epsilon(X)_\odot$	7.50	7.58	6.36
S08-336*	-3.11 $\pm$ 0.14 $\pm$ 0.07 (29)	+0.54 $\pm$ 0.16 $\pm$ 0.23	+0.67 $\pm$ 0.17 $\pm$ 0.14 (4)
S08-339	-2.92 $\pm$ 0.17 $\pm$ 0.06 (50)	+0.47 $\pm$ 0.18 $\pm$ 0.27	
S08-341*	-1.86 $\pm$ 0.14 $\pm$ 0.06 (50)		
S11-97	-2.92 $\pm$ 0.15 $\pm$ 0.03 (9)		-0.01 $\pm$ 0.16 $\pm$ 0.06 (1)
S11-100	-1.92 $\pm$ 0.15 $\pm$ 0.01 (29)	+0.20 $\pm$ 0.17 $\pm$ 0.05	+0.14 $\pm$ 0.18 $\pm$ 0.03 (7)
S11-113	-1.73 $\pm$ 0.16 $\pm$ 0.01 (50)	-0.02 $\pm$ 0.17 $\pm$ 0.08	-0.01 $\pm$ 0.18 $\pm$ 0.03 (10)
S11-127*	-2.05 $\pm$ 0.13 $\pm$ 0.05 (50)	+0.14 $\pm$ 0.15 $\pm$ 0.23	+0.06 $\pm$ 0.16 $\pm$ 0.10 (10)
S11-137	-1.97 $\pm$ 0.15 $\pm$ 0.03 (50)	+0.50 $\pm$ 0.17 $\pm$ 0.16	+0.23 $\pm$ 0.18 $\pm$ 0.07 (10)
S11-139	-1.47 $\pm$ 0.13 $\pm$ 0.03 (50)	-0.45 $\pm$ 0.15 $\pm$ 0.15	-0.03 $\pm$ 0.15 $\pm$ 0.06 (9)
S11-141*	-3.78 $\pm$ 0.14 $\pm$ 0.26 (9)		+2.44 $\pm$ 0.17 $\pm$ 0.30 (2)

## Appendix A. An appendix

Table A.9: Atomic abundances for Sc, Ti1 and Ti2. The considered solar abundances given in the first line are from Grevesse & Sauval (1998). The number of lines used to determined each abundance is indicated in brackets. The asterisks indicate stars having a signal-to-noise  $\leq 10$ .

ID	[Sc/Fe] $\pm$ err <sub>sys</sub> $\pm$ err <sub>rand</sub> (N) dex	[Ti1/Fe] $\pm$ err <sub>sys</sub> $\pm$ err <sub>rand</sub> (N) dex	[Ti2/Fe] $\pm$ err <sub>sys</sub> $\pm$ err <sub>rand</sub> (N) dex
$\log\epsilon(X)_{\odot}$	3.17	5.02	5.02
S05-10	+0.14 $\pm$ 0.15 $\pm$ 0.03 (3)		
S05-47		+0.11 $\pm$ 0.21 $\pm$ 0.19 (1)	-0.16 $\pm$ 0.17 $\pm$ 0.06 (4)
S05-60			+0.32 $\pm$ 0.15 $\pm$ 0.11 (4)
S05-67			-0.31 $\pm$ 0.16 $\pm$ 0.10 (2)
S05-70			
S05-78			
S05-84*			+0.33 $\pm$ 0.13 $\pm$ 0.20 (2)
S05-86			+0.26 $\pm$ 0.16 $\pm$ 0.11 (2)
S05-93			-0.17 $\pm$ 0.14 $\pm$ 0.14 (3)
S05-94			
S05-95*			+1.10 $\pm$ 0.13 $\pm$ 0.35 (2)
S05-98			
S05-101*			
S05-104			
S05-111			
S05-112*			+0.96 $\pm$ 0.13 $\pm$ 0.36 (2)
S05-115			
S05-123*			
S05-132*			
S05-133*			
S05-168*			+0.35 $\pm$ 0.15 $\pm$ 0.24 (3)
S07-16			+0.22 $\pm$ 0.15 $\pm$ 0.02 (3)
S07-69	-0.28 $\pm$ 0.16 $\pm$ 0.06 (2)		+0.16 $\pm$ 0.16 $\pm$ 0.04 (4)
S07-76			
S07-79			+0.24 $\pm$ 0.14 $\pm$ 0.12 (3)
S07-81			
S07-110*			-0.44 $\pm$ 0.12 $\pm$ 0.33 (2)
S07-112*			
S07-115*			+0.75 $\pm$ 0.14 $\pm$ 0.29 (2)
S08-3		-0.37 $\pm$ 0.19 $\pm$ 0.02 (2)	+0.24 $\pm$ 0.08 $\pm$ 0.02 (3)
S08-6	-0.32 $\pm$ 0.15 $\pm$ 0.04 (1)	-0.48 $\pm$ 0.23 $\pm$ 0.02 (3)	-0.03 $\pm$ 0.14 $\pm$ 0.02 (4)
S08-38	-0.06 $\pm$ 0.15 $\pm$ 0.04 (2)	-0.09 $\pm$ 0.20 $\pm$ 0.04 (1)	+0.31 $\pm$ 0.15 $\pm$ 0.04 (3)
S08-59			
S08-71			
S08-75			
S08-98			+0.34 $\pm$ 0.14 $\pm$ 0.13 (2)
S08-113*			+0.34 $\pm$ 0.15 $\pm$ 0.48 (2)

Table A.9: continued.

ID	[Sc/Fe] $\pm$ err <sub>sys</sub> $\pm$ err <sub>rand</sub> (N) dex	[Ti1/Fe] $\pm$ err <sub>sys</sub> $\pm$ err <sub>rand</sub> (N) dex	[Ti2/Fe] $\pm$ err <sub>sys</sub> $\pm$ err <sub>rand</sub> (N) dex
log $\epsilon(X)_\odot$	3.17	5.02	5.02
S08-131	-0.32 $\pm$ 0.16 $\pm$ 0.11 (2)		
S08-151*			
S08-183			-0.02 $\pm$ 0.14 $\pm$ 0.08 (3)
S08-184			+0.12 $\pm$ 0.13 $\pm$ 0.13 (2)
S08-199			+0.10 $\pm$ 0.14 $\pm$ 0.11 (4)
S08-202			
S08-203			+0.45 $\pm$ 0.13 $\pm$ 0.14 (3)
S08-222			
S08-225*			+0.86 $\pm$ 0.13 $\pm$ 0.41 (3)
S08-239	-0.38 $\pm$ 0.17 $\pm$ 0.08 (2)		+0.12 $\pm$ 0.17 $\pm$ 0.07 (3)
S08-241	-0.29 $\pm$ 0.16 $\pm$ 0.06 (2)		+0.31 $\pm$ 0.16 $\pm$ 0.07 (2)
S08-242	-0.22 $\pm$ 0.17 $\pm$ 0.07 (2)		+0.04 $\pm$ 0.17 $\pm$ 0.03 (3)
S08-245	-0.24 $\pm$ 0.12 $\pm$ 0.10 (1)		+0.40 $\pm$ 0.12 $\pm$ 0.11 (2)
S08-246			-0.04 $\pm$ 0.16 $\pm$ 0.07 (3)
S08-250	+0.02 $\pm$ 0.16 $\pm$ 0.09 (2)		+0.05 $\pm$ 0.16 $\pm$ 0.06 (3)
S08-252			+0.32 $\pm$ 0.14 $\pm$ 0.10 (2)
S08-253			-0.10 $\pm$ 0.14 $\pm$ 0.06 (3)
S08-257			
S08-258	-0.02 $\pm$ 0.14 $\pm$ 0.10 (1)		+0.48 $\pm$ 0.14 $\pm$ 0.07 (4)
S08-259	-0.25 $\pm$ 0.15 $\pm$ 0.11 (2)		+0.09 $\pm$ 0.15 $\pm$ 0.13 (2)
S08-261			
S08-264			
S08-267			
S08-274	-0.20 $\pm$ 0.12 $\pm$ 0.14 (1)		+0.51 $\pm$ 0.12 $\pm$ 0.13 (2)
S08-280			
S08-282			
S08-284			+0.30 $\pm$ 0.14 $\pm$ 0.15 (1)
S08-289	-0.10 $\pm$ 0.14 $\pm$ 0.14 (1)		+0.50 $\pm$ 0.14 $\pm$ 0.10 (3)
S08-291			+0.42 $\pm$ 0.13 $\pm$ 0.15 (4)
S08-292*			
S08-295			
S08-298			+0.18 $\pm$ 0.15 $\pm$ 0.14 (3)
S08-303			
S08-307			+0.54 $\pm$ 0.13 $\pm$ 0.15 (3)
S08-309*			
S08-316*			+1.37 $\pm$ 0.12 $\pm$ 0.47 (1)
S08-317			
S08-323			
S08-331*			
S08-332*			

**Appendix A. An appendix**

---

Table A.9: continued.

ID	[Sc/Fe] $\pm$ err <sub>sys</sub> $\pm$ err <sub>rand</sub> (N) dex	[Ti1/Fe] $\pm$ err <sub>sys</sub> $\pm$ err <sub>rand</sub> (N) dex	[Ti2/Fe] $\pm$ err <sub>sys</sub> $\pm$ err <sub>rand</sub> (N) dex
log $\epsilon(X)_\odot$	3.17	5.02	5.02
S08-336*			
S08-339			
S08-341*			
S11-97			
S11-100	-0.31 $\pm$ 0.17 $\pm$ 0.04 (2)		+0.09 $\pm$ 0.16 $\pm$ 0.04 (3)
S11-113	-0.44 $\pm$ 0.17 $\pm$ 0.07 (2)		+0.16 $\pm$ 0.17 $\pm$ 0.05 (3)
S11-127*			
S11-137			
S11-139			
S11-141*			+0.77 $\pm$ 0.15 $\pm$ 0.46 (1)

Table A.10: Atomic abundances for Cr, Mn and Co. The considered solar abundances given in the first line are from Grevesse & Sauval (1998). The number of lines used to determined each abundance is indicated in brackets. The asterisks indicate stars having a signal-to-noise  $\leq 10$ .

ID	[Cr/Fe] $\pm$ err <sub>sys</sub> $\pm$ err <sub>rand</sub> (N) dex	[Mn/Fe] $\pm$ err <sub>sys</sub> $\pm$ err <sub>rand</sub> (N) dex	[Co/Fe] $\pm$ err <sub>sys</sub> $\pm$ err <sub>rand</sub> dex
log $\epsilon(X)_\odot$	5.67	5.39	4.92
S05-10	-0.28 $\pm$ 0.24 $\pm$ 0.03 (2)	-0.74 $\pm$ 0.26 $\pm$ 0.04 (1)	
S05-47	+0.01 $\pm$ 0.25 $\pm$ 0.08 (2)		
S05-60	-0.33 $\pm$ 0.19 $\pm$ 0.14 (3)		
S05-67	-0.13 $\pm$ 0.22 $\pm$ 0.13 (1)		
S05-70			
S05-78			
S05-84*			
S05-86	-0.12 $\pm$ 0.21 $\pm$ 0.13 (3)		
S05-93	-0.15 $\pm$ 0.19 $\pm$ 0.17 (2)		
S05-94			
S05-95*			
S05-98			
S05-101*			
S05-104			
S05-111			
S05-112*			
S05-115			
S05-123*			
S05-132*			
S05-133*			
S05-168*			
S07-16	-0.21 $\pm$ 0.22 $\pm$ 0.02 (2)		
S07-69	-0.18 $\pm$ 0.21 $\pm$ 0.08 (1)		
S07-76			
S07-79			
S07-81			
S07-110*			
S07-112*			
S07-115*			
S08-3		-0.78 $\pm$ 0.22 $\pm$ 0.02 (2)	-0.12 $\pm$ 0.14 $\pm$ 0.02
S08-6		-0.37 $\pm$ 0.20 $\pm$ 0.03 (2)	-0.38 $\pm$ 0.18 $\pm$ 0.02
S08-38		-0.39 $\pm$ 0.25 $\pm$ 0.05 (2)	
S08-59			
S08-71			
S08-75			
S08-98			
S08-113*			

**Appendix A. An appendix**

Table A.10: continued.

ID	[Cr/Fe] $\pm$ err <sub>sys</sub> $\pm$ err <sub>rand</sub> (N) dex	[Mn/Fe] $\pm$ err <sub>sys</sub> $\pm$ err <sub>rand</sub> (N) dex	[Co/Fe] $\pm$ err <sub>sys</sub> $\pm$ err <sub>rand</sub> dex
log $\epsilon(X)_\odot$	5.67	5.39	4.92
S08-131			
S08-151*			
S08-183	+0.11 $\pm$ 0.19 $\pm$ 0.12 (2)		
S08-184			
S08-199			
S08-202			
S08-203			
S08-222			
S08-225*			
S08-239			
S08-241			
S08-242			
S08-245			
S08-246			
S08-250			
S08-252			
S08-253			
S08-257			
S08-258			
S08-259			
S08-261			
S08-264			
S08-267			
S08-274			
S08-280			
S08-282			
S08-284			
S08-289	-0.25 $\pm$ 0.19 $\pm$ 0.12 (2)		
S08-291			
S08-292*			
S08-295			
S08-298			
S08-303			
S08-307			
S08-309*			
S08-316*			
S08-317			
S08-323			
S08-331*			
S08-332*			



Table A.10: continued.

ID	[Cr/Fe] $\pm$ err <sub>sys</sub> $\pm$ err <sub>rand</sub> (N) dex	[Mn/Fe] $\pm$ err <sub>sys</sub> $\pm$ err <sub>rand</sub> (N) dex	[Co/Fe] $\pm$ err <sub>sys</sub> $\pm$ err <sub>rand</sub> dex
log $\epsilon(X)_\odot$	5.67	5.39	4.92
S08-336*			
S08-339			
S08-341*			
S11-97			
S11-100	-0.01 $\pm$ 0.24 $\pm$ 0.04 (2)	-0.26 $\pm$ 0.20 $\pm$ 0.08 (1)	
S11-113			
S11-127*			
S11-137			
S11-139			
S11-141*			

## Appendix A. An appendix

Table A.11: Atomic abundances for Ni, Ba and Eu. The considered solar abundances given in the first line are from Grevesse & Sauval (1998). The number of lines used to determined each abundance is indicated in brackets. The asterisks indicate stars having a signal-to-noise  $\leq 10$ .

ID	[Ni/Fe] $\pm$ err <sub>sys</sub> $\pm$ err <sub>rand</sub> (N) dex	[Ba/Fe] $\pm$ err <sub>sys</sub> $\pm$ err <sub>rand</sub> (N) dex	[Eu/Fe] $\pm$ err <sub>sys</sub> $\pm$ err <sub>rand</sub> dex
log $\epsilon(X)_\odot$	6.25	2.13	0.51
S05-10	-0.15 $\pm$ 0.19 $\pm$ 0.05 (2)	+0.29 $\pm$ 0.18 $\pm$ 0.03 (2)	+0.70 $\pm$ 0.15 $\pm$ 0.06
S05-47		-0.04 $\pm$ 0.20 $\pm$ 0.08 (2)	
S05-60		+0.35 $\pm$ 0.18 $\pm$ 0.12 (2)	
S05-67		+0.41 $\pm$ 0.19 $\pm$ 0.08 (2)	
S05-70		-0.27 $\pm$ 0.15 $\pm$ 0.12 (2)	
S05-78		+0.22 $\pm$ 0.15 $\pm$ 0.26 (2)	
S05-84*			
S05-86		+0.54 $\pm$ 0.18 $\pm$ 0.11 (2)	
S05-93			
S05-94			
S05-95*			
S05-98			
S05-101*			
S05-104			
S05-111			
S05-112*			
S05-115			
S05-123*			
S05-132*			
S05-133*			
S05-168*			
S07-16	+0.28 $\pm$ 0.19 $\pm$ 0.05 (1)	+0.62 $\pm$ 0.19 $\pm$ 0.04 (1)	
S07-69		-0.10 $\pm$ 0.18 $\pm$ 0.07 (2)	
S07-76			
S07-79			
S07-81			
S07-110*			
S07-112*			
S07-115*			
S08-3	-0.28 $\pm$ 0.14 $\pm$ 0.02 (4)	+0.33 $\pm$ 0.13 $\pm$ 0.02 (2)	+0.80 $\pm$ 0.09 $\pm$ 0.03
S08-6	-0.34 $\pm$ 0.18 $\pm$ 0.03 (2)	+0.25 $\pm$ 0.19 $\pm$ 0.03 (2)	
S08-38	+0.09 $\pm$ 0.20 $\pm$ 0.03 (3)	+0.35 $\pm$ 0.19 $\pm$ 0.04 (2)	+0.87 $\pm$ 0.16 $\pm$ 0.06
S08-59			
S08-71	+0.12 $\pm$ 0.16 $\pm$ 0.11 (2)		
S08-75		+0.38 $\pm$ 0.18 $\pm$ 0.20 (1)	
S08-98		+0.59 $\pm$ 0.16 $\pm$ 0.12 (2)	
S08-113*			

Table A.11: continued.

ID	[Ni/Fe] $\pm$ err <sub>sys</sub> $\pm$ err <sub>rand</sub> (N) dex	[Ba/Fe] $\pm$ err <sub>sys</sub> $\pm$ err <sub>rand</sub> (N) dex	[Eu/Fe] $\pm$ err <sub>sys</sub> $\pm$ err <sub>rand</sub> dex
log $\epsilon(X)_\odot$	6.25	2.13	0.51
S08-131		+0.16 $\pm$ 0.19 $\pm$ 0.10 (2)	
S08-151*			
S08-183		-0.11 $\pm$ 0.16 $\pm$ 0.19 (1)	
S08-184			
S08-199		+0.42 $\pm$ 0.16 $\pm$ 0.12 (2)	
S08-202		+0.33 $\pm$ 0.19 $\pm$ 0.22 (1)	
S08-203			
S08-222			
S08-225*			
S08-239		+0.13 $\pm$ 0.20 $\pm$ 0.08 (2)	
S08-241		+0.01 $\pm$ 0.19 $\pm$ 0.05 (2)	
S08-242		+0.26 $\pm$ 0.21 $\pm$ 0.06 (2)	+0.52 $\pm$ 0.17 $\pm$ 0.11
S08-245			
S08-246		+0.39 $\pm$ 0.19 $\pm$ 0.08 (2)	
S08-250			+0.70 $\pm$ 0.16 $\pm$ 0.13
S08-252		-0.10 $\pm$ 0.16 $\pm$ 0.09 (2)	
S08-253		+0.35 $\pm$ 0.17 $\pm$ 0.08 (2)	
S08-257			
S08-258		+0.58 $\pm$ 0.17 $\pm$ 0.08 (2)	
S08-259		-0.03 $\pm$ 0.17 $\pm$ 0.11 (2)	
S08-261		-0.42 $\pm$ 0.14 $\pm$ 0.08 (2)	
S08-264			
S08-267			
S08-274			
S08-280		+0.21 $\pm$ 0.17 $\pm$ 0.11 (2)	
S08-282		+0.13 $\pm$ 0.16 $\pm$ 0.18 (2)	
S08-284		+0.01 $\pm$ 0.17 $\pm$ 0.11 (2)	
S08-289		+0.73 $\pm$ 0.16 $\pm$ 0.14 (1)	
S08-291			
S08-292*			
S08-295			
S08-298		+0.71 $\pm$ 0.17 $\pm$ 0.11 (2)	
S08-303			
S08-307		+0.06 $\pm$ 0.15 $\pm$ 0.24 (2)	
S08-309*			
S08-316*			
S08-317		+0.29 $\pm$ 0.16 $\pm$ 0.14 (2)	
S08-323		+0.67 $\pm$ 0.16 $\pm$ 0.21 (1)	
S08-331*			
S08-332*			

**Appendix A. An appendix**

---

Table A.11: continued.

ID	[Ni/Fe] $\pm$ err <sub>sys</sub> $\pm$ err <sub>rand</sub> (N) dex	[Ba/Fe] $\pm$ err <sub>sys</sub> $\pm$ err <sub>rand</sub> (N) dex	[Eu/Fe] $\pm$ err <sub>sys</sub> $\pm$ err <sub>rand</sub> dex
log $\epsilon(X)_\odot$	6.25	2.13	0.51
S08-336*			
S08-339			
S08-341*			
S11-97		-0.64 $\pm$ 0.18 $\pm$ 0.06 (1)	
S11-100		+0.04 $\pm$ 0.20 $\pm$ 0.07 (1)	
S11-113		+0.47 $\pm$ 0.20 $\pm$ 0.06 (2)	
S11-127*			
S11-137		-0.08 $\pm$ 0.19 $\pm$ 0.14 (2)	
S11-139		+0.25 $\pm$ 0.16 $\pm$ 0.11 (2)	
S11-141*			

Table A.12: Results of the classical analysis for the sub-sample of high signal-to-noise stars: stellar parameters and abundances for Mg, Ca, Sc, Ti. The signal-to-noise ratios come from this study.

ID	$T_{eff}$ K	$\log g$	$v_{turb}$ km/s	S/N	[Fe/H] $\pm$ err dex	[Mg/Fe] $\pm$ err dex	[Ca/Fe] $\pm$ err dex	[Sc/Fe] $\pm$ err dex	[Ti1/Fe] $\pm$ err dex	[Ti2/Fe] $\pm$ err dex
S05-10	4337	0.90	1.80	71	-2.01 $\pm$ 0.03	0.22 $\pm$ 0.05	0.07 $\pm$ 0.04	0.11 $\pm$ 0.04		0.23 $\pm$ 0.06
S05-60	4792	1.57	1.40	19	-1.67 $\pm$ 0.11	-0.05 $\pm$ 0.14	-0.16 $\pm$ 0.16	0.34 $\pm$ 0.13		0.19 $\pm$ 0.13
S07-69	4737	1.51	1.50	33	-1.95 $\pm$ 0.08	0.05 $\pm$ 0.11	0.19 $\pm$ 0.11	0.09 $\pm$ 0.13		0.22 $\pm$ 0.11
S08-3	4172	0.57	2.08	117	-2.07 $\pm$ 0.02	0.22 $\pm$ 0.04	0.11 $\pm$ 0.03	0.04 $\pm$ 0.03	-0.34 $\pm$ 0.02	0.12 $\pm$ 0.03
S08-6	4312	0.73	1.90	83	-1.50 $\pm$ 0.03	-0.20 $\pm$ 0.05	-0.24 $\pm$ 0.04	-0.32 $\pm$ 0.05	-0.57 $\pm$ 0.03	-0.20 $\pm$ 0.06
S08-38	4508	1.02	1.99	69	-2.09 $\pm$ 0.04	0.11 $\pm$ 0.05	0.14 $\pm$ 0.05	-0.13 $\pm$ 0.04		0.17 $\pm$ 0.06
S08-183	4958	1.68	1.65	23	-1.56 $\pm$ 0.08	-0.41 $\pm$ 0.11	-0.04 $\pm$ 0.10	0.12 $\pm$ 0.12		-0.13 $\pm$ 0.11
S08-239	4546	1.34	1.75	51	-1.87 $\pm$ 0.05	-0.29 $\pm$ 0.07	-0.01 $\pm$ 0.06	-0.39 $\pm$ 0.07		0.04 $\pm$ 0.09
S08-241	4686	1.44	1.50	53	-1.98 $\pm$ 0.05	0.11 $\pm$ 0.09	0.21 $\pm$ 0.07	-0.11 $\pm$ 0.08		0.28 $\pm$ 0.07
S08-242	4655	1.44	1.60	38	-1.57 $\pm$ 0.06	-0.14 $\pm$ 0.11	-0.09 $\pm$ 0.08	-0.30 $\pm$ 0.07		0.00 $\pm$ 0.08
S08-246	4717	1.53	1.80	30	-1.57 $\pm$ 0.07	-0.49 $\pm$ 0.09	-0.11 $\pm$ 0.10	-0.47 $\pm$ 0.08		-0.24 $\pm$ 0.11

Table A.13: Results of the classical analysis for the sub-sample of high signal-to-noise stars: abundances for Cr, Mn, Co, Ni, Ba and Eu.

ID	[Cr/Fe] $\pm$ err dex	[Mn/Fe] $\pm$ err dex	[Co/Fe] $\pm$ err dex	[Ni/Fe] $\pm$ err dex	[Ba/Fe] $\pm$ err dex	[Eu/Fe] $\pm$ err dex
S05-10	-0.46 $\pm$ 0.05	-0.81 $\pm$ 0.07	-0.07 $\pm$ 0.05	0.39 $\pm$ 0.26	0.43 $\pm$ 0.04	
S05-60	-0.48 $\pm$ 0.15			-0.40 $\pm$ 0.19	0.27 $\pm$ 0.14	
S07-69	-0.11 $\pm$ 0.14		0.13 $\pm$ 0.11	0.58 $\pm$ 0.14	-0.10 $\pm$ 0.14	
S08-3	-0.35 $\pm$ 0.04	-0.65 $\pm$ 0.03	0.06 $\pm$ 0.04	-0.21 $\pm$ 0.02	0.16 $\pm$ 0.03	0.89 $\pm$ 0.03
S08-6	-0.38 $\pm$ 0.05	-0.21 $\pm$ 0.04	-0.32 $\pm$ 0.09	-0.32 $\pm$ 0.04	-0.01 $\pm$ 0.05	
S08-38	-0.31 $\pm$ 0.04			0.17 $\pm$ 0.07	0.23 $\pm$ 0.07	
S08-183	0.39 $\pm$ 0.13			0.17 $\pm$ 0.10	-0.52 $\pm$ 0.14	
S08-239	-0.31 $\pm$ 0.08			0.28 $\pm$ 0.09	0.00 $\pm$ 0.07	
S08-241	-0.43 $\pm$ 0.06			0.27 $\pm$ 0.09	0.21 $\pm$ 0.08	
S08-242	-0.13 $\pm$ 0.11	-0.32 $\pm$ 0.13	0.00 $\pm$ 0.09	0.12 $\pm$ 0.08	0.45 $\pm$ 0.08	0.81 $\pm$ 0.10
S08-246	-0.31 $\pm$ 0.11			-0.10 $\pm$ 0.35	-0.20 $\pm$ 0.15	

# Bibliography

- Abramowski, A., Aharonian, F., Ait Benkhali, F., et al. 2014, *Phys. Rev. D*, 90, 112012
- Abt, H. A. & Levy, S. G. 1976, in *Bulletin of the American Astronomical Society*, Vol. 8, *Bulletin of the American Astronomical Society*, 521
- Abt, H. A. & Levy, S. G. 1978, *ApJS*, 36, 241
- Adén, D., Eriksson, K., Feltzing, S., et al. 2011, *A&A*, 525, A153
- Agertz, O., Kravtsov, A. V., Leitner, S. N., & Gnedin, N. Y. 2013, *ApJ*, 770, 25
- Alonso, A., Arribas, S., & Martínez-Roger, C. 1999, *A&AS*, 140, 261
- Anthony-Twarog, B. J., Deliyannis, C. P., Rich, E., & Twarog, B. A. 2013, *ApJ*, 767, L19
- Aoki, W., Arimoto, N., Sadakane, K., et al. 2009, *A&A*, 502, 569
- Aoki, W., Beers, T. C., Christlieb, N., et al. 2007, *ApJ*, 655, 492
- Aoki, W., Beers, T. C., Lee, Y. S., et al. 2013, *AJ*, 145, 13
- Aoki, W., Honda, S., Beers, T. C., et al. 2005, *ApJ*, 632, 611
- Asplund, M., Grevesse, N., Sauval, A. J., & Scott, P. 2009, *ARA&A*, 47, 481
- Avila-Reese, V., Colín, P., Valenzuela, O., D'Onghia, E., & Firmani, C. 2001, *ApJ*, 559, 516
- Baade, W. 1944a, *ApJ*, 100, 147
- Baade, W. 1944b, *ApJ*, 100, 137
- Badenes, C., Bravo, E., & Hughes, J. P. 2008, *ApJ*, 680, L33
- Barklem, P. S., Christlieb, N., Beers, T. C., et al. 2005, *A&A*, 439, 129
- Battaglia, G., Helmi, A., Tolstoy, E., et al. 2008, *ApJ*, 681, L13
- Battaglia, G., Irwin, M., Tolstoy, E., de Boer, T., & Mateo, M. 2012, *ApJ*, 761, L31
- Battaglia, G., Tolstoy, E., Helmi, A., et al. 2011, *MNRAS*, 411, 1013

## Bibliography

---

- Battaglia, G., Tolstoy, E., Helmi, A., et al. 2006, *A&A*, 459, 423
- Battistini, C. & Bensby, T. 2015, ArXiv e-prints
- Behroozi, P. S., Conroy, C., & Wechsler, R. H. 2010, *ApJ*, 717, 379
- Bellazzini, M., Ibata, R., Martin, N., et al. 2006, *MNRAS*, 366, 865
- Belokurov, V., Zucker, D. B., Evans, N. W., et al. 2006a, *ApJ*, 642, L137
- Belokurov, V., Zucker, D. B., Evans, N. W., et al. 2007, *ApJ*, 654, 897
- Belokurov, V., Zucker, D. B., Evans, N. W., et al. 2006b, *ApJ*, 647, L111
- Bergemann, M. & Cescutti, G. 2010, *A&A*, 522, A9
- Bernstein-Cooper, E. Z., Cannon, J. M., Elson, E. C., et al. 2014, *AJ*, 148, 35
- Bethe, H. A. 1939, *Physical Review*, 55, 434
- Binggeli, B. 1994, in *European Southern Observatory Conference and Workshop Proceedings*, Vol. 49, *European Southern Observatory Conference and Workshop Proceedings*, ed. G. Meylan & P. Prugniel, 13
- Bisterzo, S., Travaglio, C., Gallino, R., Wiescher, M., & Käppeler, F. 2014, *ApJ*, 787, 10
- Boylan-Kolchin, M., Bullock, J. S., & Kaplinghat, M. 2011, *MNRAS*, 415, L40
- Bromm, V. & Loeb, A. 2003, *Nature*, 425, 812
- Brown, T. M., Tumlinson, J., Geha, M., et al. 2012, *ApJ*, 753, L21
- Burbidge, E. M., Burbidge, G. R., Fowler, W. A., & Hoyle, F. 1957, *Reviews of Modern Physics*, 29, 547
- Burkert, A. 2000, *ApJ*, 534, L143
- Burris, D. L., Pilachowski, C. A., Armandroff, T. E., et al. 2000, *ApJ*, 544, 302
- Calura, F., Pipino, A., Chiappini, C., Matteucci, F., & Maiolino, R. 2009, *A&A*, 504, 373
- Cameron, A. G. W. 1957a, *AJ*, 62, 9
- Cameron, A. G. W. 1957b, *AJ*, 62, 138
- Cardelli, J. A., Clayton, G. C., & Mathis, J. S. 1989, *ApJ*, 345, 245
- Carollo, D., Beers, T. C., Bovy, J., et al. 2012, *ApJ*, 744, 195
- Carraro, G. 2014, ArXiv e-prints
- Carretta, E., Bragaglia, A., Gratton, R. G., et al. 2010, *A&A*, 520, A95
- Carretta, E., Bragaglia, A., Gratton, R. G., & Tosi, M. 2004, *A&A*, 422, 951



- Cayrel, R., Depagne, E., Spite, M., et al. 2004, *A&A*, 416, 1117
- Cayrel, R., Perrin, M.-N., Barbuy, B., & Buser, R. 1991, *A&A*, 247, 108
- Cescutti, G., Matteucci, F., Lanfranchi, G. A., & McWilliam, A. 2008, *A&A*, 491, 401
- Christlieb, N. 2003, in *Reviews in Modern Astronomy*, Vol. 16, *Reviews in Modern Astronomy*, ed. R. E. Schielicke, 191
- Cohen, J. G., Christlieb, N., McWilliam, A., et al. 2008, *ApJ*, 672, 320
- Cohen, J. G., Christlieb, N., Thompson, I., et al. 2013, *ApJ*, 778, 56
- Cohen, J. G. & Huang, W. 2009, *ApJ*, 701, 1053
- Cohen, J. G. & Huang, W. 2010a, *ApJ*, 719, 931
- Cohen, J. G. & Huang, W. 2010b, *ApJ*, 719, 931
- Cohen, J. G., McWilliam, A., Shectman, S., et al. 2006, *AJ*, 132, 137
- Cohen, J. G., Shectman, S., Thompson, I., et al. 2005, *ApJ*, 633, L109
- Coleman, M., Da Costa, G. S., Bland-Hawthorn, J., et al. 2004, *AJ*, 127, 832
- Coleman, M. G., Da Costa, G. S., Bland-Hawthorn, J., & Freeman, K. C. 2005, *AJ*, 129, 1443
- Coleman, M. G. & de Jong, J. T. A. 2008, *ApJ*, 685, 933
- de Boer, T. J. L., Belokurov, V., Beers, T. C., & Lee, Y. S. 2014a, *MNRAS*, 443, 658
- de Boer, T. J. L., Tolstoy, E., Hill, V., et al. 2012, *A&A*, 539, A103
- de Boer, T. J. L., Tolstoy, E., Lemasle, B., et al. 2014b, *A&A*, 572, A10
- de Boer, T. J. L., Tolstoy, E., Saha, A., et al. 2011, *A&A*, 528, A119
- de Boer, T. J. L., Tolstoy, E., Saha, A., & Olszewski, E. W. 2013, *A&A*, 551, A103
- Dekel, A. & Silk, J. 1986, *ApJ*, 303, 39
- Dolphin, A. E. 2002, *MNRAS*, 332, 91
- Edmonds, Jr., F. N. 1969, *J. Quant. Spec. Radiat. Transf.*, 9, 1427
- Eggleton, P. P. & Tokovinin, A. A. 2008, *MNRAS*, 389, 869
- Faucher-Giguère, C.-A., Kereš, D., & Ma, C.-P. 2011, *MNRAS*, 417, 2982
- Feltzing, S., Eriksson, K., Kleyana, J., & Wilkinson, M. I. 2009, *A&A*, 508, L1
- Feltzing, S., Fohlman, M., & Bensby, T. 2007, *A&A*, 467, 665

## Bibliography

---

- Flores, R. A. & Primack, J. R. 1994, *ApJ*, 427, L1
- Forbes, D. A. & Bridges, T. 2010, *MNRAS*, 404, 1203
- François, P., Depagne, E., Hill, V., et al. 2007, *A&A*, 476, 935
- Frebel, A. & Bromm, V. 2012, *ApJ*, 759, 115
- Frebel, A., Christlieb, N., Norris, J. E., et al. 2006, *ApJ*, 652, 1585
- Frebel, A., Simon, J. D., Geha, M., & Willman, B. 2010, *ApJ*, 708, 560
- Frebel, A., Simon, J. D., & Kirby, E. N. 2014, *ApJ*, 786, 74
- Freeman, K. & Bland-Hawthorn, J. 2002, *ARA&A*, 40, 487
- Fulbright, J. P., McWilliam, A., & Rich, R. M. 2007, *ApJ*, 661, 1152
- Fulbright, J. P., Rich, R. M., & Castro, S. 2004, *ApJ*, 612, 447
- Gallazzi, A., Charlot, S., Brinchmann, J., White, S. D. M., & Tremonti, C. A. 2005, *MNRAS*, 362, 41
- Gao, S., Liu, C., Zhang, X., et al. 2014, *ApJ*, 788, L37
- Geisler, D., Smith, V. V., Wallerstein, G., Gonzalez, G., & Charbonnel, C. 2005, *AJ*, 129, 1428
- Gilmore, G., Kozlov, S., Norris, J. E., et al. 2013, *The Messenger*, 151, 25
- Governato, F., Zolotov, A., Pontzen, A., et al. 2012, *MNRAS*, 422, 1231
- Gratton, R. G., Carretta, E., Desidera, S., et al. 2003, *A&A*, 406, 131
- Gray, D. F. 1989, *ApJ*, 347, 1021
- Gray, D. F. 2008, *The Observation and Analysis of Stellar Photospheres*
- Grevesse, N. & Sauval, A. J. 1998, *Space Sci. Rev.*, 85, 161
- Gupta, A., Mathur, S., Krongold, Y., Nicastro, F., & Galeazzi, M. 2012, *ApJ*, 756, L8
- Gustafsson, B., Edvardsson, B., Eriksson, K., et al. 2008, *A&A*, 486, 951
- Held, E. V., Clementini, G., Rizzi, L., et al. 2001, *ApJ*, 562, L39
- Hendricks, B., Koch, A., Lanfranchi, G. A., et al. 2014, *ApJ*, 785, 102
- Hewett, P. C., Warren, S. J., Leggett, S. K., & Hodgkin, S. T. 2006, *MNRAS*, 367, 454
- Honda, S., Aoki, W., Arimoto, N., & Sadakane, K. 2011, *PASJ*, 63, 523
- Honda, S., Aoki, W., Kajino, T., et al. 2004, *ApJ*, 607, 474
- Hopkins, P. F., Quataert, E., & Murray, N. 2011, *MNRAS*, 417, 950

- Hoyle, F. & Fowler, W. A. 1960, *ApJ*, 132, 565
- Ibata, R., Irwin, M., Lewis, G. F., & Stolte, A. 2001, *ApJ*, 547, L133
- Ibata, R. A., Gilmore, G., & Irwin, M. J. 1995, *MNRAS*, 277, 781
- Ibata, R. A., Lewis, G. F., Conn, A. R., et al. 2013, *Nature*, 493, 62
- Iben, I. & Tutukov, A. V. 1984a, in *American Institute of Physics Conference Series*, Vol. 115, American Institute of Physics Conference Series, ed. S. E. Woosley, 11–30
- Iben, Jr., I. & Tutukov, A. V. 1984b, *ApJ*, 284, 719
- Irwin, M. & Hatzidimitriou, D. 1995, *MNRAS*, 277, 1354
- Irwin, M. J., Bunclark, P. S., Bridgeland, M. T., & McMahon, R. G. 1990, *MNRAS*, 244, 16P
- Ishigaki, M. N., Aoki, W., Arimoto, N., & Okamoto, S. 2014, *ArXiv e-prints*
- Ishigaki, M. N., Aoki, W., & Chiba, M. 2013, *ApJ*, 771, 67
- Iwamoto, K., Brachwitz, F., Nomoto, K., et al. 1999, *ApJS*, 125, 439
- Jarosik, N., Bennett, C. L., Dunkley, J., et al. 2011, *ApJS*, 192, 14
- Johnston, K. V., Spergel, D. N., & Hernquist, L. 1995, *ApJ*, 451, 598
- Just, O., Bauswein, A., Ardevol Pulpillo, R., Goriely, S., & Janka, H.-T. 2014, *ArXiv e-prints*
- Karakas, A. I. & Lattanzio, J. C. 2014, *PASA*, 31, 30
- Kaufer, A., Venn, K. A., Tolstoy, E., Pinte, C., & Kudritzki, R.-P. 2004, *AJ*, 127, 2723
- Kereš, D., Katz, N., Davé, R., Fardal, M., & Weinberg, D. H. 2009, *MNRAS*, 396, 2332
- Kinman, T. D. & Kraft, R. P. 1980, *AJ*, 85, 415
- Kirby, E. N., Cohen, J. G., Guhathakurta, P., et al. 2013, *ApJ*, 779, 102
- Kirby, E. N., Guhathakurta, P., Simon, J. D., et al. 2010, *ApJS*, 191, 352
- Kirby, E. N., Simon, J. D., Geha, M., Guhathakurta, P., & Frebel, A. 2008, *ApJ*, 685, L43
- Klypin, A., Kravtsov, A. V., Valenzuela, O., & Prada, F. 1999, *ApJ*, 522, 82
- Kobayashi, C., Tsujimoto, T., Nomoto, K., Hachisu, I., & Kato, M. 1998, *ApJ*, 503, L155
- Kobayashi, C., Umeda, H., Nomoto, K., Tominaga, N., & Ohkubo, T. 2006, *ApJ*, 653, 1145
- Kobulnicky, H. A. & Fryer, C. L. 2007, *ApJ*, 670, 747
- Koch, A., Grebel, E. K., Wyse, R. F. G., et al. 2006, *AJ*, 131, 895

## Bibliography

---

- Koch, A., Matteucci, F., & Feltzing, S. 2012, in American Institute of Physics Conference Series, Vol. 1480, American Institute of Physics Conference Series, ed. M. Umemura & K. Omukai, 190–193
- Koch, A., McWilliam, A., Grebel, E. K., Zucker, D. B., & Belokurov, V. 2008, *ApJ*, 688, L13
- Kormendy, J. 1985, *ApJ*, 295, 73
- Kormendy, J. & Fisher, D. B. 2008, in Astronomical Society of the Pacific Conference Series, Vol. 396, Formation and Evolution of Galaxy Disks, ed. J. G. Funes & E. M. Corsini, 297
- Kratz, K.-L., Farouqi, K., Pfeiffer, B., et al. 2007, *ApJ*, 662, 39
- Kuzio de Naray, R., Martinez, G. D., Bullock, J. S., & Kaplinghat, M. 2010, *ApJ*, 710, L161
- Lai, D. K., Johnson, J. A., Bolte, M., & Lucatello, S. 2007, *ApJ*, 667, 1185
- Lai, D. K., Lee, Y. S., Bolte, M., et al. 2011, *ApJ*, 738, 51
- Lanfranchi, G. A., Matteucci, F., & Cescutti, G. 2008, *A&A*, 481, 635
- Lawler, J. E., Wickliffe, M. E., den Hartog, E. A., & Sneden, C. 2001, *ApJ*, 563, 1075
- Lee, M. G., Park, H. S., Park, J.-H., et al. 2003, *AJ*, 126, 2840
- Lee, M. G., Yuk, I.-S., Park, H. S., Harris, J., & Zaritsky, D. 2009, *ApJ*, 703, 692
- Lee, Y. S., Beers, T. C., Masseron, T., et al. 2013, *AJ*, 146, 132
- Lemasle, B., de Boer, T. J. L., Hill, V., et al. 2014, *A&A*, 572, A88
- Lemasle, B., François, P., Bono, G., et al. 2007, *A&A*, 467, 283
- Lemasle, B., Hill, V., Tolstoy, E., et al. 2012, *A&A*, 538, A100
- Letarte, B., Hill, V., Jablonka, P., et al. 2006, *A&A*, 453, 547
- Letarte, B., Hill, V., Tolstoy, E., et al. 2010, *A&A*, 523, A17
- Lucatello, S., Beers, T. C., Christlieb, N., et al. 2006, *ApJ*, 652, L37
- Lucatello, S., Gratton, R., Carretta, E., & Beers, T. 2005, in IAU Symposium, Vol. 228, From Lithium to Uranium: Elemental Tracers of Early Cosmic Evolution, ed. V. Hill, P. Francois, & F. Primas, 473–477
- Lunney, D., Pearson, J. M., & Thibault, C. 2003, *Reviews of Modern Physics*, 75, 1021
- Lynden-Bell, D. & Lynden-Bell, R. M. 1995, *MNRAS*, 275, 429
- Magrini, L., Hunt, L., Galli, D., et al. 2012, *MNRAS*, 427, 1075
- Majewski, S. R., Kunkel, W. E., Law, D. R., et al. 2004, *AJ*, 128, 245
- Majewski, S. R., Skrutskie, M. E., Weinberg, M. D., & Ostheimer, J. C. 2003, *ApJ*, 599, 1082

- Marsteller, B., Beers, T. C., Rossi, S., et al. 2005, *Nuclear Physics A*, 758, 312
- Mateo, M. L. 1998, *ARA&A*, 36, 435
- Matteucci, F. 1994, *A&A*, 288, 57
- Matteucci, F. 2003, *Ap&SS*, 284, 539
- Matteucci, F. & Brocato, E. 1990, *ApJ*, 365, 539
- Matteucci, F. & Recchi, S. 2001, *ApJ*, 558, 351
- Mayer, L., Mastrogiuseppe, C., Wadsley, J., Stadel, J., & Moore, B. 2006, *MNRAS*, 369, 1021
- McConnachie, A. W. 2012, *AJ*, 144, 4
- McWilliam, A. 1997, *ARA&A*, 35, 503
- McWilliam, A. 1998, *AJ*, 115, 1640
- McWilliam, A. & Bernstein, R. A. 2008, *ApJ*, 684, 326
- McWilliam, A., Wallerstein, G., & Mottini, M. 2013, *ApJ*, 778, 149
- Merrill, P. W. 1952, *ApJ*, 116, 21
- Monaco, L., Bellazzini, M., Bonifacio, P., et al. 2005, *A&A*, 441, 141
- Moore, B. 1994, *Nature*, 370, 629
- Moore, B., Ghigna, S., Governato, F., et al. 1999a, *ApJ*, 524, L19
- Moore, B., Quinn, T., Governato, F., Stadel, J., & Lake, G. 1999b, *MNRAS*, 310, 1147
- Moster, B. P., Macciò, A. V., Somerville, R. S., Johansson, P. H., & Naab, T. 2010, *MNRAS*, 403, 1009
- Navarro, J. F., Eke, V. R., & Frenk, C. S. 1996, *MNRAS*, 283, L72
- Navarro, J. F., Frenk, C. S., & White, S. D. M. 1997, *ApJ*, 490, 493
- Nichols, M., Revaz, Y., & Jablonka, P. 2014, *A&A*, 564, A112
- Nomoto, K., Iwamoto, K., Nakasato, N., et al. 1997, *Nuclear Physics A*, 621, 467
- Norris, J. E., Gilmore, G., Wyse, R. F. G., et al. 2008, *ApJ*, 689, L113
- Norris, J. E., Ryan, S. G., & Beers, T. C. 1997, *ApJ*, 488, 350
- Norris, J. E., Wyse, R. F. G., Gilmore, G., et al. 2010, *ArXiv e-prints*
- Norris, J. E., Yong, D., Bessell, M. S., et al. 2013, *ApJ*, 762, 28
- North, P., Cescutti, G., Jablonka, P., et al. 2012, *A&A*, 541, A45

## Bibliography

---

- Ohkubo, T., Umeda, H., Maeda, K., et al. 2006, *ApJ*, 645, 1352
- Olszewski, E. W., Mateo, M., Harris, J., et al. 2006, *AJ*, 131, 912
- Orban, C., Gnedin, O. Y., Weisz, D. R., et al. 2008, *ApJ*, 686, 1030
- Pakmor, R., Hachinger, S., Röpke, F. K., & Hillebrandt, W. 2011, *A&A*, 528, A117
- Pasetto, S. & Chiosi, C. 2009, *A&A*, 499, 385
- Pasetto, S., Chiosi, C., & Carraro, G. 2003, *A&A*, 405, 931
- Pawlowski, M. S. & Kroupa, P. 2013, *MNRAS*, 435, 2116
- Pawlowski, M. S., Pflamm-Altenburg, J., & Kroupa, P. 2012, *MNRAS*, 423, 1109
- Perlmutter, S., Aldering, G., della Valle, M., et al. 1998, *Nature*, 391, 51
- Peter, A. H. G., Rocha, M., Bullock, J. S., & Kaplinghat, M. 2013, *MNRAS*, 430, 105
- Pietrzyński, G., Gieren, W., Szewczyk, O., et al. 2008, *AJ*, 135, 1993
- Pietrzyński, G., Górski, M., Gieren, W., et al. 2009, *AJ*, 138, 459
- Pipino, A., Calura, F., & Matteucci, F. 2013, *MNRAS*, 432, 2541
- Pompéia, L., Hill, V., Spite, M., et al. 2008, *A&A*, 480, 379
- Pontzen, A. & Governato, F. 2012, *MNRAS*, 421, 3464
- Prochaska, J. X., Naumov, S. O., Carney, B. W., McWilliam, A., & Wolfe, A. M. 2000, *AJ*, 120, 2513
- Qian, Y.-Z. & Wasserburg, G. J. 2007, *Phys. Rep.*, 442, 237
- Raiteri, C. M., Villata, M., & Navarro, J. F. 1996, *A&A*, 315, 105
- Ramírez, I. & Meléndez, J. 2005, *ApJ*, 626, 465
- Reddy, B. E., Lambert, D. L., & Allende Prieto, C. 2006, *MNRAS*, 367, 1329
- Revaz, Y. & Jablonka, P. 2012, *A&A*, 538, A82
- Revaz, Y., Jablonka, P., Sawala, T., et al. 2009, *A&A*, 501, 189
- Richter, P. 2012, in *EAS Publications Series*, Vol. 56, *EAS Publications Series*, ed. M. A. de Avillez, 225–230
- Riess, A. G., Filippenko, A. V., Challis, P., et al. 1998, *AJ*, 116, 1009
- Rocha, M., Peter, A. H. G., Bullock, J. S., et al. 2013, *MNRAS*, 430, 81
- Röpke, F. K., Gieseler, M., Reinecke, M., Travaglio, C., & Hillebrandt, W. 2006, *A&A*, 453, 203

- Rossi, S., Beers, T. C., & Sneden, C. 1999, in *Astronomical Society of the Pacific Conference Series*, Vol. 165, *The Third Stromlo Symposium: The Galactic Halo*, ed. B. K. Gibson, R. S. Axelrod, & M. E. Putman, 264
- Sadakane, K., Arimoto, N., Ikuta, C., et al. 2004, *PASJ*, 56, 1041
- Sana, H., de Mink, S. E., de Koter, A., et al. 2012, *Science*, 337, 444
- Sbordone, L., Bonifacio, P., Buonanno, R., et al. 2007, *A&A*, 465, 815
- Schlegel, D. J., Finkbeiner, D. P., & Davis, M. 1998, *ApJ*, 500, 525
- Schmidt, B. P., Suntzeff, N. B., Phillips, M. M., et al. 1998, *ApJ*, 507, 46
- Searle, L., Sargent, W. L. W., & Bagnuolo, W. G. 1973, *ApJ*, 179, 427
- Sembach, K. R., Wakker, B. P., Savage, B. D., et al. 2003, *ApJS*, 146, 165
- Shetrone, M., Venn, K. A., Tolstoy, E., et al. 2003, *AJ*, 125, 684
- Shetrone, M. D., Côté, P., & Sargent, W. L. W. 2001, *ApJ*, 548, 592
- Shetrone, M. D., Siegel, M. H., Cook, D. O., & Bosler, T. 2009, *AJ*, 137, 62
- Simon, J. D., Frebel, A., McWilliam, A., Kirby, E. N., & Thompson, I. B. 2010, *ApJ*, 716, 446
- Simon, J. D. & Geha, M. 2007, *ApJ*, 670, 313
- Smith, G. H. 1984, *AJ*, 89, 801
- Sneden, C., Cowan, J. J., & Gallino, R. 2008, *ARA&A*, 46, 241
- Sneden, C. A. 1973, PhD thesis, THE UNIVERSITY OF TEXAS AT AUSTIN.
- Spite, M. 1967, *Annales d'Astrophysique*, 30, 211
- Spite, M., Cayrel, R., Plez, B., et al. 2005, *A&A*, 430, 655
- Starkenburg, E., Hill, V., Tolstoy, E., et al. 2013, *A&A*, 549, A88
- Starkenburg, E., Hill, V., Tolstoy, E., et al. 2010, *A&A*, 513, A34
- Stetson, P. B. 1984, *PASP*, 96, 128
- Stetson, P. B. & Pancino, E. 2008, *PASP*, 120, 1332
- Tafelmeyer, M., Jablonka, P., Hill, V., et al. 2010, *A&A*, 524, A58
- Tammann, G. A. 1994, in *European Southern Observatory Conference and Workshop Proceedings*, Vol. 49, *European Southern Observatory Conference and Workshop Proceedings*, ed. G. Meylan & P. Prugniel, 3
- Teysier, R., Pontzen, A., Dubois, Y., & Read, J. I. 2013, *MNRAS*, 429, 3068

## Bibliography

---

- The Fermi-LAT Collaboration, :, Ackermann, M., et al. 2013, ArXiv e-prints
- Thielemann, F.-K., Brachwitz, F., Höflich, P., Martinez-Pinedo, G., & Nomoto, K. 2004, *New A Rev.*, 48, 605
- Timmes, F. X., Brown, E. F., & Truran, J. W. 2003, *ApJ*, 590, L83
- Timmes, F. X., Woosley, S. E., & Weaver, T. A. 1995, *ApJS*, 98, 617
- Tinsley, B. M. 1979, *ApJ*, 229, 1046
- Tolstoy, E., Hill, V., & Tosi, M. 2009, *ARA&A*, 47, 371
- Tolstoy, E., Irwin, M. J., Helmi, A., et al. 2004, *ApJ*, 617, L119
- Tolstoy, E., Venn, K. A., Shetrone, M., et al. 2003, *AJ*, 125, 707
- Travaglio, C., Gallino, R., Arnone, E., et al. 2004, *ApJ*, 601, 864
- Travaglio, C., Hillebrandt, W., & Reinecke, M. 2005, *A&A*, 443, 1007
- Tsujimoto, T. & Shigeyama, T. 2014, *A&A*, 565, L5
- Tutukov, A. V. & Yungelson, L. R. 1994, *MNRAS*, 268, 871
- Umeda, H. & Nomoto, K. 2002, *ApJ*, 565, 385
- Umeda, H. & Nomoto, K. 2005, *ApJ*, 619, 427
- Van der Swaelmen, M., Hill, V., Primas, F., & Cole, A. A. 2013, *A&A*, 560, A44
- Vargas, L. C., Geha, M., Kirby, E. N., & Simon, J. D. 2013, *ApJ*, 767, 134
- Venn, K. A., Irwin, M., Shetrone, M. D., et al. 2004, *AJ*, 128, 1177
- Venn, K. A., Shetrone, M. D., Irwin, M. J., et al. 2012, *ApJ*, 751, 102
- Venn, K. A., Tolstoy, E., Kaufer, A., et al. 2003, *AJ*, 126, 1326
- Walker, M. G., Mateo, M., & Olszewski, E. W. 2009, *AJ*, 137, 3100
- Walker, M. G., Mateo, M., Olszewski, E. W., et al. 2006, *AJ*, 131, 2114
- Walker, M. G. & Peñarrubia, J. 2011, *ApJ*, 742, 20
- Wallerstein, G., Iben, Jr., I., Parker, P., et al. 1997, *Reviews of Modern Physics*, 69, 995
- Wanajo, S. 2013, *ApJ*, 770, L22
- Wanajo, S., Sekiguchi, Y., Nishimura, N., et al. 2014, *ApJ*, 789, L39
- Webbink, R. F. 1984, *ApJ*, 277, 355



- Whelan, J. & Iben, Jr., I. 1973, *ApJ*, 186, 1007
- White, S. D. M. & Frenk, C. S. 1991, *ApJ*, 379, 52
- Willman, B., Dalcanton, J. J., Martinez-Delgado, D., et al. 2005, *ApJ*, 626, L85
- Willman, B., Masjedi, M., Hogg, D. W., et al. 2006, *ArXiv Astrophysics e-prints*
- Woolsey, S. E. 1997, *ApJ*, 476, 801
- Woolsey, S. E., Arnett, W. D., & Clayton, D. D. 1973, *ApJS*, 26, 231
- Woolsey, S. E., Heger, A., & Weaver, T. A. 2002, *Reviews of Modern Physics*, 74, 1015
- Woolsey, S. E. & Weaver, T. A. 1995, *ApJS*, 101, 181
- Woolsey, S. E., Wilson, J. R., Mathews, G. J., Hoffman, R. D., & Meyer, B. S. 1994, *ApJ*, 433, 229
- Yong, D., Norris, J. E., Bessell, M. S., et al. 2013, *ApJ*, 762, 27
- Zucker, D. B., Belokurov, V., Evans, N. W., et al. 2006, *ApJ*, 643, L103



# Acronyms

<b>2MASS</b>	Two Micron All Sky Survey
<b>AGB</b>	asymptotic giant branch star
<b>arcmin</b>	arcminutes
<b>arcsec</b>	arcseconds
<b>BCD</b>	blue compact dwarf galaxy
<b>BSG</b>	blue super-giant star
<b>Car</b>	Carina
<b>CaT</b>	calcium II triplet
<b>CCD</b>	coupled-charged device
<b>CDM</b>	cold dark matter
<b><math>\Lambda</math>CDM</b>	$\Lambda$ cold dark matter
<b>CFHT</b>	Canada–France–Hawaii Telescope
<b>CMB</b>	cosmic microwave background
<b>CMD</b>	color magnitude diagram
<b>DART</b>	Dwarf Abundances Radial velocity Team
<b>dE</b>	dwarf elliptical galaxy
<b>dex</b>	decimal exponent
<b>dI</b>	dwarf irregular galaxy
<b>DM</b>	dark matter
<b>dSph</b>	dwarf spheroidal galaxy
<b>EMP</b>	extremely metal poor star
<b>ESO</b>	European Southern Observatory
<b>EW</b>	equivalent width

## Appendix A. Acronyms

---

<b>EQW</b>	equivalent width
<b>FLAMES</b>	Fibre Large Array Multi Element Spectrograph
<b>Fnx</b>	Fornax
<b>FWHM</b>	full width at half maximum
<b>GC</b>	globular cluster
<b>GPoA</b>	Great Plane of Andromeda
<b>Gyr</b>	$10^9$ years
<b>HIRES</b>	High Resolution Echelle Spectrometer
<b>HFS</b>	Hyperfine structure
<b>HR</b>	high resolution
<b>HST</b>	Hubble Space Telescope
<b>IFU</b>	Integral Field Unit
<b>IMF</b>	initial mass function
<b>IRAF</b>	Image Reduction and Analysis Facility
<b>ISM</b>	interstellar medium
<b>K</b>	Kelvins
<b>kpc</b>	kilo parsec
<b>LAS</b>	Large area Survey
<b>LG</b>	Local Group
<b>LMC</b>	Large Magellanic Cloud
<b>LTE</b>	local thermodynamical equilibrium
<b>M31</b>	Andromeda galaxy
<b>MARCS</b>	Model Atmospheres in Radiative and Convective Scheme
<b>MDF</b>	metallicity distribution function
<b>MIKE</b>	Magellan Inamori Kyocera Echelle spectrograph
<b>Mpc</b>	mega parsec
<b>MW</b>	Milky Way
<b>Myr</b>	$10^6$ years
<b>MZR</b>	mass-metallicity relation
<b>NLTE</b>	non local thermodynamical equilibrium
<b>NS</b>	neutron star

---

<b>ODF</b>	opacity distribution function
<b>OS</b>	opacity sampling
<b>pc</b>	parsec
<b>PNS</b>	proto-neutron star
<b>RGB</b>	red giant branch star
<b>ScI</b>	Sculptor
<b>SDSS</b>	Sloan Digital Sky Survey
<b>SEGUE</b>	Sloan Extension for Galactic Understanding and Exploration
<b>Sex</b>	Sextans
<b>SF</b>	star formation
<b>SFH</b>	star formation history
<b>SFR</b>	star formation rate
<b>SIDM</b>	self-interacting dark matter
<b>SMC</b>	Small Magellanic Cloud
<b>SNe</b>	supernovae
<b>SNIa</b>	supernova of type Ia
<b>SNela</b>	supernovae of type Ia
<b>SNII</b>	supernova of type II
<b>SNeII</b>	supernovae of type II
<b>S/N</b>	signal-to-noise ratio
<b>UCD</b>	ultra cold dwarf galaxy
<b>UFD</b>	ultra faint dwarf galaxy
<b>UVES</b>	Ultraviolet and Visual Echelle Spectrograph
<b>UKIRT</b>	United Kingdom Infra-Red Telescope
<b>UT</b>	unit telescope
<b>VLT</b>	Very Large Telescope
<b>VPOS</b>	vast polar structure
<b>WD</b>	white dwarf
<b>WDM</b>	warm dark matter
<b>WFCAM</b>	Wide Field Camera
<b>WFI</b>	Wide Field Imager



# Curriculum Vitæ - Romaine Theler



## Personal details

**Date of Birth :** 24th of December 1986

**Nationality :** Swiss

**Status :** single

**Address :** Avenue Henri-Warnery 6 Bis, 1110 Morges, Switzerland

**Mobile:** 079 723 76 23

**Mail:** romaine.theler@epfl.ch

## Formation and diploma

**Since May 2011** PHD Thesis at the Laboratory of Astrophysics of EPFL

**February 2011** Master ès Physique EPFL

with a Master thesis at the Laboratory of Astrophysics of EPFL

**July 2009** Bachelor ès Physique EPFL

**June 2006** Maturité fédérale: Physics, and applied mathematics (Lycée-Collège cantonal des Creusets, Sion)

## Skills

**IT :**  $\text{\LaTeX}$ , Python, C++, Matlab

**Astrophysics :** Iraf, ds9, Daospec

## Professional experiences

**Summer 2010** Summer project at the Laboratory of Astrophysics of EPFL

## Languages

**French:** mother tongue; **english:** B2; **german:** A2.

## **Activities**

**Since 1995** Member of scout group of Sierre

**Since 2005** Adjoint leader in scout group of Sierre

**Since 2006** Formed as scout camp leader by *Jeunesse & Sport*

**Summer 2007** Member of Swiss Service Team at 21<sup>st</sup> World Scout Jamboree in United Kingdom

**Summer 2008** Troop leader at Swiss federal scout camp

**Academic year 2009-2010** Class representative at EPFL

## **Hobbies**

Scouting

Photography

Walks in nature